Tests of Quantum Electrodynamics Using $n = 2$ Positronium

Ross Edward Sheldon

A dissertation submitted in partial fulfillment

of the requirements for the degree of

Doctor of Philosophy

of

University College London.

Department of Physics & Astronomy

University College London

April 16, 2024

I, Ross Edward Sheldon, confirm that the work presented in this thesis is my own. Where information has been derived from other sources, I confirm that this has been indicated in the work.

Abstract

This work presents measurements of $n = 2$ Positronium (Ps) to explore and test bound state quantum electrodynamics theory. A pulsed positron beam was used to produce ground state Ps from a mesoporous silica target. The metastable 2^3S_1 state was produced using a single-colour, single-photon laser excitation in an electric field to generate a Stark mixed state which evolved into the pure 2^3S_1 state upon adiabatic removal of the electric field. In the first experiment the 2^3S_1 annihilation decay rate was measured by determining the 2^3S_1 population over time and correcting for losses. The final result was $\Gamma_{2S} = 843 \pm 72$ kHz, a precision of only 8.5%, but in agreement with theory at 890.0 ± 1.4 kHz. This precision it is not sufficient to test QED corrections, but does represent the first measurement of a Ps excited state annihilation decay rate. In the second experiment ~ 8.6 GHz microwave radiation from a horn antenna was used to investigate the effect of microwave reflection induced frequency dependent power on the measured resonance frequency and asymmetry of line shapes of the $2^3S_1 \rightarrow 2^3P_2$ fine structure interval. This established that horn antennas create microwave fields with a significant component of reflected radiation, inducing shifts of ± 4 MHz from the expected transition frequency but without asymmetry. Finally, in the third experiment, a new precision measurement of the $2^3S_1 \rightarrow 2^3P_2$ interval was made for a result of $8\,627.94 \pm 0.95$ MHz, 1.3σ from the theoretical value, an improvement over the previous measurement which was 4σ from theory and suffered from the reflection effects investigated in this work. However, microwave field effects within the waveguide are still the dominant source of error, therefore new interferometry techniques are proposed to overcome this.

Impact Statement

Positronium (Ps) has been used for decades as a probe to test bound-state quantum electrodynamics (QED). This is because is has only leptonic components and as such is effectively described by QED alone. This work presents the first measurement of an excited state Ps annihilation decay rate, a study of the effects of frequency dependent power of microwave radiation due to reflection effects, and a precision measurement of the $2^3S_1 \rightarrow 2^3P_2$ energy interval of Ps. The first of these, while not a precision measurement capable of testing QED, sets a benchmark for future tests and with improvements given here could achieve a higher precision capable of testing QED corrections. The second aspect of this thesis determines the significant effects of microwave reflection to precision spectroscopy, causing frequency dependent power which can cause apparent shifts to measured transition frequencies. This effect is applicable to precision measurements on any atomic species with an open microwave system which covers numerous avenues of spectroscopy. Lastly a new precision measurement further pushes the ability of Ps to test QED. If deviations from QED calculations are identified it may indicate physics beyond the Standard Model, including new particles or new forces. The current measurement is in agreement with QED predictions, testing 5th order calculations, and further experiments are discussed to test higher order QED corrections and rival other matter-based QED tests which are currently limited by quantum chromodynamic effects. An improvement in precision of three orders of magnitude from the results presented here would allow new constraints to be put on hypothetical forces with scalar mediators.

Acknowledgements

Thanks go to my supervisor, Professor David B. Cassidy, and to everyone in the Ps Spectroscopy group past and present: Dr Alberto Alonso, Dr Lokesh Gurung, Dr Tamara J. (Dr T) Babij, Dr James Palmer, Sam H. Reeder, Dr Don Newson and Rebecca J. Daly. Further thanks go to others in the department: Professor Stephen D. Hogan, Dr Matthew H. Rayment, Dr Adam Deller, Dr Simon Brawley, Professor Phil Jones, John Dumper, Rafid Jahwad, Finn Noyes and Jim Levin.

Naturally thank you to my parents and my grandpa. And also to my nan and grandma who passed away during the course of this PhD.

And lastly, thank you to all my housemates, all those other idiots at RCS: Anu, Ryan, Fran, Leon, Andy, Alex, Hannah, (Our) Shaun, Bert, Will & Bethan, Ria, Nat, Sarah, Katy, Josh, Vac, Aysu, Molly, and of course, Steve.

Contents

1 Introduction **9**

1.1 History of Positronium 9

1.2 Motivation 13

1.3 The State of Ps QED Tests 16

1.3.1 Energy Intervals 16

1.3.2 Annihilation Decay Rates 23

1.4 Contents of this Work 25

2 Theoretical Background **27**

2.1 Annihilation Rates 30

2.2 QED Energy Corrections 33

2.3 Ps in Electric and Magnetic Fields 34

2.4 Spectral Line Shapes 41

2.5 Rydberg Positronium 46

3 Experimental Methods **52**

3.1 Positron Beamline 52

3.1.1 Moderation 54

3.1.2 Positron Trapping 56

3.1.3 Beam Compression 58

3.2 Gamma-ray Detection 62

3.3 Data Acquisition & Analysis 64

3.4 Positronium Formation 68

3.5 Laser Setup . . . 74
3.5.1 Laser Beam Alignment & Selection Effects . . . 76
3.6 SSPALS & Photoionisation . . . 80
3.7 1S $\rightarrow$ 2P Line Shapes . . . 85
3.8 2^3S_1 Production . . . 88
3.8.1 High Voltage Switching . . . 92
3.9 Microwave Transitions & Line Shapes . . . 94
3.9.1 Horn Antenna . . . 96
3.9.2 Waveguide . . . 98
3.10 Rydberg Production . . . 99

4 Simulation Methods 103
4.1 Monte Carlo Atomic Distributions . . . 103
4.1.1 Alignment Induced Doppler Effects . . . 108
4.2 Trajectory Simulations . . . 109
4.2.1 Electric Field Simulations (SIMION) . . . 110
4.3 Microwave Field Simulations (CST Studio) . . . 111
4.4 Line shape Simulations . . . 114

5 Measurement of the Positronium 2^3S_1 Annihilation Decay Rate 119
5.1 Apparatus & Method . . . 120
5.1.1 Additional Loss Effects . . . 126
5.1.2 Experimental Rydberg Correction . . . 128
5.2 Results & Discussion . . . 132
5.3 Conclusion . . . 136

6 Microwave Spectroscopy of $n = 2$ Ps in Free Space 137
6.1 Experimental Setup & Methodology . . . 138
6.2 Simulations . . . 141
6.2.1 Trajectory Simulations . . . 141
6.2.2 FIT Field Simulations . . . 143
6.2.3 Line shape Simulations . . . 148

6.3 Data and Discussion 150
6.3.1 Saturation Data 150
6.3.2 Reflection Effect Data 154
6.4 Conclusions 159

7 Precision Measurement of the Ps $2^3S_1 \rightarrow 2^3P_2$ Interval 161
7.1 Experimental Setup & Methodology 163
7.2 Simulations 172
7.2.1 Microwave FIT Simulations 172
7.2.2 State Probability Simulations 175
7.3 Data and Discussion 176
7.3.1 Error Budget 179
7.3.2 Final Result 183
7.4 Conclusions 186

8 General Conclusions 187

A Appendix: Line Shape Analysis 191

Bibliography 196

Chapter 1

Introduction

The work in this thesis is all about the positronium atom (Ps), and how it can be used to test aspects of fundamental physics. Ps is the bound state of the electron and positron, and like any other atom Ps is bound together by the Coulomb force, but it has some important differences to conventional atoms due to its nature as a particle-antiparticle pair. Some of these differences make it an excellent subject for study, while others make those studies very hard. This chapter will give an overview of Ps, its history, and why it remains an interesting and evolving field of study over seventy years after its discovery.

1.1 History of Positronium

Antimatter as a concept was proposed when the positron (e^+, antiparticle of the electron, e^-) was predicted as a consequence of the Dirac equation in 1928 [100]. Experimental confirmation came in 1932 from Anderson who, when looking at cosmic rays, discovered a particle with the same mass as an electron but the opposite charge [29].

It was not long until the existence of Ps was proposed by Mohorovičić in 1934 [202]. At least three other independent predictions were made over the next 12 years [222, 233], with one also predicting polyelectrons (atoms, ions and molecules formed of electrons and positrons) [274]. One of these, Ruark in 1945, coined the name positronium for this bound state [233].

Ps was experimentally discovered almost twenty years later in 1951 by Deutsch

who observed the change in time of positron annihilation in a series of different gasses after emission from a ^{22}Na source [96], see Figure 1.1(a). This change in decay time was due to the different chemical quenching properties of the gases used, low quenching in N_2 but progressively higher quenching in O_2 and NO, respectively. After his discovery Deutsch measured the annihilation rate of the triplet ground state (ortho-Ps or o-Ps) [97], which matched the calculation of Ore and Powell [215], see Figure 1.1(b). He also measured the hyperfine splitting (HFS) of the ground state using microwave spectroscopy, with a result that deviated 4σ from theory (Figure 1.1(c)) [98]. Despite these measurements experimental progress was slow because producing the positrons necessary for Ps formation was still an inefficient process.

The development of the slow positron beam created new interest, with its first use at University College London (UCL) in 1972 [51], utilising a process known as moderation whereby the fast β^+ radiation from ^{22}Na was cooled by interactions with MgO coated Au[1]. This type of beam was used at Brandeis University for the first detection of excited state Ps by observing Lyman-α radiation from the fluorescence decay of $n = 2$ state Ps which was produced directly from positron implantation in a copper target [52]. This same beam was used for the first fine structure measurement of Ps, whereby the microwave induced change from the long lived $2\,^3S_1$ state (2S or Ps*) to the short lived $2\,^3P_2$ state (2P) was measured as an increase in the Lyman-α radiation on resonance [196].[2]

The first optical excitation was performed seven years later in 1982 by Chu and Mills using an early pulsed positron beam that used a magnetic bottle to confine and release the positrons collected from a ^{58}Co source with a cryogenically

[1] A moderator is something that turns fast positrons into slow positrons. The positrons from a particle accelerator or a radioactive source, which are the most common positron sources, usually have very high energy, > 100 keV. This means that their cross-section for Ps formation and other processes is very low, thus moderators are needed to lower the energy of the positrons to a level where Ps formation etc. is more likely. [239]

[2] The spectroscopic notation used in this work is $n^{2S+1}\ell_J(M_J)$ in the spherical basis $|nS\ell JM_J\rangle$ [43]. n is the principle quantum number, S is the total spin quantum number, ℓ is the total orbital angular momentum quantum number, $J = S + \ell$ is the total angular momentum quantum number, and M_J is the azimuthal projection of J on the quantisation axis. $\ell = 0$ is represented by S, $\ell = 1$ is represented by P, and $\ell = 2$ is represented by D.

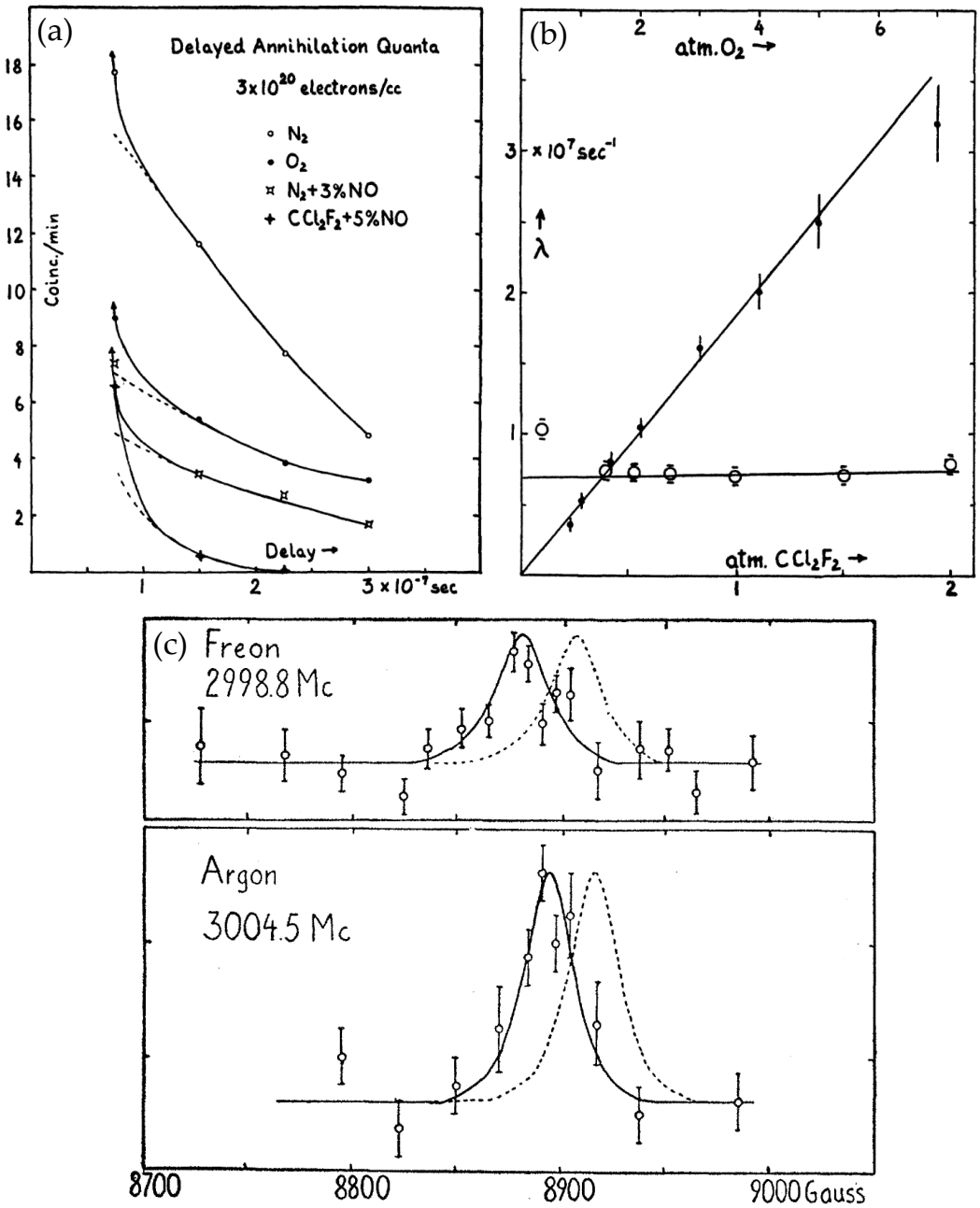

Figure 1.1: A selection of data from the investigations of Deutsch. (a) The decay of o-Ps in various gas production media as measured by the decrease in gamma radiation over time. The first detection of Ps in history. From Reference [96] (b) The decay rate of o-Ps as a function of gas pressure for O_2 and CCl_2F_2 with an extrapolation back to zero to measure the o-Ps decay rate. From Reference [97] (c) Ps annihilation as a function of magnetic field with a fit to extract the zero-field value of ν_{HFS}. From Reference [98]

cooled single-crystal Cu moderator [72]. The positrons were implanted into a Cu Ps conversion target. In this experiment a Nd:YAG pumped a tunable dye laser which drove the $1\,^3S_1 \rightarrow 2\,^3S_1$ transition. Their measurement was in agreement with the contemporary theory [110, 114], but had a significant error, primarily from a poor frequency reference [72].

Further advances in positron beam technology improved the number of positrons available. A more efficient positron moderator was developed by Mills and Gullikson in 1986 with an efficiency of $0.70 \pm 0.02\%$ [197]. Neon gas was frozen onto the positron source which resulted in a two-fold increase in efficiency over the next best moderators at the time [259]. This would again be more than doubled in 1990 using an improved geometrical structure [166]. Another significant advance was the development of the Surko buffer-gas trap which was fully realised in 1992 in the apparatus of Reference [205]. Positrons were cooled using collisions with N_2 gas while confined by a magnetic field and trapped in an electrical potential well, then ejected after a fixed accumulation time, collecting up to 10^7 positrons within 40 s.

Although slow pulsed positron beams were becoming more prevalent, work was also done using accelerator produced positron beams which typically offer larger numbers of positrons per pulse but much more limited access. In 1990 Ziock et al. observed Rydberg Ps atoms for the first time, exciting from $n = 13 - 15$ [283] and in 1993 Hagena and Ley updated the full set of $n = 2$ (triplet) fine structure measurements [134, 175]. Both of these studies continued to use metal conversion targets. Ziock et al. used Cu to make o-Ps, while Hagena and Ley used Mo to make the $2\,^3S_1$ state.

From the mid-2000s Ps research was renewed with multiple advances that are key to the work presented here[3]. In 2008 Liszkay et al. developed mesoporous silica to convert positrons to Ps with low kinetic energies [180]. In 2010 Cassidy et al. presented a new analysis technique for positron studies called SSPALS that involved

[3] And others which are not, including the first detection of the Ps molecule Ps_2 [66], the first electrostatic guiding of Rydberg Ps [90], focusing a beam of Rydberg Ps [158], and production of antihydrogen using Ps [11].

measuring the annihilation events of multiple positrons at once, rather than one at a time, dramatically improving count rates [62]. More precision studies of the o-Ps decay rate (e.g. References [153, 163]) and the $1^3S_1 \rightarrow 2^3S_1$ transition [108] were performed, as well as complementary theoretical work (e.g. References [5, 8, 105]. This thesis continues this line of work using the pulsed UCL slow positron beamline to perform QED tests on Ps, the reason for doing which is presented in the next Section.

1.2 Motivation

Ps has several challenges in its study, firstly, it is hard to produce due to the requisite source of antimatter. Secondly, Ps is typically very fast[4], even at low energy, due to the light mass of Ps ($m_{\mathrm{Ps}} = 2m_e$ where m_e is the mass of the electron) and $K = \frac{1}{2}mv^2$. Lastly, it is unstable, eventually decaying into gamma-rays due to the finite chance of the positron and electron meeting, a process known as self-annihilation. Despite this, Ps has a key characteristic which makes it attractive to study. Ps is a purely leptonic system, being made of a lepton particle-antiparticle pair, and as such has no hadronic composite particles (i.e. a proton). This means that it is described primarily by quantum electrodynamics (QED) with negligible contributions from the less well understood quantum chromodynamics (QCD) which are much more prominent in conventional atoms and anti-atoms due to the quarks in the nucleus[5]. Because of this fact Ps proves to be a valuable test-bed of bound-state QED theory, being the simplest two-particle bound system [161, 162].

Because of the difficulties involved in Ps physics, precision measurements of Ps require much work to reach an equivalent level of precision compared to hydrogen (H) and other QED test species (e.g. References [126, 159, 164, 186, 223]). For example, the $1^3S_1 \rightarrow 2^3S_1$ transition in Ps has been measured to a precision of 2.6 parts per billion (ppb), confirming QED corrections to the 5^{th} order ($\mathcal{O}(\alpha^5)$) [108], though $\mathcal{O}(\alpha^6)$ has been calculated with $\mathcal{O}(\alpha^7)$ calculations ongo-

[4] For the slowest source of Ps the average velocity is $\langle v \rangle \approx 38$ km/s [198].

[5] At a certain level of loop correction to the QED theory strong and weak force interactions will manifest but this is not true at the current level of calculation [10, 42, 122].

ing [10][6]. The same measurement in H is at a precision of 4.5×10^{-15} [186] (that's fifteen digits of precision!), where QED calculations are evaluated up to $\mathscr{O}(\alpha^7)$ with $\mathscr{O}(\alpha^8)$ ongoing. Even the equivalent measurement in antihydrogen is at a precision of 2.2×10^{-12} [14]. The precision of measurements in H has been sufficient to measure fundamental constants [240] and test Lorentz symmetry [186] for decades. The limiting factor of these measurements to test bound state QED comes from nucleus related effects such as the proton radius (which cannot be calculated to high precision and must be measured [19]) and not QED calculations [162].

Tests of QED in Ps can be done by measuring atomic energy intervals and annihilation decay rates and comparing them to QED theory. The QED model allows comprehensive calculation of Ps properties to high precision because the system is hydrogenic. It is proposed that any measured deviation from QED predictions could arise from Ps interacting with particles and forces outside the standard model [224, 260, 261]. These effects would be much smaller than first order QED corrections but could provide insight into unconfirmed particle models and 'new physics'. For example, the ratio of the interaction strength of a new force with the mass of its scalar mediator can be constrained using Ps [132]. The precision of Ps $n = 2$ fine structure energy interval measurements requires an improvement of three orders of magnitude to rival matter based experiments in this task, while the $1^3S_1 \rightarrow 2^3S_1$ measurements require only one order of magnitude improvement [132].

Positronium is the lightest and simplest atomic state, but not the only one to be described purely by bound-state QED. Muonium, the bound state of an electron and an antimuon, has been used to study bound state QED, possessing the same advantages as Ps (e.g. References [159, 214]), but it is harder to produce than Ps and has its lifetime limited by the finite muon lifetime. True-muonium[7] can theoretically exist but is even harder to produce than muonium and as yet has not been observed,

[6] QED corrections are calculated as a power series of the fine structure constant α, with higher order terms typically having smaller contributions. See Section 2 for more detail.

[7] Which has become the term for a muon-antimuon bound state. An -onium atom was originally named for the bound state of a particle-antiparticle pair. However, this is muddied by the referral of a bound electron-antimuon as 'muonium', which has become commonplace.

although experiments have been proposed for this purpose [36, 39, 154]. Other exotic atoms such as antihydrogen, muonic-hydrogen and muonic-helium do not have the advantage of being only leptonic systems and are also harder to produce than Ps, but can still be used to probe fundamental physics (e.g. References [14, 170, 223]).

Other uses of Ps include measurements of fundamental constants, such as a proposed experiment to measure the Rydberg constant [67] based on a study in H [89]. Measuring this in a system with no composite particles removes a significant source of uncertainty [67], potentially contributing to the ongoing proton radius puzzle[8], though matching the precision of current matter based measurements will require substantial advances.

Being the bound state of a particle-antiparticle pair Ps can be used to test charge-parity (CP) violation in the lepton sector, which if found may offer a possible explanation of the matter-antimatter asymmetry problem [234]. The Standard Model predicts that the creation of matter and antimatter was equal at the big bang, however the universe is highly matter dominant, hence the matter-antimatter asymmetry problem [117]. CP violation has been observed in the hadron sector, famously kaons [71], but remains to be observed in the lepton sector, while the matter-antimatter asymmetry is true for both types of particle. C violation tests in Ps can be done by observing atomic transitions which are forbidden by parity symmetry in zero external magnetic field [74, 75, 175]. To test CP violation the momentum and polarisation of annihilation quanta can be investigated [48, 246, 280], and CPT violation (where T is the time reversal symmetry) has been investigated this way too [41, 203].

Another possible explanation for the matter-antimatter asymmetry is that antimatter behaves differently in a gravitational field, be it by a different magnitude or as repulsive "anti-gravity" [169, 212, 238]. The latter option has been ruled out by a free-fall measurement of antihydrogen by the ALPHA collaboration at CERN[9], with Earth's acceleration due to gravity on antihydrogen measured

[8]This puzzle originates from several differing measurements of the proton radius, varying by about 4% [223]. Although recent results [44, 278] have partially resolved this, there is still debate surrounding the issue [160].

[9]Two other collaborations at CERN are trying to measure antimatter gravity using antihydrogen.

at $\bar{g} = (0.75 \pm 0.21)g$ (where g is the acceleration due to gravity on conventional matter) [30], though the magnitude has not yet been precisely determined. Ps based tests of antimatter gravity using a neutral atom interferometer [45, 165, 213, 235] are planned at UCL using Rydberg states [67] (utilising methods similar to those found in References [70, 217, 218, 254]), and by the QUPLAS collaboration using the metastable 2S state [33].

In this work measurements of both energy levels (the $n = 2$ triplet fine structure) and annihilation decay rates (the triplet 2S decay rate) of Ps are performed as tests of bound state QED and to help characterise a system that is intended for use in numerous other precision experiments [33, 67]. The next section contains a detailed review of the current status of energy interval and annihilation decay rate measurements in Ps.

1.3 The State of Ps QED Tests

1.3.1 Energy Intervals

The energy level structure of Ps is shown in Figure 1.2, with more details in Chapter 2. Table 1.1 shows the most recent precision measurements of Ps energy intervals and the corresponding theoretical calculations, with their respective precision given in parts-per-million (ppm). Ps energy intervals are evaluated as an expanded power series of the fine structure constant α, see Section 2.2. The 6^{th} order ($\mathscr{O}(\alpha^6)$) QED correction is fully calculated [82, 83, 282] with work on $\mathscr{O}(\alpha^7)$ ongoing (e.g. [3, 6–9, 38, 105]). Three intervals in particular have been targeted for high precision measurements: the $1\,^1\mathrm{S}_0 \rightarrow 1\,^3\mathrm{S}_1$ hyperfine splitting (HFS) interval; the $1\,^3\mathrm{S}_1 \rightarrow 2\,^3\mathrm{S}_1$ interval, and the $2\,^3\mathrm{S}_1 \rightarrow 2\,^3\mathrm{P}_J$ (2S $\rightarrow$ 2P) fine structure intervals.

The HFS interval, ν_{HFS}, was the first energy interval measured by Deutsch in 1952 using Ps produced in a gas [98]. He measured the Zeeman splitting of the o-Ps $M_J = \pm 1 \rightarrow M_J = 0$ interval in a magnetic field, which can be used to calculate ν_{HFS} as in H [206]. Multiple iterations of this experiment have been

GBAR [182, 219] and AEGIS [102, 237] both intend to use an interferometry technique and use Ps as part of the antihydrogen formation process. Muonium has also been proposed to measure antimatter-gravity using interferometry [31].

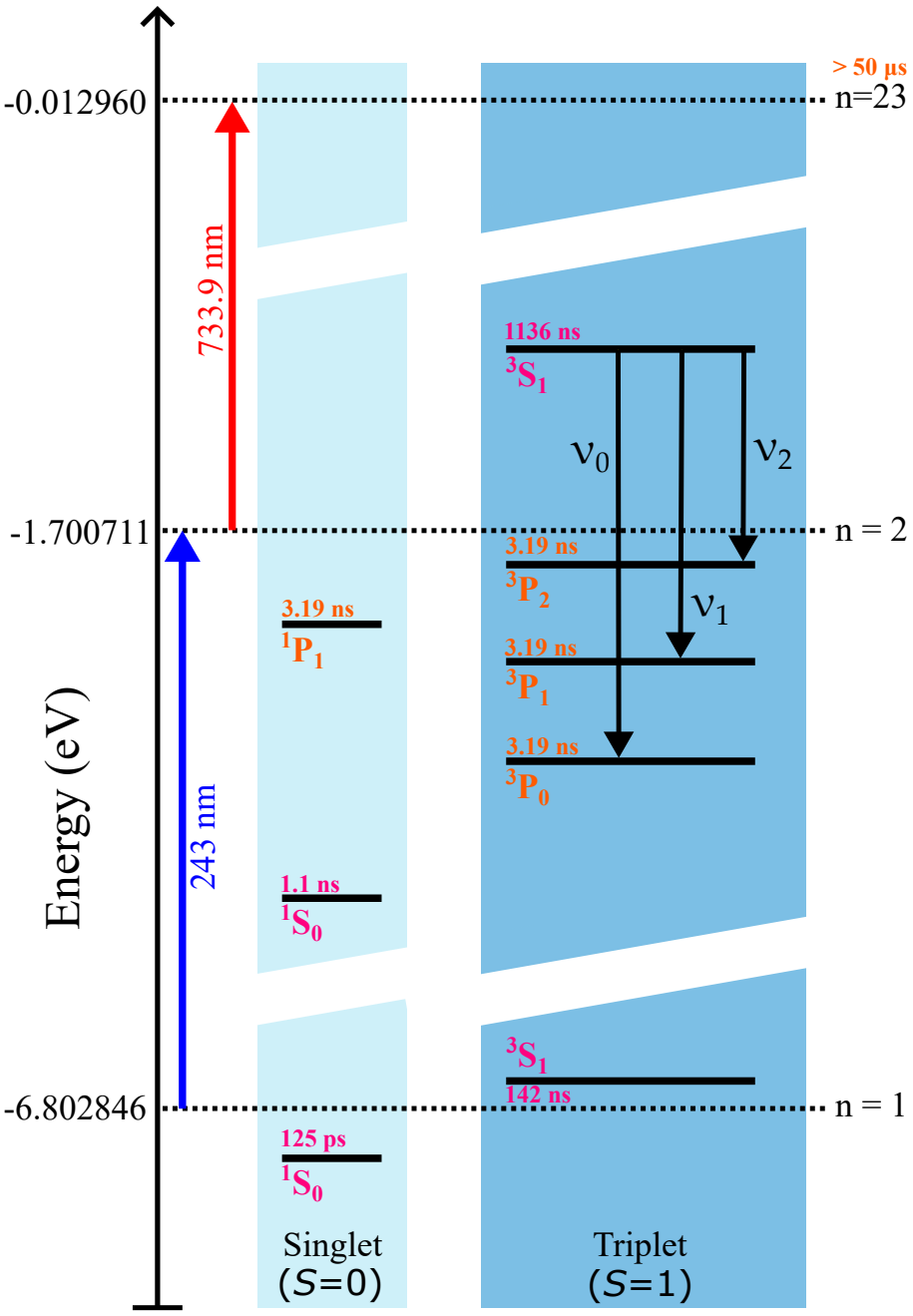

Figure 1.2: The Bohr energy levels of the $n = 1$, $n = 2$ and $n = 23$ states with the field free non-degenerate sub-states of the former two levels included. Arrows indicate allowed transitions discussed in this work. The states are labelled with their dominant decay lifetime, self-annihilation in magenta and fluorescence in orange. Adapted from Reference [24].

Transition	Measured (MHz)	$\Delta_{meas.}$ (ppm)	Theory (MHz)	$\Delta_{theo.}$ (ppm)
$1^1S_0 \rightarrow 1^3S_1$	203 394.2(2.1)	10 [153]	203 391.69(41)	2.0 [168]
$1^3S_1 \rightarrow 2^3S_1$	1 233 607 216.4(3.2)	0.002 6 [108]	1 233 607 222.18(58)	0.000 8 [83]
$2^3S_1 \rightarrow 2^3P_0$	18 501.02(66)	36 [131]	18 498.25(8)	4.8 [83]
$2^3S_1 \rightarrow 2^3P_1$	13 012.42(1.68)	129 [134]	13 012.41(8)	6.1 [83]
$2^3S_1 \rightarrow 2^3P_2$	8 624.38(1.50)	174 [134]	8 626.71(8)	9.3 [83]
$2^3S_1 \rightarrow 2^1P_1$	11 180.0(9.0)	600 [175]	11 185.37(8)	7.2 [83]

Table 1.1: A comparison of the most precise experimental measurements and theoretical calculations of Ps energy intervals designed to test QED. The precision Δ of the measurements and calculations is given in the adjacent columns in units of parts-per-million (ppm).

performed over the years [53, 54, 104, 151, 193, 195, 232, 252, 271, 272], but by 1984 the experimental value was 3.9σ from theory [232]. This discrepancy appears to have been resolved in the latest variation on this methodology by Ishida et al. [153]. Their experiment compensated for the effect of Ps thermalisation in the gas medium (which was being used to produce the o-Ps) by taking into account timing information of the positron annihilation events. They measured ν_{HFS} as a function of time to determine when thermalisation had occurred, taking their final value of ν_{HFS} from late times when the Ps was thermalised. They obtained a result of $\nu_{\mathrm{HFS}} = 203.394\,2 \pm 0.002\,1$ GHz [153], 1.2σ from theory at $203.391\,82 \pm 0.000\,46$ GHz (summarised in Reference [10]) and 2.6σ from previous experimental results $203.388\,82 \pm 0.000\,67$ GHz [193, 232], confirming $\mathcal{O}(\alpha^6)$ QED corrections.

Other techniques have been proposed to measure this interval, including (in order of current precision): a measurement of the quantum oscillation of polarised Ps in a magnetic field [236]; a direct mm-wave measurement of the interval [200, 279]; replacing rf radiation with a static periodic magnetic structure [209]; and an optical technique of using a crossover resonance in a field mixed $1^3S_1 \rightarrow 2^3P_J$ transition [64]. The best of these measurements is currently at a precision of 205 ppm [236], two orders of magnitude below the most precise measurement [153].

The most precisely calculated and measured interval in Ps is the $1^3S_1 \rightarrow 2^3S_1$ interval at $1\,233\,607\,222.18 \pm 0.58$ MHz [83] and $1\,233\,607\,216.4 \pm 3.2$ MHz [108], respectively[10]. The latest measurement comes from Fee et al. in 1993 who achieved a precision of 2.6 ppb using a two-photon Doppler free technique. This precision is sufficient to test the QED corrections up to the $\mathscr{O}(\alpha^5)$ contributions (uncalculated at the time). But this result is now almost two orders of QED corrections behind theory calculations [108]. The laser system used was continuous wave (CW), unlike the initial measurement of Chu & Mills which used pulsed lasers [72, 73]. A high laser intensity is required to drive the transition which is easiest to achieve with a pulsed laser, but pulsed systems have a large spectral bandwidth, and the larger the measured line width of the transition the lower the precision. This is why Fee et al. used a CW laser in a cavity to obtain sufficient intensity, but with a spectral bandwidth orders of magnitude lower than pulsed systems offer. The primary contribution to the error was the Te_2 frequency reference used to calibrate the laser, being 1.0 ppb of the final precision, but this could be reduced by more than an order of magnitude using a frequency comb [142]. The current state of Ps calculation puts the theoretical precision of the $1^3S_1 \rightarrow 2^3S_1$ interval at 0.8 ppb [83]. As previously stated Ps has not yet achieved the precision of H QED tests, but new experiments of the $1^3S_1 \rightarrow 2^3S_1$ transition are being planned [80, 120, 142].

The first measurement of the $n = 2$ fine structure was of the $2^3S_1 \rightarrow 2^3P_2$ interval by Mills et al. in 1975 [196]. The metastable 2S state was made directly during Ps production from positrons implanted into a Cu target which was in a circular waveguide cavity. Microwave radiation was applied driving 2^3S_1 atoms to the 2^3P_2 state and the resulting increase in Lyman-α radiation from the fluorescence of the 2^3P_2 state was observed. Subsequent measurements of all three $2^3S_1 \rightarrow 2^3P_J$ intervals where $J = 0, 1, 2$, known as the ν_J transitions, by Hatamian [140] and Hagena [134] used a similar method with a few variations such as a Mo conversion target and rectangular waveguides. The 2^3S_1 production method in these measurements has several disadvantages. The most significant of these is the low production

[10] This corresponds to a UV photon of $\sim$243 nm.

efficiency, estimated to be $< 0.1\%$ [129]. 2S atoms that are produced in this way have high energies estimated to be 1 eV on average, resulting in Doppler, transit-time and power broadening [129]. As of 1993 the most precise measurement of ν_2 had a precision of 129 ppm and was sufficient to test $\mathscr{O}(\alpha^5)$ QED calculations but not the newer $\mathscr{O}(\alpha^6)$ [134], leaving the ν_{HFS} measurement as the best current test of QED corrections in Ps.

The next measurement of these transitions was by Gurung et al. at UCL using slower Ps, more efficient production of the 2S state, and a method with higher detection efficiency [131, 132]. The methods of Ps production and excitation are the same as used in this work and will be discussed in detail in Chapter 3. In these measurements the 2S Ps flew into a waveguide after production (see Figure 1.3(a)). The waveguides were rectangular, driving electric dipole transitions, similar to those used in this work (see Section 3.9.2). A different waveguide with appropriate dimensions was used for each of the three ν_J transitions to provide the most uniform power across the frequency range of each line shape. In the waveguide the 2S atoms were driven to the 2P state using microwave radiation and the change in the time of annihilation was used to generate line shapes that could be fitted with a Lorentzian function to extract the transition frequency. This was done in multiple magnetic fields and the transition frequency was extrapolated back to zero-field to compensate for the Zeeman shift and obtain a value to compare with QED.

The value obtained for the ν_0 transition was $18\,501.02 \pm 0.61$ MHz, 4.5σ away from the theoretical value of $18\,498.25 \pm 0.08$ MHz. The ν_1 and ν_2 transition measurements were not conclusive because the line shapes were highly asymmetric, this was inconsistent with theory which suggested asymmetry should only occur at the ~ 100 kHz level of precision when quantum interference (QI) with the neighbouring J states becomes relevant. Because there was no valid line shape model that included this asymmetry the transition frequencies could not be reliably extracted from the data. An example of these line shapes and the ν_0 result are shown in Figure 1.3(c - d) and (b), respectively.

The cause of the observed shift and asymmetries was explored in a theoretical

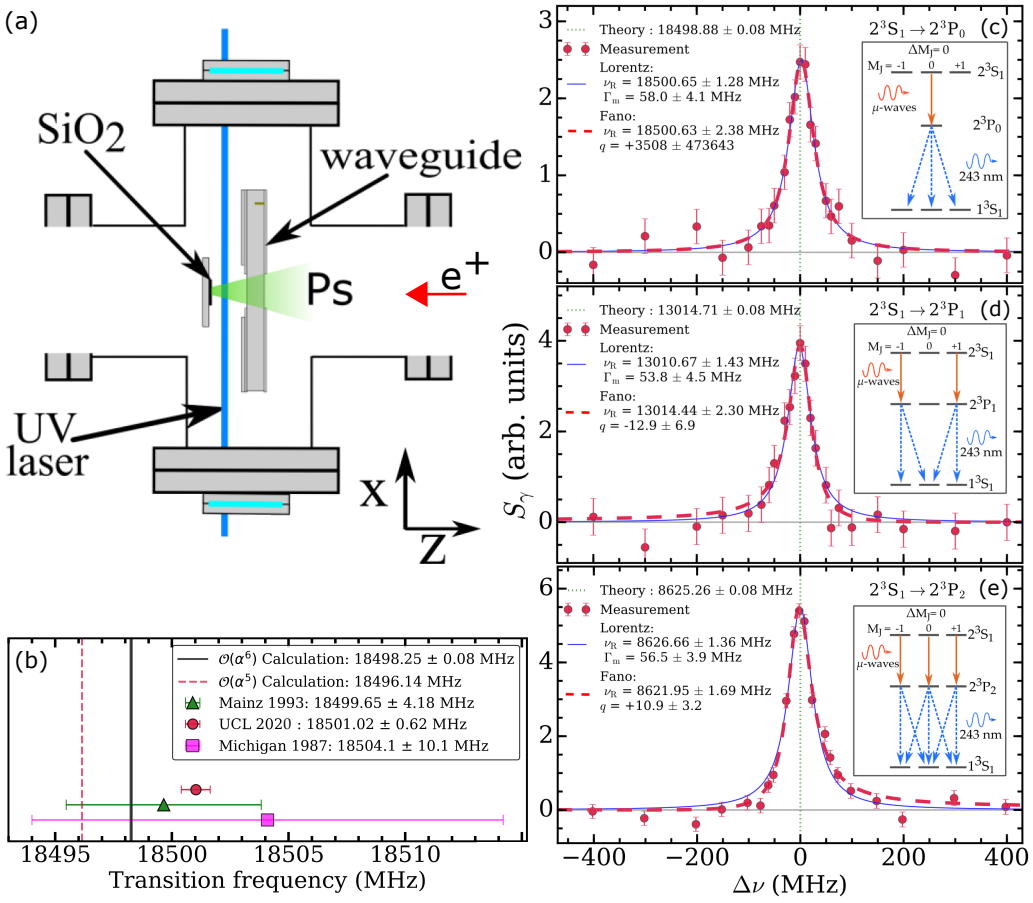

Figure 1.3: (a) The chamber and waveguide setup used in the 2020 UCL fine structure measurements. (b) The result of the ν_0 measurement with historical measurements (points) and the theory (solid black line shows $\mathcal{O}(\alpha^6)$ and dashed red line shows $\mathcal{O}(\alpha^5)$ calculations) for comparison. (c-e) Examples of the measured line shapes ν_0, ν_1 and ν_2, respectively, with the latter two displaying prominent asymmetry. The insets show the allowed transitions and decay paths, and the fits show the Lorentzian and Fano functions (see Section 2.4 for details on line shape models), the latter of which was used to quantify asymmetry. Adapted from References [15, 131, 132]

study by Akopyan et al. [15]. This was done by simulating the microwave fields in a realistic model of the waveguide and surrounding vacuum chamber and putting the simulated data into a full master equation solver with 28 states including the $n = 1$ and $n = 2$ levels. Using this model various systematics were investigated, and one was identified as the most likely cause of the shift and asymmetry. This effect was frequency dependent microwave power due to reflections of the microwave radiation. In short, microwaves emitted from the open ends of the waveguide were being reflected back into the waveguide from the metal ends of the vacuum chamber, see

Figure 1.3(a). The reflections varied with frequency resulting in an increase or decrease in power at different frequencies, depending on the magnitude of the reflections and their relative phase with the TE_{10} mode in the waveguide. This frequency dependent power can shift data points in the line shape up or down compared to the uniform power case. Figure 1.3(d) & (e) shows an example of this whereby in (e) the ν_2 points on the high frequency side of the line shape are higher than those on the low frequency side because there is more power at the higher frequencies than the lower frequencies. The Lorentzian function (which is the expected model for a line shape with minimal broadening and is symmetric by definition, see Equation 2.21) and the Fano function (which takes into account asymmetry effects, see Section 2.4 for more information) were fitted to this data and disagree with each other because of this asymmetry. Because neither of these functions accounts for the reflection effects the extracted frequencies cannot be used for precision measurements.

Lorentzian and Fano functions fitted to the simulated line shapes reproduced shifts and asymmetries on the same order of magnitude as those observed in experiment, including shifts without asymmetries. This provides a likely qualitative explanation for the asymmetry in the ν_2 and ν_1 transitions, but also introduces a systematic error on the order of MHz for the ν_0 measurement, because there may be less obvious reflection effects within the data shifting individual data points. The simulations did not exactly reproduce experimental data and without some means of measuring the power variation inside the waveguide the previous measurements cannot be corrected for this effect, requiring new measurements to be made. This frequency dependent power effect is more significant in the broad MHz wide line shapes of $n = 2$ Ps than narrower kHz wide transitions and deserves investigation to help eliminate it in future precision measurements and characterise it for other studies using microwave spectroscopy. A part of this work focuses on examining these effects and removing reflections for a new precision measurement of ν_2.

In addition to the three $n = 2$ fine structure intervals already mentioned there exists the option of driving the $2\,^3S_1 \rightarrow 2\,^1P_1$ transition which is forbidden by charge (C) conjugation symmetry and the electric dipole transition rules. This transition is

possible to drive in a magnetic field due to Zeeman mixing with the 2^3P_1 state, despite electric dipole transition rules forbidding $\Delta S \neq 0$. Two measurements have been made of this transition, though both suffer from poor statistics due to inefficient production of 2S atoms and the small dipole transition strength in the low magnetic fields used [74, 175]. As well as the energy interval measurement this experiment can place limits on the presence of C violation in Ps to explore CP violation in leptons in relation to the matter-antimatter asymmetry problem [75]. Efforts are also being made to measure the $n = 2$ hyperfine interval ($2^3S_1 \rightarrow 2^1S_0$) at ~ 25.4 GHz as a means to corroborate the $n = 1$ HFS measurements which have had historical uncertainty, as discussed above. The initial method proposed was a high Q-factor microwave resonator designed to provide the power required for the M2 magnetic dipole transition [141]. However, this would cause the states to be highly Stark shifted and Stark mixed (reducing the lifetime of the triplet 2S state) by the strong electric field component of the microwave radiation [94]. As a consequence, alternative methods are being considered such as magnetic field interferometry (as demonstrated in H [50]), static periodic magnetic fields [209], or a two photon process of $2^3S_1 \rightarrow 2^1P_1 \rightarrow 2^1S_0$ which does require a magnetic field as mentioned above.

Other optical transitions have been observed in Ps including $1^3S_1 \rightarrow 3^3P_J$, $3^3P_J \rightarrow 2^2S_1$ [12] and $2^3P_J \rightarrow n^3S/D_J$ where $n = 8-30$ [266] which could be used to perform precision tests given detailed experimental consideration similar to the Fee measurement [108][11]. And through the $n = 3$ and Rydberg states the $n = 3$ fine structure and inter-Rydberg mm-wave transitions can be targeted, respectively.

1.3.2 Annihilation Decay Rates

The annihilation decay rates of Ps have been calculated to a lower order of QED than the energy levels at $\mathcal{O}(\alpha^3)$, but experimental precision is still not yet able to

[11] The Ps negative ion, Ps^-, has also been produced and measured spectroscopically, including its photodetachment threshold [191] and a shape resonance [190] with a predicted infinite number of Feshbach resonances still to be observed [152]. However Ps^- is very short lived at just 0.479 ± 0.001 ns [69] and has no excited states [152], limiting the opportunities for precision spectroscopy. Another Ps species available for spectroscopy is the dipositronium molecule, Ps_2, which has four excited states [61, 66]. Excitation of Ps_2 has been achieved but not precise enough to perform an energy interval QED test [63].

State	Experiment (MHz)	Theory (MHz)
1^1S_0	7990.9(1.7) [213 ppm] [16]	7989.618(18) [2 ppm] [10]
1^3S_1	7.040 1(7) [99 ppm] [163]	7.039 979(19) [3 ppm] [10]

Table 1.2: A comparison of experimental and theoretical precision of the measured self-annihilation decay rates of Ps.

rival theory. A comparison of the measured and calculated Ps decay rates is shown in Table 1.2.[12]

The first measurement of a Ps decay rate was by Deutsch who measured the o-Ps decay rate, Γ_{o-Ps}, and obtained 6.8 ± 0.7 MHz by producing o-Ps inside a gas and measuring the decay rate as a function of pressure and extrapolating back to zero gas pressure [97]. As with the Ps HFS measurements described above, subsequent Γ_{o-Ps} measurements using similar techniques deviated from theory by $> 4\sigma$, e.g. References [119, 125, 273], which was dubbed the 'ortho-Ps lifetime puzzle'. This was eventually resolved after the identification of incomplete thermalisation of the o-Ps in the production gas [35], similar to the ν_{HFS} measurements. The most precise determination of Γ_{o-Ps} to date is 7.040 1 $\pm$ 0.000 7 MHz [163], which is the combination of several results up to 2009 [34, 35, 255] and is in good agreement with the theoretical value of 7.039 988(10) MHz [5]. This is sufficient to verify theory to $\mathcal{O}(\alpha^2)$, leaving room for improvement.

The only other annihilation decay rate to be measured is that of p-Ps state, Γ_{p-Ps}. The first experiment measured the natural line width of the ν_{HFS} transition which is determined by the short p-Ps lifetime. However, this type of measurement requires accurate knowledge and minimisation of all other broadening mechanisms (i.e. Doppler and power broadening) and had an error of 1.4% [253] (see Section 2.4 for an explanation of line shape broadening mechanisms). The most recent result by Al-Ramadhan was sufficient to verify the $\alpha^2 ln(\alpha)$ term of the Γ_{p-Ps} calculation at a precision of 215 ppm and a result of 7990.9 $\pm$ 1.7 MHz [16]. This result was

[12] Ps^- has had three measurements of its decay rate: the first by Mills in 1983 [194], another by Fleischer et al. in 2006 [112], and most recently by Ceeh et al. in 2011 [69]. The latest measurement has a value of $2.087\,5 \pm 0.005\,0$ GHz which was measured by counting the decrease in Ps^- ions as a function of distance from the diamond-like carbon production target [69]. The theory is fully calculated to $\mathcal{O}(\alpha^2)$ with a value of 2.087 963(12) GHz [227], in agreement with experiment.

obtained by measuring $\Gamma'_{\mathrm{o-Ps}}$ in varying magnetic fields, in higher magnetic fields more $\Gamma_{\mathrm{p-Ps}}$ is mixed with $\Gamma_{\mathrm{o-Ps}}$ and knowing the zero-field value of $\Gamma_{\mathrm{o-Ps}}$ a value of $\Gamma_{\mathrm{p-Ps}}$ can be extracted.

To date only ground state decay rates have been measured[13] leaving the theory untested for excited states. Excited state self-annihilation is suppressed due to the n^3 scaling of the annihilation decay rate. This means that states will only have a significant annihilation rate (i.e. a state where the self-annihilation decay rate is dominant over the fluorescence decay rate) if there is no available lower energy state to fluoresce to[14]. The only two states that fulfil this criteria are the $2\,^3\mathrm{S}_1$ and $2\,^1\mathrm{S}_0$ states which have calculated annihilation lifetimes of 1136 ns and 1.1 ns, respectively (from equations contained in Reference [10]). Probing a singlet state is inherently difficult due to their short lifetimes, therefore, the $2\,^3\mathrm{S}_1$ state has been targeted in order to test the excited state QED annihilation decay rate calculations and characterise it for other precision tests such as energy interval QED [244] and antimatter gravity [33] investigations.

1.4 Contents of this Work

In this work several tests of QED in Ps are performed and new systematic effects presented and explored. Chapter 1 presents the context of this research; Chapter 2 contains the relevant theory behind the measurements; Chapter 3 details the methodology used to perform the measurements (including the positron beamline, lasers, detection and analysis methods, the latter of which is further expanded upon on in Appendix A); and Chapter 4 outlines the simulation tools used to understand physical processes. Chapter 5 presents the first measurement of the annihilation decay rate of $2\,^3\mathrm{S}_1$ Ps as a step toward precision studies of excited state decay rates. Chapter 6 recounts the use of free-space microwave radiation to drive the $2\,^3\mathrm{S}_1 \rightarrow 2\,^3\mathrm{P}_2$ transition in order to investigate frequency dependent power from reflection effects which was ascribed to be the cause of previously identified shifts and asymmetries.

[13] Excited state fluorescence lifetimes have been measured but not to a high precision [85, 91]. Fluorescence lifetimes depend on the energy separation of the states involved [113] so a precision measurement would be an indirect test of energy intervals.

[14] Although Rydberg states may still self-annihilate, ℓ-state mixing reduces this by more than n^3.

Chapter 7 contains the current highest precision measurement of the $2^3S_1 \rightarrow 2^3P_2$ having minimised the reflection effects investigated in Chapter 6. Lastly, Chapter 8 presents the conclusions and outlook of this work.

Chapter 2

Theoretical Background

The atomic structure of Ps is hydrogenic, being a pair of Coulomb bound particles of equal but opposite charge. The Bohr energy levels of Ps are scaled with those of hydrogen (H) by the ratio of their reduced masses, which is almost exactly a half $\frac{\mu_{\mathrm{Ps}}}{\mu_{\mathrm{H}}} \approx 0.5003$ [43]. A diagram of the energy levels relevant to this work is shown in Figure 1.2, with Bohr energy levels calculated as [113]

$$E_n = \frac{-\alpha^2 \mu_{Ps} c^2}{2n^2} = \frac{-\alpha^2 m_e c^2}{4n^2} = \frac{-6.8 \text{ eV}}{n^2}, \tag{2.1}$$

where $\mu_{Ps} = m_{e^+} m_{e^-} / (m_{e^+} + m_{e^-})$ is the reduced mass of Ps, c is the speed of light and n is the principal quantum number. Bohr energy levels are an approximation and do not include fine/hyperfine structure, at which level the similarities between Ps and H break down, see Section 2.2 for more details and a summary in Reference [10].

The most well studied state of Ps is its ground state which is found in two forms. Ortho-Ps (o-Ps) is a triplet $|S = 1, M_J\rangle$ atom, and para-Ps (p-Ps) is a singlet $|S = 0, M_J\rangle$ atom, where S is the total spin quantum number of the atom and M_J is the azimuthal projection of the total angular momentum quantum number on the axis of quantisation. There are three o-Ps states where the spins of the two particles (which can be either spin up $\uparrow$ or spin down $\downarrow$) are arranged

$$|1,1\rangle = |\uparrow\uparrow\rangle, \tag{2.2a}$$

$$|1,0\rangle = \frac{1}{\sqrt{2}}(|\uparrow\downarrow\rangle + |\downarrow\uparrow\rangle), \tag{2.2b}$$

or

$$|1,-1\rangle = |\downarrow\downarrow\rangle, \tag{2.2c}$$

and one p-Ps state arranged as

$$|0,0\rangle = \frac{1}{\sqrt{2}}(|\uparrow\downarrow\rangle - |\downarrow\uparrow\rangle). \tag{2.3}$$

Radiative decay (fluorescence) in Ps works in the same way as conventional atoms whereby a ground state conventional atom, or even an anti-atom, is stable (barring outside influences) because there is no lower energy level for the singlet state to decay to, and electric dipole selection rules limit transitions from the triplet to singlet state [43][1]. The selection rules for electric dipole transitions govern all fluorescence decays in Ps and are written as:

$$\Delta S = 0, \tag{2.4a}$$

$$\Delta \ell = \pm 1, \tag{2.4b}$$

$$\Delta J = 0, \pm 1, \tag{2.4c}$$

$$\Delta M_J = 0, \pm 1. \tag{2.4d}$$

Where ℓ is the total orbital angular momentum quantum number, and $J = S + \ell$ is the total angular momentum quantum number.

Unlike conventional atoms however, the ground state of Ps is not stable due to its nature as a bound particle/anti-particle pair. This means o-Ps will self-annihilate with a mean lifetime of $\tau^{\text{ann.}}_{\text{o-Ps}} = 142$ ns, and p-Ps with an even shorter mean lifetime of $\tau^{\text{ann.}}_{\text{p-Ps}} = 125$ ps. The next section contains a detailed explanation of self-annihilation, and a summary of the Ps ground state can be found in Table 2.1.

The total fluorescence decay rate of a state, $\Gamma_{\text{flo.}}(n\ell)$, is calculated by sum-

[1] Magnetic dipole transitions are also possible (e.g. Reference [143]), but are much weaker than electric dipole transitions and can be ignored in this work.

State	Spin	State	$\tau_{\text{annihilation}}$(ns)	Primary Decay Path
o-Ps	1	Triplet	142 [215]	3γ
p-Ps	0	Singlet	0.125 [101]	2γ

Table 2.1: A comparison of the properties of p-Ps and o-Ps including their spin states, annihilation lifetimes and decay paths (i.e. the number of gamma-ray photons each state decays into). The annihilation lifetimes and decay paths are discussed further in Section 2.1.

ming over the decay rates of every possible decay path $A_{n'\ell',n\ell}$ (i.e. the Einstein A coefficients) [91, 116],

$$\Gamma_{\text{flo.}}(n\ell) = \sum_{n'\ell'} A_{n'\ell',n\ell}, \tag{2.5a}$$

$$A_{n'\ell',n\ell} = \frac{2e^2\omega^3_{n'\ell',n\ell}}{3\varepsilon_0 hc^3}\frac{\ell_{max}}{2l+1}\langle n'\ell'|r|n\ell\rangle^2. \tag{2.5b}$$

where $\omega_{n'\ell',n\ell} = 2\pi\nu_{n'\ell',n\ell}$ is the angular frequency of the transition, ε_0 is the permittivity of free space, h is the Planck constant, ℓ_{max} is the maximum angular quantum number of the two involved states, e is the charge of the electron (and positron), and the population of excited state atoms falls as $N = N_0 \mathrm{e}^{-\Gamma_{\text{flo.}}t}$, where N is the number of atoms at time t from an initial population N_0. The fluorescence lifetime $\tau_{\text{flo.}} = 1/\Gamma_{\text{flo.}}$ increases with n^4 (for low values of ℓ [91]). This means higher energy states will survive longer before decaying to the ground state, see Table 2.2 for lifetimes of the states relevant in this work.

Equations 2.4 also govern laser excitation from one state to another, making certain single photon excitation pathways forbidden, such as a single photon $1\,^3\mathrm{S}_1 \rightarrow 2\,^3\mathrm{S}_1$ transition. During excitation the value of ΔM_J is controlled by the polarisation of the radiation relative to the quantisation axis, defined by the direction of the applied electric and magnetic field, which in these experiments are colinear in the z-axis. When the radiation is polarised parallel to the field (i.e. the electric field of the radiation is the z direction) $\Delta M_J = 0$ transitions are driven, while if it is perpendicular (i.e. the electric field of the radiation is in the x or y direction) then $\Delta M_J = \pm 1$ transitions are driven [24].

State	$\tau_{\text{annihilation}}$ (ns)	$\tau_{\text{fluorescence}}$ (ns)
1^1S_0	0.125 [101]	–
1^3S_1	142 [215]	10^{16} [267]
2^1S_0	1.0 [10]	243 100 000 [241]
2^3P_0	100 000 [17]	3.19 [43]
2^3P_1	$\sim\infty$ [17]	3.19 [43]
2^1P_1	3 330 000 [18]	3.19 [43]
2^3P_2	384 000 [17]	3.19 [43]
2^3S_1	1 136 [10]	$\sim$243 100 000 [241]
3^3P_J		10.5 [12]
23^3S_1	$\sim$ 1 730 000 [10]	$\sim$ 50 000 [91]

Table 2.2: The calculated radiative and annihilation lifetimes in zero field for all $n = 1$ and $n = 2$ states plus the $3\,^3P_J$ and $n = 23$ state. (Adapted from Reference [24]).

2.1 Annihilation Rates

Self-annihilation of Ps occurs because the electron and positron wavefunctions ψ have a finite probability of overlapping and annihilating, converting the Ps atom to low energy gamma-rays. Self-annihilation is more likely in some atomic states than others (see Table 2.2 for examples). The probability P of annihilation depends on the electron and positron wavefunction overlap, i.e. they can only annihilate when they occupy the same space. This only happens at $\psi(0)$ in the S-states (i.e. $\ell = 0$), due to the their hydrogenic nature [113], where $P \propto |\psi(0)|^2$. Therefore, for states with $\ell > 0$ the annihilation decay rate is negligible because the fluorescence decay rate dominates (often by orders of magnitude). The wavefunction overlap, and therefore annihilation decay rate, decreases with principle quantum number scaling as n^{-3} [101] meaning any S-state with $n \geq 3$ is unlikely to self-annihilate. Instead, it will radiatively decay to the ground state.

The process of self-annihilation must be charge conjugation invariant because as a particle-antiparticle pair Ps is an eigenstate of the charge conjugation operator. Photons are their own antiparticle too and are subject to the same rule. This means the charge parity (C-parity) of the Ps (which depends on S and ℓ) must be the same as the C-parity of the resultant photons (which depends on the number of photons

produced, N). The selection rule of this process can be written as [189, 277, 281]

$$(-1)^{(S+\ell)} = (-1)^N, \tag{2.6}$$

where the left-hand side is the C eigenstate of the Ps and the right hand side is the C eigenstate of the resultant photons. Because only states of $\ell = 0$ decay by annihilation, singlet/triplet states will decay into an even/odd number of photons respectively. Decays involving fewer photons are more dominant because processes involving lower numbers of particles/interactions are more likely [5, 101]. This means that two-gamma decay for singlet states and three-gamma decay for triplet states are the primary decay channels.[2]

First order calculations show the singlet annihilation rate is faster than the triplet annihilation rate by more than a factor of α [101, 215][3],

$$\Gamma_{\text{ann.}}(^1S_0) = \frac{\alpha^5 m_e c^2}{2\hbar n^3} \approx \frac{8.0325\ \text{GHz}}{n^3}, \tag{2.7a}$$

and

$$\Gamma_{\text{ann.}}(^3S_1) = \frac{4}{9\pi}(\pi^2 - 9)\frac{\alpha^6 m_e c^2}{2\hbar n^3} \approx \frac{7.2112\ \text{MHz}}{n^3}, \tag{2.7b}$$

where $\hbar$ is the reduced Planck constant. 2γ singlet annihilation produces gamma-rays of equal energy $m_e c^2$, 180° apart in order to conserve energy and momentum. However, the triplet state can decay into many more 3γ combinations while still conserving the momentum and energy of the Ps. The angular distribution θ of the three gamma-rays with respect to the quantisation axis is dependent on the azimuthal quantum number M_J by the relations [103]

$$P_{M_J=0} \sim (\pi^2 - 9)\sin^2(\theta) + \frac{1}{6}[3\cos^2(\theta) - 1], \tag{2.8a}$$

[2] Annihilation of free atoms involving one/zero photon decay is suppressed as a third body is necessary to absorb the momentum [67], which can happen in Ps^+ and Ps^-.

[3] Several people calculated the first order Ps decay rates and came to different answers [155, 177, 215]. In 1951 Deutsch proved Ore and Powell correct [97] and their first order calculation is the one presented here.

and

$$P_{M_J=\pm1} \sim (\pi^2-9)[\cos^2(\theta)+1]+\frac{1}{6}[3\cos^2(\theta)-1]. \tag{2.8b}$$

QED corrections to the triplet state decay rate have been calculated as a power series of α up to the $\ln^2(\alpha)$ term of $\mathscr{O}(\alpha^3)$. This work has been performed by many people starting in 1968 (e.g. References [5, 68, 144, 167, 249]) and can be described by the equation [5]:

$$\begin{aligned}\Gamma_{\text{ann.}}(^3S_1) =&\Gamma_0(^3S_1)[1+A\frac{\alpha}{\pi}+\frac{\alpha^2}{3}\ln\alpha+B\left(\frac{\alpha}{\pi}\right)^2- \\ &\frac{3\alpha^3}{2\pi}\ln^2\alpha+C\frac{\alpha^3}{\pi}\ln\alpha+D\left(\frac{\alpha}{\pi}\right)^3+...],\end{aligned} \tag{2.9}$$

where the coefficients $A=-10.286\,614\,809...$ and $C=-5.517\,027\,491...$ were calculated to arbitrary precision in 2008 by Kneihl et al. [167], $B=45.06\pm0.26$ was calculated by Adkins et al. in 2000 [4, 5], and D is yet to to be calculated (see Reference [10] for a comprehensive summary of this work). For the 2^3S_1 state annihilation rate measured in this work Equations 2.7b & 2.9 give an annihilation rate of $\Gamma_{2S}^{calc}=880.0\pm1.2$ kHz where the error is from the uncertainty in B and a factor of half the $\mathscr{O}(\alpha^3)$ logarithmic terms to account for the uncalculated value of D. Table 2.3 shows successive orders of correction and the last column shows the experimental precision required to confirm each order of correction.

Correction Order	Decay Rate (kHz)	Correction Magnitude (kHz)
	901.400	NA
α^1	879.863	21.563
α^2	880.004	0.140
α^3 (Incomplete)	880.003	0.001

Table 2.3: The annihilation decay rate of the 2^3S_1 state of Ps calculated to varying orders of QED correction according by the results and formulas summarised in Reference [10]. The last column shows the experimental precision required to confirm each order of correction.

2.2 QED Energy Corrections

According to the Bohr model (Equation 2.1) all the fine and hyperfine structure states of $n = 2$ are degenerate. This is of course not the case. In zero-field there are six non-degenerate $n = 2$ states, and the calculations in this section pertain to the field free energies of these states. The degeneracy of the fine and hyperfine states is lifted by QED corrections to the energy levels which are expressed as a power series of α. The first corrections are $\mathscr{O}(\alpha^4)$ which include annihilation, spin-spin, spin-orbit and relativistic effects and were initially given by Pirenne [222] and Berestestski [40], but later corrected by Ferrell [109, 110] to,

$$\Delta E^{(4)} = \frac{m_e \alpha^4 c^2}{n^3}\left[\frac{11}{64n} - \frac{1}{2(2\ell+1)} + \frac{7}{12}\delta_{\ell=0}\delta_{S=1} + \frac{\delta_{\ell\neq 0}\delta_{S=1}}{4\ell(\ell+1)(2\ell+1)}C_{J\ell}^{(0)}\right], \tag{2.10}$$

where,

$$C_{J\ell}^{(0)} = \begin{pmatrix} \frac{-(\ell+1)(3\ell-1)}{2J+1}, \ell = J+1 \\ -1, \ell = J \\ \frac{\ell(3\ell+4)}{2J+1}, \ell = J-1 \end{pmatrix}, \tag{2.11}$$

and $\delta_{i=j}$ is a Kronecker delta function. These equations are included as an example of how complex the corrections can be, subsequent orders of correction are not written here in full as they get even more complex, but are summarised in Reference [10].

The $\mathscr{O}(\alpha^5)$ terms were calculated for $n = 2$ by Fulton & Martin [114, 115] (the general solution coming later [221]) and include contributions from vacuum polarisation, recoil effects and virtual annihilation. The $\mathscr{O}(\alpha^6)$ terms took over 25 years to be fully calculated with the results for $\ell = 0, 1$ being given in Reference [83]. $\mathscr{O}(\alpha^7)$ terms including recoil effects, lamb shifts, ultrasoft contributions, one photon annihilation and vacuum polarisation have begun but are as yet incomplete (e.g. References [3, 8, 105, 216]). The $\mathscr{O}(\alpha^7)$ contributions are estimated to have an uncertainty of 0.08 MHz, which is derived from the expected value of the numerically largest term in the $\mathscr{O}(\alpha^7)$ corrections, $\mathscr{O}(\alpha^7 \ln(\alpha)^2)$ [10].

Correction Order	Energy Interval (MHz)	Required Precision (MHz)
α^4 [110]	8 394.45	NA
α^5 [221]	8 625.25	230.8
α^6 [83]	8 626.71	1.46

Table 2.4: The energy interval of the ν_2 transition of Ps calculated to varying degrees of QED correction according to the results and formulas of Reference [83].

For the two states of interest in this work we can use the expressions [83],

$$E(2^3\mathrm{S}_1) = \frac{m_e c^2}{8}\left(-\frac{\alpha^2}{2} + \frac{65}{384}\alpha^4 + A_{S5}\alpha^5 + A_{S6}\alpha^6 + A_{S7}\alpha^7 + ...\right), \quad (2.12)$$

and

$$E(2^3\mathrm{P}_2) = \frac{m_e c^2}{8}\left(-\frac{\alpha^2}{2} - \frac{43}{1920}\alpha^4 + A_{P5}\alpha^5 + A_{P6}\alpha^6 + A_{P7}\alpha^7 + ...\right), \quad (2.13)$$

where A_{S5} & A_{S6}, A_{P5} & A_{P6} have been calculated, and A_{S7} & A_{P7} remain mostly uncalculated. The results of these two equations give the current theoretical ν_2 transition interval of $E(2^3\mathrm{S}_1) - E(2^3\mathrm{P}_2) = \nu_2^{\mathrm{calc}} = 8\,626.71 \pm 0.08$ MHz. A breakdown of the QED contributions to ν_2^{calc} are given in Table 2.4 and show that current measurements are on the cusp of confirming the $\mathscr{O}(\alpha^6)$ calculation with the best historical experiment having an error of 1.5 MHz [134], on the same order as the $\mathscr{O}(\alpha^6)$ contribution. Experiment is far from confirming the $\mathscr{O}(\alpha^7)$ contribution which, although still being calculated, is expected to improve the precision of theory by an order of magnitude.

2.3 Ps in Electric and Magnetic Fields

The application of electric and magnetic fields provides control of atomic properties, which can be useful in experiments. In an electric field, $\vec{F}$, and a magnetic field, $\vec{B}$, the Hamiltonian, $\hat{H}$, becomes [67]

$$\begin{aligned}\hat{H} &= \hat{H}_0 + \hat{H}_Z + \hat{H}_S \\ &= \hat{H}_0 - \vec{\mu}_{mag}\vec{B} - e\vec{F}.\vec{r},\end{aligned} \quad (2.14)$$

where $\hat{H}_0$ is the field free Hamiltonian (including QED corrections), $\hat{H}_Z$ is the Zeeman Hamiltonian, $\hat{H}_S$ is the Stark Hamiltonian, $\vec{\mu}_{mag} = \vec{\mu}_{e_-} + \vec{\mu}_{e_+}$ is the total magnetic moment of the atom and $\vec{r}$ is the relative position of the positron and electron. The eigenfunction of this Hamiltonian, $\hat{H}\Psi = E\Psi$, can be solved to obtain the eigenvalues E corresponding to the Stark and Zeeman shifted state energies.

In this work the eigenfunction is solved in the spherical basis $|nS\ell JM_J\rangle$ [43] which describes the $n = 2$ state as a 16×16 matrix, one row and column for each of the 16 sub-states present. Only the $n = 2$ state is solved for as the adjacent states do not significantly mix with $n = 2$ within the fields found in this work. The eigenvectors and values are computed from the Hamiltonian using the Python function *numpy.linalg.eig($\hat{H}$)* which solves the eigenfunction using numerical methods [248].

In a field an atom in state $|A\rangle$ may mix with another state, $|B\rangle$, creating a statistical admixture of the two states, $|A'\rangle$. Not all states can mix together and those that do will do so with different strengths. $|A'\rangle$ will share characteristics of both constituent states, dependent on the relative fraction of $|A\rangle$ and $|B\rangle$ in $|A'\rangle$. The stronger the field the larger the fraction of $|B\rangle$ in $|A'\rangle$ will become. And the larger the fraction of $|B\rangle$ in $|A'\rangle$ the more similar the properties of $|A'\rangle$ will be to $|B\rangle$. The fraction of $|B\rangle$ character present within $|A'\rangle$ can be extracted from the eigenvectors of the solved eigenfunction Ψ where $\Psi^2_{A,B}$ corresponds to the fraction of $|B\rangle$ character present in $|A'\rangle$. This interaction is not limited to two states, any number of states may mix together if the situation allows, in which case the property $\sum_j \Psi^2_{A,j} = 1$ for a system with j total states must be true.

Whether or not two states mix together in a field can be determined from the expanded Hamiltonian. When a magnetic field is applied in the z direction alone (i.e. $\vec{B} = (0,0,B_z)$) the Hamiltonian is given by [20],

$$\hat{H}_Z = (g_{e_-}\mu_B\hat{s}_{z_{e^-}} - g_{e_+}\mu_B\hat{s}_{z_{e^+}})B_z \tag{2.15}$$

where μ_B is the Bohr magneton, g_{e_-} (g_{e_+}) is the spin-g factor of the electron ($\equiv$ positron), and $\hat{s}_{z_{e^-}}$ ($\hat{s}_{z_{e^+}}$) is the projection operator of the electron (positron) spin in

the quantisation axis, z. This can be given in matrix form for $n = 2$ as [95],

$$\begin{aligned}\langle n\ell' S' J' M'_J|\hat{H}_Z|n\ell SJM_J\rangle =&\mu_B B\sqrt{3(2J'+1)(2J+1)}\\ &\times\delta_{\ell',\ell}\delta_{M'_J,M_J}(-1)^{\ell+M_J}[(-1)^{S+S'}-1]\\ &\times\begin{pmatrix} J' & 1 & J\\ -M'_J & 0 & M_J\end{pmatrix}\begin{Bmatrix} S' & \ell' & J'\\ J & 1 & S\end{Bmatrix},\end{aligned} \tag{2.16}$$

where the matrix in curved brackets is the Wigner-3j symbol and the matrix in curly brackets is the Wigner-6j symbol which represent the rules for addition of angular momentum[4]. The orbital angular momentum component of the magnetic moment of Ps is zero because of the equal masses of the electron and positron, resulting in the Zeeman mixing being independent of ℓ [81]. Therefore the non-diagonal terms in the Zeeman Hamiltonian[5] couple states of $\Delta S = \pm 1$ and $\Delta\ell = 0$.

The Hamiltonian in an electric field (ignoring spin-spin, spin-orbit, Darwin and relativistic correction contributions) can be given as [25]

$$\hat{H} = \frac{\hbar^2}{2\mu_{Ps}}\nabla^2 - \frac{e^2}{4\pi\varepsilon_0 r} + e\vec{F}\vec{r}, \tag{2.17}$$

where for a field along the axis of quantisation, i.e. $\vec{F} = (0,0,F)$, the last term becomes eFz. For the case where the field is along the quantisation axis the Stark Hamiltonian can be written in matrix form as [95],

$$\begin{aligned}\langle n\ell' S' J' M'_J|\hat{H}_S|n\ell SJM_J\rangle =&eF\langle n'\ell'|r|n\ell\rangle\sqrt{\max(\ell',\ell)(2J'+1)(2J+1)}\\ &\times\delta_{S',S}(-1)^{S+\ell+M'_J}\\ &\times\begin{pmatrix} J' & 1 & J\\ -M'_J & 0 & M_J\end{pmatrix}\begin{Bmatrix} S' & \ell' & J'\\ 1 & J & \ell\end{Bmatrix},\end{aligned} \tag{2.18}$$

and be solved analytically with no $\vec{F}\times\vec{B}$ effects. For the Stark Hamiltonian the Wigner symbols govern the selection rules as follows: the top row of the Wigner-3j

[4]These symbols are equivalent to the Clebsch-Gordon coefficients. A Wigner-9j symbol is also available.

[5]Note $\hat{H}_0$ is diagonal in this basis.

symbol fulfills the triangle rule $|J'-J| \leq 1 \leq J'+J$, the bottom row $-M'_J+0+M_J = \Delta M_J = 0$, and the Wigner-6j symbols enforce the rules $S' = S$ and $\Delta\ell = |\ell-\ell'| = \pm 1$. The Kronecker deltas perform a similar function, preventing states of unequal M_J and S mixing together.

As stated magnetic fields mix states of equal ℓ & equal M_J, but $\Delta S = \pm 1$. This mixes singlet and triplet states together, a technique which was used to measure the ν_{HFS} interval [99] and $\Gamma_{\mathrm{p-Ps}}$ [16]. Within the $n = 2$ manifold Zeeman mixing shortens the lifetime of the $2\,^3\mathrm{S}_1$ state (denoted as $2\,^3\mathrm{S}'_1$ when in a field) which gains $2\,^1\mathrm{S}_0$ state character. This is shown in Figure 2.1 which demonstrates the reduction in the $2\,^3\mathrm{S}'_1$ mixed-state annihilation lifetime due to the increasing contribution from the 1.1 ns lifetime of the singlet state. Because the $2\,^{2S+1}\mathrm{P}_J$ state has the same dominant lifetime component for both the triplet and singlet states the $2\,^3\mathrm{P}'_J$ lifetime does not change with magnetic field but does have an increased chance of decaying to the p-Ps state, which has such a short lifetime that any state decaying by this path is lost from the population, a process known as magnetic quenching [136].

The total decay rate of a mixed state $|A'\rangle$ (such as that in Figure 2.1) can be

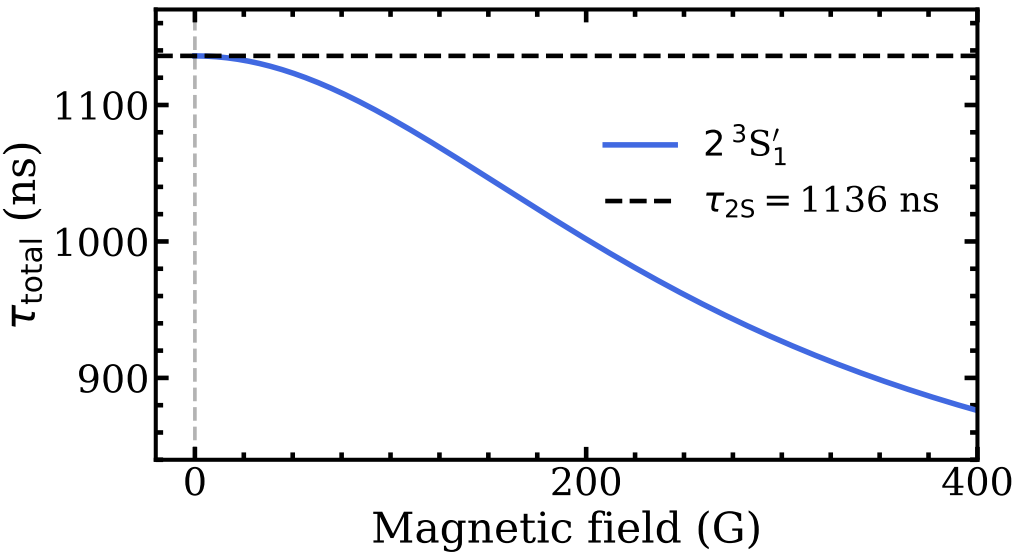

Figure 2.1: The calculated lifetime of the $2\,^3\mathrm{S}'_1$ state within a magnetic field (solid blue line). The dashed line is the zero-field $2\,^3\mathrm{S}_1$ lifetime.

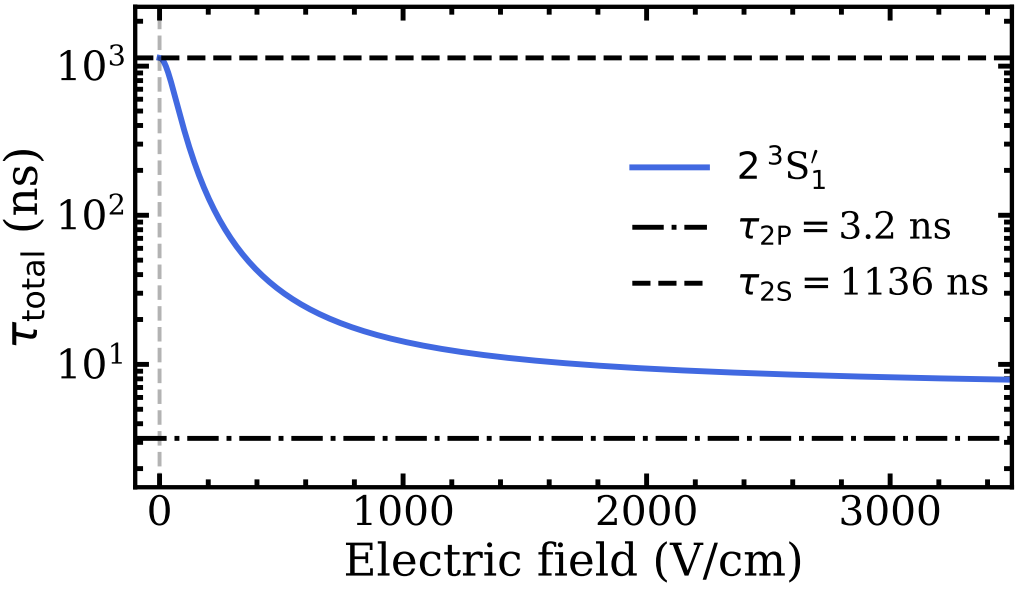

Figure 2.2: The calculated lifetime of the $2^3S_1'$ state within an electric field (solid blue line). The dashed line is the zero-field 2^3S_1 lifetime and the dot-dashed line is the zero-field 2^3P_J lifetime.

calculated in an electric and magnetic field (F_z, B_z) according to the relation [24],

$$\Gamma_A^{\text{total}}(F_z,B_z) = \sum_j [\Psi_{A,j}^2(F_z,B_z)\Gamma_j^{\text{flo.}} + \Psi_{A,j}^2(F_z,B_z)\Gamma_j^{\text{ann.}}], \tag{2.19}$$

where $\Gamma_j^{\text{flo.}}$ is the field free fluorescence rate of state j, $\Gamma_j^{\text{ann.}}$ is the field free annihilation rate of state j, and j is all the states mixing with $|A\rangle$. For the $n = 2$ manifold there are a total of sixteen sub-states to be summed over, the lifetimes for which are given in Table 2.2.

An electric field induces mixing of different ℓ-states, mathematically represented by the non-diagonal terms in the Stark Hamiltonian which couple states of $\Delta\ell = \pm 1$, but of equal S and equal M_J. An example of this can be seen in Figure 2.2 where for $2^3S_1'$ atoms there is a strong dependence of τ_{total} on the electric field. This is because the short lived 2^3P_J fluorescence lifetime begins to dominate the long lived 2^3S_1 annihilation lifetime, reducing the $2^3S_1'$ state τ_{total}. Stark mixing will cause the rapid annihilation of the $2^3S_1'$ state through fluorescence to the o-Ps state and subsequent self-annihilation, a process that is utilised in this work. [24]

As well as changing decay rates, application of fields also changes the energy

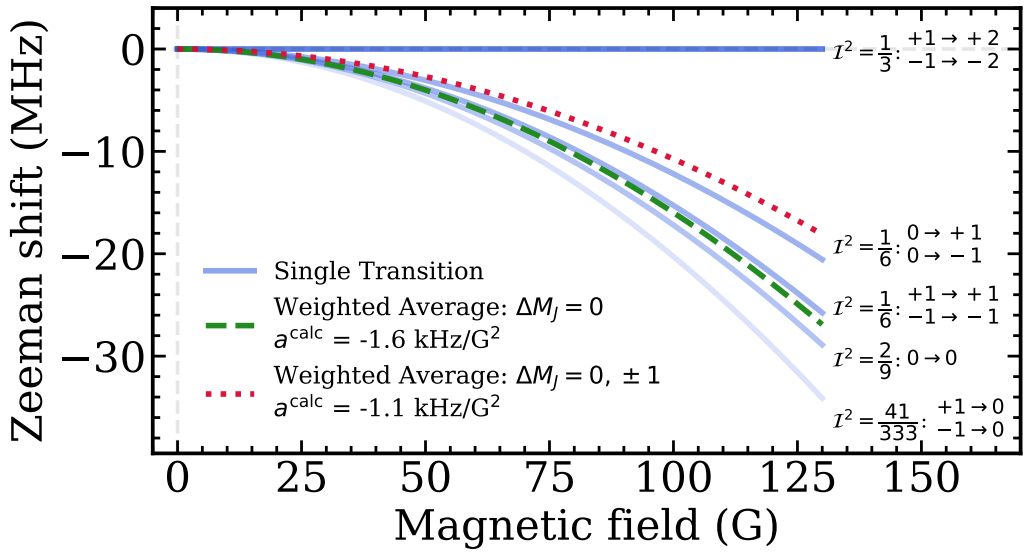

Figure 2.3: The calculated Zeeman shifts of the $2^3S_1 \rightarrow 2^3P_2$ transition (solid blue) where the transparency represents $\mathscr{I}^2$. The labels give the value of $\mathscr{I}^2$ and the corresponding $M_J^i \rightarrow M_J^f$ quantum numbers of the relevant transitions. The weighted average Zeeman shifts for the unpolarised (dotted red) and $\Delta M_J = 0$ (dashed green) cases are also shown, calculated as described in the text.

levels of the states. Consider the interval of interest to this work, ν_2. The 2^3S_1 state has three M_J sub-states ($M_J = 0, \pm 1$), and the 2^3P_2 level has five M_J sub-states ($M_J = -2$ to 2), which offer a total of nine allowed transitions in the ν_2 interval. Applying a field will remove the field free degeneracy of these transitions. In a magnetic field some states, i.e. $2^3S_1(\pm 1)$ and $2^3P_2(\pm 2)$, are not shifted at all because the Zeeman Hamiltonian does not allow these states to mix with any of the other available states, while others are shifted towards each other, causing a negative Zeeman shift. This results in large variation in the magnitude of the Zeeman shifts of the ν_2 transitions, which are shown in Figure 2.3. The Zeeman shift is calculated as the difference of the energy between each allowed pair of states as a function of magnetic field, $\Delta\nu_{\text{Zeeman}}(B_z) = E_{2S_{M_J}}(B_z) - E_{2P_{M_J'}}(B_z)$.

The direction of polarisation of the microwave radiation with respect to the magnetic field will change the ΔM_J selection rules and different subsets of the available transitions will be driven. The Zeeman splitting of the transitions driven in this work in any particular field was at most 3 MHz. This small difference was not resolvable in experiment due to significant broadening mechanisms, as

described in the next section, hence the Zeeman shift is evaluated as its average value $\Delta\nu^{avg}_{\text{Zeeman}}(B_z)$. $\Delta\nu^{avg}_{\text{Zeeman}}(B_z)$ is calculated by averaging $\Delta\nu_{\text{Zeeman}}(B_z)$ for each allowed transition as dictated by the microwave polarisation. The average is weighted by the square of the spectral intensity of each transition $w_{(2S,M_J),(2P,M'_J)} = S^2_{(2S,M_J),(2P,M'_J)}$ as calculated by the general equation [43],

$$S_{(n,\ell,S,J,M_J),(n',\ell',S',J',M'_J)} = (-1)^{J-M_J}\sqrt{(2J+1)(2J'+1)} \times \begin{pmatrix} J & 1 & J' \\ -M_J & \Delta M_J & M'_J \end{pmatrix} \begin{Bmatrix} \ell & J & S' \\ J' & \ell' & 1 \end{Bmatrix} \langle n'\ell'|er|n\ell\rangle. \tag{2.20}$$

Because the ν_2 transitions all have the same radial integral $\langle n'\ell'|er|n\ell\rangle$, the weights become the angular component only, $w = \mathscr{I}^2 = S^2/\langle n'\ell'|er|n\ell\rangle^2$. These weighted averages are shown in Figure 2.3 as a dotted line for the unpolarised case (i.e. all transitions allowed) and a dashed line for the parallel polarised case ($\Delta M_J = 0$), which are the cases present in this work. To quantify the Zeeman shifts a quadratic function is fitted to the calculated Zeeman curves from Figure 2.3. The function has the form $\Delta\nu_{\text{Zeeman}} = a^{\text{calc}}B_z^2$ where a^{calc} is a constant. This fit returns val-

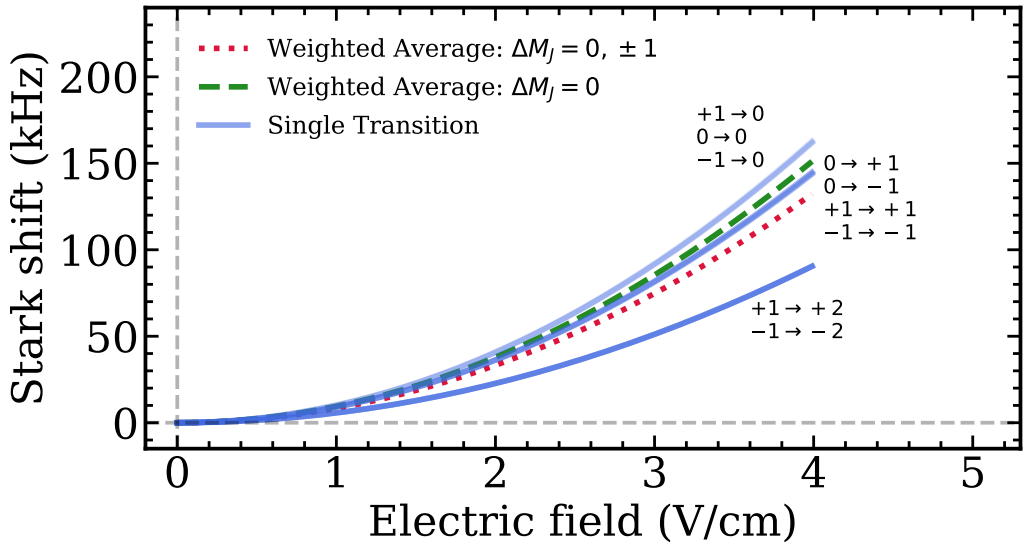

Figure 2.4: The calculated Stark shifts of the $2^3S_1 \rightarrow 2^3P_2$ transition (solid blue) where the transparency represents the weights $\mathscr{I}^2$. The labels give the $M_J^i \rightarrow M_J^f$ quantum numbers of the relevant transitions. The weighted averages for the unpolarised (dotted red) and $\Delta M_J = 0$ (dashed green) cases are also shown.

ues of $a^{\text{calc}} = -1.6 \times 10^{-3}$ MHz/G^2, $a^{\text{calc}} = -1.1 \times 10^{-3}$ MHz/G^2, and $a^{\text{calc}} = -0.8 \times 10^{-3}$ MHz/G^2 for the $\Delta M_J = 0$, unpolarised, and $\Delta M_J = \pm 1$ cases, respectively. This allows the transition frequency at any magnetic field to be calculated as $\nu_2^{\text{calc}}(B_z) = \nu_2^{\text{calc}} + a^{\text{calc}} B_z^2$.

Figure 2.4 shows the Stark shift of the ν_2 interval for a range of fields present in experiment, including the weighted average for the parallel polarisation and unpolarised cases calculated as described above. The Stark shifts present in this work are not large enough to require detailed description, with measures being taken to reduce electric fields as much as possible, as described in the relevant sections. As a result of this, experimental Stark shifts are over two orders of magnitude less than experimental Zeeman shifts.

2.4 Spectral Line Shapes

When an atom is excited/de-excited from one state to another by a photon, the measured change in population as a function of the frequency of the driving radiation will not be a simple Dirac delta function at the resonance frequency, ν_R. Multiple factors, some inherent in the atom and others environment and method dependent, will give this line a full width at half maximum (FWHM) of Γ. This width can be used to understand the dynamics of the system, but is also a limiting factor of precision measurements, whereby it is harder to perform a precision measurement of an energy interval with a broader line shape due to loss of definition at the resonance.

The most fundamental broadening is the natural line width. This is due to the Heisenberg uncertainty principle $\Delta E \Delta t \geq \hbar/2$, whereby the rate of decay from either of the states involved in the transition causes an energy uncertainty up to the limit of the uncertainty principle. The energy spread of the transition can be derived from the Fourier transform of the exponential decay function and the line shape is described by a Lorentz function [94],

$$L(\nu) = \frac{2A/\pi\Gamma}{1 + 4[(\nu - \nu_R)/\Gamma]^2}, \tag{2.21}$$

where A is an arbitrary scaling constant, and ν is the applied radiation frequency.

The natural line width is a homogeneous effect, i.e. something which effects the probability of excitation/decay equally for all atoms in a population, and homogeneous broadening effects are described by Lorentz functions [94].

For the $n = 2$ fine structure of Ps the natural line width is determined by the combined decay rate of the two levels involved, the $\tau_{2S} = 1136$ ns and $\tau_{2P} = 3.19$ ns mean annihilation and fluorescence lifetimes, respectively. These combine to give the natural line width as [94]

$$\Gamma_{\text{natural}} = \frac{1}{2\pi}\sqrt{\frac{1}{\tau_{2S}^2} + \frac{1}{\tau_{2P}^2}}, \tag{2.22}$$

where the factor of $1/2\pi$ converts from angular frequency to frequency. This can change in a field due to Stark or Zeeman mixing altering the state lifetimes, but within this work the fields are negligible and the 2P lifetime is highly dominant[6] and therefore the 2P lifetime remains the dominant component to the natural line width for an expected width of $\Gamma^{\nu_2}_{\text{natural}} = 50$ MHz.

Power broadening is the next most important homogeneous broadening mechanism in this work. For increasing power of the interrogating radiation (and therefore increasing intensity) the probability of excitation at ν_R nears saturation (i.e. the transfer between states is at its maximum), but the probability of exciting an atom far from ν_R continues to increase at a faster rate, broadening the line shape. This is inherent in the equation for the Rabi frequency which governs the rate of change in the probability density of a two-level system [94],

$$\Omega_R = E_0 \frac{\mathscr{I}\,|\langle n_2\ell_2|\mu|n_1\ell_1\rangle|}{\hbar}, \tag{2.23}$$

where $\mu = er$ is the dipole operator, E_0 is the intensity of the radiation, and the probability of excitation is $|c_2|^2 \propto \sin^2(\Omega_R t/2)$ [94]. However, the ν_2 transition

[6] Zeeman mixing with the $2\,^1S_0$ state will reduce the lifetime of the 2S' state, but if the magnetic field was large enough that the Zeeman mixed 2S' lifetime was the dominant broadening mechanism then the magnetic field would quench the 2S population before any microwave excitation could take place (and singlet and triplet 2P atoms posses the same decay rate resulting in no change from Zeeman mixing). Electric fields within the experiment were small, on the order of a few V/cm, and as this only mixes the two states already involved in the transition no change in line width will occur.

is not a true two-level system due to the rapid radiative decay of the 2P state to the ground state. This loss creates a 'flat-top' line shape effect at sufficient power ($I \approx 140$ W/m), whereby the line shape no longer conforms to a Lorentzian model [15]. The power broadening of the ν_2 transition line width in the low-power regime was calculated to be $\Delta\nu_{power} = 6.6$ MHz/mW [15] for the waveguide setup used in reference [132]. The result was obtained by propagating a realistic Ps distribution through simulated microwave fields and calculating the time dependent density matrix with a master equation solver to generate line shapes that were fitted with a Lorentzian model to extract the width as a function of microwave intensity [15].

The line width due to power broadening scales with power according to [132],

$$\Gamma = \Gamma_0 \sqrt{1 + bP_{\text{input}}}, \tag{2.24}$$

where b is a constant, P_{input} is the power of the applied radiation, and Γ_0 gives the effective 'zero-power' line width at the y-axis intercept (i.e. the width of the transition due to all broadening mechanisms except power broadening). bP_{input} is the saturation parameter, which defines saturation as occurring above the limit $bP_{\text{input}} > 1$, where $P_{\text{sat.}} > 1/b$. Higher radiation intensity also increases the signal amplitude (denoted S_γ which is explained in Section 3.6) according to the relation [113]

$$S_\gamma = A\left[1 - \frac{1}{1 + bP_{\text{input}}}\right], \tag{2.25}$$

where bP_{input} is the same saturation parameter as above, and A is the maximum achievable signal which depends on experimental details such as detection efficiency, interaction time of the atoms with the radiation etc. If amplitude and power saturation data is obtained and fitted with these functions for the same experimental conditions then the parameter b should be the same in both fits, but may vary due to other experimental effects such as the selection of new populations when the radiation intensity is increased.

The last homogeneous broadening mechanism considered here is transit-time

broadening which is calculated by the equation $\Gamma_{\mathrm{TTB}} \approx v/d$, where v is the velocity of the atom and d is the width of the atom-radiation interaction region [94]. When the atoms in question have a broad velocity distribution this type of broadening can be more akin to an inhomogeneous broadening mechanism, which is where variation in the atoms themselves (e.g. velocity or collisions) results in each individual atom having a different resonant transition frequency [94]. Inhomogeneous broadening is approximated here as a Gaussian distribution (because the velocity distribution is Gaussian) and the relative amount of inhomogeneous and homogeneous broadening dictates the line shape model used to fit data, Lorentzian for homogeneous and Gaussian for inhomogeneous. The Gaussian function is given by [94],

$$G(\nu) = A\mathrm{e}^{\dfrac{-(\nu-\nu_R)^2}{2\sigma^2}}, \tag{2.26}$$

where σ is the standard deviation which sets the width of the Gaussian.

The primary inhomogeneous broadening effect in this work is Doppler broadening. An atom travelling at a velocity v_x in the axis of the applied radiation has a Doppler shift of,

$$\nu' = \nu \frac{1}{1+\dfrac{v_x}{c}}, \tag{2.27}$$

where $\lambda = c/\nu$ is the wavelength of the transition. If the v_x distribution of the Ps population is symmetric then the transition is broadened, but if the v_x distribution is asymmetric there will be a Doppler shift due to the average velocity $\langle v_x \rangle$ being non-zero. While this effect is small for the fine structure transitions it is the dominant broadening of the $n = 1 \rightarrow 2$ transition as discussed in Section 3.7.

The different broadening components combine as a convolution, so if both homogeneous and inhomogeneous mechanisms are present then a Voigt function $V(\nu) = L(\nu) \otimes G(\nu)$ can be used which is effectively an inhomogeneous distribution of Lorentzian line shapes [94]. As an example of the ν_2 measurements presented in this work a sample of data from Chapter 7 (a total of 88 line shapes taken in the $+x$ propagation direction, without microwave absorbing foam, obtained using

methods described in Chapter 3.9 and Appendix A) was fitted with a pseudo-Voigt function of the form $V_p(\nu) = mL(\nu) + (1-m)G(\nu)$, where m is the fraction of Lorentzian character in the Voigt function. The resulting fits have a dominant average fraction of $97.6 \pm 0.1\%$ Lorentzian, and the fitted centroid value is in good agreement with a Lorentzian fit for all line shapes. This is expected as the natural line width and power broadening are the dominant broadening mechanisms in this work. A Lorentzian and Gaussian fitted to the data sample had an average reduced chi square parameter χ^2_{reduced} of 0.90 for the Lorentzian and 1.29 for the Gaussian, while the psuedo-Voigt was 0.88, confirming a Lorentzian is the closest fit to the data[7]. Because of this the ν_2 line shapes in this work are fitted with a Lorentzian function to extract information on ν_R and Γ.[8]

Another property of line shapes to be considered is asymmetry. Neighbouring states can influence each other due to a range of effects, broadly known as quantum interference (QI) [150]. These effects can cause a skew in the line shape towards the adjacent state, though in some cases do not [185]. The Ps ν_2 transition is susceptible to QI from the other 2P states, causing a skew to higher frequencies due to the off-resonant excitation pathways they present. As a rule of thumb [150] a measurement of ν_2 will be sensitive to QI effects if the measurement error is less than $\Delta\nu \approx \Gamma^2/2\Delta = 608$ kHz for transitions of the same line width Γ, where $\Delta = 4\,385.7$ MHz is the separation of the $2\,^3\text{P}_2$ and $2\,^3\text{P}_1$ state. Fits of Lorentzian functions to the line shapes measured in this work typically produce an error in ν_R of > 1 MHz, and shifts from QI were calculated to be on the order of 30 kHz in similar experiments [15], so we will not be sensitive to this effect here.

In previous works [15, 132] the Fano function was used to quantify asymmetry [107],

$$F(\nu) = A\left[\frac{(q_F+\varepsilon)^2}{(1+q_F^2)(1+\varepsilon^2)}\right], \tag{2.28}$$

[7] $\chi^2_{\text{reduced}} = \chi^2/\xi$, where $\xi = N - D - 1$ in which N is the number of data points and D is the number of degrees of freedom.

[8] The line shapes will in fact be the sum of two or more Lorentzians due to the Zeeman splitting of the ν_2 transitions. As already stated the small splittings present in this experiment are too small to resolve, see Section 2.3. In addition, no dependence of Γ or q_L on B_z is observed, indicating the Zeeman splitting has no effect on the line shape, see Chapter 7 for details. [132]

where $\varepsilon = (\nu - \nu_R)/\Gamma$ and q_F is the asymmetry parameter whereby $q_F \to \pm\infty$ indicates a symmetric line shape, low q_F indicates an asymmetric line shape, and $q_F = 0$ is a symmetric anti-resonance condition. Neither this work or previous studies were sensitive to QI effects as already discussed, with any asymmetry originating from frequency dependent power [15]. This means that although the Fano function is a valid line shape for QI effects it is not a valid line shape model to extract ν_R in this work, though it can still be used to quantify how asymmetric a measured line shape is.

However, the Fano function is overly sensitive to the initial fitting parameters of the least squares fitting routine used in this work due to the way its asymmetry parameter is defined. To avoid this problem, asymmetry in this work is quantified by replacing the fixed width Γ of the Lorentzian with a sigmoidally varying equivalent $\Gamma_A(\nu)$ [247],

$$\Gamma_A(\nu) = \frac{2\Gamma}{1 + \exp[q_L(\nu - \nu_R)]}, \tag{2.29}$$

where q_L is the asymmetry parameter for which $q_L = 0$ returns a fully symmetric Lorentzian, but $q_L \to \pm\infty$ indicates increasing skew in the appropriate direction. The Lorentzian and asymmetric Lorentzian function are not susceptible to the initial parameter sensitivity of the Fano function, with the asymmetric Lorentzian fitted to the same data sample as described above having an average $\chi^2_{\text{reduced}} = 0.87$. Once again, the asymmetric Lorentzian is an arbitrary function chosen to quantify asymmetry, and can therefore not be used to extract meaningful values of ν_R from measured line shapes.

2.5 Rydberg Positronium

States that have a high principle quantum number are known as Rydberg states. The ℓ-states of Rydberg Ps become highly mixed with each other in any experimentally realistic level of electric or magnetic field [188]. This gives Rydberg Ps extremely long annihilation lifetimes because each mixed state possesses minimal S-state character (which is the only ℓ-states with a significant annihilation decay rate). Their eventual annihilation manifests from fluorescence to the ground state

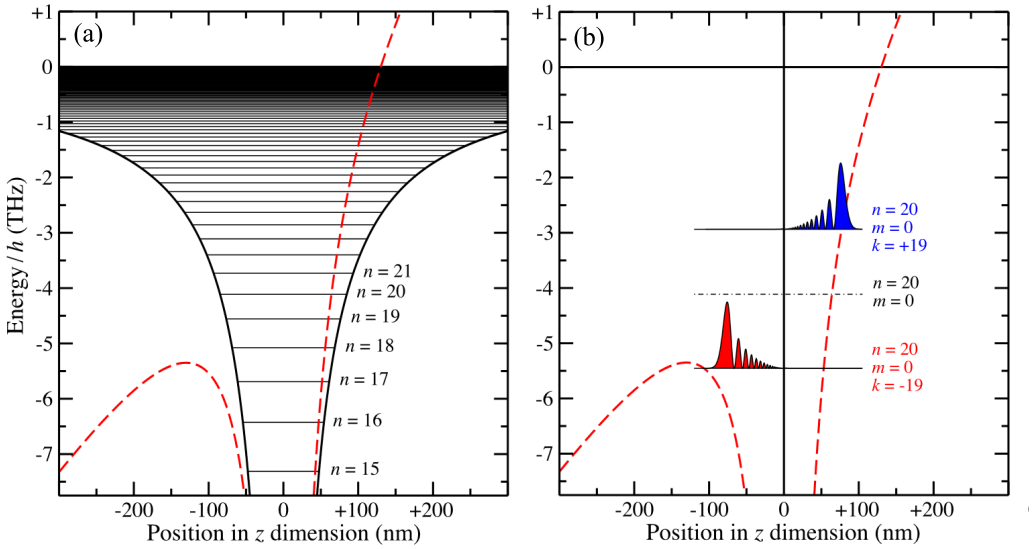

Figure 2.5: (a) The calculated coulomb potential of a field-free Ps atom with labeled energy levels (black), and the calculated distorted Coulomb potential in a field of 850 V/cm (red), with the saddle point antiparallel to the field. (b) The energies and radial charge distribution of the two extreme k-states of $n = 20$, $k = \pm 19$ (with $m = 0$) in a field of 850 V/cm. The dot-dashed line is the zero field energy of $n = 20$. From reference [25].

which self-annihilates at the rate of Γ_{o-Ps}.

The Schrodinger equation cannot be analytically solved for Rydberg Ps states using the spherical basis that describes low n states. This is due to perturbations to the coulomb potential of the atom. In zero-field the Coulomb potential is spatially symmetric, however, in an electric field the potential becomes asymmetric, as described by the third term in Equation 2.17. The electric field causes a three dimensional saddle point in the Coulomb potential in the opposite direction to the field. A 2-D representation of the distorted Coulomb potential of a Ps atom in an electric field $F_z = 870$ V/cm with the relative energies of the n-states is shown in Figure 2.5(a). The Coulomb potential along the perpendicular axes, x and y, maintains the $1/x$ and $1/y$ dependence as long as no field is applied in these axes. [25]

The Schrodinger equation in this system is analytically solvable in the parabolic basis which uses the quantum numbers $|n,n1,n2,m\rangle$, where $n = n_1 + n_2 + |m| + 1$ and m is the projection of ℓ on the axis of quantisation, similar to J and M_J in the spherical basis [116]. This basis provides a quantum number which can uniquely identify each state within an electric field, defined as $k = n_1 - n_2$. k

has a range of $-(n-|m|-1)$ to $+(n-|m|-1)$ in intervals of 2 and each k-state (also known as a Stark state) describes states that are non-degenerate in an electric field. The Stark shifts of k-states can be calculated to third order using the analytical equation [87, 149]

$$\begin{aligned} E_{Stark} =& \frac{3}{2} nkea_{Ps}F \\ & - \frac{1}{16} n^4 (17n^2 - 3k^2 - 9m^2 + 19) \frac{e^2 a_{Ps}^2}{E_h} F^2 \\ & + \frac{3}{32} n^7 k (23n^2 - k^2 + 11m^2 + 39) \frac{e^3 a_{Ps}^3}{E_h^2} F^3. \end{aligned} \tag{2.30}$$

Where F is the applied electric field, $a_{Ps} = 2a_0$ is the Bohr radius of the Ps atom (a_0 is the Bohr radius of hydrogen) and the Hartree energy is $E_h = 2hcR_{Ps}$, in which $R_{Ps} = R/2$ is the Rydberg constant of Ps and R is the Rydberg constant of hydrogen. Calculations of the energy levels using Equation 2.30 can be seen in Figure 2.6 for the Stark manifold of several n-states relevant to this work. The separation in energy of the Stark states increases with electric field. This produces two possible effects when undergoing laser excitation from the $n = 2$ state. At lower electric fields this results in a broadening of the line shape, an effect known as Stark broadening. However, at higher fields, if the Stark states are shifted beyond the effective experimental line width (i.e. all other broadening mechanisms such as Doppler, laser bandwidth, transit time etc.) then it is possible to uniquely excite individual Stark states [266]. The upper and lower k-state energy levels of two adjacent n-states, n and $n+1$, begin to overlap in a maximum electric field of [116]

$$F_{\text{overlap}} = \frac{1.285 \times 10^9}{3n^5}, \tag{2.31}$$

where the numerical constant is to convert the electric field from atomic units to V/cm, $e/4\pi\varepsilon_0 a_{\text{Ps}}^2 = 1.285 \times 10^9$ V/cm. In experiment this will occur at a lower electric field due to the non-zero effective experimental line width.

Electric dipole selection rules still apply to the $n = 2\,^3\text{P}_J \rightarrow n\,^3\text{S/D}_J$ transition used to produce Rydberg states. Because each Stark state contains character

of all possible ℓ-states mixed together the transition strength to each Stark state is determined by the fraction of the S and D states present within the Stark state in question. To calculate the transition strength from a $2\,^3\mathrm{P}_J$ state to a Stark state the dipole transition strengths are first calculated to all possible ℓ'-states in the spherical basis (from Equation 2.20). These are are summed and transformed into the parabolic basis by a transformation coefficient [116, 145],

$$\begin{aligned} S_{(n,\ell,S,J,M_J),(n',n_1',n_2',m',k')} = &\sum_{\ell'} (-1)^{\ell'+(1-n'+m'+k')/2}\sqrt{2\ell'+1} \\ &\times S_{(n,\ell,S,J,M_J),(n',\ell',S',J',M_J')} \\ &\times \begin{pmatrix} (n'-1)/2 & (n'-1)/2 & \ell' \\ (m'+k')/2 & (m'-k')/2 & -m' \end{pmatrix}, \end{aligned} \tag{2.32}$$

where the matrix is the Wigner-3j symbol.

For Ps spectroscopy, Rydberg states have several advantages. Firstly, their long lifetimes allow complex operations such as atom interferometry to be performed (see Reference [217] as an example with Rydberg He atoms). Secondly, they posses a large electric dipole moment, meaning their motion can be controlled with the application of static or dynamic electric field gradients [276][9]. Thirdly, their longer lifetimes reduce their contribution to the natural line width to the kHz level, making precision measurements easier if all other broadening mechanisms are eliminated.

Another advantage of Rydberg Ps is that the phenomena of field ionisation (FI) can be used to control when the positron in each Ps atom annihilates. Upon application of sufficient electric field Rydberg atoms are ionised and the positron is free to annihilate on a surface. This is because of the asymmetry in the perturbed Coulomb potential of the atom in an electric field. When the energy of the atom is on the order of the energy of the saddle point the excited states can ionise directly, or they can tunnel through the coulomb barrier. A threshold electric field at which FI will occur for each n-state can be calculated based on the location of the saddle point: $F_{\text{ion.}} = (2hcR_{Ps})/(16ea_{Ps}n^4)$ [116].

[9] Ps Rydberg states have been guided [90] and focused [158] using electric fields, and with further work likely decelerated and trapped like conventional atoms [263].

Parabolic quantum numbers can be used to describe this process in more detail. States with $k > 0$ (known as low field seeking states, LFS, due to their dipole moment polarity) have dipoles anti-parallel to the field according to the equation,

$$\mu_{elec} = -nkea_{Ps}3/2, \tag{2.33}$$

(from the first order Stark shift of Equation 2.30). This causes the electron to be localised next to the continuous potential, see Figure 2.5(b), making the rate at which they ionise slow. States of $k < 0$ (known as high field seeking states, HFS) have parallel dipoles and the are localised toward the side with the saddle point, increasing the rate at which they ionise. [25]

There is a semi-empirical formula for the tunnel ionisation rate of Rydberg Ps Stark states which is given by [86, 87],

$$\begin{aligned}\Gamma_{n,n_1,n_2,m} =& \frac{E_{h,Ps}}{\hbar}\frac{(4R_{Ps})^{2n_2+m+1}}{n^3 n_2!(n_2+m)!} \\ & exp[-\frac{2}{3}C - 1/4n^3\frac{ea_{Ps}F}{E_{h,Ps}} \\ & (32n_2^2 + 34n_2m + 46n_2 + \\ & 7m^2 + 23m + \frac{53}{3})],\end{aligned} \tag{2.34}$$

where

$$C = \frac{1}{ea_{0,Ps}\sqrt{2hcE_{h,Ps}}}\frac{(-2E_{n,n_1,n_2,m})^{3/2}}{F_z}, \tag{2.35}$$

$E_{n,n_1,n_2,m} = -(hcE_{h,Ps}/2n^2) + E_{Stark}$ and $E_{h,ps} = 2hcR_{Ps}$. This formula was devised for hydrogen but is scaled here for Ps. Unlike the classical calculation Equation 2.34 accounts for higher order terms in Equation 2.30 which become relevant at higher fields in which the $k > 0$ states shift closer to the saddle point and tunneling becomes more likely. In Figure 2.6 the plotted energies are terminated for ionisation rates $>$1 GHz which is effectively instantaneous within the experiment. All FI thresholds in this work will be given as the field required to FI the state in question at a rate of 1 GHz.

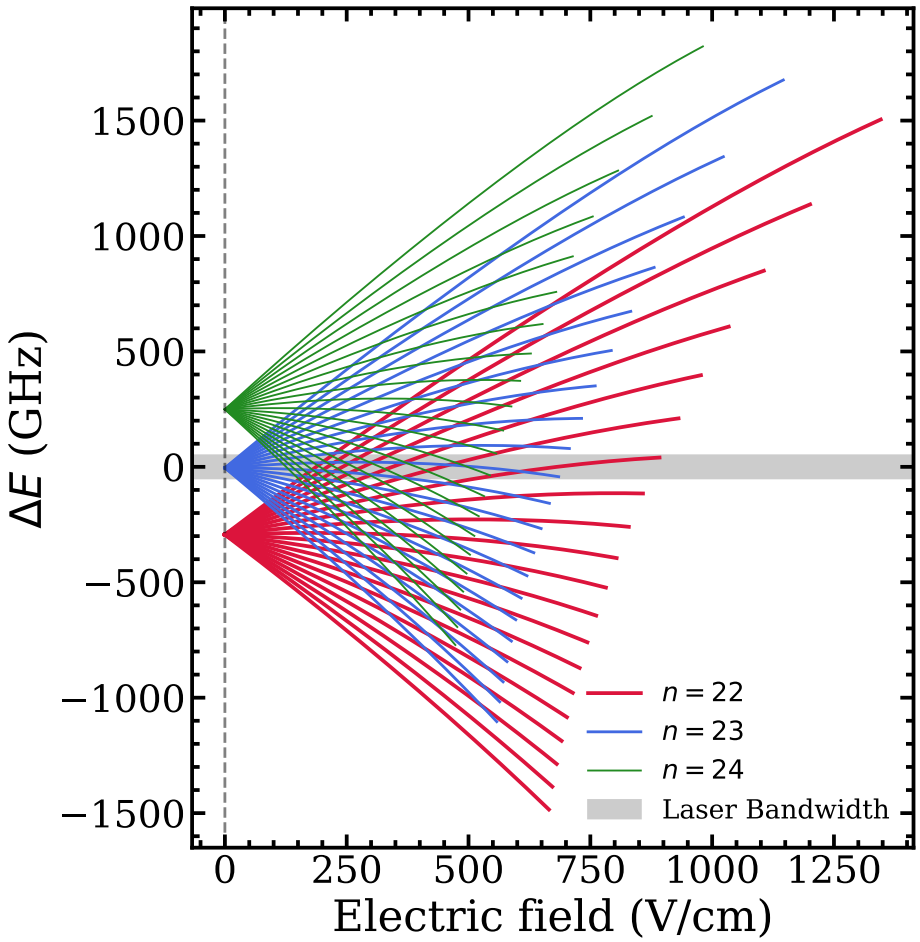

Figure 2.6: The calculated energy splitting of the $n = 22$ (red), $n = 23$ (blue) and $n = 24$ (green) Ps atoms relative to the $n = 23$ zero-field energy, calculated using Equation 2.30. The lines terminate where the ionisation rate exceeds 1 GHz as calculated using Equation 2.34. The grey shaded area represents the maximum 100 GHz bandwidth of the 2-step laser excitation used in this work, centered around the $n = 23$, $k = 0$ transition.

Chapter 3

Experimental Methods

This section describes the experimental basis of this work including pulsed positron beams, mesoporous silica $e^+ \rightarrow Ps$ converters, gamma-ray detectors, the single shot positron annihilation lifetime spectroscopy (SSPALS) measurement technique, and the laser setup as developed in previous studies. The production and characterisation of $n = 2$ and Rydberg Ps states will also be detailed, as well as the application of electric, magnetic and microwave fields.

3.1 Positron Beamline

The source of positrons is the β^+-decay of radioactive ^{22}Na, a typical source used in the production of positrons due to its >90% branching ratio for β^+ radiation and $\sim$ 2.6 year half-life. However, due to this short half-life the activity of the ^{22}Na source used in this work decreased from 1340 to 660 MBq during the course of this research. ^{22}Na emits β^+ with a broad energy range up to 545 keV, with a mean of $\sim$215 keV [204]. A schematic of the source stage of the beamline can be seen in Figure 3.1.

Before the positrons can be trapped to produce a pulsed beam they must be cooled. This is done by a process known as moderation, which slows and narrows the energy distribution of the β^+ particles. Once moderated a Surko buffer gas trap is used to capture and pulse the positrons, see Figure 3.2.

After the trap the positron pulses are temporally compressed using a buncher, see Figure 3.3. The positrons are guided to the target chamber where they are con-

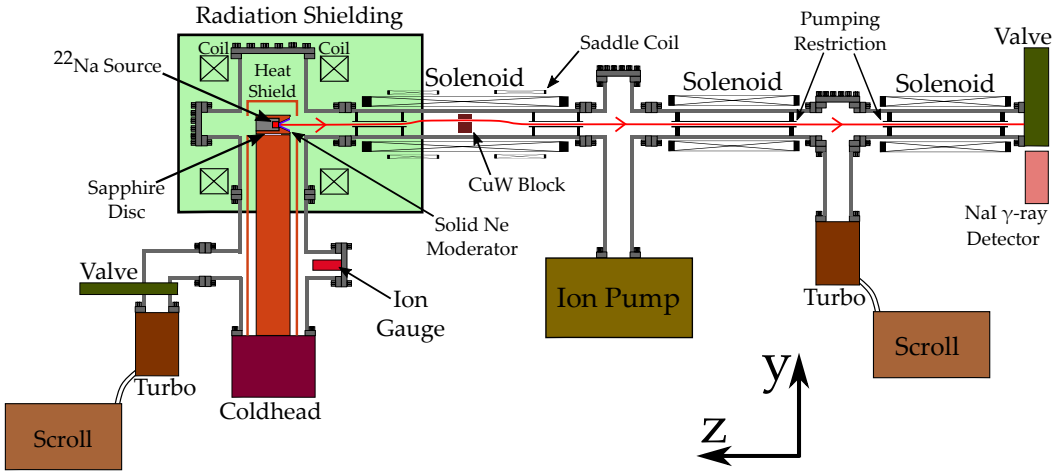

Figure 3.1: A schematic diagram of the source stage of the beamline. Positrons start at the source (red block) on the left and travel right, through the Ne moderator frozen to the coldhead (blue layer). The source is surrounded by lead shielding (green) to terminate unmoderated β^+ particles and gamma-rays. Moderated positrons (red line) are guided by solenoids and magnetic coils, with a pair of saddle coils guiding the beam through an off axis hole in a CuW block to terminate unmoderated on-axis β^+ particles. Various pumps keep the chamber at $\sim 1 \times 10^{-9}$ mbar to limit positron scattering. Pumping restrictions in each solenoid prevent trap gasses contaminating the moderator.

verted into Ps and excited using lasers, a description of the target chambers used in this work can be found in the appropriate chapters. A more detailed description of the entire beamline can be found in Reference [79] and the various stages will be discussed here.

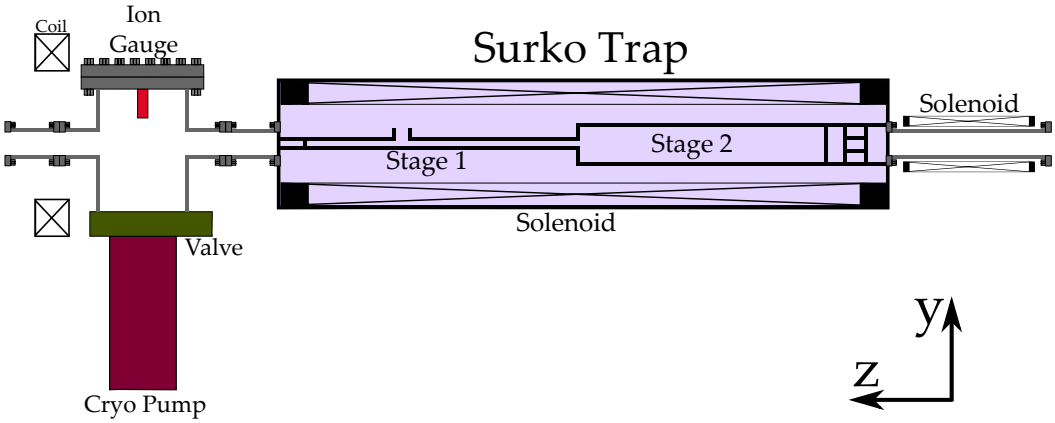

Figure 3.2: A schematic diagram of the trap stage of the beamline. Positrons come from the source on the left and travel right, through the trap. The pressure in the trap can be on the order of 10^{-3} mbar, however, the rest of the beamline is kept at pressures of $< 1 \times 10^{-7}$ using differential pumping with pumping restrictions.

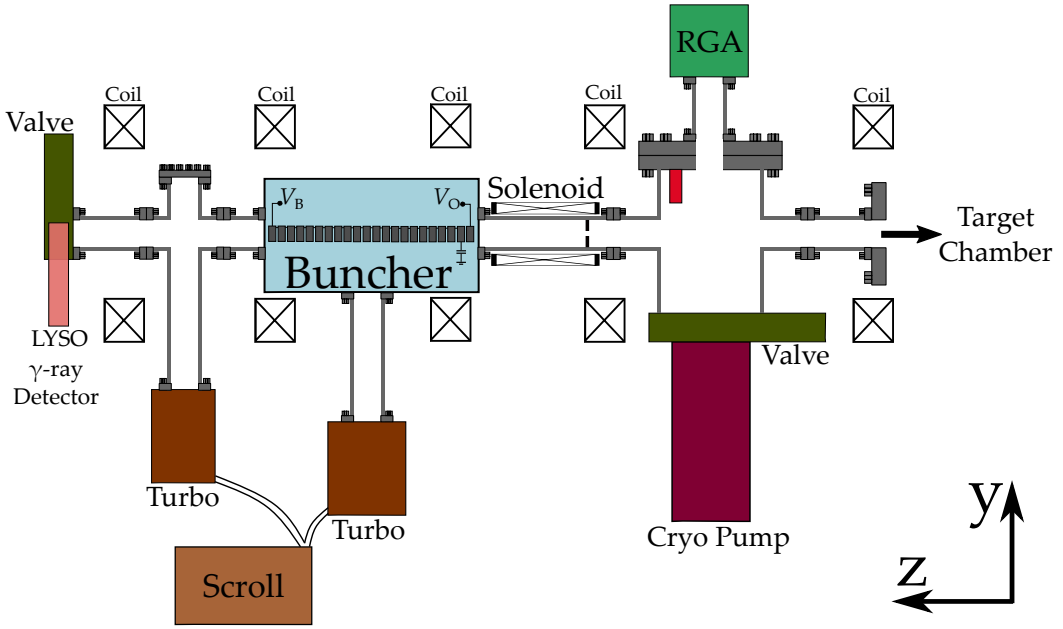

Figure 3.3: A schematic diagram of the buncher stage of the beamline. Positrons come from the trap on the left and are temporally compressed by the buncher. Positrons exit on the right into the various target chambers used in this work. Pumps keep the chamber at $\sim 1 \times 10^{-9}$ mbar. Sections of the beamline can be isolated using manual and pneumatic values.

3.1.1 Moderation

The function of the moderator is to reduce the energy of the β^+ particles emitted from the source so that they can efficiently interact with the buffer gases in the trap. Currently, the most efficient known moderator is solid Ne [197] which, in a cylindrical configuration, has been recorded as having an efficiency (the percentage of β^+ which are successfully slowed by the moderator) of up to $0.70 \pm 0.02\%$, providing an energy spread of 0.58 eV FWHM [197]. The β^+ enter the bulk Ne and lose energy by inelastic collisions where they generate electron-hole pairs or excitons (the electron-hole bound state) [128]. When the energy of the positrons inside the Ne drops below the energy threshold required to excite the electronic transitions (20 eV for solid Ne [197]), then it can only lose energy by generating acoustic-phonons [128]. At this stage the diffusion rate of the positrons in the Ne is high because the maximum phonon energy is small [128], and the positrons can encounter the surface of the moderator. If the positron has not thermalised it will be emitted from the bulk because the positron work function for Ne is small (on the

order of 1 eV) [197, 256].

This work uses a conical configuration, see Figure 3.1, which can provide up to double the efficiency of a cylindrical configuration by increasing the likelihood of escaping the aperture [166]. However, the moderator efficiency of this beam was measured to be $\sim 0.7\%$, likely due to incomplete cooling, positron capture in defects etc. [79]. The moderator is grown by passing a jet of 99.999% pure Ne gas over an oxygen-free Cu conical aperture which is separated from the source by a Ti window. This results in a background pressure of 1×10^{-3} mbar in the source chamber. The Ne freezes to the surface of the aperture which is cooled by a closed-cycle helium cryostat to 7.5 K during moderator growth. The Ne solidifies on the surface of the aperture and the gas jet is stopped once the number of moderated positrons begins to plateau. This is monitored by counting the annihilation events recorded by a NaI gamma-ray detector (see Section 3.2 for details on gamma-ray detectors). [79]

The background pressure of the system will depend on the source temperature and evaporation rate of the moderator, the latter of which is also dependent on contamination in the Ne which can occur due to leaks in the gas line used to supply Ne to the aperture. The moderator is kept at a constant temperature of 7 K using a heater, approximately 1 K above the base temperature of the cold head, where fluctuations in the cryostat operation can cause variation of $\sim$0.5 K. This temperature improves the efficiency of the moderator, either due to temporary annealing of the structure [127, 199, 220] or removal of contaminants, though it slightly increases the rate of evaporation. To limit contaminants the Ne line is pumped down to $< 1 \times 10^{-5}$ mbar between moderator growths to remove contaminant gas and several pumping restrictions between the source and the trap prevent trap gasses reaching the cold head. The resultant source chamber pressure is $< 6 \times 10^{-9}$ mbar when no moderator is present.

Due to evaporation of the Ne over time the moderator needed to be regrown every 2 - 5 weeks. This gradual deterioration and the low temperature required to produce these moderators (which necessitates a complex cooling setup) highlights

the disadvantages of solid Ne over other moderators (e.g. a room temperature tungsten mesh which has an efficiency of 0.1% [275]), but their efficiency makes up for this. The number of positrons entering the trap varied between three to six million per second due to the moderator decay, calculated using the solid angle coverage and count rate of the NaI gamma-ray detector.

The source holder, the part of the 4 K cold head containing the source and the moderator, is electrically isolated from the rest of the cold head by a sapphire disk, retaining good thermal conductivity while allowing the source holder to be biased, see Figure 3.1. The source holder is biased to $V_S = +47$ V to eject the moderated positrons away from the source to facilitate transport along the beam line. The positrons are confined and guided along the beamline using axial magnetic fields on the order of 100 G, with the charged particles following the magnetic field lines away from the source. To remove unmoderated β^+, the positrons are steered through an off-axis slit in a tungsten-copper alloy block using a saddle coil configuration. Unmoderated β^+ posses too much kinetic energy to be deflected by the magnetic field and annihilate on the block. [79]

3.1.2 Positron Trapping

Moderated positrons are guided into a Surko buffer gas trap (BGT) [250]. This Penning-type trap uses a uniform axial magnetic field of ∼500G to trap particles radially, and an electric potential to trap them axially, allowing molecular gasses to cool the positrons through inelastic collisions. Figure 3.4 shows the potentials and pressures throughout the trap, with the inset at the top showing a schematic of the electrodes. The positrons are incident from the left hand side and leave from the right hand side. Note the peak gas pressure in the trap is considerably larger than the rest of the beamline; this is maintained by differential pumping.

The incident positrons have an energy of ~ 47 eV upon entering the trap, as set by V_S. The first electrode of the trap, the inlet electrode, was set to 38 V to prevent cooled positrons leaving the trap while allowing moderated positrons from the source to enter. Stage 1 of the trap has a bias of 30 V and a pressure of $\sim 10^{-3}$ mbar. The buffer gas is a mixture of N_2 and SF_6. Initial capture in Stage 1

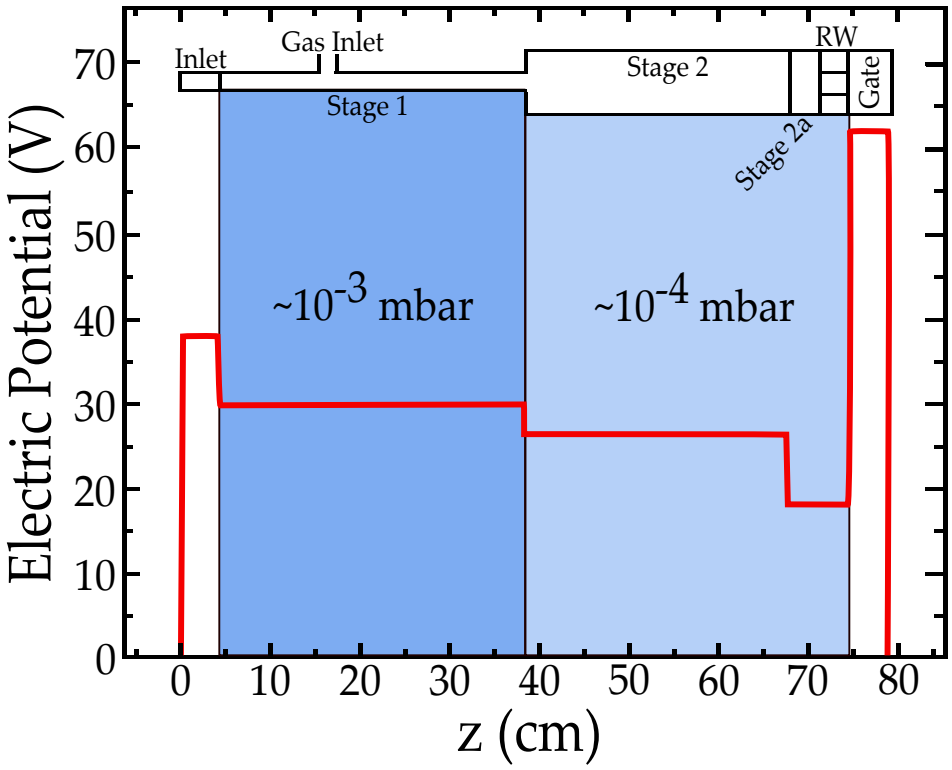

Figure 3.4: The axial electric potential (red line) and buffer gas pressure (blue shading) along the length of the trap with a schematic representation of the chamber inset at the top. Positrons are incident from the left and exit on the right. The magnetic field along the entire length is ∼500G. Adapted from Reference [79].

is through electronic excitation of the N_2 where ~ 9 eV is lost per collision [205], meaning just two collisions are required for the positrons to fall into the first stage of the trap. Once the kinetic energy of the positrons is insufficient to excite this transition, lower energy vibrational transitions (76 and 188 meV [124]) in the SF_6 promote rapid cooling in Stage 2 [124, 210]. This stage has a lower pressure to limit annihilation ($\sim 10^{-4}$ mbar) and a lower potential (27 V) to confine the cooled positrons.

Finally, the positrons fall into Stage 2a at 19 V, in which a rotating wall electrode is present (see next section). The trap accumulates positrons in this stage for 1 s, releasing about 10^5 positrons per pulse at a repetition rate of 1 Hz. The pulses are released by lowering the potential on the gate electrode at the end of the trap from 62 V to 0 V in ~ 80 ns. All these voltages, as well as the buffer gas pressure and ratio, are optimised for maximum trap output signal (as measured by

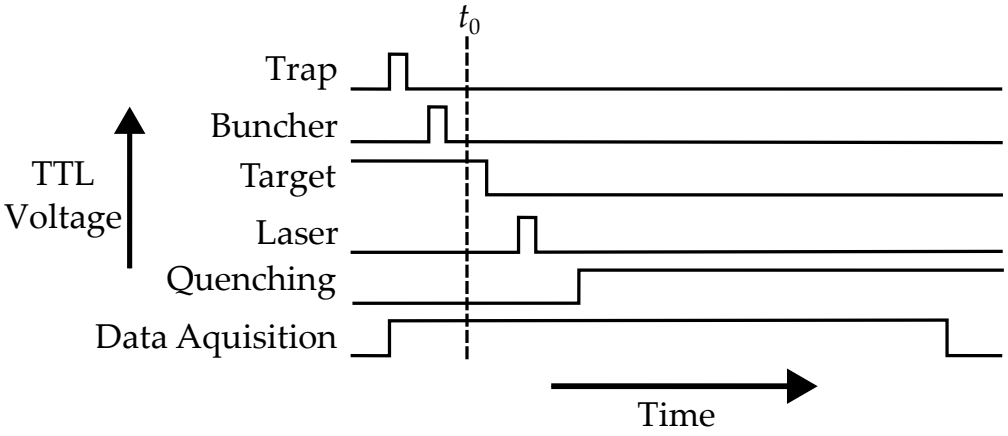

Figure 3.5: A schematic diagram showing the timing of events relative to the positron arrival time at the target, t_0. The trap is first, simultaneous with the start of data acquisition to ensure all events are recorded. The buncher is next with E_T switched off shortly after positron implantation and just before the laser pulse. Quenching by electric field or microwaves happens some time after this with the quenching means kept on for the duration of the Ps lifetime to ensure proper quenching. Not to scale.

a permanent LYSO gamma-ray detector after the trap, but before the buncher, see Section 3.2 for details on detection), balancing the number of collisions required to drop into each stage with annihilation losses. Ps formation with the buffer gas is the primary positron loss mechanism in the trap, though pick-off annihilation with the gas and the walls is also present.

The timing of all events is controlled by a set of digital pulse generators (Stanford Research Systems DG 645). These generators have < 25 ps root-mean-square (rms) jitter, which is several orders of magnitude better that required in this experiment, ensuring all timing signals were consistent for each shot of the positron beam. All trigger timings are defined relative the trap gate electrode being lowered, which releases the positrons. Subsequent events such as the buncher, laser, HV switches and microwaves are triggered by TTL pulses relative to the trap gate. A schematic representation of the order of events is shown in Figure 3.5.

3.1.3 Beam Compression

Positrons stored in the trap gradually diffuse outward due to collisions with the buffer gasses, eventually annihilating on the walls of the trap, limiting the accumulation of trapped positrons. To minimise this effect and compress the beam a

rotating wall (RW) is placed inside the trap around the positron cloud [123], which causes inward transport away from the walls meaning annihilation in the trap is from interactions with the buffer gas only [60]. The RW consists of a ring electrode divided longitudinally into eight equal segments, each covering an angle of $\pi/4$ radians. The segments are divided into $N = 4$ pairs, where the pairs are formed of adjacent electrodes covering a continuous $\pi/2$ radians. A time varying sinusoidal voltage $V_{\mathrm{RW}}(t) = V_{\mathrm{RW}} \sin(\omega_{\mathrm{RW}} t + N\phi)$ is applied to the electrodes, with each pair of electrodes (i.e. N and $N+1$) differing by a phase of $\phi = \pi/2$ to produce a rotating dipole field around the longitudinal trapping axis, z. The frequency and amplitude of the RW potential are optimised to minimise the positron spot size and maximise the number of positrons, where an optimal configuration is typically $V_{\mathrm{RW}} = 1$ Vpp and $\omega_{\mathrm{RW}} = 4.6$ MHz [79]. Compression is achieved because ω_{RW} is close to the axial bounce frequency of the positrons in the trap and acts to compress the positron cloud while in the non-plasma, single-particle regime [123].

The positron beam profile was optimised using an on-axis MCP and phosphor screen mounted at the end of the positron beam, just after the Ps production and spectroscopy region. Figure 3.6 shows an image of the positron beam taken using the on axis MCP with the front plate biased to -250 V to accelerate the positrons into the detector, and a gain of 1200 V between the front and back plates. A phosphor screen behind the back plate, which had a 950 V potential difference, was used to image the beam in conjunction with a triggered CCD Pixelfly camera. The data was fitted with a 2-D Gaussian function to extract the width. The example in Figure 3.6 has a FWHM of $r_{beam} = 1.90 \pm 0.01$ mm, though a width of 3 mm is more typical.

The magnetic guiding field at the Ps production region, B_z, controls the ultimate positron beam spot size with the proportionality $r_{beam} \propto \sqrt{B_z}$. To measure B_z a bench-top analogue of the electromagnetic coils around the chamber was made for each setup used in this work, taking into account coil separation, orientation and height. B_z was measured using a hall probe as a function of position (z and $r = \sqrt{x^2 + y^2}$) and coil current (I). With linear extrapolation to account for the variation in I a 2-D field map could be produced and used to determine the magnetic field

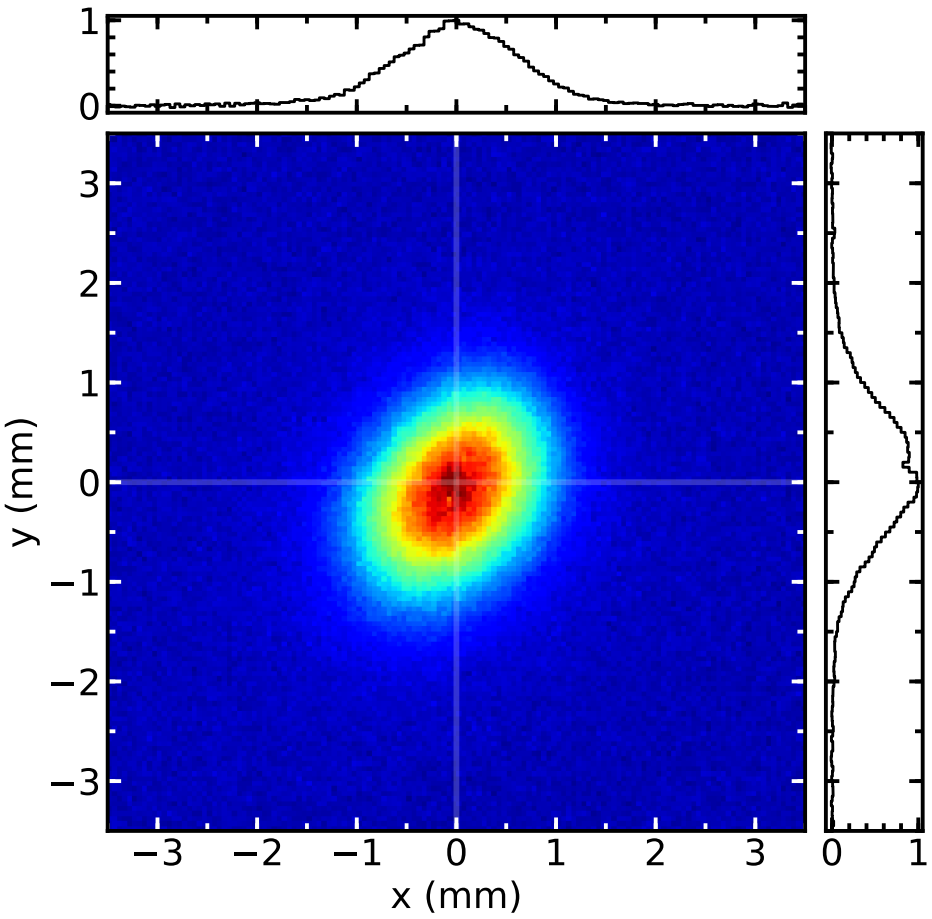

Figure 3.6: An image of the positron beam taken with a MCP/phosphor screen/CCD camera setup. The white lines pass through the centre of the spot and the plots at the top and right hand side show the 1-D slice along these lines, with normalised intensity. The radial FWHM of the beam is $r_{beam} = 1.90 \pm 0.01$ mm and the temporal width is 3 ns.

at any location within the chamber and any I. The bench-top measurements were validated with in-situ measurements at select positions within the vacuum chamber. The physical restrictions of the setup prevented obtaining a full magnetic field measurement set in-situ.

After the trap a buncher was used to compress the positron pulse in time. This is accomplished by applying a parabolic electric potential $V_B(d)$ along the positron path (high at the start, lower at the end) that is switched on once the entire positron pulse has entered the buncher [20]. The potential is of the form $V_B(d) = kd^2/2$, where k is the harmonic number and d is the distance to the positronium conversion target. This potential compresses the positrons because the slowest positrons enter

last and are spatially separated from the faster positrons, experiencing a larger electric potential and more acceleration. This causes them to catch up to the positrons at the front, all arriving at the end simultaneously as it is a simple harmonic potential [192].

The buncher is made up of thirty-nine ring electrodes with a resistor between each ring for a total measured resistance of 67 Ω, see Figure 3.7(a). V_{B} is applied between the first ring and the thirty-ninth ring, which is grounded. A linearly increasing inter-electrode resistance creates a spatially stepped parabolic potential across the rings. Figure 3.7(b) shows the measured ∼30 ns rise time of the buncher for $V_{\mathrm{B}}^{max} = 350$ V, which was applied using a Behlke HTS-03-GSM switch and was measured using a fast ×100 attenuating probe between the switch output and the electrode. The positrons only experience the initial rise of the pulse, being accelerated out of the buncher before the pulse begins to decay. A final electrode is separate from the parabolic set and is biased to $V_{\mathrm{O}} = +30$ V to block slow positrons that leave the trap after the buncher is pulsed. This is because the buncher pulse cuts off the slowest positrons to achieve the best temporal resolution [192].

The temporal width of the positron beam is optimised by tuning the trigger time of the buncher pulse (thereby changing where the positrons are in the electric potential) to give the minimum positron pulse width. To measure the temporal width the time varying voltage of the on-axis phosphor screen was picked off using a high-pass filter to strip out the large DC bias and displayed on a fast oscilloscope. The MCP is typically separated from the conversion target by ∼ 0.5 - 2 m, but optimising the positron signal at the MCP has been confirmed to optimise the Ps signal due to the buncher having a large spatial focus. An example of the signal measured by the on axis MCP is shown in Figure 3.7(c) and has a typical FWHM of 3 - 4 ns.

Once compression was optimised the positron beam was aligned to the conversion target by steering the beam with several movable electromagnetic coils in the buncher and target regions of the beamline. A 2 mm hole in the electrode beneath the conversion target is used to align the beam to the correct location and the target

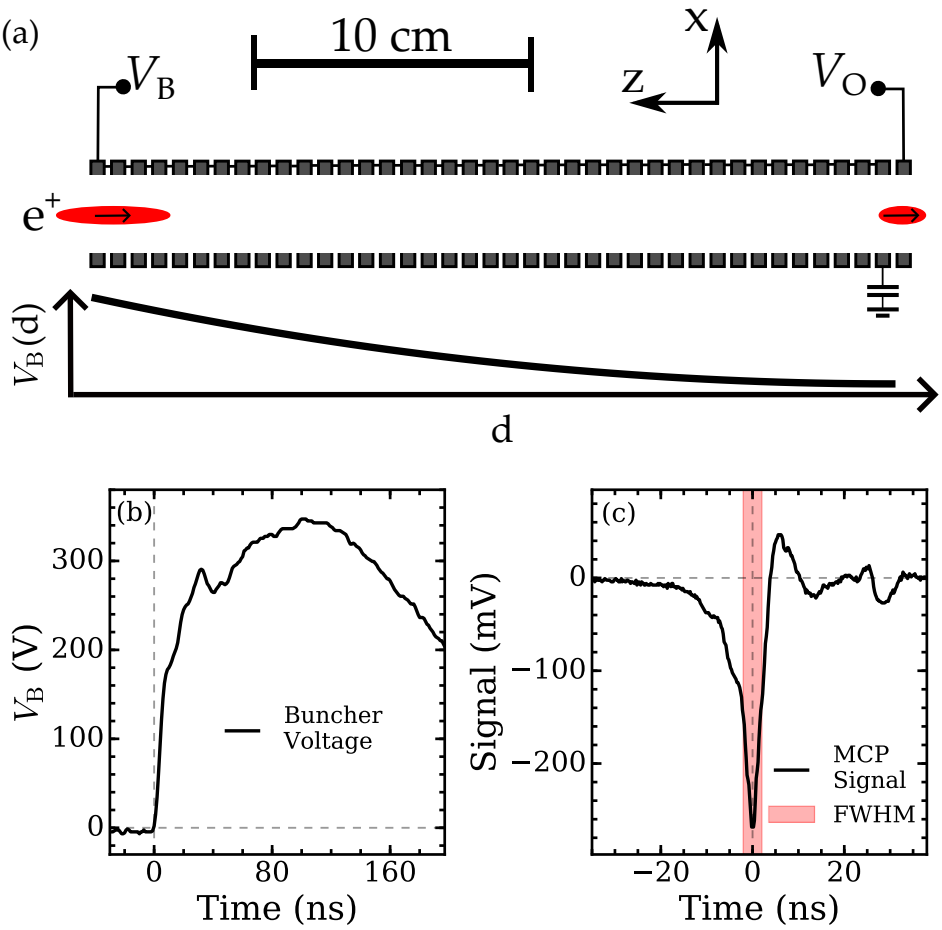

Figure 3.7: (a) A schematic of the buncher electrodes and potentials. V_B is the buncher voltage and V_O is the outlet electrode voltage, the latter of which is shown as a function of distance from the Ps conversion target d. Positrons are incident from the left with >10 ns width and exit the buncher with <4 ns width. (b) The profile of $V_B(t)$ for $V_B^{max} = 350$ V. (c) The temporal profile of the positron beam as measured by the on axis MCP for the buncher pulse in (b) with a temporal width of 4.1 ns as indicated by the shaded red band.

lowered into the beam using an $xyz\theta$ manipulator stage.

3.2 Gamma-ray Detection

Time-resolved gamma-ray spectroscopy is used to quantify Ps production, laser excitation and quenching. This requires a gamma-ray detector sensitive to the annihilation radiation of the positron, and capable of providing time-resolved data on experimental timescales. The detectors used are made of a scintillator crystal, an acrylic light guide and a photo-multiplier tube (PMT), see Figure 3.8 for a schematic.

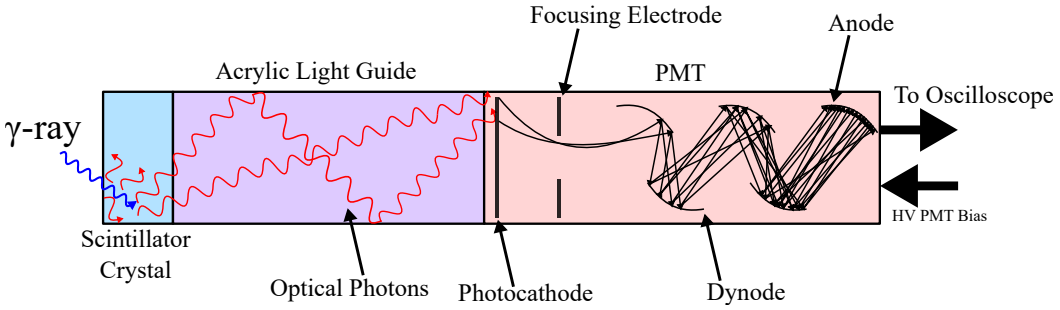

Figure 3.8: Annihilation gamma-ray radiation (blue arrow) incident on the scintillator (blue block) is turned into lower energy photons (red arrows) which are guided to the PMT by an acrylic light guide (purple block). This causes a cascade of electrons (curved black arrows) in the PMT (orange block), the output of which is recorded onto an oscilloscope.

When a gamma-ray strikes a scintillator crystal it emits many lower-energy optical photons. The total gamma-ray detection efficiency of the scintillator is dependent on the stopping power (how efficiently gamma-rays interact with the crystal), and light output of the scintillator (how many photons are emitted per incident gamma-ray). The efficiency is also strongly dependent on the solid angle coverage of the detector. The solid angle will depend on the scintillator surface area and distance from the annihilation events. Detector placement was either optimised for maximum signal-to-noise ratio (SNR) (see Chapters 6 & 7), or for uniform solid angle coverage (see Chapter 5), as described in the relevant chapters.

The primary scintillation crystal used in this work is lutetium yttrium oxyorthosilicate (LYSO) and all experimental data presented uses LYSO scintillators, except where mentioned. LYSO has a decay time of 40 ns (i.e. the time it takes for a gamma ray induced light pulse to decay to $1/e$ of its peak value) [76] and provides good signal-to-noise ratio for studies of long lived atoms from low-intensity pulsed positron beams due to its high light output [21]. The LYSOs in this work were made of arrays of $2 \times 2 \times 25$ mm LYSO crystals in order to keep the photons confined to increase the chance of them entering the light guide and PMT. The crystals were arranged in 5×5 cm squares or 7.5 cm diameter circles.

Two other types of scintillator were used. A $PbWO_4$ (PWO) scintillator to monitor o-Ps production, and a NaI scintillator to monitor moderated positron count rates. PWO has a higher gamma ray stopping power than LYSO but a much lower

light output, making it less suited to spectroscopy [21]. However, it has a shorter decay time of 12 ns [62], making it ideal to observe the short lived ground state. The NaI is not suitable for spectroscopy because of its > 100 ns decay time, but a high stopping power makes it ideal for recording continuous count rates.

An acrylic light guide transports photons produced in the scintillator to the PMT. This is to keep the PMT outside regions of high magnetic field, which can affect a PMTs operation by changing the electron trajectories between dynodes. The PMT turns a single photon into an electron using a photocathode, and a series of sequentially charged dynodes multiplies the number of electrons. The resultant cascade of electrons produces a time-dependent voltage $V(t)$, which is proportional to the number of incident gamma-rays and is recorded using an oscilloscope. The PMT reduces the temporal resolution of the system by another few ns due to the response time of the dynodes. Each PMT is biased with a high voltage to amplify the signal, the higher the bias the higher the gain.

3.3 Data Acquisition & Analysis

The oscilloscopes used to record the detector signals were a 12-bit Lecroy HDO4104 and an 8-bit Agilent InfiniVision DSO6104A, both with a 1 GHz bandwidth, and a temporal resolution of $dt = 2$ ns on all channels. The scopes were triggered to record a 4μs time window at the repetition rate of the beam starting at the same time the trap gate was lowered. This ensured that all possible Ps events were measured, and typically involved ~ 1 μs of delay between triggering and positron arrival at the conversion target (i.e. t_0).

The entire beam is controlled remotely by a computer using LabView 2017. The software records the raw data of sixty shots of the positron beam (which equates to one minute of DAQ time) from the oscilloscope to the computer. The computer then goes to the next controlled variable (i.e. a change in laser delay, laser wavelength or microwave frequency etc.) and records another sixty shots[1]. Once the

[1] Sixty shots between variable changes allows variation of the beam over time to be accounted for while also optimising data acquisition time, as waiting for variable changes is slow.

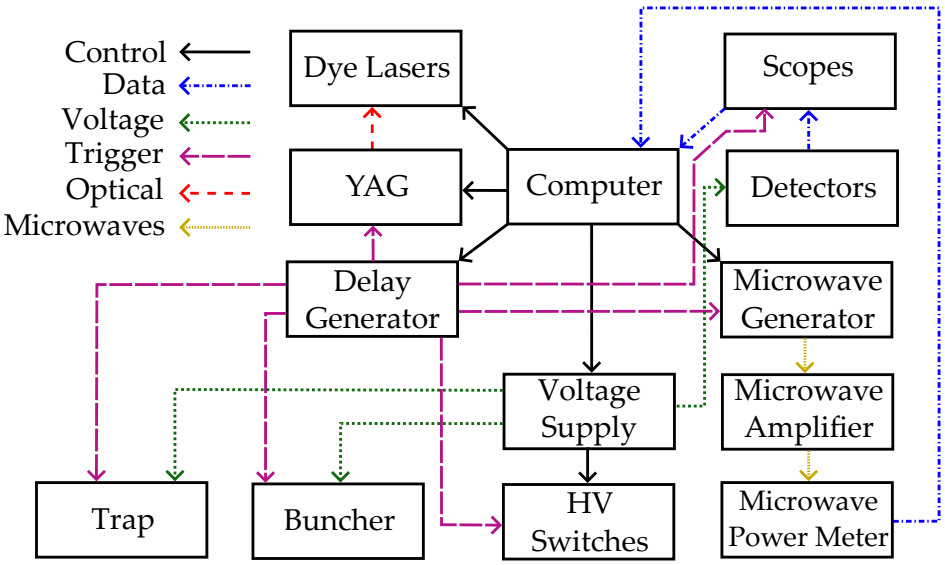

Figure 3.9: A schematic representation of the information flow of the system between all the equipment. Control is shown as solid black arrows, data is dot-dashed blue, voltages are large dotted green, trigger pulses are large dashed purple, optical inputs are small dashed red and microwaves are small dotted yellow. The microwave amplifier was only present for the work presented in Chapter 6, and the microwave power meter is not present during Ps data acquisition.

program has recorded sixty shots for each controlled variable[2] programmed into a data run (i.e. a line shape or a laser delay optimisation scan) it will repeat the process. Figure 3.9 shows a diagram of the signal flow in the system demonstrating how all the processes are controlled and linked.

The output of each detector was passed through a 50 Ω splitter[3], to split the signal in two. This reduced the amplitude of the signal by half for both outputs of the splitter, but allowed the scope settings to be changed to provide a low-gain and high-gain channel for each detector. The low-gain channel was set so that the whole signal was recorded by the scope, from noise floor to peak. The high-gain channel was set so that the top of the initial positron annihilation peak was cut off, but the tail was still visible, see Figure 3.10(c). This provides higher resolution of $V(t)$ in the tail end of the signal and because $V(t)$ has an exponential decrease this gives better SNR for the low amplitude events at the end of $V(t)$ which corresponds to long lived Ps. The high-gain channel has a scope selected range which is $\sim$2% of

[2]The order of which is randomised.
[3]The PMT and scope impedance is 50 Ω.

the low-gain channel with around 150 ns of the peak cut off.

Data analysis is performed in Python [257, 258], during which the high and low gain channels are recombined to provide one complete time spectra per shot of the positron beam per detector. Examples of this are shown in Figure 3.10(c) where all data of $V(t) < 10$ mV is from the high gain channel. Any DC offset is removed by averaging and subtracting the first one-hundred data points of the scope trace, ~ 800 ns before the positrons arrive at the conversion target. The maximum signal amplitude V_{max} of each shot of the positron beam occurs when the positron pulse hits the conversion target and is known as the prompt peak[4]. The V_{max} of each shot within a data run were compared and any shots outside the scatter of the V_{max} values were discarded. This is because anomalously low V_{max} values indicate a misfire of the trap/buncher or other accumulation/timing issues which can have a dramatic impact on the SNR of the processed data due to the incorrect relative timing of the system. Figure 3.10(a) shows an example of the recorded V_{max} for one data run taken in Chapter 7 with only one shot being discarded. In a typical data run there will be fewer than 0.05% of shots discarded.

In the data analysis, t_0 is defined as the arrival time of the positron pulse at the target. t_0 was extracted from the recorded data by applying constant fraction discrimination (CFD) [118] to the rising edge of the prompt peak. This was performed uniquely for each detector and each individual shot of the positron beam. This ensured that t_0 is at the same relative amplitude of the prompt peak in each shot of the beam, compensating for fluctuations in the intensity of the positron beam (and so V_{max}) and any detector dependent effects. This also ensured that any small variations in the arrival time and width of the positron pulse were taken into account. The measured jitter of t_0 was < 1 ns on average, which does not impact the timing of later events.

Figure 3.10(b) shows an example of the calculated t_0 relative to the start time of the data acquisition for the same data as in panel (a). The shot with an anomalous V_{max} value (#4310) also has an anomalous t_0 value. But some shots have an

[4]Note that for these measurements the high voltage gains of the detector PMTs were set to provide a consistent V_{max} of ~ 250 mV across all detector.

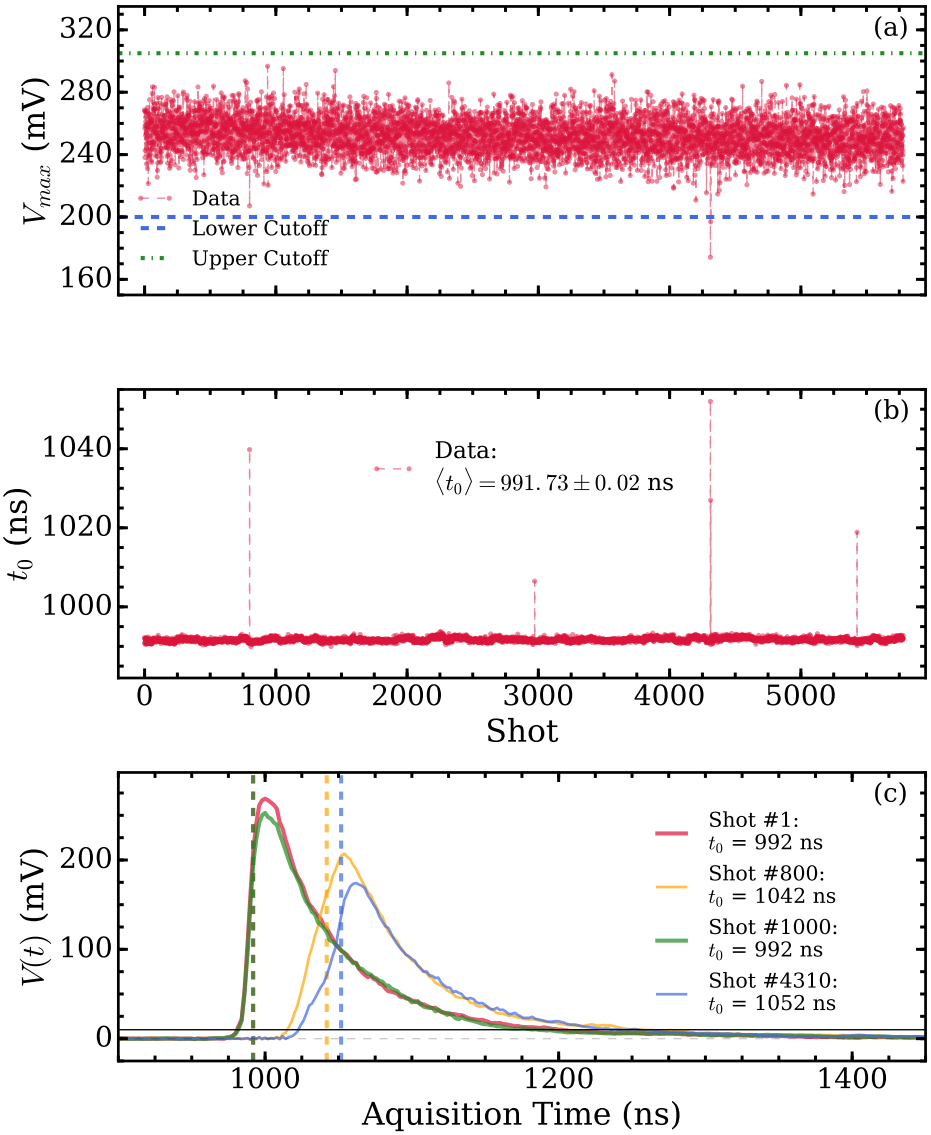

Figure 3.10: (a) An example of the maximum amplitude of the recorded SSPALS spectra for each shot of the positron beam for one detector recorded during the work in Chapter 7. (b) The jitter in the arrival time of the positrons as measured by CFD methods described in the text for the same data as in (a). (c) An example of the CFD process on four sample SSPALS spectra from the data in this figure. The threshold is at 80% of the peak height for all these shots with shots #1 and #1000 being typical and shots #800 and #4310 being anomalous. The horizontal line in (c) is the maximum voltage threshold of the high gain channel.

anomalous t_0 but not an anomalous V_{max} and so were not excluded by this method and will reduce the SNR of the data. Examples of good and bad shots are shown in Figure 3.10(c) with the bad shots (#800 and #4310) visually different from the two

good shots (#1 and #1000). The bad shots arrive later, but also have a longer rise time indicating the positron pulse was not its optimal ∼3 ns duration. The constant fraction used to determine t_0 was 80% of V_{max}, which corresponds to most of the positron pulse being implanted into the conversion target and a few ns before Ps emission (positron implantation and Ps emission are separated by $\sim$ 10 ns for the converter used in this work [93], as discussed in the next section).

3.4 Positronium Formation

A mesoporous silica target was used as a positron to Ps converter due to its low Ps emission energy and reasonable conversion efficiency of ∼30 % [58]. The mesoporous silica is a ~ 1 μm thick film on a substrate of silicon, consisting of bulk silica interspersed with voids of radius $r_{\text{pore}} = 2.5 \pm 0.5$ nm which are connected to the surface (the growth methods of which can be found in References [179, 180][5]), see Figure 3.11 for a schematic.

Incident positrons form Ps in the bulk silica [251], whereby the positrons can free many bound electrons in inelastic collisions[6]. Once the positron has cooled sufficiently it can capture one of the newly free electrons (those that have not recombined with the ions), forming Ps [201]. The Ps then diffuses into the voids with an energy of $\sim$ 1 eV [208] where it cools through inelastic collisions with the void walls [207]. The Ps travels through the voids to the surface and is emitted into vacuum within $\sim$ 10 ns [92].

Ps is almost entirely formed in the ground state and can be either o-Ps or p-Ps, being produced equally in each of the four sub-states with each combination of spins being equally likely [67]. There is one singlet level and three triplet levels, thus 75% of the produced Ps is the desired o-Ps state. Any p-Ps formed is indistinguishable from positrons that annihilate during implantation due to its very short lifetime of 125 ps. Only the o-Ps lives long enough to be cooled and emitted from the voids into vacuum.

[5] In this instance using Pluronic F-127 ethyleneoxide/propyleneoxide block copolymer (BASF) with a 0.016 F-127/Si molar ratio.

[6] The bandgap of Si is 1.1 eV [176] so many electrons are freed when the positrons are implanted at a high energy.

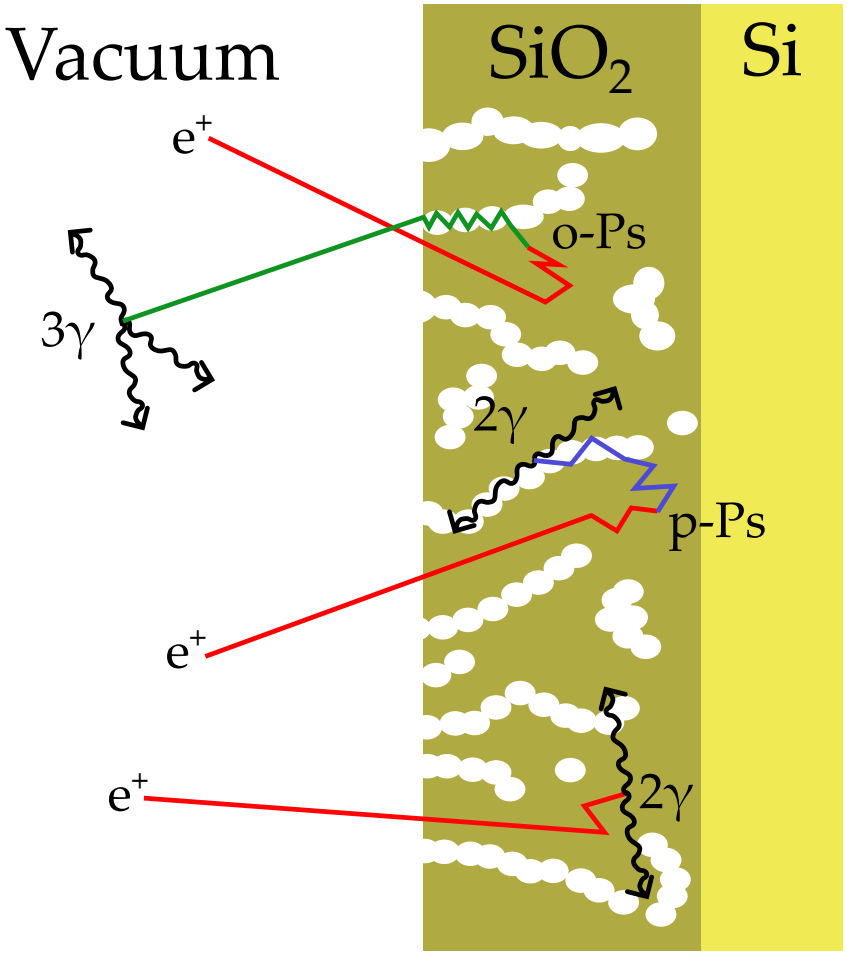

Figure 3.11: A diagram showing the structure of the mesoporous silica targets and the Ps formation process. Incoming positrons (red) can form positronium in the bulk after freeing electrons. p-Ps (blue) will annihilate in the target but o-Ps (green) can escape into vacuum to be laser excited. Wiggly black lines are gamma-rays from annihilation. Not to scale. Adapted from Reference [77]

A negative potential V_T is applied to the silica, which is sitting on an electrode E_T, to accelerate positrons into the target. The larger V_T the slower the emitted o-Ps. This is because higher energy positrons are implanted deeper into the silica film, meaning the resultant Ps experiences more cooling interactions within the pores on its way to the surface [58]. The minimum energy, E_{min}, of the emitted Ps is determined by the zero-point energy of the Ps due to quantum confinement of the de Broglie wavelength in the pores [58]. E_{min} is given by the formula $E_{min} = \pi^2\hbar^2/2m_{Ps}r_{\text{pore}}^2$ which equates to 30 meV for the sample used in this work [58]. Cooling to E_{min} takes ~ 5 ns for implantation energies and targets similar

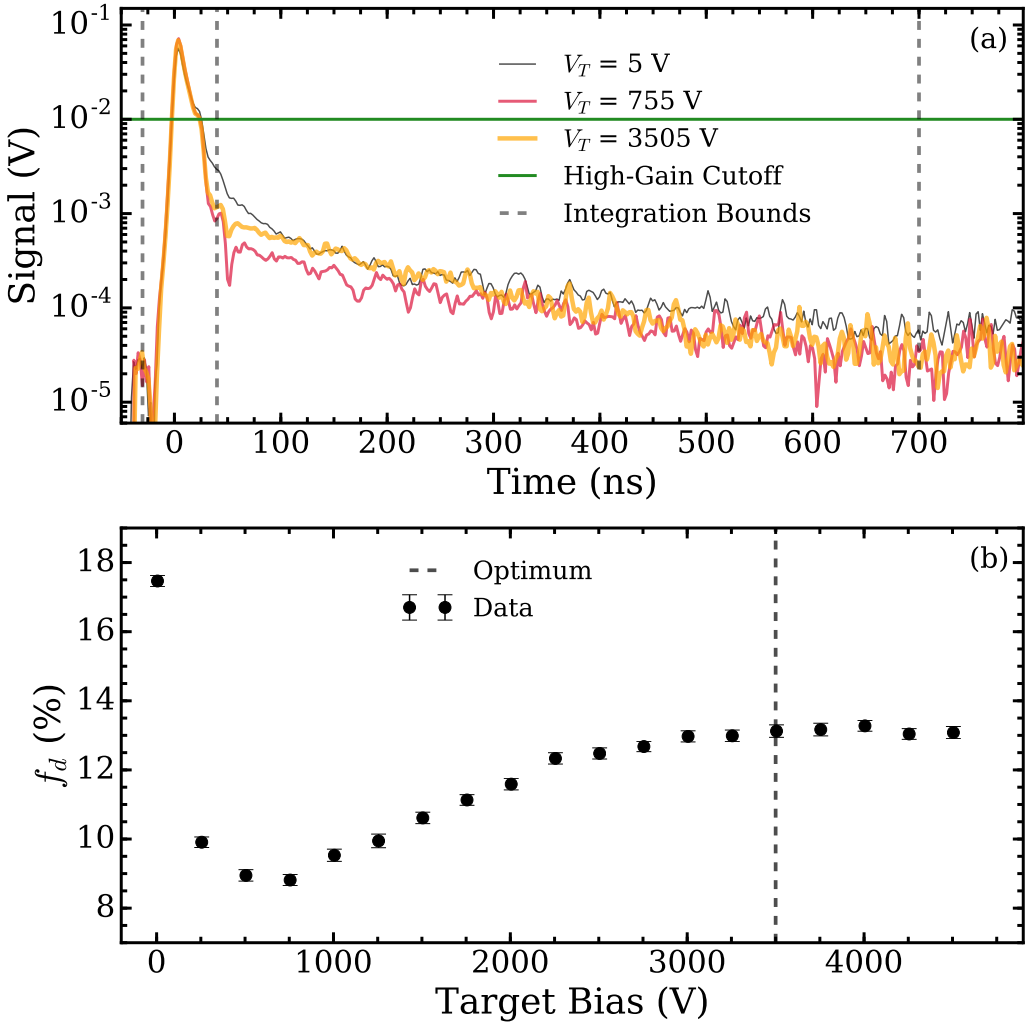

Figure 3.12: (a) Example spectra from the PWO detector at: $V_T = 0$ V showing positrons reflecting from E_T (black), at $V_T = 755$ V showing implantation but no o-Ps emission (red), and at $V_T = 3505$ V showing implantation and o-Ps emission. The dashed vertical lines are the integration bounds A, B and C used to obtain f_d, see Section 3.6. The horizontal line is the maximum voltage of the high-gain channel of the oscilloscope. (b) The delayed fraction f_d as a function of V_T for the silica conversion target with the dashed line showing the value of V_T used in experiments. Each spectra was 180 shots of the positron beam.

to that used in this work [92].

In this work the potential applied to the target for positron implantation was $V_T = -3.5$ kV. The bias was kept as low as possible, while maintaining efficient Ps production and cooling, in order to minimise the effect of Stark quenching of the 2S state and Stark shifts of microwave transitions. Figure 3.12(b) shows the optimisation of V_T where f_d is proportional to the amount of Ps being produced (and is

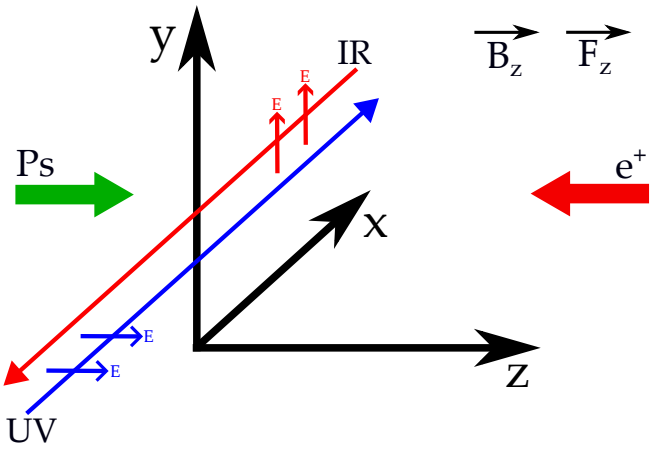

Figure 3.13: The coordinate system used in this work. Positrons (large red arrow) were incident from the $-z$ direction and the Ps (green arrow) was emitted in the opposite direction in reflection geometry. The electric and magnetic fields were both aligned along the z-axis. The IR laser (thin red arrow) propagated in the $-x$ direction, polarised orthogonal to the applied fields. The UV laser (blue arrow) propagated in the $+x$ direction, polarised parallel to the applied fields. The y-axis is the vertical axis.

explained in detail in Section 3.6). This data was recorded using a PWO scintillator due to the faster decay time offering improved temporal resolution. Figure 3.12(a) shows the corresponding SSPALS spectra of a ground state Ps signal for 180 shots of the positron beam at different implantation energies. With zero, or near-zero, implantation energy positrons are reflected from E_T which causes a large f_d and a broad prompt peak, but no Ps formation. As the positrons are more efficiently implanted f_d drops but still no Ps is emitted, narrowing the prompt peak. Finally enough Ps is made and emitted to start to increase f_d again with the SSPALS spectra tail forming an exponential of $\tau_{o-Ps} = 142$ ns.[7]

The conversion target is a reflection target, meaning the o-Ps is emitted back along the same direction as the incident positrons. The coordinate system used defines the direction of Ps emission as the positive z-axis, see Figure 3.13, with the lasers propagating in the x-axis and magnetic fields also in the z-axis.[8] Figure 3.14

[7] Note the horizontal green line in Figure 3.12(a) shows the cutoff between the high- and low-gain channels of the recorded data.

[8] A reflection target is limited by the fact that the Ps experiment must take place in the same region as the positron beam, sharing fields and apparatus. But reflection mesoporous silica targets are easier to make and have higher production efficiency than their transmission counterparts because positrons are not lost in the substrate [28,184]. Other transmission converters such as thin film metals (e.g. [191] which produces Ps and Ps^-) and smoked MgO [130] produce faster Ps than mesoporous

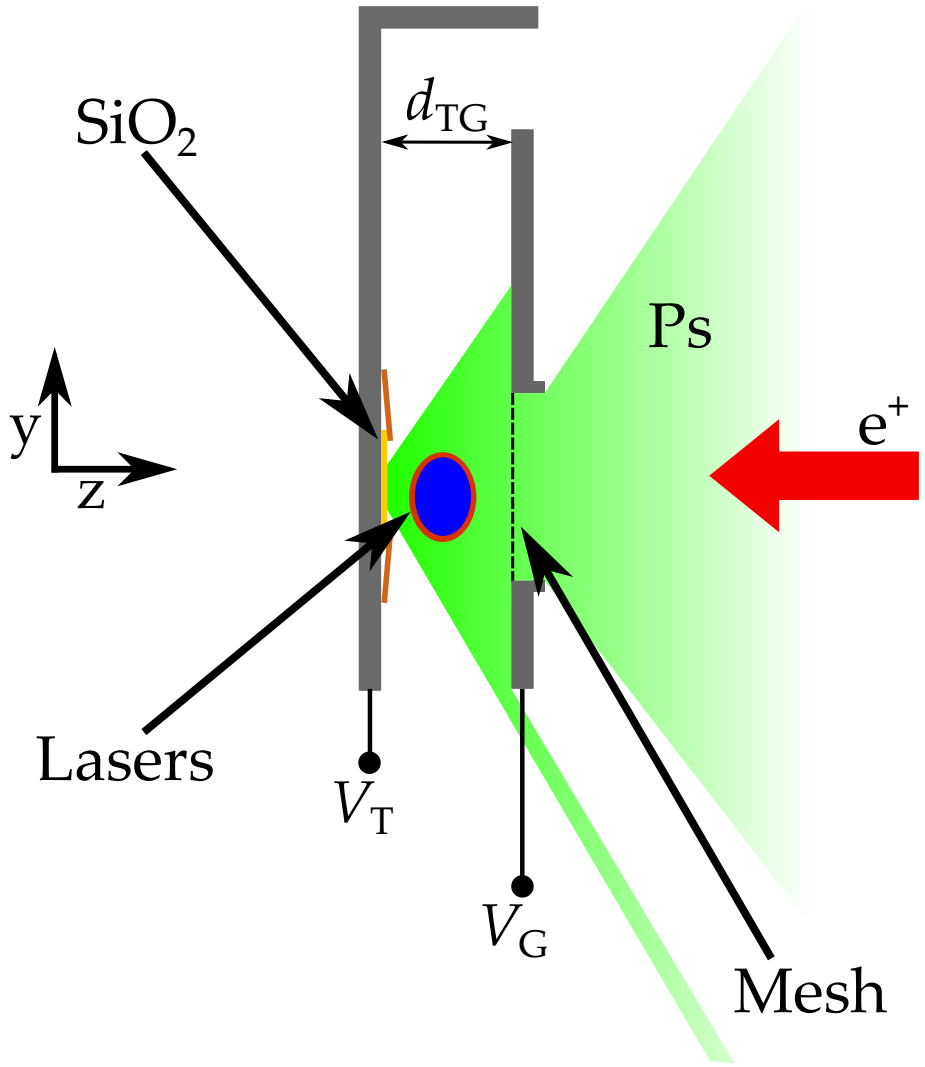

Figure 3.14: A close up of the excitation region between the target E_T and grid E_G electrodes, both made of Al. The dashed line on E_G is the tungsten mesh, which has a diameter of 16 mm. The red arrow shows positrons incident from the right and the green shading represents the Ps cloud as it spreads out in the opposite direction, with some escaping underneath the grid. The yellow is the silica target fixed to E_T by the Cu (brown) clamps. The blue and red spots represent the UV and IR lasers, respectively.

shows the target electrode E_T with the silica target affixed to it with copper clamps. The electrode E_G, being a distance d_{TG} and electrically isolated from E_T by ceramic insulators, is there to allow control of the electric field in the laser excitation region (LER) between E_T and E_G. The electric field, F_{TG}, was in the z direction, parallel to the guiding magnetic field B_z. Incident positrons and emitted Ps pass through a

silica.

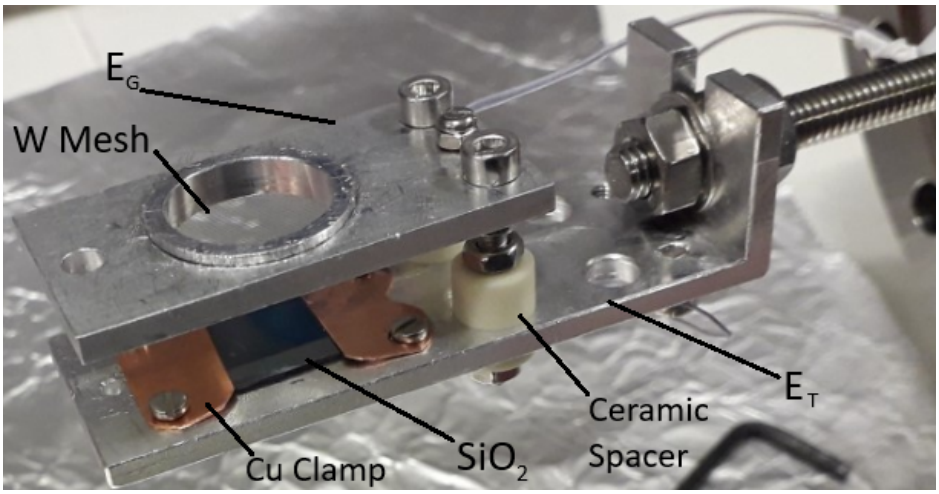

Figure 3.15: A photograph of the target E_T and grid E_G electrode with $d_{TG} = 11$ mm.

$\sim$95% transmission tungsten mesh with a 16 mm diameter. Figure 3.15 shows a picture of the setup used in this work.

E_G is grounded in most experiments but is sometimes biased to $V_G = -400$ V. This is because although incoming positrons possess an energy of ~ 300 eV from the buncher, they can reflect or be deflected from the electrodes if a component (such as an insulator) charges up, or if a component (such as a screw) is slightly magnetic. A negative bias on E_G allows incoming positrons to overcome any repulsing potential and pass through the grid to be implanted in the conversion target. $V_G = -400$ V was the minimum bias required to prevent the back-scattering process. Positron back-scatter is not desirable because it can cause distortions to the SSPALS spectra which is detrimental to some experiments and will be stated as such in the appropriate chapter.

Although the minimum energy of the Ps in this work is $E_{min} = 30$ meV the average o-Ps atom is much faster than this at ~ 120 meV [229]. The longitudinal velocity distribution v_z in our coordinate frame is always positive, moving away from the target. Ps from similar mesoporous silica targets has a measured average longitudinal velocity of $v_z^{rms} \approx 180$ km/s, but with a broad range of 20 - 450 km/s [22,92]. The radial velocity $v_r = \sqrt{v_x^2 + v_y^2}$ is expected to be uniform in all directions due to the random alignments of the pores and have a cosine distribution [22]. This has been measured by Doppler spectroscopy of the 1S $\rightarrow$ 2P transition, see Section 3.7

for details, with typical average velocities of $v_r^{rms} = 95$ km/s.

3.5 Laser Setup

This experiment required laser light with wavelengths of 243 nm and ~ 734 nm for the Ps $1\,^3S_1 \rightarrow 2\,^3P_J$ and $2\,^3P_J \rightarrow n\,^3S/D_J$ transitions respectively, see Figure 1.2 for a diagram of the excitation scheme. The laser setup used to produce these wavelengths started with a Continuum Surelite II Nd:YAG laser which was pumped by a Xe lamp running at 10 Hz producing pulses of $\lambda = 1064$ nm light at a 1 Hz repetition rate to match the positron beam. The 1064 nm beam had a temporal width of $\Delta t = \sim 5$ ns, a diameter of 7 mm and an energy of ~ 650 mJ per pulse. The 1064 nm light was frequency doubled to 532 nm using non-linear processes in a dihydrogen phosphate (KDP) second harmonic generation (SHG) crystal. The fundamental and second harmonic were frequency tripled using a second KDP crystal to give 355 nm light. The phase-matching of the harmonic crystals is optimised to give maximum 355 nm power and the resultant pulses had the same spatial and temporal characteristics as the original 1064 nm pulses. See Figure 3.16 for a full layout of the laser setup.

The 355 nm light (typically ~ 100 mJ) pumped a Sirah Cobra Stretch dye laser with a single amplifier stage. The dye used was Coumarin-480[9] and with the resonator tuned to $\lambda = 486$ nm the dye has a gain of $\sim 10\%$. The resonator cavity is not made from a diffraction grating, as is typical in ns dye lasers to minimise the bandwidth of the laser pulse. Instead it is made from a set of prisms and a mirror designed to give the maximum bandwidth possible, in this case $\Delta\nu_{FWHM} = 100$ GHz. This is done to maximise the addressed population of the Doppler broadened $1\,^3S_1 \rightarrow 2\,^3P_J$ transition which has a width of 500 GHz, as discussed further in Section 3.7.

The laser pulse from the Sirah dye laser (the fundamental) was frequency doubled using a BBO crystal to 243 nm. The second harmonic was separated from the remaining fundamental light (the SHG process having an efficiency of $\sim 6\%$) using a set of four Pellin-Broca prisms, see Figure 3.16, which removed the unwanted

[9] Or Coumarin-102 depending on your naming preference. Which has a tunable range of 459 - 508 nm.

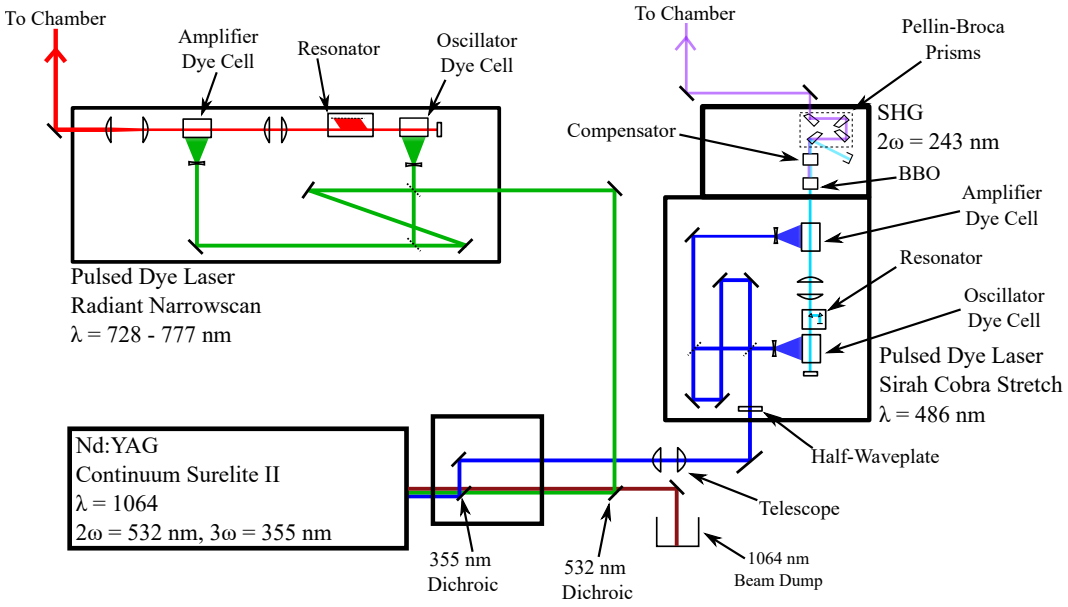

Figure 3.16: A diagram of the laser setup at UCL. The 355 nm (blue) from the YAG laser pumps the Sirah dye laser to produce 486 nm (light blue) which is doubled to 243 nm (purple) which goes into the chamber. The 532 nm (green) from the YAG pumps the Radiant dye laser to produce IR radiation (red) which is sent to the chamber.

fundamental wavelength while preserving the beam alignment as the wavelength changed. The resultant UV beam was capable of scanning the full line width of the $1\,^3S_1 \rightarrow 2\,^3P_J$ transition by tuning the resonator cavity. The SHG crystal was automatically phase matched as a function of resonator wavelength using a lookup table designed to provide maximum UV power.

The UV beam was transported to the vacuum chamber using excimer laserline mirrors designed for 248 nm radiation but which still have >97% reflectivity at 243 nm at an angle of incidence of 45° and 180°. The final UV beam at the Ps conversion target propagates in the $+x$ direction, is linearly polarised parallel to the electric and magnetic fields, has $\Delta t = 5$ ns, $\Delta\nu_{FWHM} = 100$ GHz, and a spatial FWHM of 7.5 mm vertically and 5.1 mm horizontally (as defined by the dye laser). The UV beam entered the vacuum chamber through UV suitable vacuum windows with a power loss of $\sim 10\%$. The energy of the UV laser pulses had a shot-to-shot rms stability of $\sim 4\%$ and varied over time from 0.2 to 0.6 mJ due to decay of the laser dye efficiency, which resulted in the laser dye being changed every two to four weeks. The 1S $\rightarrow$ 2P transition was confirmed to saturate down to at least 0.18 mJ,

hence the change in pulse energy should have no significant effect on excited state production.

The 532 nm light from the YAG (typically ~ 45 mJ) pumped a Radiant Precision Scan dye laser with one amplifier stage. The dye used was Styryl-8[10] which has a tunable range of 715 - 779 nm with a peak gain of 16% at 743 nm. The wavelength could be tuned to excitation of $n = 2 \rightarrow 8$ at 777.7 nm, to photoionisation ($n = 2 \rightarrow e^+ + e^-$) at 728.4 nm. A Bristol Instruments Model 821 wavemeter was used to calibrate the output IR wavelength of the Radiant to a precision of 0.02 nm. The IR beam at the Ps conversion target propagates in the $-x$ direction, is linearly polarised orthogonal to the electric and magnetic fields, has $\Delta t = 5$ ns, $\Delta\nu_{FWHM} = 5$ GHz (the resonator cavity in this dye laser is grating based and so has a narrower bandwidth than the Sirah), and a spatial FWHM of $\sim$8 mm. The IR beam was made deliberately larger than the UV beam using a telescope in order to ensure any $n = 2$ Ps was addressed by the IR laser. The pulse energy of the IR laser also had a $\sim 4\%$ rms stability, and varied from 3 to 7 mJ primarily due to instability in the internal alignment of the dye laser optics. This variation occurred on the scale of several months and did not affect the laser excitation process within this work.

3.5.1 Laser Beam Alignment & Selection Effects

The laser beams were aligned in the vacuum chamber to be between E_T and E_G, the laser excitation region (LER), see Figure 3.17. The broad longitudinal Ps velocity distribution meant that the Ps ensemble was spatially larger than the laser spot shortly after emission from the conversion target. The slowest o-Ps velocity in the z-axis was ~ 20 km/s, and the fastest was ~ 450 km/s [92]. If two atoms with this velocity are emitted with a large temporal separation of 4 ns, as per the positron beam temporal width, then the atoms will be over 5 mm apart within < 10 ns (5 mm being the horizontal spot size of the UV laser which dictates spatial selection). Because of this the lasers excite a subset of the Ps v_z distribution, for more information on this see Section 4.1. The laser pulse is 5 ns long meaning that some atoms may fly into and out of the laser beam while it is present, further complicating the

[10] Or LDS-751 depending on your naming preference.

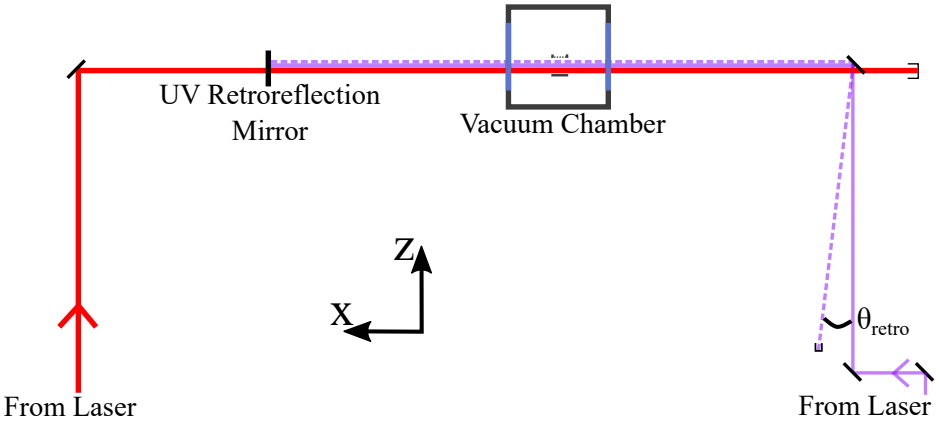

Figure 3.17: A diagram of the laser setup at the vacuum chamber. The IR beam (red) is incident from the left and the UV beam (purple) is incident from the right. The dashed purple line is the retro-reflected beam which is dumped before it goes back into the laser with an angular deviation from the incident beam of θ_{retro}.

selection process.

In the y-axis the maximum velocity was $v_y \approx 350$ km/s, resulting in the atoms being outside the ~ 8 mm UV spot in < 6 ns, compounded by the ~ 3 mm spot size of the positron beam. This means that the further the laser is from the conversion target the more extreme the y-axis selection effect will be because the atoms will take longer to reach the laser spot. Atom selection in the x-axis, being the axis of the laser beams, is determined by spectral overlap, not spatial overlap, and will be explained later in this section.

The laser position was aligned by optimising the laser induced signal (in this case a photoionisation signal that uses the UV and IR beams to ionise the Ps, see Section 3.6 for more detail) to address the maximum possible populations of atoms. The optimal horizontal laser position was $\sim$2 mm from the surface of the conversion target, allowing most of the laser spot to address the Ps, but near enough to the target that the Ps had not spread out too much. The optimal vertical laser position is at the centre of the Ps ensemble, i.e. aligned to the vertical centre of the positron beam. The lasers were aligned to be parallel to the surface of the conversion target in order to only Doppler select the component of the velocity distribution which were symmetric around $v_x = 0$ km/s (see Section 4.1).

As mentioned in Section 3.1.2 the laser is triggered relative to the trap gate

release. A TTL pulse from the SRS DGS649 triggers the YAG flashlamp 178 μs before the trap gate is lowered. The Q-switch (which opens the resonant cavity of the laser and emits the laser pulse) is triggered by a separate TTL pulse a few hundred ns after the trap gate release. The relative flashlamp and Q-switch delay is defined by the laser properties and chosen for maximum pulse power. The exact Q-switch delay is determined by multiple factors including the electronic lag in the system, the time it takes for the positrons to arrive at E_T, and the laser beam path length from the YAG laser to the chamber. The UV and IR beam path lengths were designed to be the same to ensure that their arrival time at E_T did not differ by more than 2 ns, and the YAG has a jitter of 1 ns, which will not significantly effect Ps excitation.

t_{lsr} is defined as the arrival time of the laser at E_T with respect to t_0. This was measured using a plastic scintillator with a fast rise time ($\sim$ 2 ns), and a decay time of $\sim$ 10 ns, coupled to a PMT. Normally the detectors in this work were completely covered in blackout material to prevent ambient light and the laser pulse causing events on the PMT. However, this detector had a small pinhole in the end to let in the laser light. This allowed the positron and laser pulses to be observed on the same device and the relative timing to be determined to within 2 ns. Figure 3.18

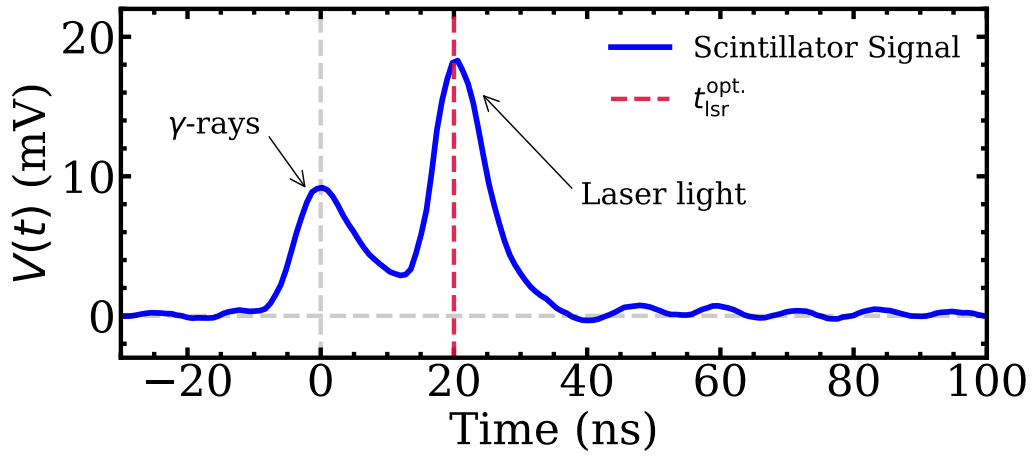

Figure 3.18: An oscilloscope trace recorded using the plastic pinhole scintillator detector described in the text used to measure the relative timing of the positron and laser pulse. The first pulse at t_0 is the positron pulse and the second pulse is the lasers at $t_{lsr} = t_{lsr}^{opt.}$. This trace is the average of 30 shots of the positron and laser beams.

shows an example of this data for the optimal value of $t_{\mathrm{lsr}} = t_{\mathrm{lsr}}^{\mathrm{opt.}}$, as defined below.

The temporal overlap of the laser with the Ps is optimised by scanning the delay of the YAG Q-switch, and therefore the value of t_{lsr}, to find the maximum photoionisation signal. This changes the subset of the o-Ps distribution that is excited by the laser, whereby different parts of the broad v_z distribution will be within the laser beam profile at different times. Delaying the Q-switch in this manner does not affect the power as the change in flashlamp/Q-switch timing is negligible and so the signal change can be entirely attributed to velocity selection effects. An example of a laser delay optimisation scan is shown in Figure 3.19 with a typical optimum $t_{\mathrm{lsr}}^{\mathrm{opt.}}$ of $+20$ ns. The signal is given as the S_γ parameter (explained in the next section) which is proportional to the amount of Ps addressed by the laser. Ps is emitted from the conversion target ~ 10 ns after implantation [92], and as established earlier the Ps cloud is larger than the laser spot within 10 ns after emission. $t_{\mathrm{lsr}}^{\mathrm{opt.}} = +20$ ns is therefore the latest time at which the laser and Ps overlap will be at its maximum.

Although t_{lsr} is typically selected to address the maximum amount of Ps, sometimes it is desirable to change the energy of the Ps but reduce the excitable population. By making the laser delay earlier than the optimum (i.e. $t_{lsr} < t_{\mathrm{lsr}}^{\mathrm{opt.}}$ ns) a faster slice of the total Ps distribution will be targeted, and when the laser delay is later than the optimum ($t_{lsr} > t_{\mathrm{lsr}}^{\mathrm{opt.}}$ns) it will target a slower portion of the atoms. The speed can be measured by Doppler spectroscopy, as discussed in Section 3.7.

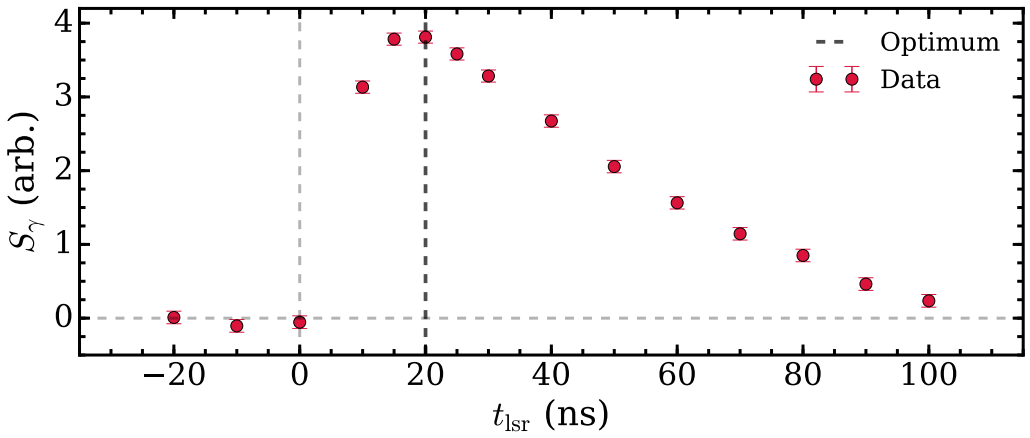

Figure 3.19: A laser delay scan (red points) showing that the time at which the lasers address the most Ps is at $t_{\mathrm{lsr}}^{\mathrm{opt.}} = +20$ ns as indicated by the dashed line.

One excimer mirror was used to retro-reflect the UV beam back through the chamber in the $-x$ direction after it has addressed the Ps once on its incident, $+x$ direction, pass, see Figure 3.17. This, while also increasing the total UV laser power, has the primary benefit of compensating for any Doppler selection effects due to wavelength drift which can happen due to temperature and humidity fluctuations in the dye laser. If the laser wavelength is detuned from resonance then atoms moving away from/toward the laser will be preferentially excited depending on the direction of drift. By retro-reflecting the beam this effect, and any recoil from the energy of the photons, is exactly reversed, resulting in $\langle v_x \rangle = 0$ km/s.

The retro-reflected beam must be well aligned to the incident beam to ensure proper Doppler selection. The beam was overlapped precisely in the horizontal direction to ensure the velocity selection of v_z did not change, and slightly misaligned in the vertical direction to allow the beam to be blocked before it re-entered the laser to prevent damage. This resulted in a $\theta_{\text{retro}} < 0.6^\circ$ divergence, for a misalignment of < 3 mm at E_T meaning a reasonable spatial overlap between incident and retro-reflected beam. The retro-mirror was $\sim$ 30 cm from the conversion target meaning the retro pulse would be delayed from the incident pulse by 2 ns. Given the 5 ns duration of the laser pulse this gives the retro-beam good temporal overlap with the incident beam, whereby the Ps will travel < 1 mm in this time. The retro-reflected beam typically has its power reduced by $< 25\%$ relative to the incident beam. This is due to transmission through the UV vacuum window twice and reflection from the excimer mirror. The IR beam can pass through the retro-reflection mirror with $>90\%$ transmission allowing retro-reflection to be confirmed through the observation of a Lamb dip in Doppler scans as shown in Figure 3.23 and explained in Section 3.7, demonstrating sufficient power and good alignment.

3.6 SSPALS & Photoionisation

Time-resolved gamma-ray spectroscopy is used to detect and quantify the Ps signal, with the particular method used being single shot positron annihilation lifetime spectroscopy (SSPALS), first demonstrated by Cassidy et al. in 2006 [62]. It works

by measuring many decay events simultaneously from pulsed positron sources using the detectors described above and analysing the time-resolved data. An example of the recorded oscilloscope data has already been shown in Figure 3.12(a) which shows $V(t)$ for a PWO detector at different values of V_{T} demonstrating the formation of Ps.

For laser induced signals a LYSO detector is used, an example of which can be seen in Figure 3.20(a) for two different cases. The grey, dashed line is Ps production from mesoporous silica but no laser excitation (i.e. 'laser off'), this case shows self-annihilating o-Ps events. The second case in solid green is where the o-Ps is photoionised immediately after formation by the UV and IR lasers described above in a two-step, two-colour process (i.e. 'laser on'). This is a technique known as REMPI (Resonance Enhanced Multi Photon Ionisation) [94] where the IR photon is tuned to be on resonance with the $n = 2$ to ionisation threshold energy interval, the full process is: $1\,^3\mathrm{S}_1 \xrightarrow{\lambda=243\ \mathrm{nm}} 2\,^3\mathrm{P}_J \xrightarrow{\lambda=728.2\ \mathrm{nm}} e^- + e^+$. This causes the positron and electron to be freed, whereupon the positron is attracted to the negatively biased target still at -3.5 kV, and has a 70% chance of annihilating, causing a peak in the measured SSPALS spectra. The example given here is a photoionisation signal occurring at $t_{\mathrm{lsr}} = t_{\mathrm{lsr}}^{\mathrm{opt.}}$ for T$= -3.5$ kV and $\mathrm{E_G} = 0$ V (both DC). It is possible to see the decrease in the photoionised signal at late times compared to the spectra with the 'laser off', from 200 - 500 ns, however the increase in early annihilation at t_{lsr} is harder to see due to the dominating annihilation from the incident positrons.

This early part of the signal, the prompt peak, is caused by instantaneous annihilation of incident positrons and p-Ps which dominates the smaller and more spread out o-Ps related signals, bearing in mind that 70% of positrons will annihilate upon implantation into the SiO_2 converter. To make changes in annihilation time clearer we can define the laser off spectra as the background and the laser on spectra as the signal. Subtracting the background from the signal produces a background subtracted (or b-sub) spectra which shows very clearly the increase in early annihilation events corresponding to the application of the laser pulse, see Figure 3.20b. The negative signal at later times shows when the o-Ps annihilated in

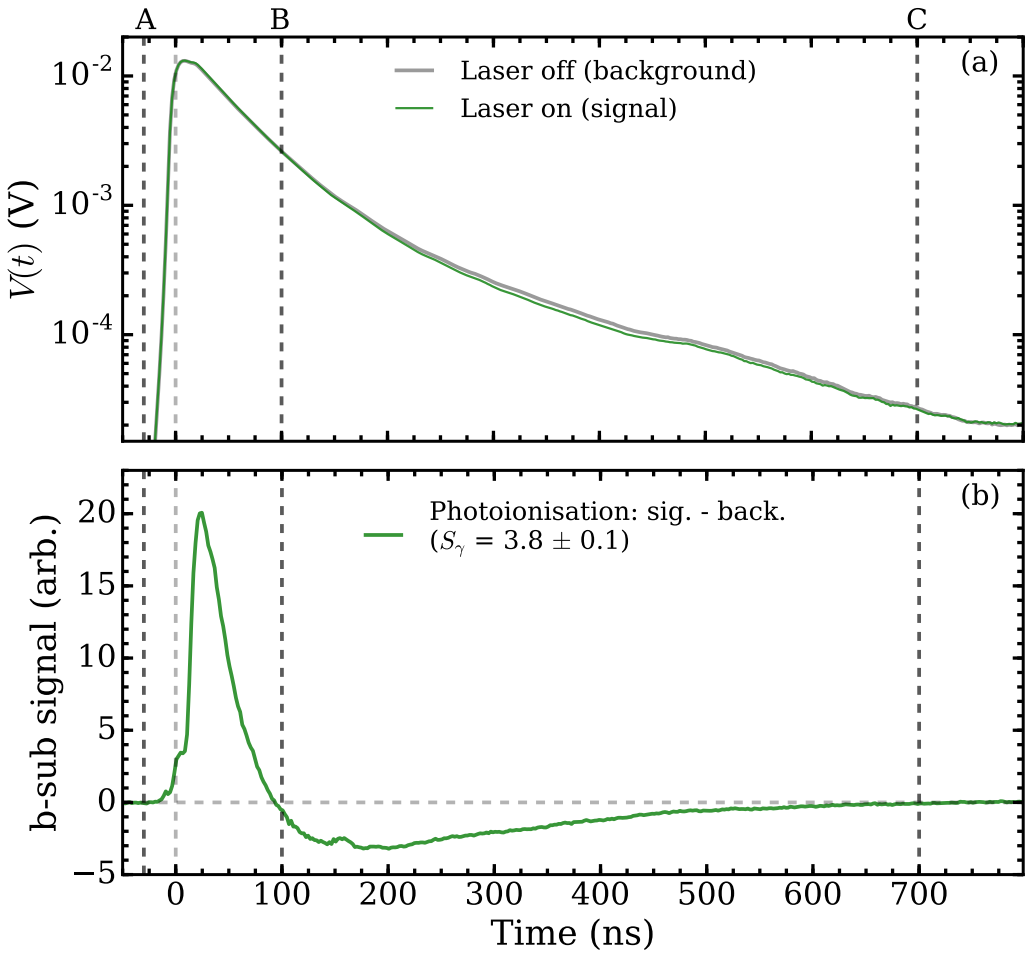

Figure 3.20: An example of a photoionisation signal. (a) shows the SSPALS spectra with the laser on (green) and off (grey) taken using a LYSO detector. A small difference can be seen between the two signals in (a) which becomes clearer in (b) which shows the background subtracted difference spectra of (a). The bump centered around 20 ns shows there is more annihilation at early times when the o-Ps is photoionised. The subsequent dip shows when those annihilation events happened in the background signal. The dashed lines represent the integration boundaries A= −35 ns, B= 100 ns, and C= 700 ns used to obtain S_γ. This is the average of 6 680 shots of the positron beam.

the background signal.

SSPALS quantifies the change in annihilation time by analysing the fraction of events that occur in the latter part of the spectrum, representing long-lived atoms. The fraction of the spectra that is delayed can be obtained by integrating the signal such that

$$f_d = \frac{\int_{\mathrm{B}}^{\mathrm{C}} V(t)dt}{\int_{\mathrm{A}}^{\mathrm{C}} V(t)dt}, \tag{3.1}$$

where A, B and C define time windows. A to C is the total signal and B to C is the delayed events, these bounds are shown in Figure 3.20 for photoionisation spectra. f_d is used to quantify Ps production efficiency, as shown in Figure 3.12, whereby f_d will increase with increased Ps production. All background subtracted signals are normalised to the total area $\int_{\mathrm{A}}^{\mathrm{C}} V(t)$ to account for moderator decay which would otherwise lead to a drop in signal amplitude over long data acquisition times. f_d is self-normalising, being a fraction of events which does not depend on the number of positrons or Ps atoms produced.

It is important to note that while f_d is proportional to the amount of long-lived Ps produced it is not the true fraction of Ps produced due to solid angle variation between events in the prompt peak and the tail, saturation effects of the PMT, the limited temporal resolution of the scintillator and PMT, the two and three gamma ray detection efficiency etc. [57].

The difference between two signals can be quantified by comparing their values of f_d as a fractional difference,

$$S_\gamma = \frac{(f_{bk} - f_d)}{f_{bk}}, \tag{3.2}$$

where f_d is the delayed fraction of the signal and f_{bk} is the delayed fraction of the background. This can be used to quantify and compare different events such as photo ionisation, 2S production and Rydberg FI. In this work a positive S_γ corresponds to more early annihilation events in the signal than the background, meaning the perturbation applied the Ps is causing earlier annihilation (e.g. photoionisation, various quenching effects or field ionisation of Rydberg states). A negative S_γ indicates more late annihilation in the signal compared to the background, meaning the conditions are promoting long-lived Ps (e.g. metastable $2^3\mathrm{S}_1$ or Rydberg production). Figure 3.19 gives an example of how S_γ is used to optimise the laser timing, displaying positive S_γ due to the earlier annihilation of photoionised Ps than o-Ps.

The integration windows of f_d (which are always the same for every shot in a data run) depend on what Ps state or behaviour is being observed (e.g. $2^3\mathrm{S}_1$ production, Stark quenching or photoionisation) and the detector being used. A

is always set before t_0 to include the entire prompt peak. B is chosen based on the event being viewed, whereby the event must cause a change in the annihilation fraction from the region AB to the region BC. The exact value of B is chosen based on the optimum SNR of the S_γ parameter, providing the best contrast between early and late events, see Figure 3.21. C is set as late as possible while excluding noise from the integration region and also optimised for maximum SNR, optimising the amount of signal vs noise in the tail. [62]

Statistical uncertainties in the measurement are calculated from the standard error in the mean of S_γ as calculated for each individual shot. Or when the amplitude of the background subtracted spectra is being extracted it is the standard error in the mean of the shot averaged signals at each individual sampling time.

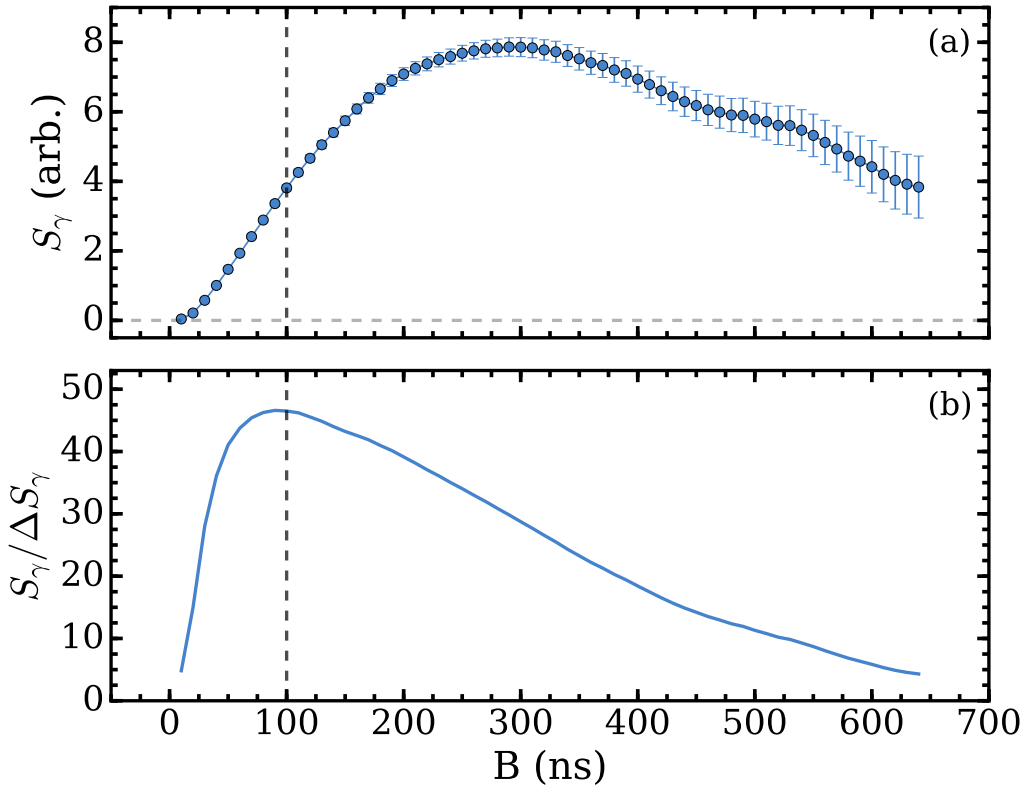

Figure 3.21: An optimisation of the photoionisation signal shown in Figure 3.20 as a function of the integration bound B. (a) shows the S_γ and (b) shows the SNR, the dashed line shows the chosen optimum of 100 ns. This was done for fixed values of A = -30 ns and C = 700 ns.

3.7 1S → 2P Line Shapes

Figure 3.22 shows a line shape of the $1^3S_1 \rightarrow 2^3P_J$ transition, referred to as a Doppler line shape because Doppler broadening is the dominant broadening mechanism for this transition. The line shape is a photoionisation signal measured as a function of UV wavelength (with the IR laser set to the photoionisation wavelength $\lambda = 728.4$ nm, only photoionising Ps that has been targeted by the UV laser). The Doppler line shape allows identification of the centroid UV wavelength which can vary due to the relative alignment of the Ps and the laser (because of asymmetric excitation from Doppler effects), and environmental effects within the laser. Although environmental effects can be compensated for by measuring the output wavelength of the laser, Doppler shifts cannot be, hence the use of Doppler line shapes to monitor the wavelength. During these experiments the UV wavelength was always tuned to the centre wavelength of the measured Doppler line shapes.

As well as determining the optimal UV wavelength, the width of the Gaussian function fitted to the data is a measurement of the average kinetic energy of

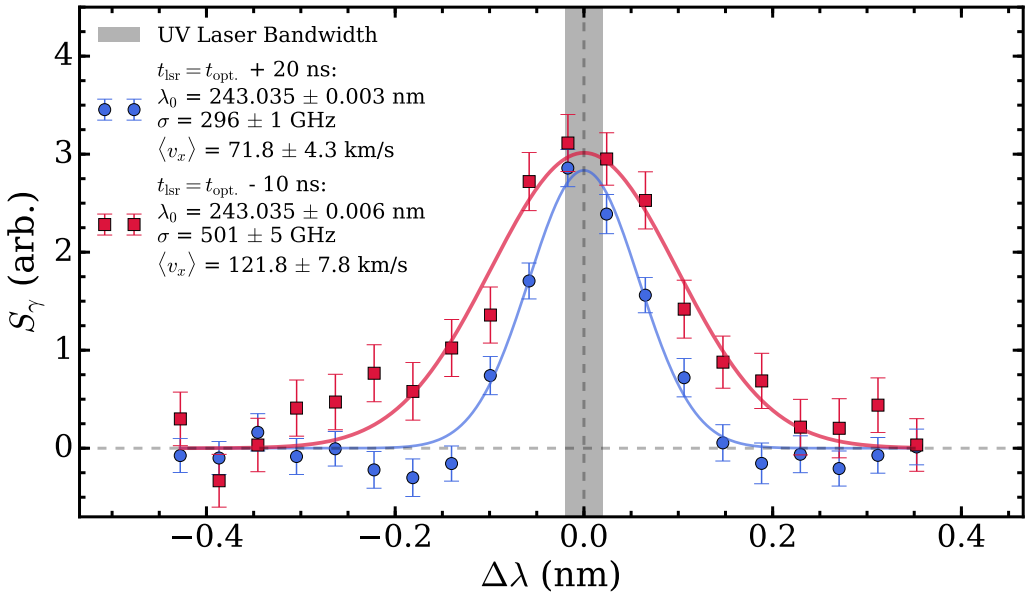

Figure 3.22: Normalised Doppler profiles of the 1S → 2P transition as measured during the work in Chapter 7. The blue (circles) profile was taken at $t_{lsr} = t_{lsr}^{opt.} + 20$ ns while the red (squares) profile was taken at $t_{lsr} = t_{lsr}^{opt.} - 10$ ns. This shows the significant change in velocity obtainable by adjusting t_{lsr}. The shaded region represents the 100 GHz FWHM UV bandwidth.

the Ps in the x-axis which is calculated using the formulas $\langle v_x^2 \rangle = (c\sigma/\lambda_0)^2$ and $KE = m_e \langle v_x^2 \rangle$. This is because the Doppler broadening is significantly larger than any other broadening effect. The measured FWHM of the transition is ~ 500 GHz, and the 100 GHz laser bandwidth is the next largest determining factor of the line width (transit-time broadening, power broadening, and the natural line width are all less than 1 GHz). Figure 3.22 shows two line shapes, the $t_{\mathrm{lsr}} = t_{\mathrm{lsr}}^{\mathrm{opt.}} + 20$ ns data (blue circles and line) has a larger width than the $t_{\mathrm{lsr}} = t_{\mathrm{lsr}}^{\mathrm{opt.}} - 10$ ns data (red squares and line), corresponding to greater Doppler broadening, and therefore higher energy. The two different Ps energies are obtained by varying the delay of the laser excitation from positron implantation, selecting a different subset of atoms as discussed above.

The Doppler profiles measure the transverse kinetic energy in the x-axis, which can also be applied to the y-axis due to symmetry in the pores of the silica. Figure 3.22 demonstrates the symmetry of the Ps velocity distribution, indicating uniform Ps emission from the target in all directions. Time of flight (ToF) measurements to measure v_z are not used in every experiment as they require specialist setups with precisely defined annihilation points [229], which is not always possible, whereas the UV laser is present in all experiments, hence Doppler profiles are used to determine the energy of the Ps atoms.

Doppler profiles were used to confirm retro-reflection of the UV beam. A retro-reflected Doppler profile is shown in Figure 3.23, the proof of retro-reflection being the Lamb dip in the centre of the line shape [173, 187]. The Lamb dip at the resonance is due to both the incident and retro beams targeting the same subset of the v_x velocity distribution (those atoms that had a velocity within the 100 GHz bandwidth of the UV laser), whereby if the laser power is close to or above saturation power, then no more atoms can be excited by the addition of the retro beam [64]. However, if the laser is detuned from the centroid by greater than the Doppler free line width of the transition σ_{LW} (i.e. the line width not including Doppler broadening, but including all other broadening mechanisms such as laser bandwidth, power broadening etc.) then the subset of atoms moving faster than $v_x = 0$ km/s by one line

widths worth of Doppler shift $\pm\lambda_{LW}$ can be excited in both directions, increasing the amount of Ps being addressed by the laser.

If the retro and incident beams are saturating the transition, perfectly overlapped, and there is minimal other broadening then the Lamb dip should be almost 50% of the peak amplitude. This is because the number of atoms moving at a velocity corresponding to $\pm\lambda_{LW}$ will be fractionally less than the number at $v_x = 0$ km/s due to the Gaussian distribution, and thus when summed together will be almost twice the magnitude of the $v_x = 0$ km/s contribution. This is not the case here with a dip of only $\sim 18\%$ of the amplitude. This is likely due to the imperfect spatial and temporal overlap of the incident and retro beams not targeting the exact same subset of the velocity distribution. The profile is fitted with two Gaussian functions with the same width σ and with a fixed separation δ from the centroid λ_0, representing

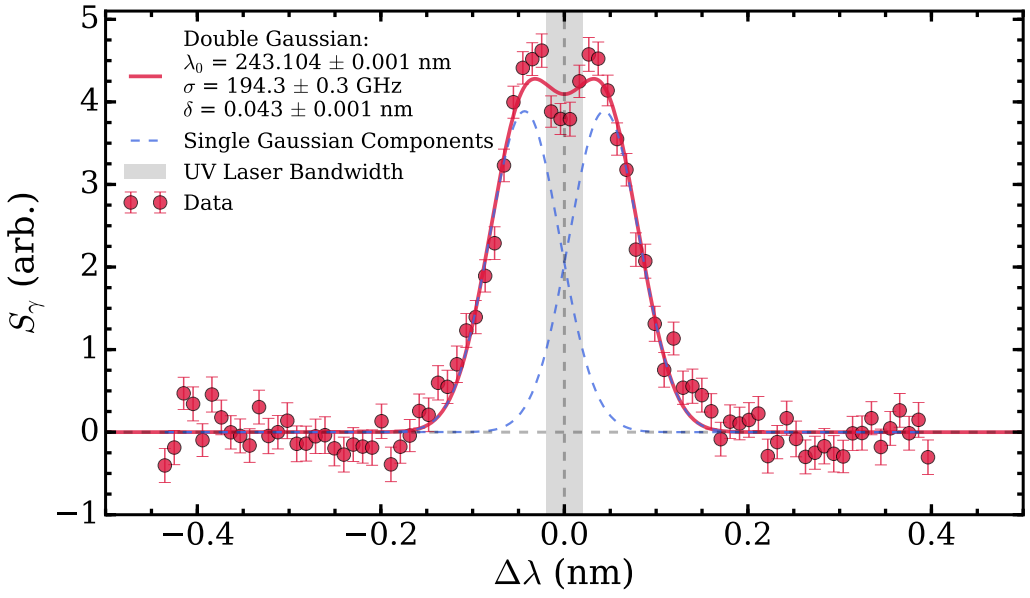

Figure 3.23: A retro-reflected Doppler line shape of the $1\,^3S_1 \rightarrow 2\,^3P_J$ transition (red circles) measured using the photoionisation signal during the work in Chapter 7. The data is fitted with the double Gaussian function given Equation 3.3 (solid red line). The blue dashed lines show the single Gaussian components of the fitted double Gaussian and the shaded band is the UV laser bandwidth.

the two populations being excited by the incident and retro beams,

$$G_{\text{retro}}(\lambda) = A\left(\mathrm{e}^{\frac{-(\nu-\lambda_0+\delta)^2}{2\sigma^2}} + \mathrm{e}^{\frac{-(\nu-\lambda_0-\delta)^2}{2\sigma^2}}\right). \tag{3.3}$$

3.7.0.1 Model Fitting

Mathematical models, such as the Gaussian used to quantify the Doppler profiles, were fitted to data using two methods. For data that only had an error associated with the measured variable a least squares fitting algorithm was used, namely *scipy.optimize.curve_fit* [262]. However, when data had an error on the controlled variable as well as the measured variable the fit was performed using the orthogonal distance regression method (ODR), implemented using the Python scipy.odr module [46], because the least squares fitting algorithm cannot account for error in both variables.

3.8 2^3S_1 Production

As already discussed the 2^3S_1 state is hard to produce due to electric dipole selection rules forbidding single-photon excitation from the ground state. This work utilises Stark mixing of the 2S and 2P states to allow single-photon production of 2S atoms to occur. The Ps atoms are excited from the ground state to $n = 2$ by the UV laser while in an electric field. This produces a mixed state $2^3S_1'$ which has 2^3S_1 and 2^3P_J character as described in Section 2.3.

If, while in this mixed state, the electric field is adiabatically lowered to zero (i.e. slow enough for the probability density to adapt to the changing conditions and maintain its eigenstate [47]) then some portion of the atoms will evolve into the pure 2^3S_1 state with a maximum efficiency of 25%. This is due to the branching ratio of the excited mixed state to the $n = 2$ states upon field removal. i.e. there are nine triplet 2P states and three triplet 2S states that make up the mixed state, all of which may be created upon adiabatic field removal [26]. Because the field that allows the transition to occur also shortens the $2^3S_1'$ lifetime the electric field needs to be lowered as fast as possible to minimise losses from fluorescence while

continuing to be adiabatic to ensure the states evolve into the desired 2S states, not any possible state in the $n = 2$ manifold [20]. The removal rate of the field is limited by the high voltage switches used to remove the field (see Section 3.8.1), and as such the maximum possible switching rate has not been established. No benefit is gained from optimising the excitation field because although a higher field makes the $2^3S_1'$ state decay faster it also makes the laser excitation more efficient, and the opposite was the case at lower fields [26].

The mixed state is more favourably created when the laser polarisation and electric field are parallel (meaning $\Delta M_J = 0$). This preferentially excites the outer triplet Stark states which couple more strongly to the long-lived 2^3S_1 and suppresses magnetic quenching of the atoms to singlet states, allowing more Ps to evolve into pure 2^3S_1 [23, 24]. Due to this selection rule the 2S state is produced with the same atomic polarisation (i.e. the distribution of M_J values in the population) as the ground state with equal distribution across all three M_J sub-states making the 2S atoms unpolarised (barring any polarisation of the positron beam itself which can be up to 30% polarised in similar setups [65], although this has not been confirmed for this experiment).

For 2S production the target electrode E_T was biased for positron implantation, as described above, and the grid electrode E_G was at 0 V, or close to 0 V. The electric field used for excitation is a result of the potential difference between V_T and the low

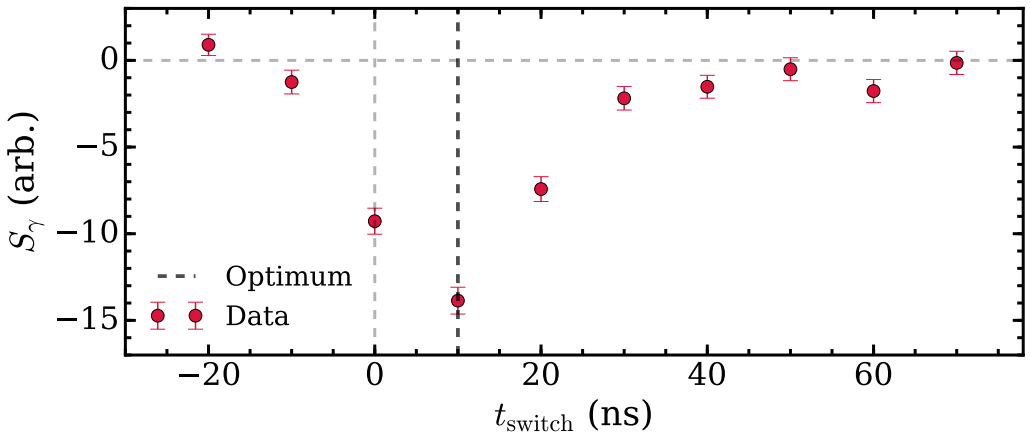

Figure 3.24: 2S production as a function of switching time. The optimum is ∼10 ns after t_0 and ∼10 ns before $t_{\text{lsr}}^{\text{opt.}} = 20$ ns.

(or no) bias on E_G, $F_{TG} = (V_T - V_G)/d_{TG}$. The electric field was lowered by turning off the electrode potentials with Behlke GHTS-60B HV ultra-fast, high voltage (HV) switches, which can lower the applied bias in 30 ns and are described in detail below. Figure 3.24 shows the optimisation of the 2S production as a function of switch trigger time, with the optimum switching time being between positron implantation and laser excitation. This enabled the field seen by the mixed state atoms to be removed as fast as possible while not impeding positron implantation. All 2S signals were produced with E_T being switched off, while all photoionisation signals are produced at a constant $E_T = -3.5$ kV, i.e. no switching.

Figure 3.25 shows an example of a background subtracted 2^3S_1 spectra similar to those used to make the switch optimisation scan in Figure 3.24. The background spectra is an o-Ps signal, i.e. no laser excitation, and the signal spectra is a 2^3S_1 signal, i.e with the laser present. An early dip and a late bump shows the shifting of events from early to late times upon application of the laser (both signal and background had V_T being switched off at the same time as this can affect the incoming positrons which can change the SSPALS spectra). The S_γ is negative as more events occur in the later part of the spectra within the integration time windows selected when the laser in on.

The main disadvantage of this production method is that electric fields are essential. These fields can cause undesired effects within the experiment and if the field is not switched off fast enough significant losses can occur [13]. However, this scheme produces useful amounts of metastable Ps using just one relatively low-powered laser when compared to other optical methods. Other demonstrated methods[11] of producing the 2^3S_1 state include: (1) two-photon Doppler-free excitation from the 1^3S_1 state [72], (2) stimulated emission from the 3^3P_J state [13, 32], and (3) direct production in the metastable state during Ps formation in a positron-Ps converter [74,211]. Each method has its downside; Doppler-free excitation requires

[11] An as yet undemonstrated method is direct excitation from the 2^3P_J state. If enough microwave power is applied to saturate the $2P \rightarrow 2S$ within its short lifetime the 2S state could be produced from a two-photon, two-colour excitation. The main experimental limitation of this method is expected to be the high microwave intensity requirement which is estimated to be > 70 W/m^2 for the Rabi frequency to be on the order of the 2P decay rate, based on Equation 2.23.

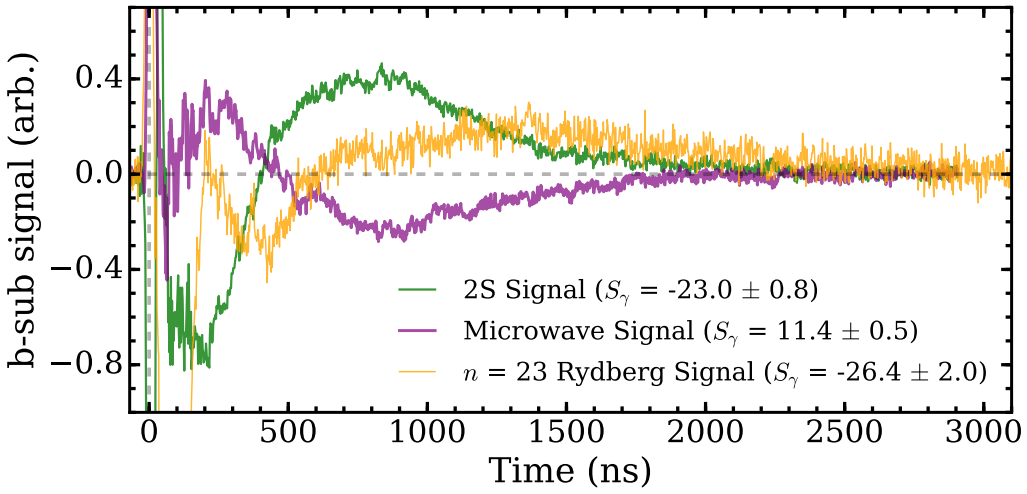

Figure 3.25: An example of a 2^3S_1 (green, laser on - laser off), microwave perturbed 2^3S_1 (purple, microwaves on - microwaves off) and Rydberg (yellow, laser on - laser off) background subtracted SSPALS spectra. The 2S and microwave signal are the average of 11 565 shots taken during the work in Chapter 7 using a waveguide. The $n = 23$ Rydberg signal is an average of 12 738 shots taken during the work in Chapter 5, with methods described in Section 3.10. The Rydberg atoms annihilate later than the 2S because of the longer lifetime of the $n = 23$ state, but also the setup of that experiment resulted in less early collisions with electrodes and chamber walls. The 2S and microwave signal integration bounds were A = -30 ns, B = 700 ns, and C = 1600 ns. The Rydberg signal integration bounds were A = -30 ns, B = 1000 ns, and C = 2000 ns.

high laser power (typically $>$ 10 mJ per pulse) to excite the intermediate state, though this method does achieve the best 2^3S_1 production efficiency. Stimulated emission requires a complex laser setup to excite the 3^3P_J state ($n = 1 \rightarrow 3$ is at 205 nm) and simultaneously stimulate emission to the 2^3S_1 state ($n = 3 \rightarrow 2$ is at 1312 nm). The amount of $n = 2$ created directly in a positron-Ps converter is very low, with all $n = 2$ states produced equally, of which 2^3S_1 is only a small fraction (3/16) [26].

Figure 3.25 shows a background subtracted microwave SSPALS spectra where rf radiation drives the 2S $\rightarrow$ 2P transition which causes the atoms to fluoresce to the ground state and annihilate earlier than the unperturbed, background 2S population (see Section 3.9). A similar process, called Stark quenching, can be performed with the application of electric fields. Just as an electric field makes 2S production possible it can also be used to trigger early decay from the 2S state, causing it to annihi-

late by the following path: $2^3S_1 \xrightarrow{\text{Stark mixing}} 2^3S_1' \xrightarrow{\text{fluoresence}} 1^3S_1 \xrightarrow[\tau_{\text{mean}}=142\text{ns}]{\text{self-annihilation}} 3\gamma$. A field of 3 kV/cm will result in a total decay rate of 0.1 GHz ($\tau_{\text{total}} = 8.1$ ns) for the $2^3S_1'$ state, with the ground state decaying at Γ_{o-Ps}.

3.8.1 High Voltage Switching

Behlke GHTS-60B HV ultra-fast switches were used to control time dependent electric fields. These can switch between two voltages, V_1 and V_2, with a maximum difference of $\Delta V = |V_1 - V_2| = 6000V$ in a minimum rise time of $t_{\text{rise}} = 20$ ns (rise times given as the 10%-90% value). In practice this time is larger due to the resistance and capacitance of the circuit, i.e. from cables, electrodes, vacuum feedthroughs etc.

The switch rise time was measured by connecting the output of the HV switch (while still connected to the electrode to preserve the characteristics of the system) to a 500 MHz, 1 MΩ impedance oscilloscope using a $\times 100$ attenuating, 500 MHz

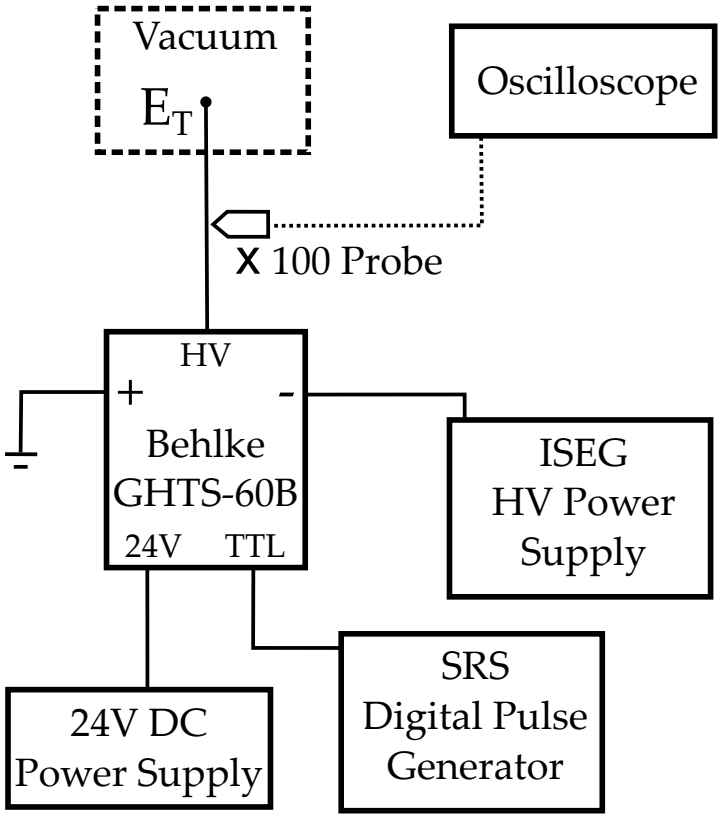

Figure 3.26: The circuit diagram of the HV switching circuit for the target electrode E_T. The HV probe is not present during experimental data taking.

HV probe, see Figure 3.26 for the circuit diagram. The effect of this probe on the switching time is expected to be minimal and depend more on the switch behaviour and electrode capacitance because the probe circuit has a low RC value [26]. An example of this signal can be seen in Figure 3.27 which was recorded for $-3 \rightarrow 0$ kV on E_T and E_G = 0 V. The t_{rise} of each electrode in each experiment will be given in the relevant sections as this can vary due to different cable lengths, d_{TG} and vacuum feedthroughs. In this example $t_{rise} = 32$ ns, which was typical minimum value.

If there is significant capacitance or impedance mismatching in the system then ringing can occur in the switching profile of the HV output, see the oscillations after switching in Figure 3.27. This example has an amplitude of up to 65 V and lasts for >1000 ns. This ringing (and the target bias itself) can create a potential beyond the grid in E_G [183, 230] which can be estimated by [230],

$$\phi = \chi_m s F_{TG} \tag{3.4}$$

where $s = 0.5$ μm is the separation of the wires, and $\chi_m = 0.219$ is a constant

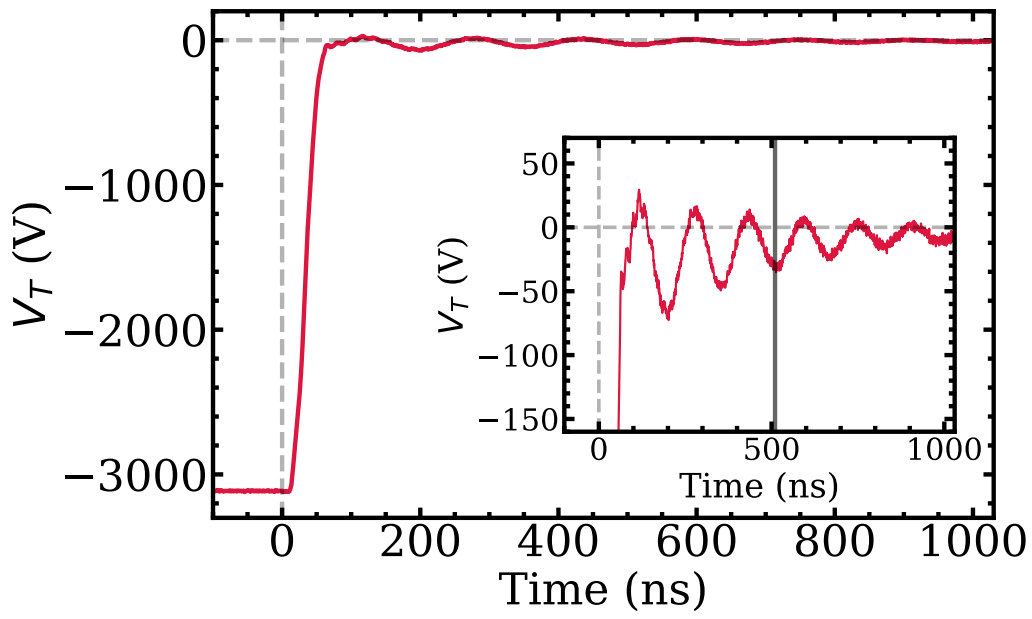

Figure 3.27: The HV output of a GHTS-60B switch demonstrating the fast rise time (t_{rise} = 32 ns) and subsequent ringing of the voltage for $E_T = -3 \rightarrow 0$ kV and $G = 0$ V. The inset shows a zoomed in picture of the ringing component where the vertical line is $t_\mu = 510$ ns from Chapter 6.

dependent on s and the grid wire radius $r = 10\ \mu$m. This field leakage can cause Stark shifts in microwave experiments and decrease the 2S lifetime through Stark mixing with the 2P state and is not desired but is sometimes unavoidable.

3.9 Microwave Transitions & Line Shapes

Microwave radiation is applied to drive long lived 2S atoms to the short lived 2P state in order to measure the line shape of the ν_2 transition. This causes the late annihilation of the 2S to shift earlier, producing a positive S_γ when the 2S signal without microwaves applied is used as a background. The 2S and microwave signals can be seen in Figure 3.25. This work targets the ν_2 transition, and so upon application of the microwave radiation at ∼8.6 GHz the process is as follows: $2^3S_1 \xrightarrow{\text{stimulated emission}} 2^3P_2 \xrightarrow[\tau_{\text{mean}}=3.2\text{ns}]{\text{fluoresence}} 1^3S_1 \xrightarrow[\tau_{\text{mean}}=142\text{ns}]{\text{self-annihilation}} 3\gamma$. On resonance the transfer to the 2P state will be the most efficient with detuned frequencies having

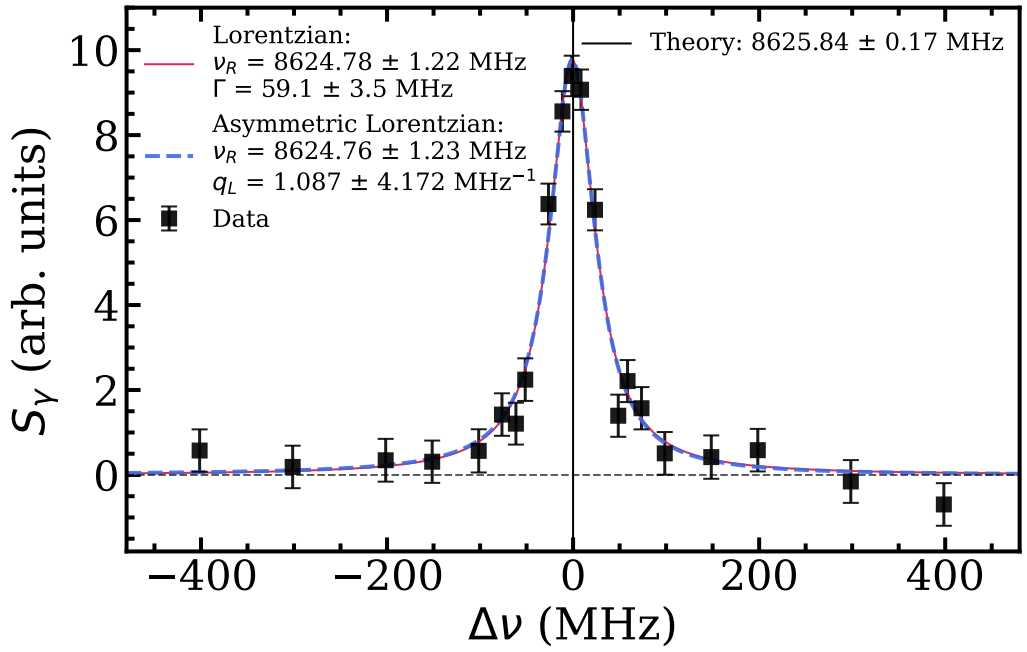

Figure 3.28: An example of a line shape measured during the work presented in Chapter 6 for $L_x = 21$ cm, $P_{\text{input}} = 94$ mW, and $\theta_H = 0°$. The data are fitted using Lorentzian (solid red) and asymmetric Lorentzian (blue dashed) functions, with corresponding fit parameters shown in the legend. The solid vertical line at $\Delta\nu = 0$ corresponds to the Zeeman shifted theoretical transition frequency 8625.84 MHz. The data were recorded in a magnetic field of ≈ 32 G. From Reference [243].

lower efficiency and so lower S_γ. By measuring S_γ across a range of microwave frequencies a line shape can be generated, an example of this is shown in Figure 3.28. For more information on how line shape data is processed see Appendix A.

Microwave radiation was generated by a Keysight N5173B signal generator. This generator has a range of 10 MHz to 40 GHz with a sub-Hz precision and bandwidth, making it highly suitable for precision spectroscopy. The radiation was transmitted via coaxial SMA cables. The radiation was applied to the Ps using either an external horn antenna or an in-vacuum waveguide, see Figure 3.29 for a schematic of the microwave circuit in both these instances.

All microwave components (generator, cables, vacuum feedthroughs and am-

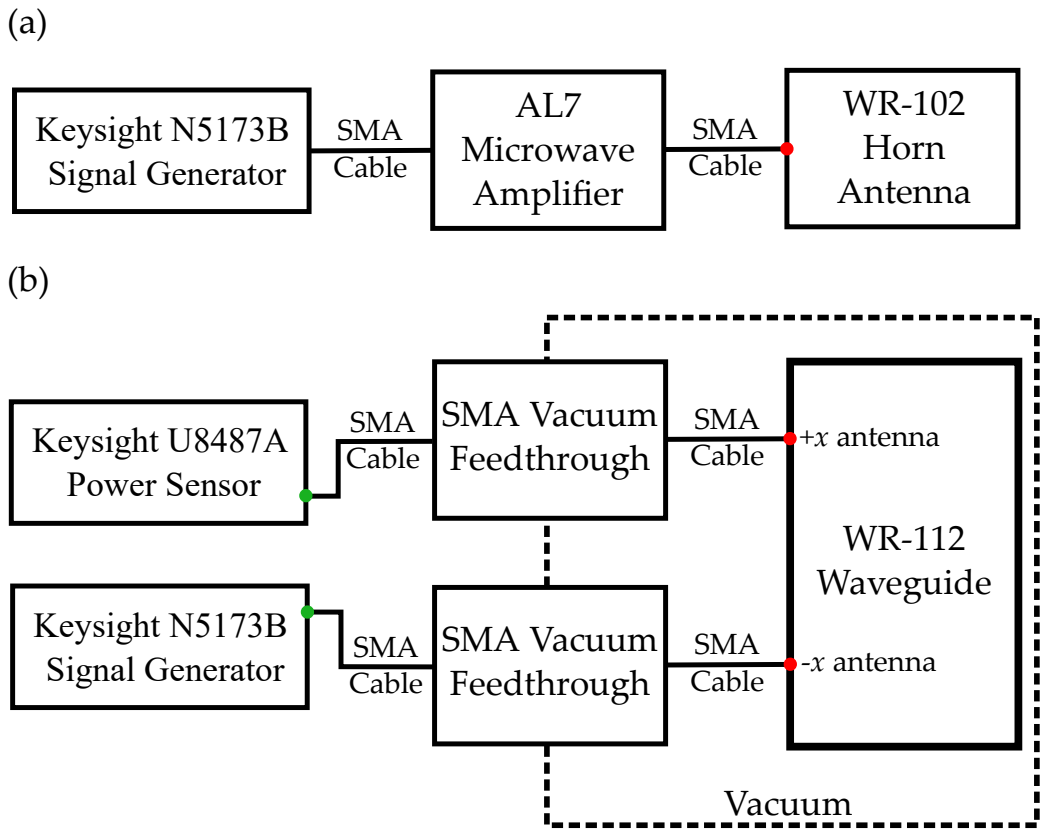

Figure 3.29: A schematic of (a) the microwave circuit used with the horn antenna in Chapter 6, and (b) the microwave circuit used with the horn antenna in Chapter 7. The microwave generator in (b) could be connected to two different antennas at either end of the waveguide using two different vacuum feedthroughs by swapping the generator and power sensor at the connections shown by the green dots. The green dots were also the points at which the vector network analyser in Chapter 7 was connected. The red dots at the antennas show the points up to where the microwave power was levelled as described in the text.

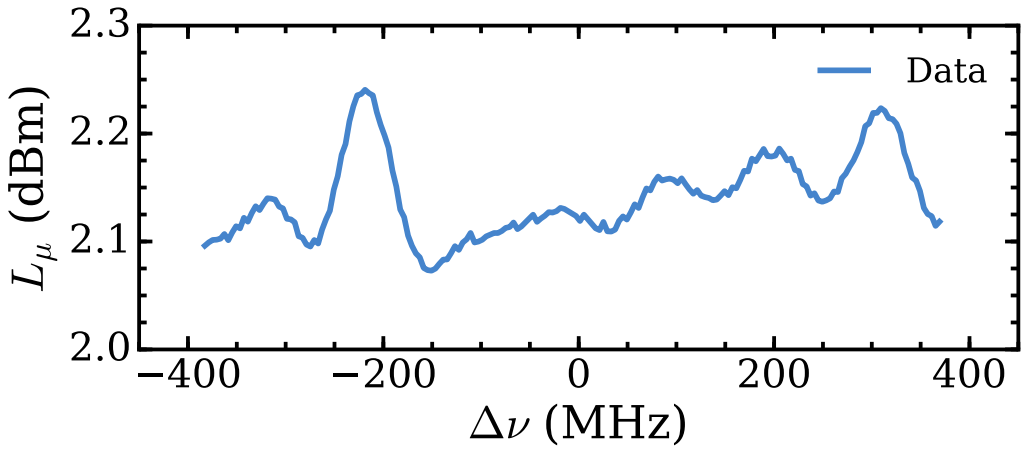

Figure 3.30: The measured loss L_μ of the microwave circuit shown in Figure 3.29(b) for the experiment in Chapter 7 ($-x$ direction antenna). The central frequency is the calculated zero-field $\nu_2 = 8\,626.71$ MHz transition frequency.

plifiers) have a frequency dependent power loss, or in the case of an amplifier, gain. To ensure that the power into the antennas, P_{input}, was constant a correction was applied to the output power of the generator P_{output} as a function of frequency. The correction was unique to all experiments and was determined by attaching a Keysight U8487A power sensor and N1913A power meter to the last SMA connection before the antennas (as shown by a red dot in Figure 3.29) and measuring the loss of the components, $L_\mu(\nu)$, to an accuracy of 0.01 dBm. Figure 3.30 shows an example of the frequency dependence of L_μ as measured for the experiment in Chapter 7. To obtain a constant microwave power into the antenna the correction was applied as $P_{\text{input}} = P_{\text{output}}(\nu) + L_\mu(\nu)$ which reduced the power variation to < 0.02 dBm. However, the total uncertainty in P_{input} was ± 0.05 dBm due to changes in the impedance of the system when the SMA cables were reconnected to the antenna which was verified to cause power fluctuations of up to 0.05 dBm.

3.9.1 Horn Antenna

The horn antenna used (Pasternack PE9857/SF-15) consisted of a WR-102 waveguide coupled to a horn of 15 dBi gain[12]. The emitted radiation was incident along

[12]This means that compared to an isotropic antenna which emits uniformly in all directions the peak power in the direction of the horn was 15 dB larger.

the $-x$ direction with a 3 dBm angular spread of 29.6°[13]. The gain of the horn antenna is frequency dependent and not accounted for in these measurements due to the high degree of reflection effects, which will be discussed further in Section 6.2.2.

Within a distance of $d_{FF} = 26$ cm from the exit of the horn antenna the microwave radiation was in the near-field regime. This means that the electric and magnetic field components of the microwaves ($\vec{E}$ and $\vec{H}$) are not in phase and may not be orthogonal to the direction of motion, resulting in unpredictable polarisation. After d_{FF} the radiation was in the far-field regime where the electric and magnetic components are in phase, orthogonal to the direction of propagation, and the wavefronts are planar. The boundary distance of the far-field for a horn antenna is obtained by $d_{FF} = 2D^2/\lambda$ (e.g. [264]) where $D = 6.86$ cm is the largest dimension of the horn and $\lambda = c/\nu$ where $\nu = 8\,626.71$ MHz. The far-field regime is the desired regime for excitation because is has reliable polarisation and direction of propagation.

Experiments using the horn antenna required the rf output of the microwave generator to be pulsed to prevent extreme Stark shifts in the LER from the laser excitation field. The radiation had a turn on time of $<$10 ns, within which the path length for an average Ps atom travelling at $\sim$ 100 km/s is $<$1 mm. Because Ω_R was on the order of 2 MHz or less in these experiments the transfer of Ps between the 2S and 2P states will happen on a much longer time scale than the switch on time, resulting in any effects associated with the switch on time being negligible to the microwave transition signal.

To increase the power into the horn antenna a low-noise amplifier was used, connected as shown in Figure 3.29(a). This amplifies the power without affecting the frequency. The amplifier used was a Microwave Amps AL7-8.4-8.8-20-30 with a gain of 21 dBm in the frequency range 8.4 - 8.8 GHz, gradually decreasing outside this range which was compensated for by the power correction $L_\mu(\nu)$.

[13]The 3 dBm angular spread represents the cone which contains 50% of the rf power.

3.9.2 Waveguide

The waveguide used in this work was a custom built WR-112 rectangular waveguide (12.62×28.50 mm)[14] made of Al, with open ends and 40×28.50 mm W meshes in the centre to allow passage of the positrons and Ps through the waveguide [129], see Chapter 7 for a diagram. Inside the waveguide only the TE_{10} mode was propagated [226] with all the radiation polarised in the z-axis which was parallel to the magnetic field and therefore drove $\Delta M_J = 0$ transitions. The microwaves were applied as continuous wave (CW) radiation because the amplitude of the microwave fields outside the waveguide were an order of magnitude lower than inside the waveguide, meaning transitions within the LER during HV switching were not significant, see Section 7.2.2. This also meant that an amplifier was not needed because the power supplied from the generator confined in the waveguide provided a field strength high enough to saturate the transition.

To get the radiation into vacuum 40 GHz vacuum SMA feedthroughs were used along with vacuum suitable SMA cables, see Figure 3.29(b) for a diagram of the microwave circuit. Microwave radiation was delivered into the waveguide by gold-plated stub antenna at either end of the guide. The antenna were $\lambda/4$ long and $\lambda/4$ in from the end of the waveguide to produce the optimal standing wave pattern, where $\lambda = 34.75$ mm is the wavelength of the zero-field ν_2 transition. The antenna were designated the $+x$ and $-x$ antenna in reference to the direction of microwave propagation experienced by the Ps atoms. One antenna at a time was used, and to change the direction of propagation the SMA cable from the microwave generator was attached to the appropriate vacuum feedthrough and the other antenna grounded with the 50 Ω load of a Keysight U8487A power sensor used to monitor the power.

Waveguides have an intrinsic difference in the relationship between electric field strength and power compared to free space radiation which is frequency dependent. The correction C_{power} is defined by [134],

$$E_z^2 \propto C = \frac{P_{\text{input}}}{\sqrt{1 - \nu_c^2/\nu^2}}, \tag{3.5}$$

[14] This size of waveguide is also called a WG-15 or an R-84.

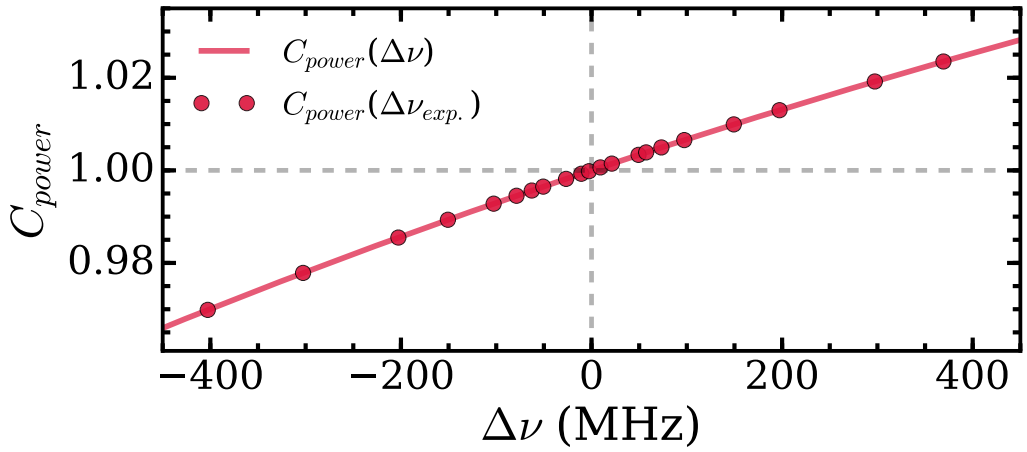

Figure 3.31: The power correction C_{power} as a function of frequency (line) and at the experimental frequencies (points) for a WR-112 waveguide as calculated by Equation 3.6.

and

$$C_{power} = \frac{C(\nu)}{C(\nu_2^{\text{calc.}})}, \tag{3.6}$$

where $\nu_c = 5.26$ GHz is the cutoff frequency for the WR-112 waveguide[15]. See Figure 3.31 for the correction as a function of ν which demonstrates the correction is at most $\pm 3\%$, where the typical measured error on a point is $> 15\%$. This correction was applied to the measured data in the form $S_\gamma^{corr} = S_\gamma C_{power}$. The change to ν_R of a Lorentzian fit on one line shape (the same one as in Figure A.2) was 120 kHz which is an order of magnitude smaller than the typical > 1 MHz error on these line shapes. This is because the waveguide used was optimal within the experimental frequency range and any effect from this is below the sensitivity of the statistics in this experiment.

3.10 Rydberg Production

Excitation of Rydberg states was performed by a two-photon, two-colour process. The UV laser excites the $2\,^3\mathrm{P}_J$ state and an IR laser pulse is applied concurrently with the UV pulse so that the short lived 2P atoms are driven to the Rydberg state before they fluoresce back to the ground state. To give the full process: $1\,^3\mathrm{S}_1 \rightarrow$

[15]The cutoff frequency is the lowest frequency that can propagate within the spatial constraints of the waveguide.

$2\,^3\mathrm{P}_J \rightarrow n\,^3\mathrm{S/D}_J$. The target Rydberg state for this work was $n = 23$ which required $\lambda_{\mathrm{IR}} = 733.9$ nm. Figure 3.25 shows an example of a background subtracted signal of an $n = 23$ Rydberg state. It is similar in structure to a 2S excitation, but extending later due to its longer lifetime of $\tau > 50$ μs (and a suitably long flight path with minimal collisions).

It should be restated that, because of field mixing, the Rydberg atom is described in the parabolic basis using quantum numbers $|n,k,m\rangle$. The value of m is set by the polarisation of the two lasers and the associated angular momentum transfer from the photon. The UV laser was linearly polarised parallel to the field and so does not contribute to the total m, but the IR laser was linearly polarised in the y-axis, orthogonal to the electric and magnetic field, and therefore drives $\Delta m = +1$ transitions. This results in the Rydberg atoms in this work having $m = 1$.

Which Stark states were excited depended on the electric field present in the LER F_{TG}, see Figure 3.14, and the wavelength of the laser. This is because in an electric field the energy of the Stark states shifts according to Equation 2.30, with LFS increasing in energy and HFS reducing in energy. At a fixed IR wavelength the Stark states selected by the narrow bandwidth IR laser will be strongly dependent on which states have been shifted into resonance with the laser by F_{TG}.

As with all other laser processes in this work Rydberg excitation occurs in the LER, between the electrodes $\mathrm{E_T}$ and $\mathrm{E_G}$. For Rydberg production the electrodes were set to $V_{\mathrm{T}} = V_{\mathrm{G}} = -3.5$ kV to create zero electric field within the LER to minimise the Stark broadening and merging of separate n-states. This also keeps the positron implantation energy at 3.5 keV. However, V_{T} and V_{G} had to be switched off before the atoms passed out of the LER to prevent electric fields beyond $\mathrm{E_G}$ causing FI. This process induced a small field during Rydberg excitations due to the different switching rates of the electrodes.

Stark broadening of low n transitions can be used to measure the electric field in the LER. As an example of this method Figure 3.32 shows a line shape of the transition $n = 2 \rightarrow 13$, centred on $\lambda_{\mathrm{IR}} = 746.7$ nm, taken during the work described in Chapter 5 at a laser delay of $t_{\mathrm{lsr}} = t_{\mathrm{lsr}}^{\mathrm{opt.}} + 20$ ns. A small field was present dur-

ing the excitation causing the line to be broadened from the minimum width (set by the Doppler and laser broadening) to $\sigma = 93 \pm 3$ GHz. The excitation process was modelled as described in Section 2.5 by calculating the energy of each Stark state according to Equation 2.30, and their dipole transition strengths according to Equation 2.32. The resultant state distribution, the green bars in Figure 3.32, was convolved with the dominant laser and Doppler broadening Gaussians of 5 GHz and 50 GHz FWHM, respectively. This produces a model line shape (the dashed blue curve, which is very similar to a Gaussian) which can be compared to the experimental data, and if the value of F_{TG} input into the calculation is changed then the calculated line shape will change width accordingly. The electric field required to match the broadening of the calculation to that of experiment was $F_{\mathrm{TG}} = 340 \pm 10$ V/cm. The upper limit on F_{TG} is the FI threshold, which if exceeded creates a photoionisation-like signal and produces no Rydberg atoms.

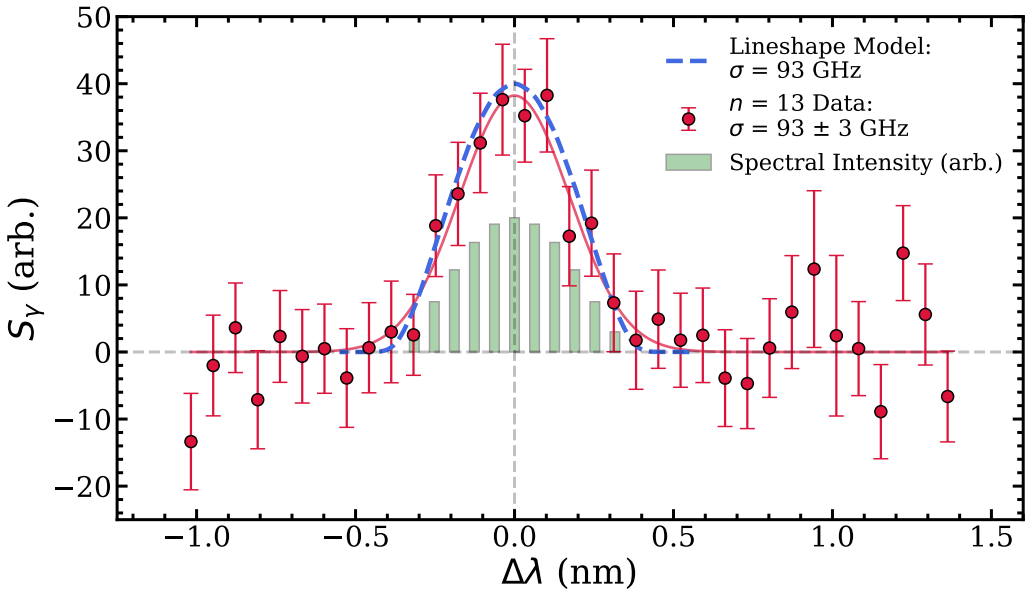

Figure 3.32: Line shape of the $2^3\mathrm{P}_J \rightarrow 13^3\mathrm{S/D}_J$ transition by IR laser as described in the text. The points are experimental data and the solid line is a Gaussian fit to extract the Stark broadened width of 93 ± 3 GHz. The dashed line shows a model fitted by the methods described in Section 2.5 matched to the experimental width, this model is a Gaussian convoluted with the Stark shifts of the Stark states. The shaded bars represent the relative spectral transition strength of the individual Stark states and their energy. The background of this signal was the ground state atoms with UV laser present.

The velocity distribution of the Ps upon the application of the IR laser will be the same as the 2S atoms if certain conditions are fulfilled. (1) The spot size of the IR laser beam is larger than the UV beam to ensure that all 2P atoms produced by the UV laser are excited to Rydberg states (see Section 3.5). This was indeed the case and means there were no additional selection effects on the v_y and v_z distributions. (2) The Stark broadening is sufficient to split the Stark states to the 50 GHz Doppler bandwidth, which will bring them back into resonance with the narrow 5 GHz bandwidth of the IR laser. This was again the case, and for $n = 23$ the Stark manifold is broadened to 50 GHz in < 40 V/cm, which will mean the v_x distribution remained unchanged. (3) The electric field gradient is small enough that the electric dipole moment given in Equation 2.33, which can result in velocity changes of the Rydberg atoms according to the acceleration $\vec{a} = \mu_{elec}\vec{F}/m_{\mathrm{Ps}}$, causes no velocity change. The Rydberg atoms in this work were only exposed to low electric fields for short periods of time (< 50 ns) upon production, therefore this effect is not significant.

Chapter 4

Simulation Methods

Simulations are a key part of understanding experimental results and this work contains three primary forms of simulation: (1) Monte Carlo simulations of Ps trajectories provide knowledge of where and when Ps quenching and annihilation is taking place; (2) finite integration techniques are used to calculate 3-D maps of the microwave field strength in order to understand the distribution of radiation in experiments; and lastly (3) a Lindblad master equation solver is used to solve the coupled rate equations which describe the rate of change in the density matrix of Ps atoms in microwave fields to determine how the microwave field distribution can effect line shape measurements.

4.1 Monte Carlo Atomic Distributions

To simulate a Ps atom we need to know its initial conditions: t_0, x_0, y_0, z_0, and $\vec{v} = (v_x, v_y, v_z)$. The probability density function of these properties has been measured in experiment and these distributions can be randomly sampled in a Monte Carlo algorithm to generate the initial conditions of one atom. Sampling multiple atoms from these distributions gives an indication of the behaviour of the Ps ensemble in experiment.

t_0, x_0 and y_0 were sampled from a Gaussian distribution defined by the measured FWHM values of $\Delta t = 3$ ns and $\Delta r = 3$ mm obtained from MCP measurements of the positron beam, as described in Section 3.1.3. The positron beam spot was treated as being radially symmetric, hence $r = \sqrt{x^2 + y^2}$. $z_0 = 0$ mm by defi-

nition because the coordinate frame is defined with the origin on the surface of the conversion target, at its centre.

Figure 4.1 shows the simulated velocity distribution of the atoms in all three axes post laser excitation (solid black). The v_x distribution is defined by Doppler selection of the ground state atoms from the 100 GHz FWHM of the UV laser pulse. This bandwidth at $\lambda = 243$ nm produces an average $v_x^{rms} = 15$ km/s which is much slower than the velocity in the other axes allowing us to exploit the smaller divergence and lower Doppler broadening of the atoms in the x-axis.

The v_y distribution is unaffected by the laser (except from any correlation with the selected parts of v_x and v_z) and is therefore the natural emission profile of the silica target. This was measured during each experiment for v_x using Doppler profiles, see Figure 3.22 for an example. The emission in the x- and y-axis is expected to be symmetric due to the random distribution of pores in the silica target, thus the measurement in x can be applied to y. Typically $v_y^{rms} \approx 80$ km/s though this can vary slightly in each experiment due to small variation in the laser position and delay, or deliberate changes of the laser delay to select colder Ps.

v_z was extracted from time-of-flight (ToF) data of $n = 19$ Rydberg Ps travelling 125 mm through a multi-ring electrostatic Rydberg guide [229] for the same silica target, implantation energy and similar excitation parameters as used in this work[1]. The ToF data was converted to a velocity distribution from the known distance travelled and a skew-normal function was fitted to characterise it. This function is arbitrary and not based on a physical model, but provides a good fit to the data, see Figure 4.2 which shows the skew-Gaussian fitted to two measured ToF profiles in units of km/s. The distribution was measured for different values of t_{lsr} due to the limited temporal overlap of the laser pulse and the Ps ensemble changing the v_z velocity selection. Figure 4.2 shows ToF data at $t_{\mathrm{lsr}} = t_{\mathrm{lsr}}^{\mathrm{opt.}}$ and $t_{\mathrm{lsr}} = t_{\mathrm{lsr}}^{\mathrm{opt.}} + 20$ ns with the average velocity changing by 7.9 km/s. Randomly sampling the fitted

[1] An electrostatic Rydberg guide uses the large dipole moment μ_{elec} of Rydberg atoms to confine low field seeking (LFS) states in a region of low electric field surrounded by high electric fields, whereby the LFS are accelerated back into the central low field region if they stray into the high field region with a force $\vec{\mathscr{F}}$ proportional to the field gradient $\nabla\vec{F}$, $\vec{\mathscr{F}} = \mu_{elec}\nabla\vec{F}$. This enables the transport of the atoms long distances without collisional losses on surfaces, which can result from the large divergence of Ps made in SiO_2 production targets. [90]

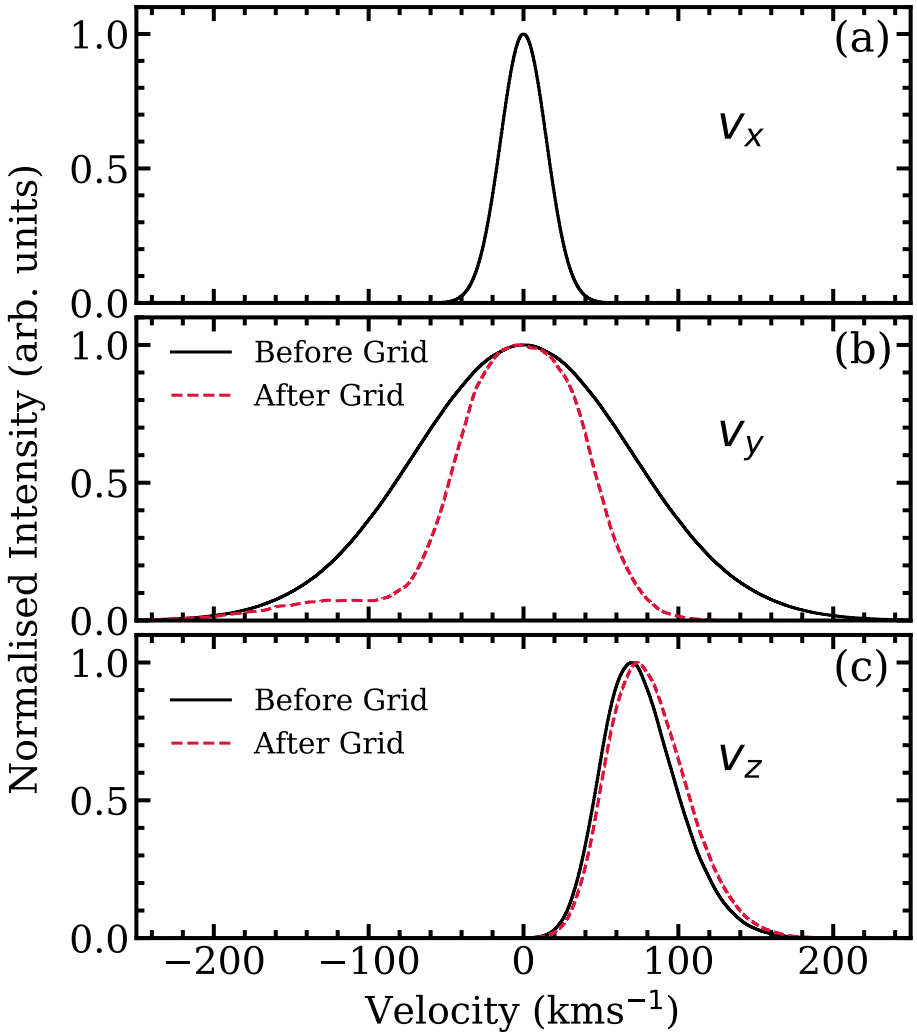

Figure 4.1: The velocity distribution for each axis of motion of the laser excited Ps. (a) The spread in x based on the Doppler selection of the 100 GHz Gaussian bandwidth of the UV laser. (b) The distribution in the y-axis, determined by the Gaussian width of the measured Doppler profile (solid black). The red dashed line shows the effect of collimation from E_G, the bump to the left is due to some fast atoms escaping underneath the electrode. (c) The distribution of v_z extracted from previous data at $t_{lsr} = t_{opt.} + 20$ ns as discussed in the text, with the red dashed line showing the slight reduction in slow atoms from collimation.

skew-normal function provided the v_z distribution with a typical average velocity of $v_z^{rms} \approx 94$ km/s for $t_{lsr} = t_{lsr}^{opt.}$.

Each initial condition discussed here was assigned randomly to an atom. This was done because there is no known relationship for the correlation of the velocity components or the total energy, of either ground state or excited state Ps, emitted from mesoporous silica. The random assignment gives a total excited state average

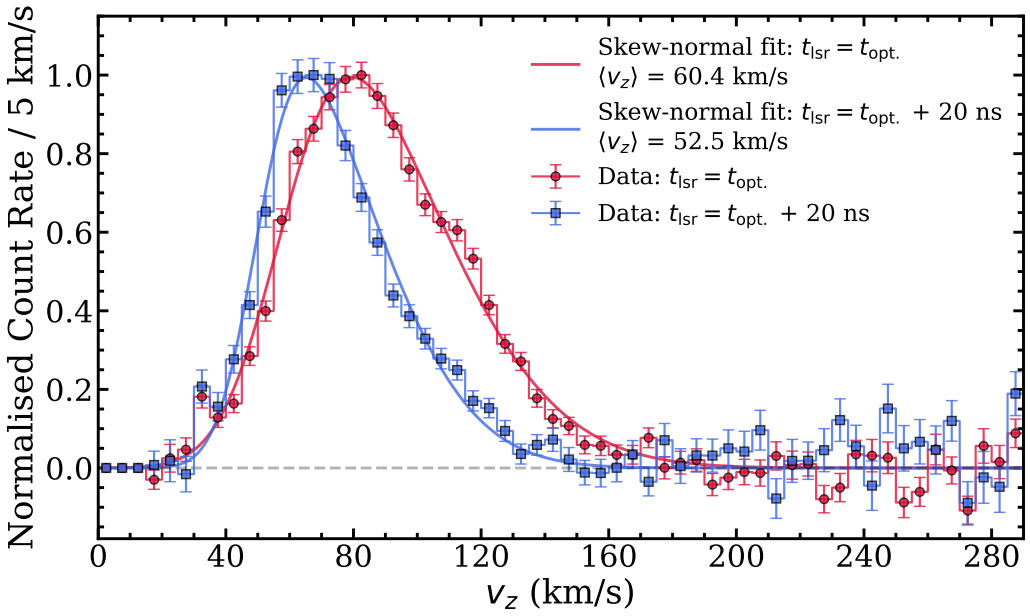

Figure 4.2: ToF measurements of v_z from Reference [229]. Red circles show the experimental data for $t_{lsr} = t_{opt.}$ and the blue squares show the data for $t_{lsr} = t_{opt.} + 20$ ns. The solid lines show the corresponding skew-normal fits to the data with the average velocity of the later laser slower by almost 10 km/s.

kinetic energy of 132 meV (for a v_y Doppler width of $\sigma = 366$ GHz and $t_{lsr} = t_{lsr}^{opt.}$) which is consistent with previous estimates based on extrapolation of the energy in a single direction to all three degrees of freedom [15].

The v_z distributions measured in Reference [229] may be slightly different to the ones in this work because of the nature of the electrostatic Rydberg guide, this is primarily due to two reasons. (1) The exact phase acceptance of the guide was unknown. The most divergent trajectories had the lowest acceptance into the guide, partly due to collimation on the electrodes, but primarily due to the inability of the fields to capture them [229]. (2) Spectral selection of v_x by the IR laser may be increased if the field during excitation was not large enough to Stark broaden the line shape to the point that fast atoms were Doppler shifted back into resonance with the laser. Either of these effects may change the v_z distribution due to unknown correlation between v_z and v_r. But these effects are expected to be small as grid collimation in this experiment will also remove extremely divergent trajectories, though to a lesser extent than in the ring guide. The electric field required to Stark broaden Rydberg transitions is typically less than 100 V/cm which is a reasonable

field in the excitation region during the ring-guide experiment due to the lack of a grid to provide uniform fields. In addition to this the velocity range of the ToF data is comparable to the expected velocity distribution based on the laser timing and position.[2]

When the Ps excited by the laser flies through the 16 mm diameter grid in E_G, the atoms are collimated, with a significant fraction annihilating on the surface of the electrode. This is shown in Figure 3.14 where the spatial distribution of the Ps is narrowed by the electrode, and the velocity distributions are subject to a similar effect. In order to simulate this effect the initial velocity distribution $\vec{v}$ was propagated from $t = 0$ ns using the trajectory methods described in Section 4.2, removing any atoms that collided with E_G at a distance $d_{TG} = 11.5$ mm in order to evaluate the velocity distribution after collimation losses $\vec{v}'$. The collimated v'_x distribution is not significantly affected because it is already narrowed by Doppler selection and passes through E_G with minimal losses. However, the v'_y distribution was appreciably narrowed compared to its pre-collimated state, as shown in red on Figure 4.1(b). Some atoms could escape underneath the electrode, hence the asymmetry of the collimated distribution, but are not seen in experiment due to being far from the detectors or not subject to applied electric and microwave fields. This process also increases $v_z'^{rms}$ because slower v_z atoms are the ones that collide with the electrode before passing through.

The atoms of interest in this work are the collimated atoms, but all simulations were started with the initial excited state distribution $\vec{v}$ to ensure that collimation was fully accounted for in the unique electrode and chamber geometry of each experiment. If the positron beam was not exactly centred in the middle of E_G it would change the collimation of the atoms, preferentially selecting Ps moving is a certain direction. Using the same methods mentioned in the previous paragraph atoms were propagated through a physical structure with a vertical offset to their starting position of $\Delta y_0 = -3.5$ mm, which is estimated to be the maximum possible offset due

[2]Within the guide there may also be effects from dynamic fields causing Stark acceleration/deceleration [146]. However, the dynamic fields involved were small enough to only cause minor shifts in the distribution which can be discounted.

to the finite size of the silica target and positron beam. The change in the collimated distribution was found to be negligible, with $v_y^{\prime rms}$ only varying by 1 km/s.

4.1.1 Alignment Induced Doppler Effects

In this work we require knowledge of the angle dependent velocity selection of the laser to quantify the maximum possible Doppler shifts of the ν_2 transition measurements in Chapters 6 & 7. Although retro-reflection will negate UV wavelength drift and recoil Doppler effects, any misalignment of the UV laser relative to the conversion target, and therefore the Ps reference frame, can cause the v_x velocity distribution to be asymmetric as seen by the microwave radiation (from either a horn antenna or a waveguide). To simulate this a ground state atom population was generated with a v_x and v_y distribution set by the width of the measured Doppler profiles $\Delta\lambda = 0.078 \pm 0.001$ nm in Chapter 7, and v_z was defined by a skew Gaussian distribution extracted from a fit to the entire ToF data set to account for the fastest and slowest atoms in the ground state [229].

If the laser is aligned perfectly parallel to the target in the x direction then the Doppler selected v_x profile will be symmetric and if the microwaves are also aligned perfectly to the x direction then this will only result in a Doppler broadening of the microwave transition, with no Doppler shift. In these simulations we consider what happens when the laser was rotated compared to the Ps reference frame as set by the orientation of the target electrode E_T.

To do this a 3-D rotation matrix was applied to the ground-state velocity distribution about the y-axis[3] to transform it into a laser coordinate frame where the laser was rotated from the Ps reference frame by an estimated maximum value of $\Delta\theta_{\rm lsr} = \pm 3^\circ$. This transformation was of the form,

$$\vec{v}' = \begin{bmatrix} \cos\theta_{\rm lsr} & 0 & \sin\theta_{\rm lsr} \\ 0 & 1 & 0 \\ -\sin(\theta_{\rm lsr}) & 0 & \cos(\theta_{\rm lsr}) \end{bmatrix} \vec{v}. \tag{4.1}$$

[3] Any vertical misalignment about the z-axis should keep v_x symmetric because v_y is also symmetric, causing only additional broadening.

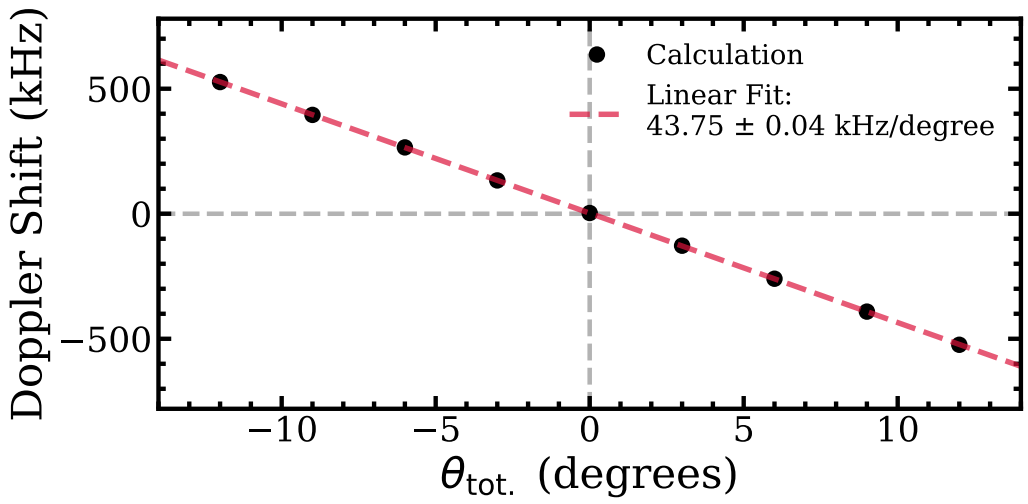

Figure 4.3: A calculation of the Doppler shift versus misalignment angle of the laser to the Ps as described in the text. The dashed red line shows a linear fit to the data for a shift of 43.75 ± 0.04 kHz/degree.

Laser selection with an exaggerated 150 GHz bandwidth (to replicate a worst case scenario) was then applied to the transformed v'_x distribution. The Doppler selected v' distribution was then transformed to the microwave coordinate frame, which was also estimated to vary by $\Delta\theta_\mu = \pm 3^\circ$ maximum, using the same transformation matrix. This final v''_x distribution was used to calculate the average Doppler shift from any resultant asymmetry. The results of this angular shift (displayed as the total angular misalignment $\Delta\theta_{tot.} = \Delta\theta_{\text{lsr}} + \Delta\theta_\mu$) are shown in Figure 4.3 where at a worst case scenario of $\theta_{tot.} = 6^\circ$ the shift is $\sim$0.26 MHz for the ν_2 transition.

4.2 Trajectory Simulations

The initial distribution of atoms is propagated through space by the simple relation $\vec{r} = \vec{v}t$, because the atoms feel no accelerating forces due to their low dipole moment and zero charge so the velocities remain constant[4]. During propagation atoms were considered to have annihilated by several mechanisms which differed according to the requirements of the simulation. These mechanisms were: collision, self-annihilation and microwave transition. Fluorescence was not required as only the $2\,^3S_1$ state was considered in these simulations with no electric field present,

[4] All trajectory and Monte Carlo simulations were performed using Python 3 [257].

therefore Stark mixing with the $2\,^3P_J$ state was not included.

Self-annihilation was taken into account by defining a lifetime for the atom, randomly sampled from an exponential distribution with a decay time of τ_{SA}, defined as the Zeeman mixed value of τ_{2S} calculated using Equation 2.19 in Section 2.3.

A geometrical structure of the electrodes and vacuum chamber was defined using a full computer-aided design (CAD) model of the experimental set up and the SIMION package (see next section). If an atom occupied the same space as an electrode or the chamber wall it was deemed to have annihilated through pick-off annihilation. Specular reflection of Ps from insulating materials has been observed [268], but this is considered negligible for this case as most surfaces are metal. This method of loss is responsible for the collimation and velocity selection undergone by the Ps atoms from collisions with the grid electrode, E_G, as described above. The $\sim$5% loss from passage through tungsten grids was ignored as this results in uniform losses across the whole atomic distribution.

Microwave transitions were deemed to happen instantaneously as if in a strongly saturating microwave field. This was done to extract positional information of the atoms upon rf application. The location of the subsequent annihilation will depend on the intensity of the microwave field, the intensity distribution of microwaves in the chamber, the 142 ns ground state lifetime, and the atomic velocity.

The simulations were given finite spatial and temporal bounds to improve the speed of computation. Any atom that passed outside the bounds were ignored. Atoms outside the spatial bound were considered too far from the detectors to be measured and anything after the temporal bound ($t_{end} = 3000$ ns) was too late to be within the SSPALS integration window. The ground state atoms that were not excited by the laser were disregarded as they constitute a constant background.

4.2.1 Electric Field Simulations (SIMION)

To calculate the electric field strength within the experimental volume the software SIMION 8.1 [2] was used. SIMION takes a 3-D structure made using a CAD modelling software, with each electrode defined as a unique object. The software defines

a finite volume of finite elements from this geometry with a user defined resolution of 1 mm^3, which is limited by computational resources. The software solves Laplace's equation ($\vec{\nabla} \cdot \vec{E} = 0$) at each point in the 3-D volume to extract the electric field $\vec{E}$, treating the electrodes as the boundary conditions. The voltage applied to each electrode can be chosen to extract the field for any combination of voltages on the electrodes. The CAD structure can be exported from SIMION and allows us to include complex chamber geometries in trajectory simulations to account for collision losses.

4.3 Microwave Field Simulations (CST Studio)

The CST Studio Suite software package simulates high frequency electromagnetic fields within a finite volume using a time domain solver [1]. This solver utilises finite integration technique (FIT) methods to discretise the integral form of Maxwell's equation to obtain Maxwell's grid equations (MGE) [171, 269, 270]. The MGE are then solved, and propagated in the time domain using a leap frog algorithm.

The grid that the MGE are applied to is a finite element mesh built around a realistic model of the experimental setup created in a separate CAD software. This model included representations of the vacuum chamber, vacuum windows and electrodes and was imported into CST with each material assigned properties based on the CST materials library. Close to the model the mesh was allowed to conform to surfaces with the smallest mesh cell being 0.1 mm^3. Far from the model the mesh was defined to have fifteen cells within the smallest simulated wavelength ($\sim$3 cm) to ensure suitable sampling of the waveform. The resolution of the simulation was set as high as computational resources would allow, but no significant change in the results was observed for lower resolution meshes (down to ten cells per wavelength) because the wavelength was always suitable sampled.

In the simulation microwave radiation was propagated from a source over a finite frequency range, in this case the operational frequency range of the waveguide involved (7 - 11 GHz for the WR-102, and 7.05 - 10 GHz for the WR-112). Full 3-D maps of different properties of the microwave field can be extracted from simu-

lations at discrete user-defined frequencies i.e. electric field vectors, magnetic field vectors, Poynting vectors etc. The first of these used in this work is the far-field data which provides the directional gain of the antenna, G. G describes the increase in directional power compared to an isotropic antenna (i.e. an antenna which has uniform emission across a full 4π solid angle). G is in units of dBi where $G > 0$ dBi is an increase in the power in that direction compared to an isotropic antenna, and $G < 0$ dBi is a decrease.

Figure 4.4 shows a polar far-field plot of the radiation pattern from the WR-102 horn antenna used in Chapter 6 pointed along the $-x$ axis in free space at a frequency of $\nu = 8\,624.38$ MHz. The graph shows a 2-D slice in the xz-plane where $\theta = 0^\circ$ is the $-x$ direction and $\theta = 90^\circ$ is the $+z$ direction. The increase in forward directed radiation and decrease in backward directed radiation is clear, with a simulated maximum gain of $G_{max} = 15.3$ dBi at $\theta = 0^\circ$ and an angular spread of 50% power within a 31.7° arc. This is in reasonable agreement with specs of the antenna as given by the manufacturer, which are 15 dBi and 29.6°. The value of G_{max} can be extracted as a function of frequency and used to evaluate the frequency dependent gain of the horn antenna with and without the experimental setup present.

The second property of the simulation that is extracted is the electric field. This returns the real and imaginary components in the x, y and z axis of the amplitude of the microwave electric field in its steady state (i.e. for continuous microwave radiation). These can be used to determine the microwave field experienced by an atom as a function of time by propagating a simulated atomic distribution through the 3-D field map and extracting the field it experiences in discrete time steps. It can also be used to extract the polarisation of the radiation. The polarisation in this work should be parallel to the magnetic field (i.e. in the z- axis) due to the orientation of the horn antenna and waveguide used in this work. The fractional polarisation is calculated from the absolute microwave field strengths as,

$$P_z = \frac{E_z}{\sqrt{E_x^2 + E_y^2 + E_z^2}}. \tag{4.2}$$

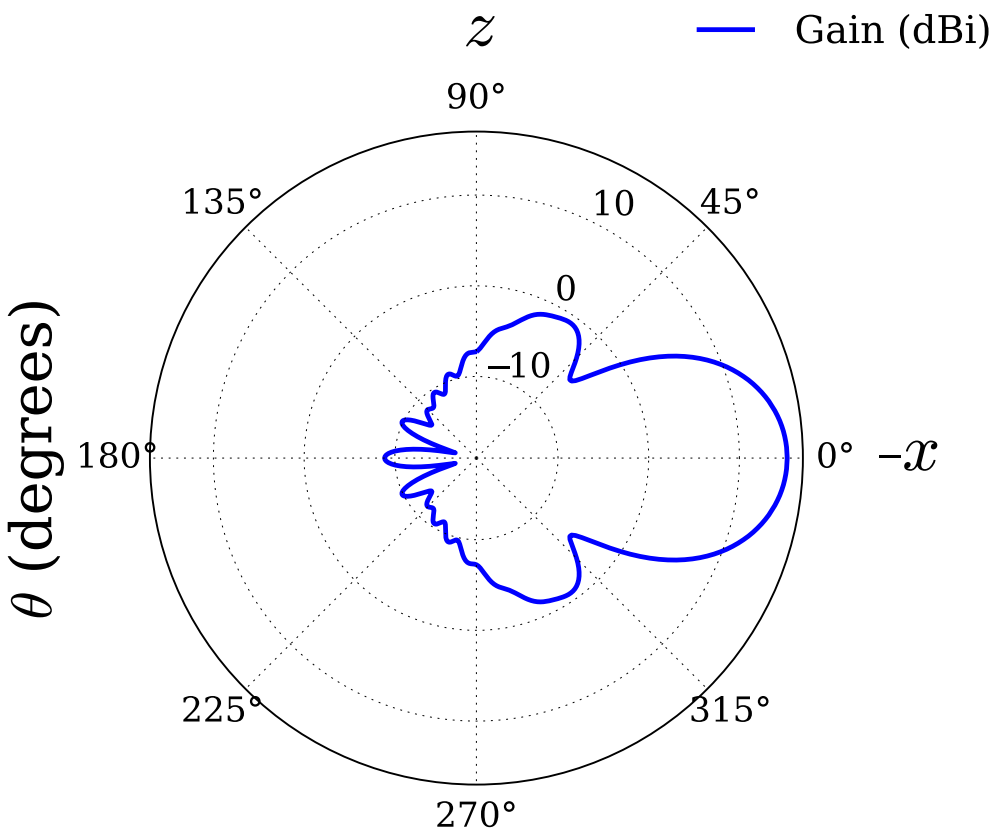

Figure 4.4: A simulation of the gain G (displayed on the radial axis as a solid blue line) of the Pasternack WR-102 horn antenna in the xz-plane as a function of angle $\theta = \sin^{-1}(z/x)$. The maximum gain $G_{max} = 15.3$ dBi is at $\theta = 0^\circ$ which is the direction in which the horn is pointed. Relating this to the experiment the x and z directions are indicated by the labels on the graph where 0° is the $-x$ direction and 90° is the $+z$ direction.

P_z polarised radiation will drive transition of $\Delta M_J = 0$, while radiation polarised in the x- and y-axes will drive transitions of $\Delta M_J = \pm 1$.

These simulations have limitations in their accuracy due to their ability to precisely replicate the exact details of the experimental chamber and setup (e.g. welded seams, smaller components, surface imperfections etc.) and the finite element size. Any field maps and far-field results should therefore not be regarded as an exact calculation of the microwave field, but as a representation of the effects present and their magnitude.

4.4 Line shape Simulations

Although the CST simulations cannot be taken as a 100% accurate representation of experiments, the generated electric field maps can be used to perform line shape simulations which provide insight into the effects of the microwave field distributions. Full quantum dynamic calculations of this system have been performed including all 16 $n = 2$ sub-states, all 4 $n = 1$ sub-states and several vacuum states [15]. The results of these calculations were found to be similar to those of a simplified model using only states directly involved in the interaction [132]. The simplified model uses the open-source QuTip Python package [156, 157] to solve for the density matrix of the system ρ as a function of time t using the Lindblad Master Equation (ME) [121, 178],

$$\hbar\frac{\partial\rho}{\partial t} = -i[H(t),\rho] + ... + \sum_k \Gamma_k \left(L_k \rho L_k^\dagger - \frac{L_k^\dagger L_k \rho}{2} - \frac{\rho L_k^\dagger L_k}{2} \right), \qquad (4.3)$$

where $H(t)$ is a time dependent Hamiltonian and L_k are collapse operators that account for dissipation and decoherence[5]. The system solved for is a four-state system where an atom is subject to time dependent microwave fields due to its movement through the steady-state microwave field (as simulated in CST).

To obtain the time dependent microwave field strengths a distribution of atoms as described in Section 6.2.1 was propagated through the steady-state simulated microwave field at a fixed time step of $dt = 1$ ns. This time step corresponds to $<$0.1 mm path length for the average atom. Figure 6.6 shows the structure in the microwave field is on a larger scale than this, therefore this time step ensured sampling of all microwave field spatial structure. Only collisions with surfaces were considered as a method of annihilation in the trajectory simulations. Self-annihilation and microwave transitions being accounted for in the QuTip simulations.

The electric field experienced by each atom along its trajectory was recorded as a function of its position, which was converted to a time dependent field, $E_0(t)$, based on the atomic velocity. This was used as an input for the ME solver. Fig-

[5] See Reference [185] for an example of this approach.

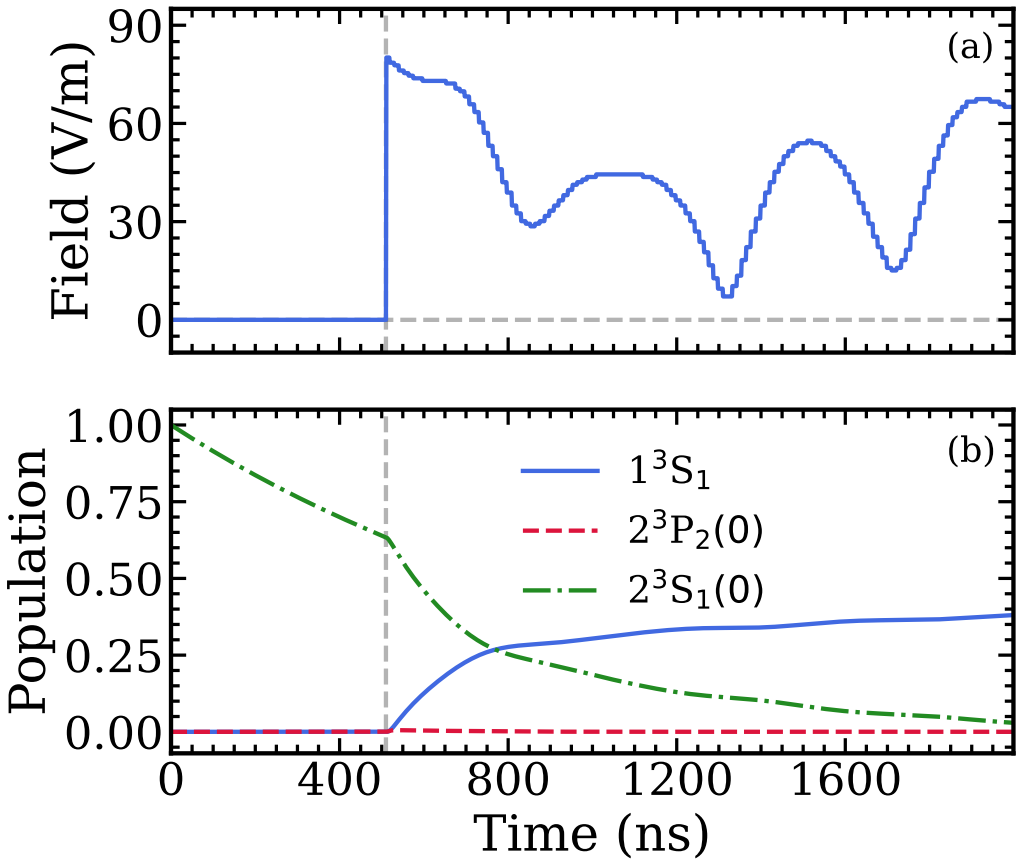

Figure 4.5: (a) The time dependent field felt by a single Ps atom travelling along the z-axis at a velocity of 90 km/s. (b) The state population transfer undergone by the atom represented in (a) at an applied frequency of 8624.38 MHz for a resonance of 8625.84 MHz.

ure 4.5(a) shows an example of the time dependent field felt by a single Ps atom travelling along the z-axis at a velocity of 90 km/s, with microwave radiation at 8624.38 MHz applied by a horn antenna, pulsed on at 510 ns as in Chapter 6. These data are discrete due to the nature of the CST simulations. To verify that the discrete nature of the data does not affect the results of the ME solver the time dependent field data was smoothed and interpolated with no change seen in the resultant density matrix.

Within the solver four states were considered: (1) the initial $2^3S_1(M_J = 0)$ state; (2) the $2^3P_2(M_J = 0)$ state to which the microwave transition was driven; (3) the $1^3S_1(M_J = 0)$ ground state to which the $2^3P_2(M_J = 0)$ state decayed; and (4) a vacuum state for self-annihilations of the $2^3S_1(M_J = 0)$ state to decay to. To

simplify the model only one transition was considered between the available sub-states with no major differences in the possible transitions expected except a slight change in transition strength and Zeeman shift. Neighbouring 2^3P_J states were not considered as effects from QI have been shown to be too small to measure in these experiments, with an expected magnitude of < 200 kHz shifts to Lorentzian fits [15].

The Hamiltonian of the system with the states in the order listed above, in units of angular frequency, is

$$\hat{H} = \begin{bmatrix} 0 & -0.5E_0(t)\mathscr{I}R/\hbar & 0 & 0 \\ -0.5E_0(t)\mathscr{I}R/\hbar & \omega_\mu - \omega_{\text{Zeeman}} & 0 & 0 \\ 0 & 0 & \omega_\mu - 100000 & 0 \\ 0 & 0 & 0 & \omega_\mu - 100001 \end{bmatrix}, \tag{4.4}$$

where ω_{Zeeman} is the Zeeman shifted frequency of the $2^3S_1(M_J = 0) \rightarrow 2^3P_2(M_J = 0)$ transition, $\omega_\mu = 2\pi\nu_\mu$ is the applied microwave frequency, $\mathscr{I} = \sqrt{2}/3$ is the angular component of the dipole coupling between the $2^3S_1(M_J = 0)$ and $2^3P_2(M_J = 0)$ states, $R = \langle 2P|er|2S\rangle \approx 5.196a_{\text{Ps}}$ is the radial integral between the 2^3S_1 and 2^3P_2 state, and $E_0(t)$ is the time dependent microwave field amplitude as extracted from the trajectory and CST simulations[6]. The diagonal elements of the matrix represent the energy separation of the states relative to the frequency of the microwave radiation, with the $2^3S_1(M_J = 0)$ defined as zero-energy. The off diagonal elements are equivalent to the Rabi frequency of the $2^3S_1(M_J = 0) \rightarrow 2^3P_2(M_J = 0)$ transition, representing the interaction of the microwave field with the atom as a function of $E_0(t)$. The separation of the $n = 2$ states from the ground and vacuum state is an arbitrary energy designed to limit coupling effects but enabling efficient computation of the system, the real value being on the order of PHz.

The self-annihilation decay of the $2^3P_2(M_J = 0)$ state, and the fluorescence

[6]Room temperature black-body radiation at 8.6 GHz is disregarded, being many orders of magnitude less intense than the applied radiation.

decay of the $2\,^3\mathrm{P}_2(M_J = 0)$ state are given as collapse operators in the form of $\sqrt{\tau}$,

$$L_k = \begin{bmatrix} 0 & 0 & 0 & 0 \\ 0 & 0 & 0 & 0 \\ \sqrt{\tau_{SA}(B)} & 0 & 0 & 0 \\ 0 & \sqrt{\tau_{2\mathrm{P}}} & 0 & 0 \end{bmatrix}. \tag{4.5}$$

where $\tau_{SA}(B)$ is the Zeeman mixed $2\,^3\mathrm{S}_1'$ self-annihilation lifetime. The fluorescence decay of the 2P population was considered only by the $\Delta M_J = 0$ channel because the decay rate to the ground state was uniform for all simulated parameters and was sufficiently rapid (as shown in Figure 4.5(b)) for the $\Delta M_J = \pm 1$ channels to be neglected. The decay of the ground state to the vacuum state was not considered as we are only interested in atoms that annihilate via the $2\,^3\mathrm{S}_1(M_J = 0) \rightarrow 2\,^3\mathrm{P}_2(M_J = 0) \rightarrow 1\,^3\mathrm{S}_1(M_J = 0) \rightarrow 3\gamma$ decay path, for which the ground state population in this simulation is a suitable proxy.

With these inputs the ME solver returns the state population as a function of time, see Figure 4.5(b) for an example. The value of $E_0(t)$ along the atom trajectory varies by an order of magnitude which has some visible effect on the 2S state population. The transfer to the 2P state upon application of microwaves is not visible in this graph due to the rapid decay rate to the ground state, but in a 30 V/m field has a Rabi frequency of 1.9 MHz which is consistent with conditions found in the experiments. The ground state population does not decrease as the decay to the vacuum state is not considered here.

To generate a line shape the ME solver was run for the $E_0(t)$ of five hundred atom trajectories in order to sample multiple paths through the rf field. The same five hundred atoms were run through the solver for a set of frequencies chosen to be the same as the ones in the experiment being replicated. The metric used as an analogue for the experimental S_γ parameter was the summation of the ground state population across all five hundred atoms at $t = 2000$ ns at each unique frequency. This time was chosen because the $2\mathrm{S} \rightarrow 2\mathrm{P}$ transfer rate should be negligible by this time, this is shown in experiment by the lack of change in background subtracted

signal in Figure 3.25 which is usually outside the SSPALS integration bounds, and in simulation from the minimal change in the state population by the cutoff of Figure 4.5(b). The population sampling time used was verified to have no appreciable effect on the line shape produced.

The QuTip simulation includes natural, transit-time and power broadening, with Doppler broadening small enough to ignore in these transitions. The natural and transit-time broadening will come from the collapse operator and the trajectory sims, respectively. But because the simulated E_0 values are not directly comparable to experiment, due to the arbitrary input power of CST, the simulated field has to be corrected by a constant scaling factor. The scaling factor is chosen so that the simulated line width matches the measured line width, and therefore power broadening of the experimental data. To obtain this factor line shapes are simulated for a range of powers which produce power broadening on the same order as experiment. A fit of Equation 2.24 is then made and the power required to match the experimental line width extracted. The data in Figure 4.5 were power matched this way with the resulting values being comparable to expected experimental parameters.

Chapter 5

Measurement of the Positronium 2^3S_1 Annihilation Decay Rate

This chapter presents work found in:

Measurement of the annihilation decay rate of 2^3S_1 positronium. R. E. Sheldon, T. J. Babij, B. A. Devlin-Hill, L. Gurung and D. B. Cassidy, *EPL*, **132**, 13001 (2020) DOI:10.1209/0295-5075/132/13001

Historically there has been a large difference ($> 4\sigma$) between the measured value of the o-Ps decay rate $\Gamma_{\mathrm{o-Ps}}$ and the calculated value due to systematic effects in some measurements that have since been largely resolved [34]. Measuring the excited state decay rates, which are calculated by $\Gamma_{\mathrm{n}} = \Gamma_{\mathrm{o-Ps}}/n^3$ as per Equation 2.7b for triplet states, can provide a comparison to the ground state measurements. This chapter presents the first measurement of an excited state annihilation decay rate of Ps.

The methodology of this experiment involved measuring the number of 2^3S_1 atoms in free space as a function of time. This was done by applying an electric field at 75 ns time intervals to quench the atoms, mixing them with the 2^3P_J state. When the quenching field was applied the following process happened: $2^3S_1 \rightarrow 2^3S_1' \rightarrow 1^3S_1 \rightarrow 3\gamma$ causing the atoms to annihilate, and a corresponding increase in the measured gamma-ray signal which was proportional to the number of 2^3S_1 atoms remaining at that time. Any additional loss mechanisms beyond the self

annihilation of the 2^3S_1 atoms was compensated for using long-lived Rydberg states which have negligible decay of their own due to their tens of microsecond long fluorescence lifetime (and no self-annihilation losses). The Rydberg population was measured as a function of time and any losses were attributed to additional loss mechanisms such as collisions with surfaces and solid angle effects of the detector. The lost fraction of Rydberg atoms can then be used to correct the measured 2^3S_1 population for additional losses. An exponential function was fitted to the measured 2^3S_1 population vs time (as corrected by the Rydberg measurements) and a decay rate extracted.

5.1 Apparatus & Method

The positron beamline was as discussed in Section 3.1 with the positron pulse having a spot size of 2 mm, and a duration of 3 ns FWHM. The positrons were implanted into a mesoporous silica conversion target as discussed in Section 3.4, biased to $V_T = -3.5$ kV. A grid electrode E_G was $d_{TG} = 11.5$ mm away from E_T, see Figure 5.1. The electrode was held at $V_G = -400$ V for 2S production to limit back-scattering of positrons that caused distortions to the SSPALS spectra, see Section 3.4, as measured using the methods and detectors described in Sections 3.2, 3.3 & 3.6. Figure 5.1 shows a schematic of the experimental setup including E_T, E_G, the detector, guiding coils etc.

2S production is explained in Section 3.8, whereby a single UV photon excitation from the 1S state was performed in an electric field using the laser setup described in Section 3.5 to excite a mixed state 2S'. This produced pure 2S atoms once the electric field was adiabatically switched zero. The arrival time of the laser pulse at the target was delayed from optimum 2S production by $t_{lsr} = t_{lsr}^{opt.} + 20$ ns, targeting a slower subset of the o-Ps distribution for an average velocity of $\vec{v}_{rms} = (15, 50, 85)$ km/s (see Section 4.1 for a summary of velocity measurements). The slower velocity distribution was chosen to limit the number of fast atoms that would collide with the vacuum chamber and electrodes within experimental timescales, though it also lowered the number of 2^3S_1 atoms produced by $\sim$30%, see Fig-

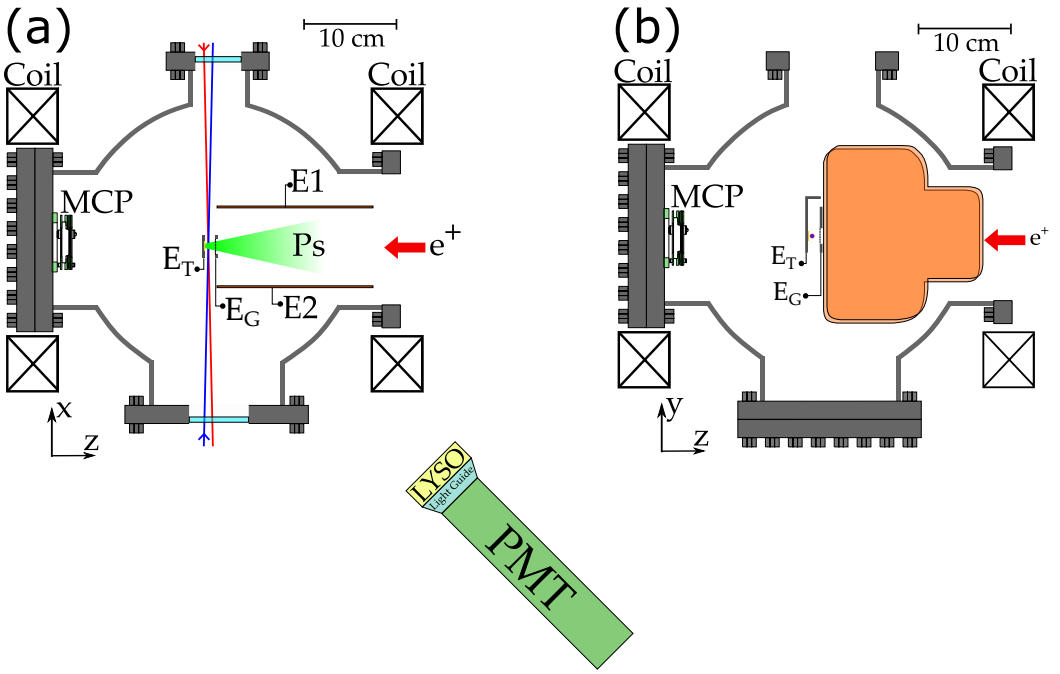

Figure 5.1: Schematic of the target chamber. (a) A view of the chamber in the xz-plane at $y = 0$ mm showing the excitation region between Target (E_T) and grid (E_G); and the quenching region between the two electrode plates E1 and E2. The positrons (red arrow) are incident from the right and the Ps are emitted back along the same axis (green shading). The lasers propagate in the x-axis and enter the vacuum through UV transparent windows. The detector position shown here is to scale, being roughly 34 cm from the centre of the chamber. (b) A view of the chamber in the yz-plane at $x = 0$ mm, displaying the shape of the electrodes. The MCP at the rear was used to image the positron beam. The coils shown generate the magnetic field to guide the positron beam. Adapted from Reference [242].

ure 3.19. Note that retro-reflection of the UV beam was not present in this experiment requiring the daily measurement of a Doppler profile to confirm the on resonance UV wavelength and prevent asymmetric Doppler selection of v_x, see Section 3.7.

The target and grid were switched to 0 V using the methods given in Section 3.8.1 with an electric field of $F_{TG} \approx 2.3$ kV/cm present at $t_{\rm lsr}$, so at the moment of excitation the $2^3S_1'$ mixed state lifetime was $\sim$10 ns. The $2^3S_1'$ state evolved into pure 2S atoms over the course of the switch times which were measured to be $t_{\rm T,rise} = 65$ ns and $t_{\rm G,rise} = 120$ ns.

The number of 2S atoms was measured as a function of time by applying an electric quenching field once the atoms passed through E_G and were propagating

freely in vacuum, this is designated the quenching region (QR). Upon application of the field the 2S atoms undergo the following decay path $2^3S_1 \xrightarrow{\text{Stark mixing}} 2^3S_1' \xrightarrow[\Gamma > 50\text{ MHz}]{\text{Fluoresence}} 1^3S_1 \xrightarrow[\Gamma \approx 7.0\text{ MHz}]{\text{Self-annihilation}} 3\gamma$. Once in the ground state, quenched 2S atoms decay with a mean ground state lifetime of 142 ns, meaning that annihilation from quenched 2S atoms was not simultaneous with the quenching field being switched on. The quenching of all the 2S atoms simultaneously causes a peak in annihilation events as measured by the SSPALS technique, see Section 3.6, which is proportional to the number of 2S atoms at that time.

There was no electric field present in the QR after E_T and E_G stabilised at 0 V, resulting in no Stark mixing with the 2P state until quenching began. However, the average magnetic field from the positron guiding coils within the QR was $\langle B_z \rangle = 50$ G, with a range of ± 30 G. This was measured using a Hall probe as described in Section 3.1.3. B_z was large enough to cause the triplet 2S state to mix with the singlet 2S state for an average self-annihilation lifetime of $\tau_{SA} = 1124$ ns within the QR, corresponding to a decay rate of 890 kHz. The minimum B_z field present would cause a decay rate of 881 kHz, and the maximum field a decay rate of 904 kHz. Because the Ps ensemble has a large spatial distribution and because this variation is below the statistical error of the experiment the average value is taken as the theoretical prediction. Measuring the height of the annihilation peaks as a function of quenching time should therefore produce an exponential decay with a decay constant of $\tau_{\text{exp.}} = \tau_{SA}$.

The electric field used to quench the 2S atoms in the QR was applied by two parallel electrodes, E1 and E2. The electrodes could not be placed too close together due to fast atoms colliding with the electrodes causing unwanted losses. The electrode spacing was therefore maximised to reduce collisions within the experimental time frame. The narrow v_x velocity distribution (see Section 4.1 for details) was exploited for this purpose and allowed the electrodes to be placed close enough together to provide a sufficient quenching field while not causing losses from collisions. E1 and E2 were placed 8.5 cm apart and centered on the yz-plane, see Figure 5.1(a). Collisions with the electrodes are not expected for ~ 1000 ns based

on the maximum v_x of $\sim$40 km/s. Collisions on the chamber walls 150 mm away start as early as 600 ns, however, due to the fast v_z and v_y distributions.

To quench the 2S atoms E1 was switched from 0V to -4 kV and E2 from 0V to +4 kV which created a field of $F_Q = 0.94$ kV/cm between the plates. The rise time of the plates was $t_{\mathrm{E,rise}} = 42$ ns which was deliberately increased slightly by 50Ω resistors in series between the switch outputs and the electrodes. This was done to minimise the switch noise in the signal as discussed below. Within the boundary of the plates the field was well defined. Figure 5.2 shows the electric fields in (a) the xz-plane and (b) the yz-plane. These field maps were calculated using SIMION as described in Section 4.2.1 to show the quenching field for the potentials T = G = 0 V, E1 = -4 kV and E2 = $+4$ kV. Around the end of the electrodes the field varied slightly due to the proximity of the grounded chamber. However, the last quenching time was 1000 ns, at which point the fastest atoms would still be inside the QR meaning 2^3S_1 atoms decay to the ground state in $<$20 ns in F_Q.

The 2S population was measured at ten separate times by pulsing E1 and E2; the first at $t_{\mathrm{switch}} = 270$ ns and in 75 ns intervals thereafter. The annihilation signal of the quenched atoms was detected using a single LYSO detector, see Section 3.2. The detector was approximately 34 cm from the centre of the chamber (pointed roughly at the target) with an active area of 45 cm^2, see Figure 5.1a. This distant position was chosen to decrease the variation in the solid angle over the region where annihilation was possible. The average solid angle was low however, leading to a detection efficiency of around 1% due to solid angle effects alone. This, combined with the low 2^3S_1 production efficiency, required six data runs to be made to overcome statistical error, totaling 166 hours of data acquisition time. Due to these low statistics, noise in the signal was smoothed out by convolution with a Hamming window [138] 60 ns wide (using the PyAstronomy Python package [84]). This was done for both the 2S and Rydberg signals though it was less important on the latter due to the better statistics.

The HV switching of E1 and E2 induced a pick-up signal in the detector which was present in the recorded SSPALS spectra. Figure 5.3(b) shows an example of

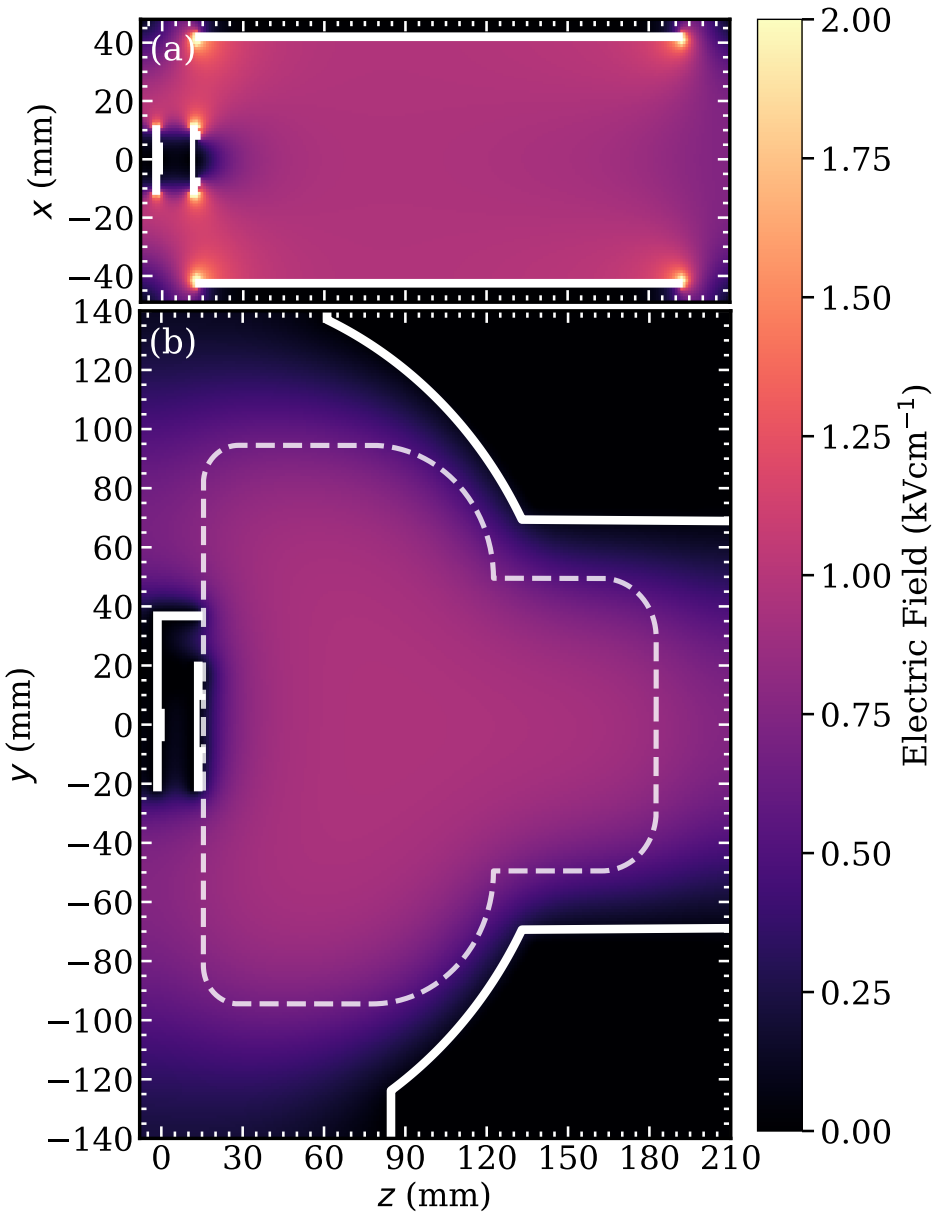

Figure 5.2: These two panels show the electric field within the quenching region calculated using SIMION. In both panels T = G = 0 V while E1 = −4 kV and E2 = +4 kV. The chamber is grounded. (a) A slice in the xz-plane at $y = 0$ and (b) the yz-plane at $x = 0$. In (b) it is possible to see how atoms that leave the region between the plates will still experience sufficient field for quenching. In (a) a small region of low field is present after the grid.

the 'switch noise' in a Rydberg FI signal, chosen for better statistics but the process was applied to 2S and Rydberg data identically. This could not be removed with a standard single background subtraction of $V(t)^{lsr\ on}_{switch\ on} - V(t)^{lsr\ on}_{switch\ off}$. However, the switch noise was reproducible from shot to shot and could therefore be treated as

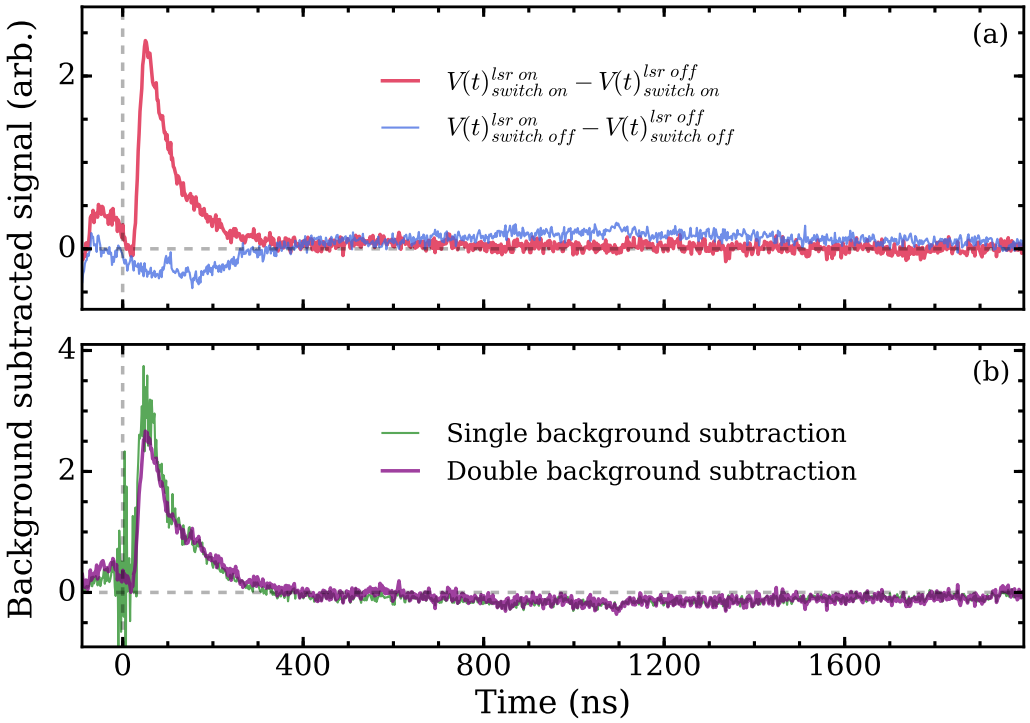

Figure 5.3: An example of the double background subtraction for a Rydberg ($n = 23$) field ionisation signal at 270 ns (where the time is shown relative to the switch pulse). (a) The two components of the double background subtracted signal. The FI component is shown in red (thick line) and the Rydberg signal is shown in blue (think line). (b) The double background subtracted FI signal (thick purple line) and the single background subtracted signal with switch noise $V(t)^{lsr\ on}_{switch\ on} - V(t)^{lsr\ on}_{switch\ off}$ (thin green line).

a constant background and subtracted out of the signal. This required an additional second background and a double background subtraction of the form

$$\left[V(t)^{lsr\ on}_{switch\ on} - V(t)^{lsr\ off}_{switch\ on}\right] - \left[V(t)^{lsr\ on}_{switch\ off} - V(t)^{lsr\ off}_{switch\ off}\right]. \tag{5.1}$$

See Figure 5.3(b) for a comparison between the double and single background subtracted signal. The two components of the double background subtraction can be seen in Figure 5.3(a). The first term is a FI Rydberg signal with ground state background, where the switch is pulsed in both cases. The second term is the unperturbed Rydberg signal with the switch not pulsed.

5.1.1 Additional Loss Effects

Decay from self-annihilation is not the only contribution to the loss of 2S atoms once in the QR. Because the position of the Ps cloud is different at each quenching time the solid angle of the atoms as seen by the detector changes too (despite attempts to limit the solid angle variation by placing the detector far from the quenching region as mentioned above). If the detector has a higher detection efficiency at one end of the QR than the other then the population measurement will be skewed accordingly, introducing a component into the amplitudes that is not due to the exponential self-annihilation decay. The detector had an active area of 45 cm^2 but the area of the QR was $\sim$100 cm^2 in the yz plane, meaning that if the detector was placed close to the detection region for maximum detection efficiency the solid angle variation across the QR would be large, $> 100\%$. This necessitated the placement of the detector far from the QR to mitigate the position sensitivity of the small detector, resulting in a $< 20\%$ variation in solid angle across the measured quenching positions. This was estimated by calculating the area of a sphere subtended by the detector A with respect to: (1) the conversion target $d = 34$ cm away from the detector, and (2) at the point $z = 24$ cm on the z-axis, which is 5 cm further than the end of the QR and level with the detector in the z axis so $d = 24$ cm. The solid angle was calculated as $\Omega = A/d^2$, where d is the displacement between the detector and the detection point. The detection efficiency is $2\Omega/4\pi$, where the factor of two comes from the minimum 2γ annihilation of the positron.

Another cause of loss is the broad spread of velocities. Despite losses on E1 and E2 being suppressed by the narrow Doppler selected v_x distribution some slower atoms do not enter the quenching region for $\sim$450 ns, remaining in the laser excitation region (LER). At later times atoms collide with the vacuum chamber, see Figure 5.4(a) & (b), which shows the simulated trajectories of Ps atoms up to $t = 1000$ ns, with no quenching field applied and no decay processes. The atoms were considered to have annihilated only upon collision with a surface. Simulated velocity distributions described in Section 4.1 were matched to measured experimental parameters of $t_{\mathrm{lsr}} = t_{\mathrm{lsr}}^{\mathrm{opt.}} + 20$ ns to define v_z, 100 GHz to define v_x, and

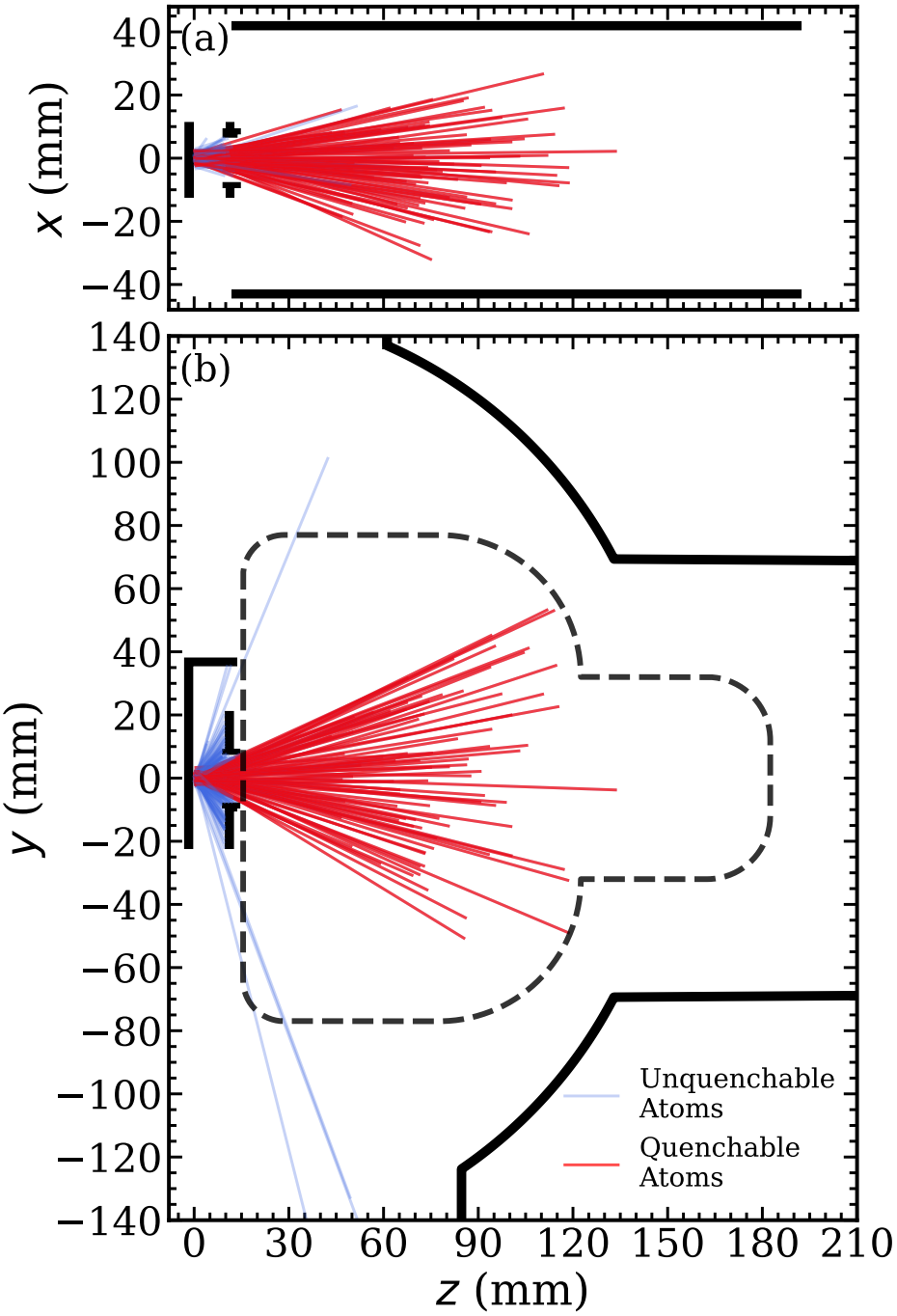

Figure 5.4: Trajectories of 200 Ps atoms at $t = 1000$ ns for (a) the xz-plane ($y = 0$) and (b) the yz-plane ($x = 0$). The blue trajectories are atoms that are not quenched, and the red trajectories are atoms that are quenched within the field of the QR. Only collisions are taken into account as a permanent loss mechanism.

$\Delta\lambda = 0.057$ nm to define v_y, see Figure 4.1. The blue trajectories in this figure show atoms that were not in the QR at $t = 1000$ ns, and the red lines show atoms

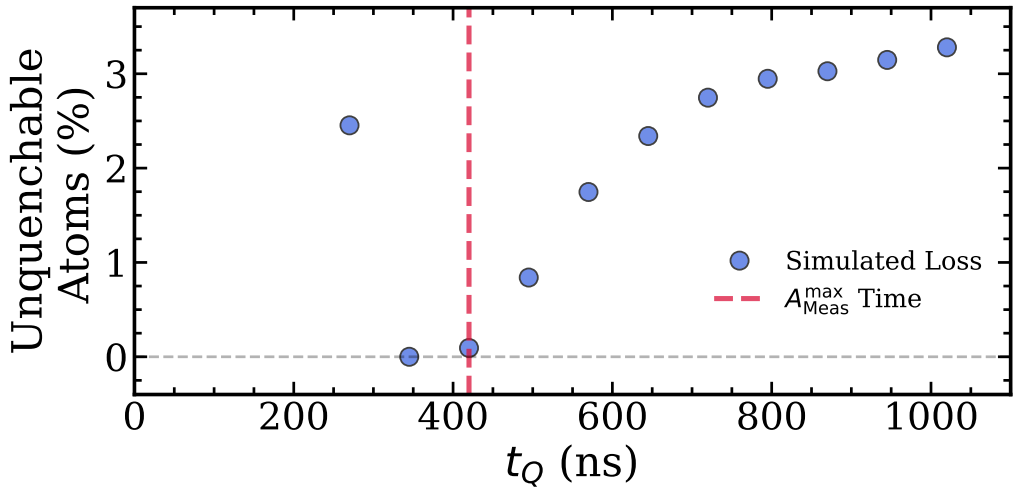

Figure 5.5: The simulated percentage of the Ps population that cannot be quenched at the experimental quenching times due to having not entered or having left the quenching region (blue circles). The red dashed line indicates the experimental peak occupation as measured with Rydbergs.

that were in the QR (and could be quenched) at $t = 1000$ ns.

Figure 5.5 shows the simulated percentage of atoms that were not in the QR at the experimental quenching times, relative to peak quenching. At each quenching time the simulated atoms were considered unquenchable if they had not yet made it through the grid into the QR, or if they had annihilated on a surface. Atoms that annihilated on a surface were permanently removed from the simulation, whereas atoms still in the LER were considered quenchable at later times if they subsequently entered the QR before annihilating on a surface.

5.1.2 Experimental Rydberg Correction

To quantify the effect of collision losses, slow atoms and solid angle variation, Rydberg atoms with high principle quantum number were excited. High n Rydberg states live for tens of microseconds [91] and so in the time scale of the experiment the losses due to fluorescence are negligible. Therefore, by field ionising the Rydberg atoms using E1 and E2 at the experimental quenching times, any reduction of the peak amplitude can be attributed to non-radiative losses. This gives a measurement of the relative decrease for each of the $2\,^3S_1$ quenching peaks from loss effects. Despite minor differences between the two situations this experimental method of

correction is more comprehensive than a simulation, accounting for unknown effects and minor details impossible to isolate and quantify in simulations.

Excitation of $n = 23$ Rydbergs at $\lambda_{IR} = 733.9$ nm is described in Section 3.10 and was performed at the same laser delay as 2S production. The main difference from 2S production was that T = G = -3.5 kV to perform the excitation in minimal field to prevent FI. However, the two electrodes had different switching rates ($t_{\text{rise,T}} = 65$ ns and $t_{\text{rise,G}} = 150$ ns) leading to an electric field of $F_{TG} = 340 \pm 10$ V/cm at excitation, see Section 3.10 for details on how this was measured.

Because of this field the laser was resonant with several different n states due to Stark and Doppler shifts, see Section 3.10 for details on these selection effects. The states excited were $|n = 23, k = \pm 1\rangle$, $|n = 22, k = +12, +10\rangle$, $|n = 24, k = -12\rangle$, and $|n = 25, k = -17\rangle$, calculated by seeing which Stark states where shifted according to Equation 2.30 into the 100 GHz effective bandwidth of the excitation. This made the range of fluorescence lifetimes present 42 - 70 μs [91] and resulted in $<1\%$ loss on experimental time scales in the worst case scenario of all $n = 22$ LFS. The velocity distributions should match well between Rydberg and 2S atoms as discussed in Section 3.10. Though some states may be preferentially faster or slower in v_x as they were only excited due to being Doppler shifted into resonance with the narrow band IR laser. It should not matter where the atoms end up however, because all excited states were capable of being FI in the 0.94 kV/cm field within the QR.

However, while quenched 2^3S_1 atoms self-annihilate anywhere within the quenching region, positrons freed from FI Rydberg atoms are rapidly attracted to the negatively charged plate, E1, and annihilate there. The full process upon application of the ionising field being $n = 23 \xrightarrow[\Gamma > 1000\text{ GHz}]{\text{FI}} e^+ + e^- \rightarrow N\gamma$ for $n = 23$ Rydbergs, where N will depend on the electron that annihilates with the positron. This difference in annihilation location changes the detection efficiency of the 2S and Rydberg states. However, the difference will be minimal due to the distant placement of the detector minimising solid angle variation, and because the change

in annihilation location will be consistent along z, and thus only change the absolute detection efficiency between the 2S and Rydberg signals not the relative change over time as measured in the Rydberg data.

The Rydberg FI signal was obtained for the same switching times t_{switch} as the 2S data, see the coloured spectra in Figure 5.6(a), and the peak values extracted, $A_{\text{Ryd.}}(t)$, see Figure 5.6(b) for the normalised data. Collisions will still occur during the 42 ns rise time of the field, hence the peak time is the sampled time. The first two points were not considered because some unknown fraction of atoms remains in

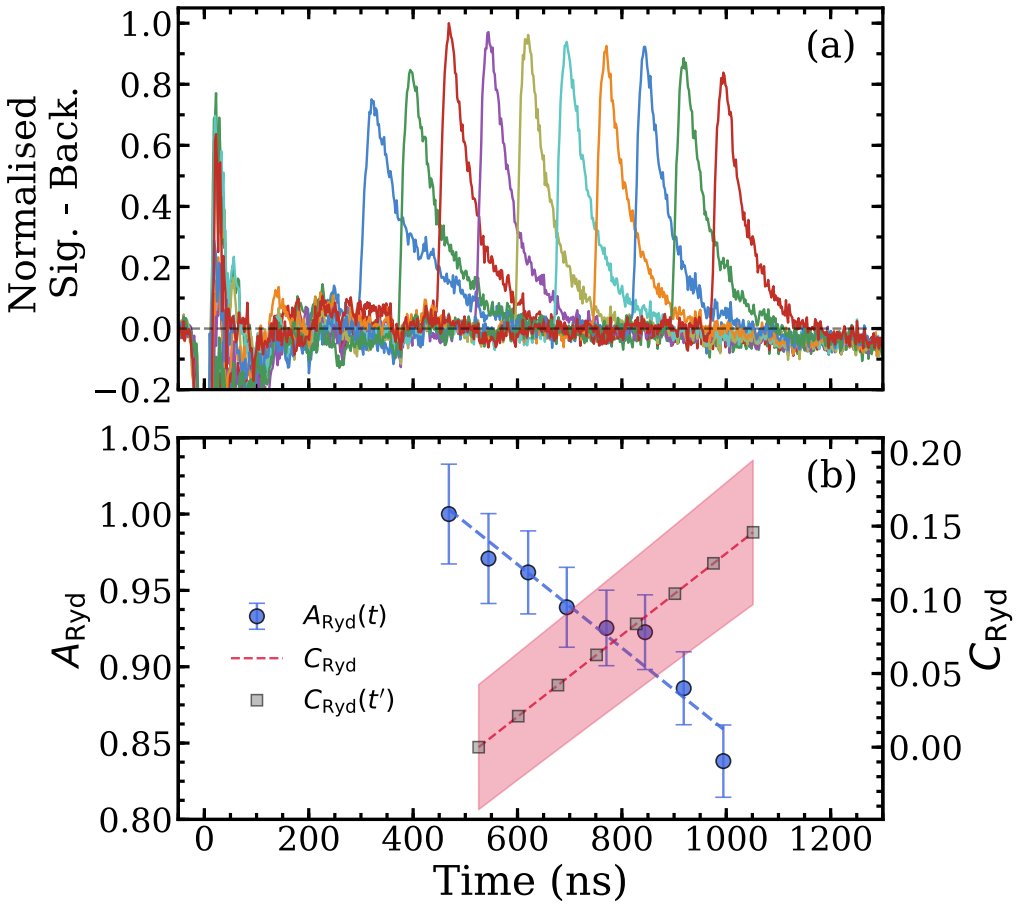

Figure 5.6: (a) $n = 23$ Rydberg Ps electric field ionisation data, normalised to the maximum amplitude at 486 ns. Each coloured spectra shows the time and magnitude of annihilation of the FI Rydberg states at different values of t_{switch}. (b) The normalised Rydberg peak amplitudes $A_{\text{Ryd.}}(t)$ and corresponding time-shifted correction factors, $C_{\text{Ryd.}}(t')$, derived from a linear fit (dashed line) to the data, as described in the text. The shaded bar represents the $C_{\text{Ryd.}}(t')$ error obtained from the fit. From Reference [242].

the LER and there is a region of low field following the grid (see Figure 5.2) where 2^3S_1/Rydbergs may not be quenched/ionised. This is demonstrated in Figure 5.6(a) where FI peaks before the highest peak are broader as slower atoms fly into regions of ionising field after the field is switched. The simulated fraction of unquenchable atoms is in good agreement with the trends seen in the Rydberg data, suggesting solid angle effects are minimal.

To account for the o-Ps decay of the quenched 2S atoms the Rydberg correction must be adjusted for arbitrary times. To do this a linear fit was made to this data, normalised to the third data point at $t = 486$ ns $A_{\text{Ryd.}^{max}}$, which represents the peak occupation of the QR. The first two quenching times occurred during the period when atoms were still entering the QR and are therefore subject to losses we cannot include in the correction. The fit was of the form $A_{\text{Ryd.}}(t) = mt + c$, where $m = (-0.94 \pm 0.11) \times 10^{-3}$ ns^{-1} and $c = 1.13 \pm 0.03$, to allow the calculation of the correction for arbitrary times. A correction factor calculated from the normalised signal was defined as $C(t') = 1 - A_{\text{Ryd.}}(t')$ which is shown as a line in Figure 5.6(b), the shaded band corresponding to the error from the least squares fitting procedure. The loss indicated by this correction is up to 15% relative to $A_{\text{Ryd.}^{max}}$, which is five times higher than simulations predict.

Determining the correct time to extract the peak height of the 2S quenching data t' (and evaluate the Rydberg correction) is not simple due to the low statistics, see Figure 5.7(a). In the uniform field of the quenching region the 2S quenching peak should always be the same time after the switching pulse and therefore the same time after the Rydberg peak. By using the Rydberg peaks as a reference point the 2S quenching peaks A_{2S} were evaluated at time t', where t' is a fixed distance from the Rydberg peak times $t' = t_{\text{Ryd.}} + T$, and T is defined as the average separation between $t_{\text{Ryd.}}$ and the maximum of each corresponding 2S quenching peak t_{max}:

$$T = \frac{1}{N-2} \sum_{i=3}^{n} (t_{i,max} - t_{i,Ryd.}). \tag{5.2}$$

T was determined for each of the six data runs and had an associated error calculated as the standard error in the mean of Equation 5.2. For example, for Run #6,

$T = 69 \pm 12$ ns and the correction evaluated at these times $C_{\text{Ryd.}}(t')$ is shown in Figure 5.6(b).

5.2 Results & Discussion

An example of a 2S quenching measurement from Run #6 is shown in Figure 5.7(a) with the smoothed (black) and unsmoothed (coloured) data shown. The vertical lines show the value of t' with the corresponding amplitude values shown in the panel below, (b). The first two greyed out points are the unused points susceptible to slow atoms not being quenched as discussed above.

The amplitudes of each data run were adjusted by the Rydberg correction relative to the maximum 2S signal $A^{\text{max}}_{\text{Meas}} = A_{\text{Meas}}(526\text{ ns})$ of that run which represented the initial 2S population to which the unwanted loss effects were happening. The correction was applied using the equation

$$A_{\text{Corr}}(t') = A_{\text{Meas}}(t') + A^{\text{max}}_{\text{Meas}} C(t'), \tag{5.3}$$

with an example of the data pre- and post-correction data shown in Figure 5.7(b). This correction does not account for the self-annihilation of the corrected fraction of atoms added back onto the data as this does not occur in the Rydberg spectra. Calculations show that less than 5% of corrected fraction of atoms would self-annihilate, based on the calculated annihilation lifetime. This induces an error far lower than the error inherent in the correction.

An exponential fit of the form $Ae^{-\Gamma t}$ (where t is time, A is the amplitude at t_0, and Γ is the decay constant, or the inverse of the lifetime $1/\tau$) was fitted to the corrected amplitudes. An example of this fit can be seen in Figure 5.7(b) for both corrected and uncorrected data. The shorter lifetime of the uncorrected data is consistent with the effect of late collisional losses. This fit was performed on each of the six data runs with the extracted Γ values shown in Figure 5.8. The final answer from the Rydberg corrected data averaged over all six runs was $\Gamma_{\text{exp}}(2^3\text{S}_1) = 843 \pm 72$ kHz.

Because of the high statistical error inherent in the measurement systematic

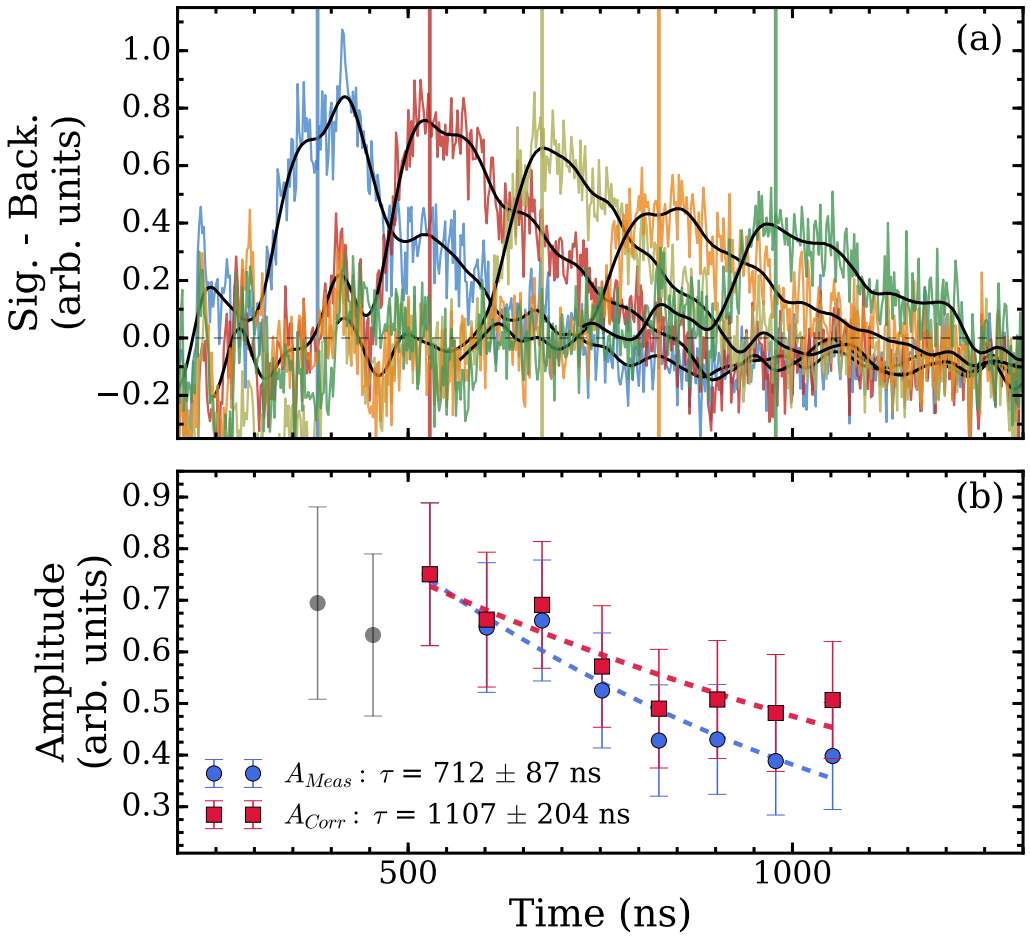

Figure 5.7: (a) Double background subtracted 2S quenching peaks with smoothing (black lines), and without smoothing (coloured lines), for run #6, as described in the text. (b) The corresponding peak amplitudes from (a) (blue points), and the Rydberg corrected amplitudes (red points). The vertical lines in (a) represent the times at which the peak amplitudes are evaluated, and the dashed lines in (b) are exponential fits to the data from which the lifetime is obtained. For clarity only alternate quenching peaks are shown in (a). The first two (gray) points in (b) were not included in the exponential fit, as discussed in the text. Adapted from Reference [242].

errors are negligible. The main systematic changes to the 2S lifetime come from Zeeman mixing, motional Stark effects and stray electric fields. The Zeeman mixing of the triplet and singlet 2S state increases the annihilation rate by an average of 10 kHz, far below the experimental uncertainty and in agreement with the result. The electric dipole moment of an atom travelling through a magnetic field perpendicular to its motion can induce electric fields[1] which can quench the 2S states by

[1]This is the motional Stark effect, where the field produced is $\vec{F}_{M-Stark} = \vec{v} \times \vec{B}$ where $\vec{v}$ is the

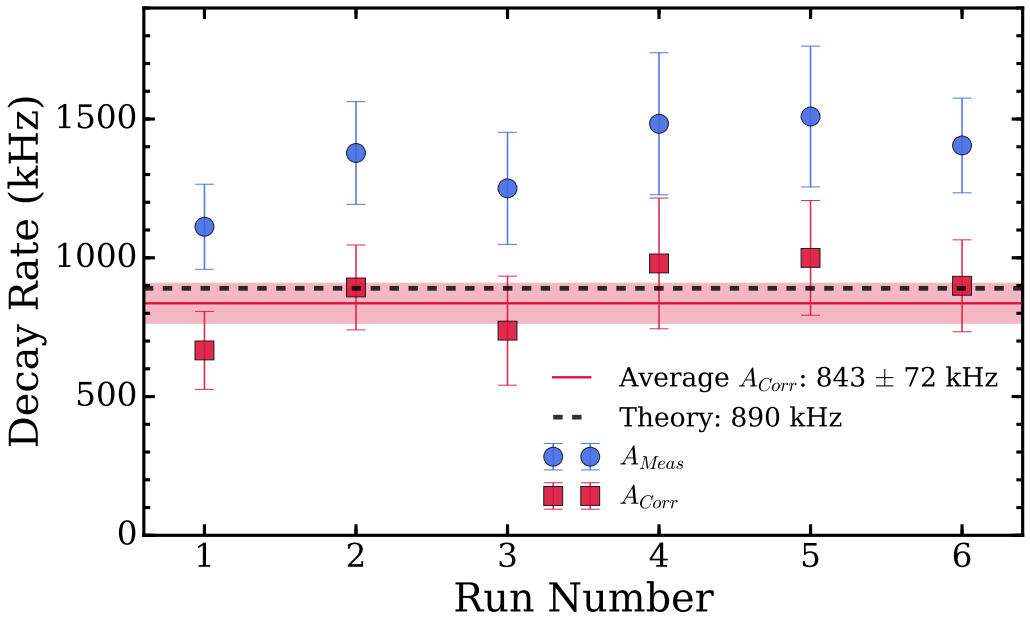

Figure 5.8: Decay rates measured in all six runs, with and without the Rydberg correction. The solid horizontal line at 890 kHz is the Zeeman shifted theoretical 2^3S_1 decay rate. The dashed horizontal line is the weighted average of all corrected data, and the shaded band around the average is the error. Adapted from Reference [242].

Stark mixing with the 2P states. In this experiment, based on the simulated velocity distributions, the change to the 2S lifetime is on the order of just 0.1%. There was no ringing measured on E_T and E_G during these experiments, and most Ps was far from the electrodes so residual fields will be lower than the motional Stark effect.

The value of $\Gamma_{2S} = 843 \pm 72$ kHz is in agreement with theory, which is 890.0 ± 1.4 kHz [5] post Zeeman mixing adjustment, with the error coming from the QED calculation and variation in the average magnetic field. However, the error in the measurement is $\sim 8.5\%$ and the lowest order QED corrections differ by 3%, see Table 2.3, meaning this measurement is not precise enough to test even the lowest order correction. It is feasible to get the experimental error down to this level of precision with some modifications to the method:

- Multiple detectors of larger active area (e.g. [203]) can remove solid angle effects, reducing the need for correction and enabling better detection efficiency of the atoms.

velocity vector and $\vec{B}$ is the magnetic field vector [81].

- Colder Ps would limit losses from collisions and reduce solid angle effects as the Ps will spread out over smaller areas compared to faster Ps sources. Unfortunately, slower Ps sources are hard to make and unstable [198]. Selecting slower parts of the existing Ps distribution would adversely affect statistics. Alternatively, Ge[2] can be given a narrow t_0 distribution by triggering photoemission with ultrafast lasers for more precise timing information and reduced spread [78], though this would also require faster scintillators.

- Improvements to the E_T and E_G assembly can be made. Lowering the switching time of both electrodes would increase $2\,^3S_1$ production. This can be done by reducing the capacitance of the electrodes, allowing them to charge/discharge faster. A modified electrode setup where d_{TG} is smaller would reduce the time it takes slow atoms to reach the quenching region, but may worsen the capacitance of the system. Placing the grid on the QR face of E_G to minimise the low field region will also allow earlier data to be used.

- Using microwave radiation to drive 2S atoms to the 2P state (where they will fluoresce to the ground state and annihilate) would not require any electrodes which can limit flight times and could allow the use of a larger chamber. But a powerful microwave source sufficient to uniformly saturate the transition would be required to ensure that annihilation was triggered in all Ps locations.

- Switching the positron guiding coils off was considered, but due to high coil inductance this was not feasible as the time constant of the coil switching is $\tau \approx L/R = 15$ ms, where $L = 12$ mH is the inductance of the coils and $R = 0.8\Omega$ is the resistance. A transmission target would allow for proper termination of magnetic fields, but these often result in faster Ps or lower production efficiency (e.g. References [27, 225]).

As an extension to any future experiment, mixing the singlet and triplet 2S state using magnetic fields allows a measurement of the $2\,^1S_0$ annihilation lifetime to be

[2]Ge produces faster and more collimated Ps that mesoporous silica with higher efficiency at $\sim 72\%$ [231].

made, similar to the method used to measure the singlet ground state lifetime [16]. This would represent a complete set of annihilation decay rate measurements in Ps. The decay rate of the $2\,^1S_0$ state is too fast to be measured directly, however, if the Zeeman mixed decay rate of the triplet 2S state is measured over a range of magnetic fields the zero field $2\,^1S_0$ decay rate can be extrapolated from the data. This requires highly uniform, precisely known magnetic fields on the order of hundreds of Gauss, which could be achieved with the appropriate Helmholtz coil setup and low divergence Ps source.

5.3 Conclusion

A measurement of the $2\,^3S_1$ annihilation decay rate has been made using time dependent electric field quenching, with a result of $\Gamma_{2S} = 843 \pm 72$ kHz. This is in agreement with Zeeman shifted theory calculations $\Gamma_{2S}^{calc} = 890.0 \pm 1.4$ kHz [5], but is not sufficiently precise to confirm any bound-state QED corrections. However, this represents the first measurement of an excited state self-annihilation decay rate in Ps. The result can be improved upon, requiring a six fold increase in experimental precision to test the lowest order of QED correction. This should be achievable with the methods stated here, with the primary improvements being removal of the need for Rydberg correction and improved statistical error. It is estimated a precision on the 1% level could be achieved this way.

Chapter 6

Microwave Spectroscopy of $n = 2$ Ps in Free Space

This chapter presents work found in:

Microwave spectroscopy of positronium atoms in free space. R. E. Sheldon , T. J. Babij, S. H. Reeder , S. D. Hogan, and D. B. Cassidy, *Phys. Rev. A*, **107**, 042810 (2023) DOI: 10.1103/PhysRevA.107.042810

Recent measurements of the Ps $n = 2$ fine structure have shown large apparent shifts and asymmetries in the measured line shapes [132]. These effects have been attributed to frequency dependent microwave reflection, whereby the power felt by the atomic population changes as a function of frequency due to standing waves set up by reflections from the vacuum chamber, setting up a pseudo-cavity with unknown properties [15]. Horn antenna and other reflection-prone microwave sources are used in many spectroscopy studies (e.g. References [49, 55, 111, 181]), in which this effect may also be present, so understanding the effect of reflections is important. This work presents an exploration of these effects using free-space microwave radiation from a horn antenna.

In addition to this, future measurements of inter-Rydberg transitions will require free-space radiation because the waveguide corresponding to the > 700 GHz radiation used, the WR-1.0, has dimensions of 0.254×0.127 mm. This tiny size makes it impossible to propagate Ps through any WR-1.0 waveguide without large

selection effects and losses. Therefore a good understanding of horn antenna and free-space radiation is required.

6.1 Experimental Setup & Methodology

During the work in this chapter the positron beam had a typical spot size of 3 mm and 2 ns, as described in Section 3.1. The positrons were incident on a mesoporous silica target mounted on electrode E_T, biased to V_T = -3.5 kV for implantation, see Section 3.4. The grid electrode E_G was a distance d_{TG} = 8 mm from E_T, and was kept grounded during laser excitation of the 2S atoms, with a resultant F_{TG} = 4.4 kV/cm field. The applied magnetic field was the same during all measurements and is discussed in detail in Section 6.2.1. Figure 6.1 shows a diagram of the experiment in (a) the *xz*-plane, and (b) the *yz*-plane.

The UV laser used to excite the $2^3S_1'$ state was set to $t_{lsr} = t_{lsr}^{opt.}$ for optimum Ps production, see Section 3.5, exciting the 2S' mixed state in F_{TG}. E_T switched from -3.5 kV to 0 V in t_{rise} = 35 ns to evolve the 2S' into pure 2^3S_1 atoms, see Section 3.8 for more information. Retro-reflection was not implemented in this experiment,

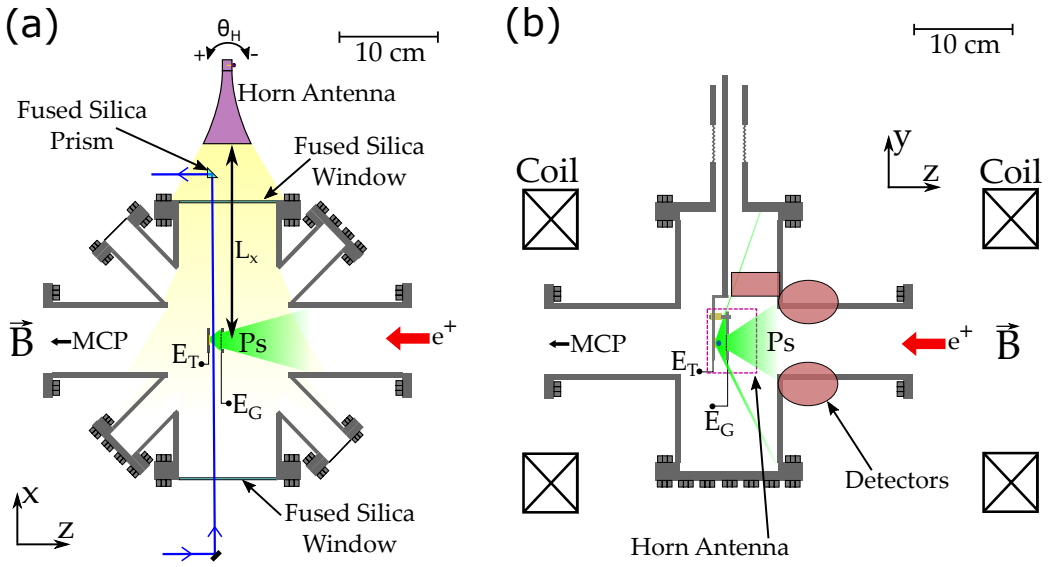

Figure 6.1: A schematic diagram of the experimental setup in (a) the *xz*-plane and (b) the *yz*-plane showing the horn antenna (purple), Ps cloud (green), UV laser (blue), incident positrons (red), the silica target (yellow), the chamber (dark grey) and electrodes (light grey). In addition to this (a) shows the microwaves (pale yellow), and (b) shows the detectors (pale red) and the placement of the magnetic coils. Adapted from Reference [243].

instead a fused silica prism was located on the $+x$ side of the chamber to prevent the UV beam damaging the horn antenna and to allow entry of the IR laser for photoionisation to perform laser delay optimisation and Doppler scans. The prism was mounted on a plastic rod to minimise microwave reflection and attenuation.

Three gamma-ray detectors, see Section 3.2 & 3.3, were used to record SSPALS spectra, as discussed in Section 3.6, to observe the changes in annihilation caused by the application of microwave radiation to the 2S atoms. Microwave radiation at ~ 8.6 GHz drives the 2^3S_1 atoms to the 2^3P_2 state and causes early annihilation by fluorescence to the ground state which can be observed using SSPALS as a positive S_γ value. Microwaves were applied with a WR-102, 15 dBi gain horn antenna as described in Section 3.9.

The horn antenna was placed on the $+x$ side of the chamber, with the emitted radiation travelling along the $-x$ direction. The horn was centered at $y = 0$ mm and $z = 10$ mm to ensure the maximum amount of microwave radiation enters the vacuum chamber, this being the centre of the fused silica window. The x position of the horn, L_x, is defined as the distance in the x-axis between the exit aperture of the horn antenna and the centre of the Ps ensemble at $x = 0$ mm. Measurements in this work were performed at two values of L_x, 21 and 34 cm, which correspond to the near-field and far-field regime respectively. The boundary is at a distance $d_{FF} = 26$ cm from the horn antenna output face, marking the point where the unpolarised near-field regime becomes the polarised, planar-wave far-field regime. However, complex microwave field patterns due to reflection effects causes effectively randomised polarisation in both regimes, as discussed fully in the next section. Figure 6.2 shows an example of the simulated polarisation at the two experimental values of L_x, calculated using Equation 4.2.

The angle of the horn antenna θ_H could be changed using a manual rotation stage upon which the horn was mounted. This will change the direction from which the microwaves intersect the Ps atoms and change the reflection effects within the experiment. Figure 6.3 shows an image of the setup at $\theta_H = +10^\circ$. Although the accuracy of the relative angle change on the rotation mount was $< 0.5^\circ$ the

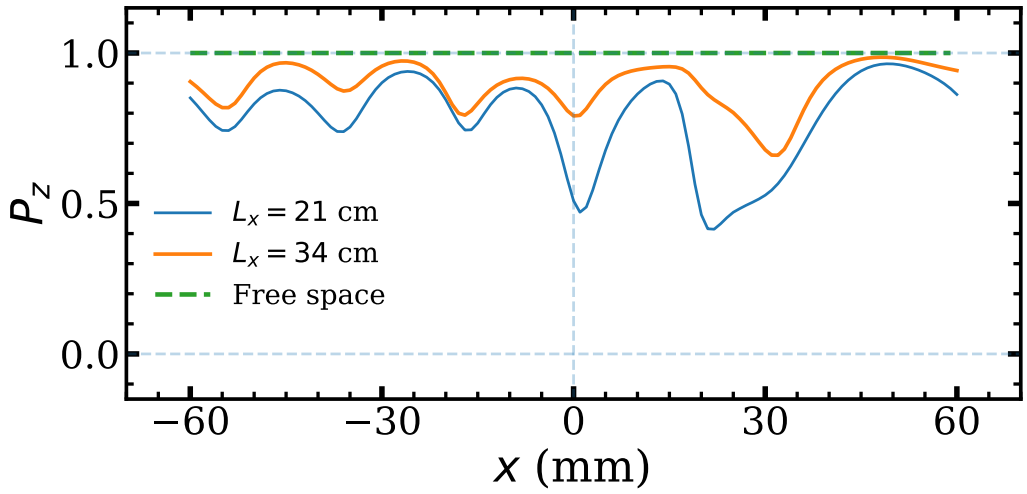

Figure 6.2: The simulated polarization in the z-axis for a free space horn antenna (dashed green line), a horn antenna in the experimental setup at $L_x = 21$ cm (thin orange line), and again in the experimental setup at $L_x = 34$ cm (thick blue line). This data was simulated as described in Section 6.2.2 at $\theta_H = 0^\circ$ and $\nu = 8\,624.38$ MHz.

alignment of the horn to the x-axis of the experiment was subject to error which we estimate to be $\pm 2^\circ$ due to the difficulty of aligning the horn antenna to the production target.

Some electric fields were still present after 2S production due to ringing on E_T from the HV switch which can have a magnitude of up to $F_{TG} = 100$ V/cm based on the maximum recorded ringing voltage and d_{TG}, see Section 3.8.1. To prevent Stark shifts the application of microwaves was therefore delayed by $t_\mu = 510$ ns to allow the majority of the Ps ($> 95\%$) to leave the LER and enter the region beyond the grid, the quenching region, QR. At t_μ the field in the LER was $F_{TG} = 40 V/cm$ but most Ps was beyond E_G in a field of < 1 V/cm (calculated by Equation 3.4). A later delay would allow more Ps to leave the LER and let the ringing voltage decay further. But increased losses from self-annihilation and collisions would impact statistics so the delay was chosen to be as early as possible while allowing the majority of the Ps distribution to enter the QR.

Line shapes were generated by measuring the S_γ parameter as a function of microwave frequency to quantify the transfer from the 2^3S_1 to the 2^3P_2 state, as discussed in Section 3.9. The line shapes measured by each detector were fitted with

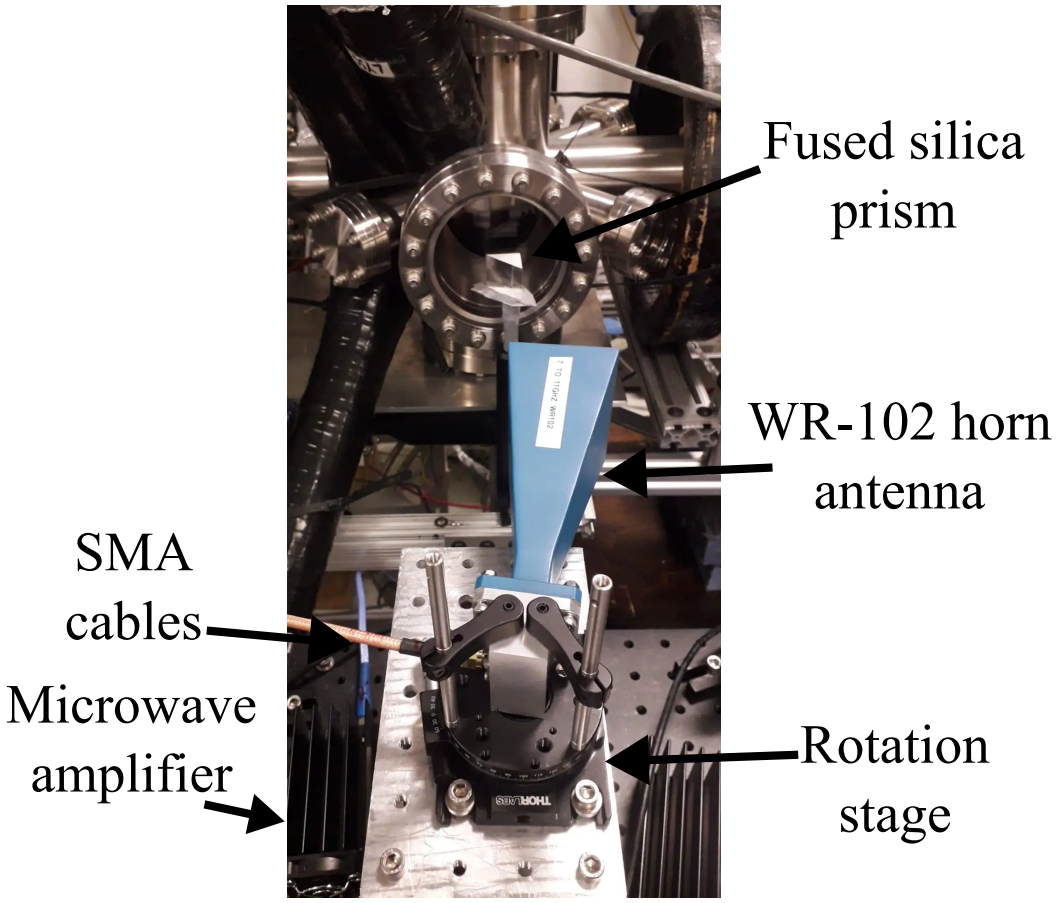

Figure 6.3: A photograph of the setup with the horn at $\theta_H = +10°$, $L_x = 34$ cm. The prism is present in front of the window, and the black tubes on the left are LYSO detectors around the chamber.

Lorentzian and asymmetric Lorentzian functions to extract values of the centroid, width and asymmetry, (see Section 2.4). The data presented in this chapter is an average of the fitted values across the three detectors and multiple data runs unless specified, see Appendix A for more detail on how this data was processed.

6.2 Simulations

6.2.1 Trajectory Simulations

Monte Carlo trajectory simulations of the Ps atoms were performed to better understand the location of microwave transitions and determine the best time to apply the microwave radiation, see Section 4.2 for details. The initial distribution of atoms was determined by experiment with the measured Doppler width being

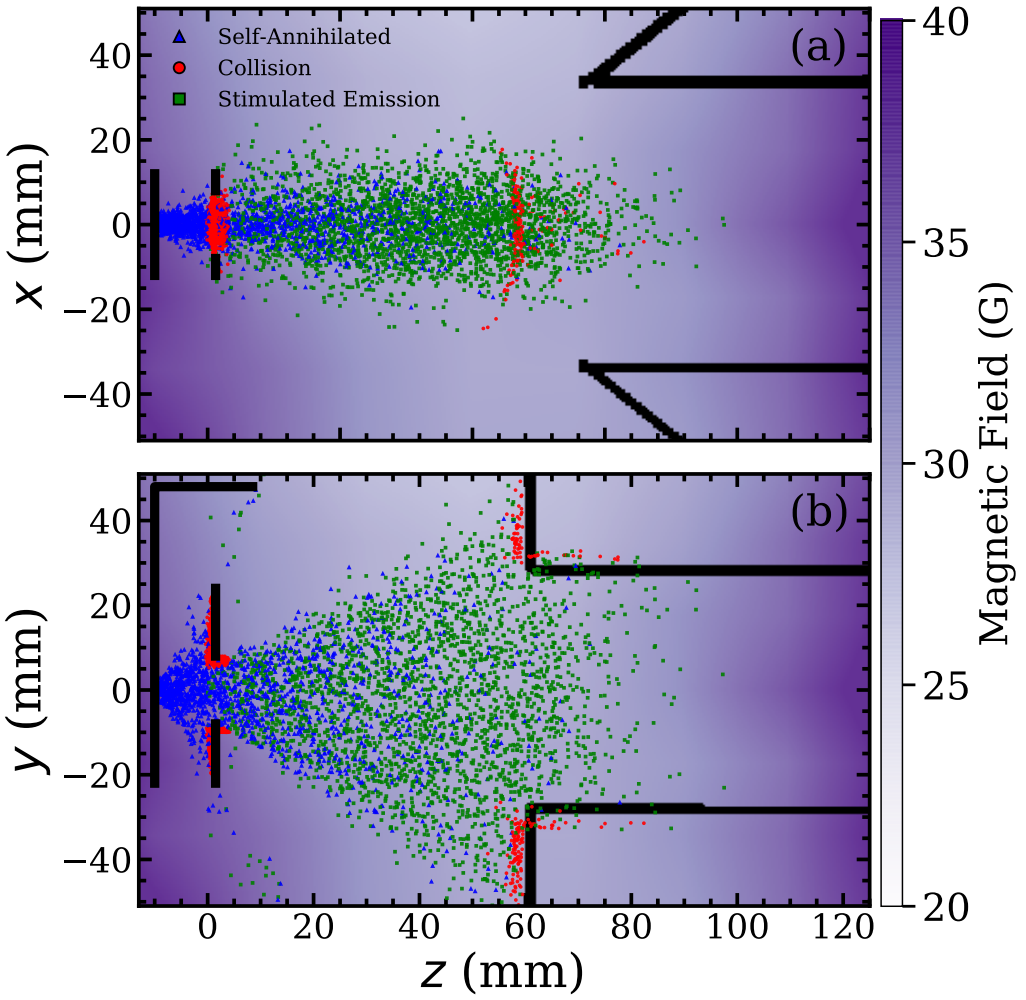

Figure 6.4: Monte Carlo simulations of the location of microwave induced $2^3S_1 \rightarrow 2^3P_2$ transitions at $t_\mu = 510$ ns (green squares), and self-annihilation events (blue triangles), and collisions of Ps atoms (red circles) before this time. (a) is the xz-plane and (b) is the yz-plane. The arc of red dots at $z \approx 60$ mm in (a) is collisions of atoms with fast v_y colliding with the curved chamber as seen in (b). Solid black lines denote solid metal objects, namely, the target and grid electrodes and the vacuum chamber. The colour map shows the magnetic-field strength in and around the vacuum chamber. $z = 0$ mm is the centre of the chamber in this figure, not the starting location of the Ps atoms, which remains E_T. Adapted from Reference [243].

$\Delta\lambda = 0.080$ nm and the laser delay being $t_{\text{lsr}} = t_{\text{opt.}}$ which gave the average velocity vector $\vec{v}_{\text{rms}} = (15, 99, 94)$ km/s, see Section 4.1. The atoms were assigned an annihilation lifetime sampled at random from an exponential distribution of $\tau_{SA} = 1120$ ns, which is the lifetime of the 2S state in the average magnetic field of $B_z = 32$ G.

Figure 6.4 shows the location of Ps atoms at $t_\mu = 510$ ns in the xz- and yz-plane.

The red dots indicate collisions, demonstrating collimation on the grid electrode and collisions with the vacuum chamber. Blue dots show self-annihilating atoms, where 30 % of the initial population was lost to self-annihilation before t_μ. Green dots represent the location of the surviving atoms at t_μ, with no atoms remaining in the LER by this time. The green dots to not represent where the microwave driven atoms annihilate, simply where they are when the radiation is applied. This is due to the complexity of the processes upon application of the microwaves which involve a non-saturating microwave intensity, the fluoresce from 2P $\rightarrow$ o-Ps and the ground state decay rate $\Gamma_{\mathrm{o-Ps}}$. These processes will be considered in Section 6.2.3 of this chapter.

The colour map in Figure 6.4 shows a 2-D map of the magnetic field strength within the experimental region at $x = 0$ mm and $y = 0$ mm as measured by techniques described in Section 3.1.3. The magnetic field at the location of each atom at t_μ was extracted from the measured field map with the population in an average magnetic field of 32.0 ± 2.3 G with the range of magnetic fields being 28 to 41 G. According to QuTip simulations (see Figure 4.5) microwave transitions can occur up to 1 μs after t_μ, although the fraction of atoms remaining at this point will not be significantly contributing to the measured signal. As a conservative estimate, more than 50% of quenching events will occur by $t = 1200$ ns, at which point the average magnetic field is 39.9 ± 11.1 G and the range of fields is 29 to 74 G due to the Ps spreading out. Taking the initial 32.0 ± 2.1 G field the average Zeeman shift will be -1.13 ± 0.15 MHz at t_μ, and -1.75 ± 1.11 MHz at $t = 1200$ ns. Note the value of $\tau_{SA} = 1120$ ns used in the final simulation was calculated based on the average field determined using the zero-field $\tau_{SA} = 1136$ ns 2S lifetime in an initial simulation. Changing the value of τ_{SA} had no effect on the simulated magnetic field distribution.

6.2.2 FIT Field Simulations

A full 3D CAD model of the experimental setup was imported into CST Studio Suite to simulate the microwave properties of the system, in particular to observe the effects of microwave reflection of intensity and polarisation. These simulations were performed using methods described in Section 4.3.

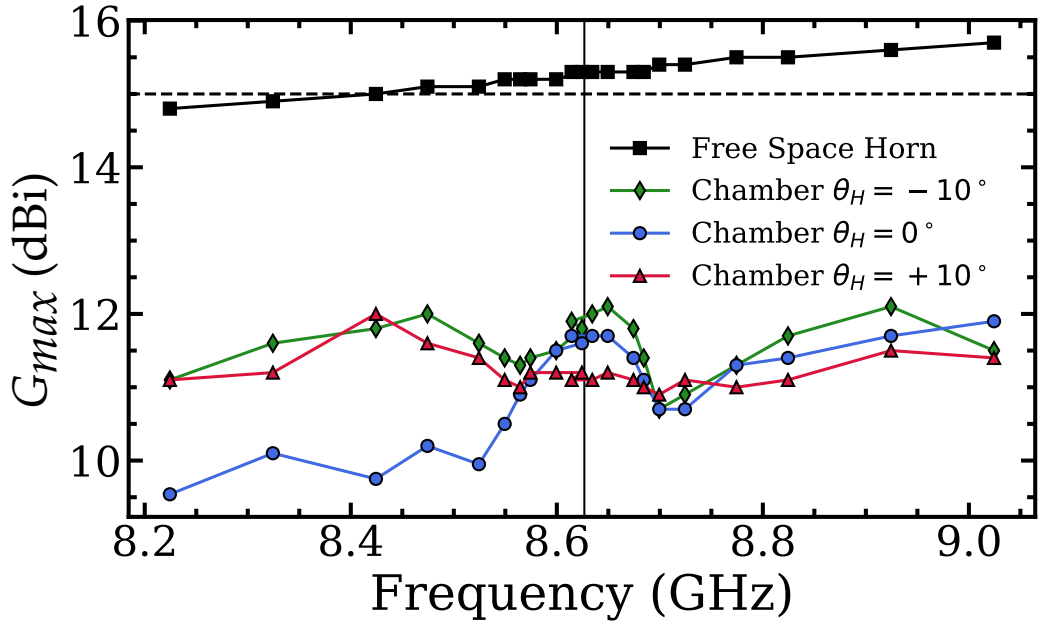

Figure 6.5: The simulated gain of the WR-102 horn antenna in the $-x$ direction in free space (black squares), and with the experimental setup present for $\theta_H = -10°$ (green diamonds), 0° (blue circles) and +10° (red triangles). The dashed horizontal line indicates the manufacturer specified gain, the vertical line shows the zero-field ν_2 transition frequency, and the lines joining the points are a guide for the eye.

As mentioned above the maximum gain of the horn antenna G_{max} will have a small frequency dependent variation in free space which could distort line shape measurements. Figure 6.5 shows a CST simulation of the free space G_{max} compared with G_{max} with the experimental setup present. This demonstrates that the intrinsic gain response of the horn is insignificant due to the dominant effect of reflections by the chamber and hence has not been corrected for in experiment. In addition to this, G_{max} was simulated for a range of θ_H values, with the large variation between results indicating that the G_{max} is dependent on the exact geometry of the system.

To further investigate the microwave radiation the electric field pattern was simulated at 8626.71 MHz for three values of θ_H, shown in Figure 6.6. Figure 6.6(a) shows the horn radiation decreasing in intensity continuously the further from the antenna you are for the free space case ($E_0 \propto 1/x$). When the experimental setup is included (Figure 6.6(b-d)) the radiation pattern displays large variation due to reflected radiation. The peaks and troughs in the field amplitude show interfer-

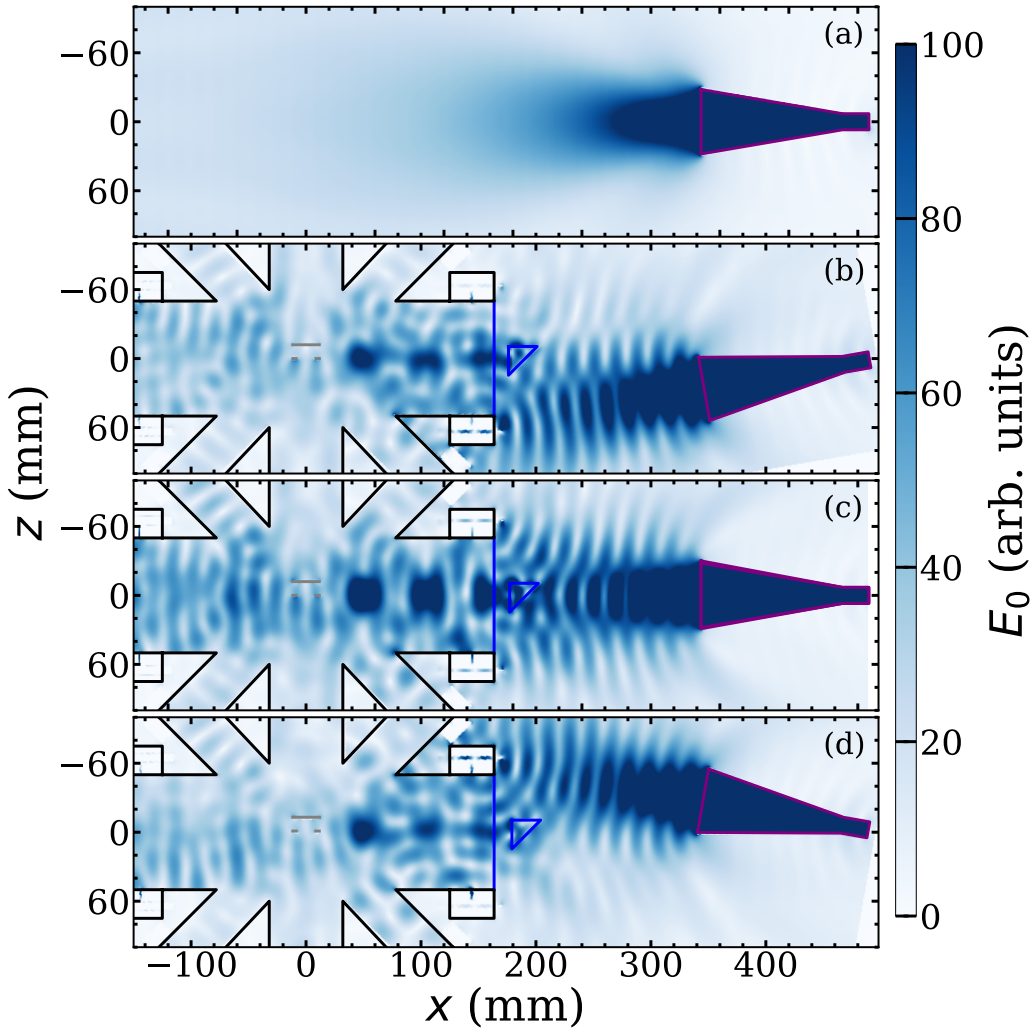

Figure 6.6: FIT simulations of the spatial distribution of the magnitude of the electric-field component E_0 of 8626.71 MHz microwave radiation in (a) free space and (b)-(d) the experimental vacuum chamber with a horn antenna angle $\theta_H = -10°$, 0°, and +10°, respectively, for $L_x = 34$ cm. The vacuum chamber is outlined in black, the electrodes in grey, the prism in blue and the horn antenna in purple. $z = 0$ mm is the centre of the chamber in this figure, not the starting location of the Ps atoms, which remains E_T. Adapted from Reference [243].

ence patterns in the standing wave. Inherent in all these situations is that atoms moving towards the horn in the $+x$ direction are subject to a higher microwave intensity, leading to preferential excitation, but any Doppler effects will be limited by the narrow spread of v_x as discussed further below. It is also notable that Ps atoms will experience different time dependent microwave fields for different horn angles due to the changing radiation pattern. In particular, asymmetric components such as the prism and E_T & E_G, cause θ_H dependent variation.

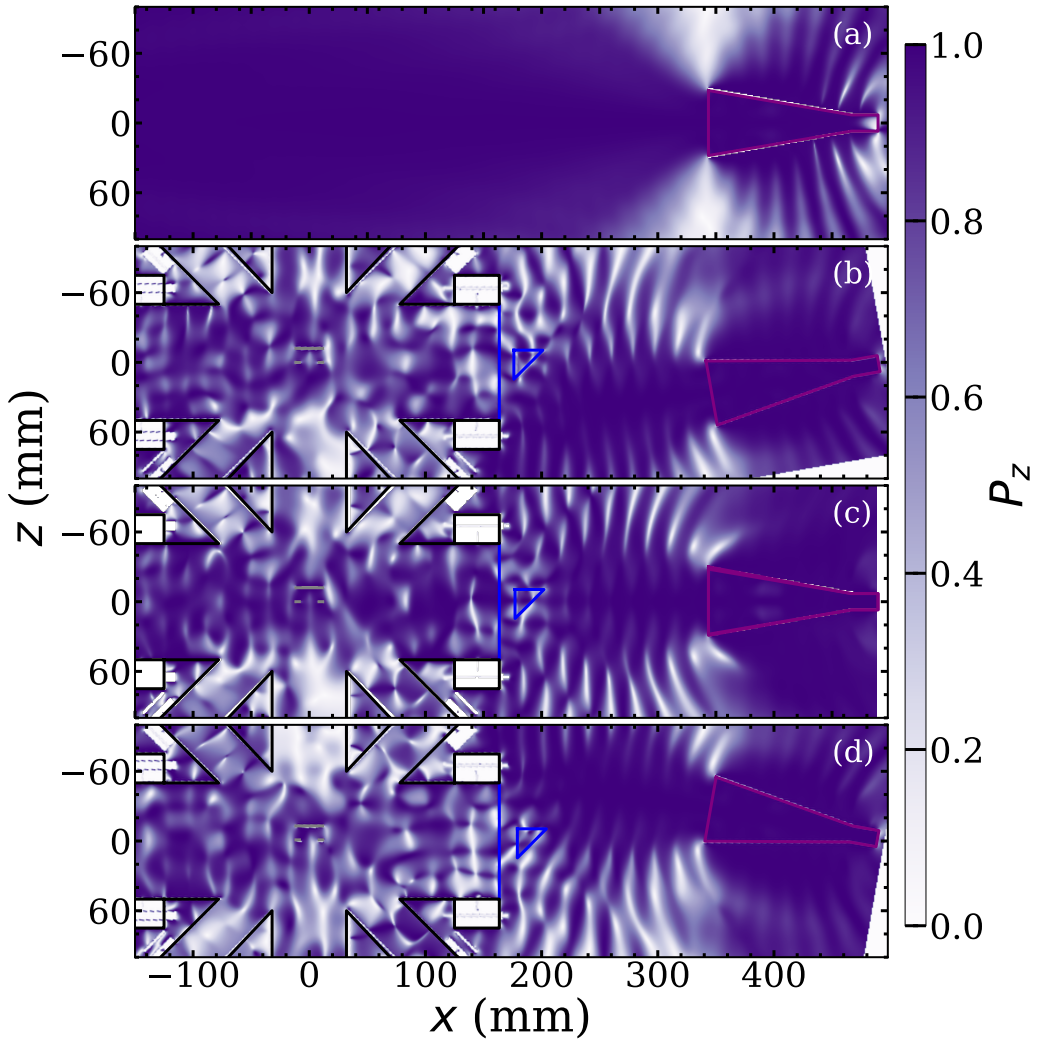

Figure 6.7: The simulated polarisation P_z of microwave radiation in the xz-plane at $y = 0$ mm emitted from a WR-102 horn antenna at $\nu = 8\,624.38$ MHz and $L_x = 34$ cm. This is for four different cases: (a) a free space horn antenna, (b) the experimental setup at $\theta_H = -10°$, (c) the experimental setup at $\theta_H = 0°$, and (d) the experimental setup at $\theta_H = +10°$. The vacuum chamber is outlined in black, the electrodes in grey, the prism in blue and the horn antenna in purple. $z = 0$ mm is the centre of the chamber in this figure, not the starting location of the Ps atoms, which remains E_T

The field in Figure 6.6 is represented as the peak field, $E_0 = \sqrt{E_x^2 + E_y^2 + E_z^2}$, because radiation of every polarisation is present as discussed above in Figure 6.2, and thus transitions for which $\Delta M_J = 0, \pm 1$ are possible. This figure shows the simulated polarisation data extracted along the line $y = 0$ mm, $z = 20$ mm, calculated using Equation 4.2. This data demonstrates that the vacuum chamber and other experimental components cause the polarisation to vary. The free-space case has

100% polarisation in the z-axis as expected for a horn antenna with the antenna orientated along the z-axis as is the case here. A larger value of L_x improves the polarisation, likely a combination of being in the far-field regime and less of the side band intensity from the antenna is incident into the chamber, making the radiation more directional and less likely to reflect.

Figures 6.7(a) shows a 2-D map of P_z for the free space case where the 100% polarisation of the forward direction is clear, though the side bands are not clearly polarised. Figures 6.7(b-d) show 2-D maps of P_z in the xz-plane at $y = 0$ mm for $\theta_H = -10°, 0°$ and $+10°$ at $L_x = 34$ cm and $\nu = 8\,624.38$ MHz. From these maps it is evident that there is a large amount of polarisation variation from $P_z = 1$ to 0, therefore the ΔM_J of the transition will be spatially dependent with unknown weightings between the possible sets of transitions.

Figure 6.8 shows 2-D E_0 and P_z maps of the simulated radiation field at two frequencies and demonstrates that the frequency of the radiation changes both the spatial intensity distribution and the polarisation distribution due to the standing

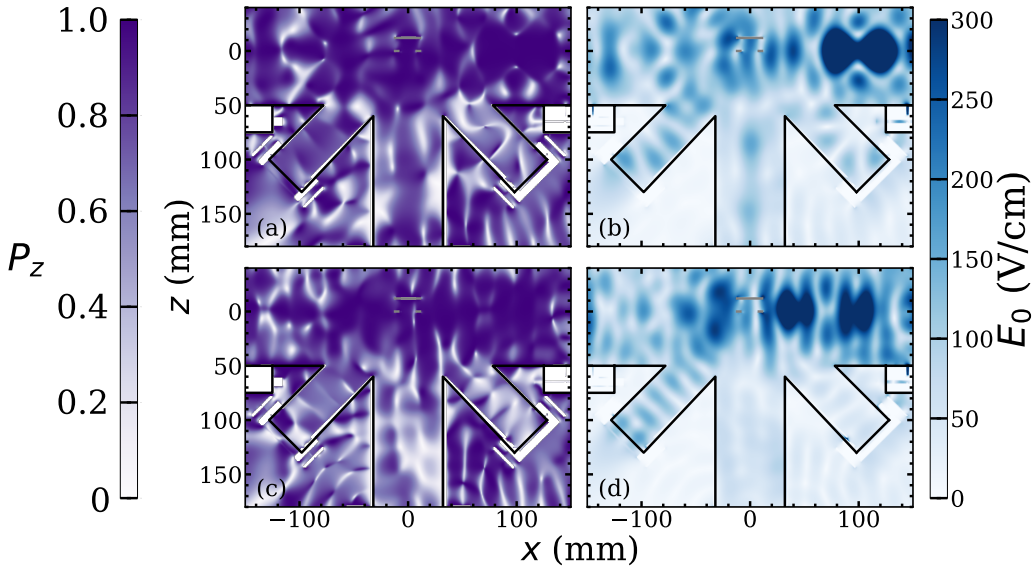

Figure 6.8: Electric field E_0 maps (right hand side, blue) of the microwave radiation at $\theta_H = 0°$ and $L_x = 34$ cm for (b) $\nu = 8\,224.38$ MHz, and (d) $\nu = 9\,024.38$ MHz. Microwave polarisation P_z maps (left hand side, purple) of the microwave radiation at $\theta_H = 0°$, $L_x = 34$ cm for (a) $\nu = 8\,224.38$ MHz and (c) $\nu = 9\,024.38$ MHz. All at $y = 0$ mm. The vacuum chamber is outlined in black and the electrodes in grey. $z = 0$ mm is the centre of the chamber in this figure, not the starting location of the Ps atoms, which remains E_T

waves being highly reflection (and therefore wavelength) dependent.

Because the spatial distribution and intrinsic power of the radiation are highly dependent on ν, θ_H and L_x the microwave fields within this experiment are highly inhomogeneous, and can be regarded as effectively random. Because of this the simulations will be limited by the highly complex interactions of the numerous reflections which are dependent on the exact physical properties of the setup that we cannot digitally reproduce with high precision. These simulations can therefore not be used to obtain exact experimental reproductions of the line shapes, but can be used to gauge the magnitude of any possible effects these variations may have. Any change in ν or θ_H may not only change the intensity of the microwave field but also its spatial distribution resulting in spatial selection of different subsets of atoms or different allowed transitions.

6.2.3 Line shape Simulations

Line shape simulations were performed using QuTip to examine the effect of inhomogeneous microwave fields on the line shapes measured in this work. See Section 4.4 for a detailed explanation of the method. The full 3-D electric field component of the microwaves was simulated at each experimental microwave frequency at each value of θ_H and L_x, similar to the simulations in the section above using methods described in Section 4.3. Five hundred Ps atoms with the initial conditions described in Section 6.2.1 were propagated through the simulated field as a function of time to obtain the time dependent field strength felt by each atom $E_0(t)$. An example of this time dependent field for one atom can be seen in Figure 4.5(a). This data was used as the microwave field strength input of the QuTip ME solver with a Zeeman shifted transition frequency of $\nu_{\text{Zeeman}} = 8\,625.84$ MHz and a Zeeman mixed 2S lifetime of $\tau_{SA} = 1120$ ns.

The microwave field strength was simulated in CST for an arbitrary microwave input power and needed to be scaled to be representative of experiment. This was done by matching the power broadening of the simulated line shapes to that of the measured line shapes as explained in Section 4.4. An example of this is shown in Section 6.3 for line shapes at $L_x = 21$ cm ($\theta_H = 0^\circ$) which were produced to in-

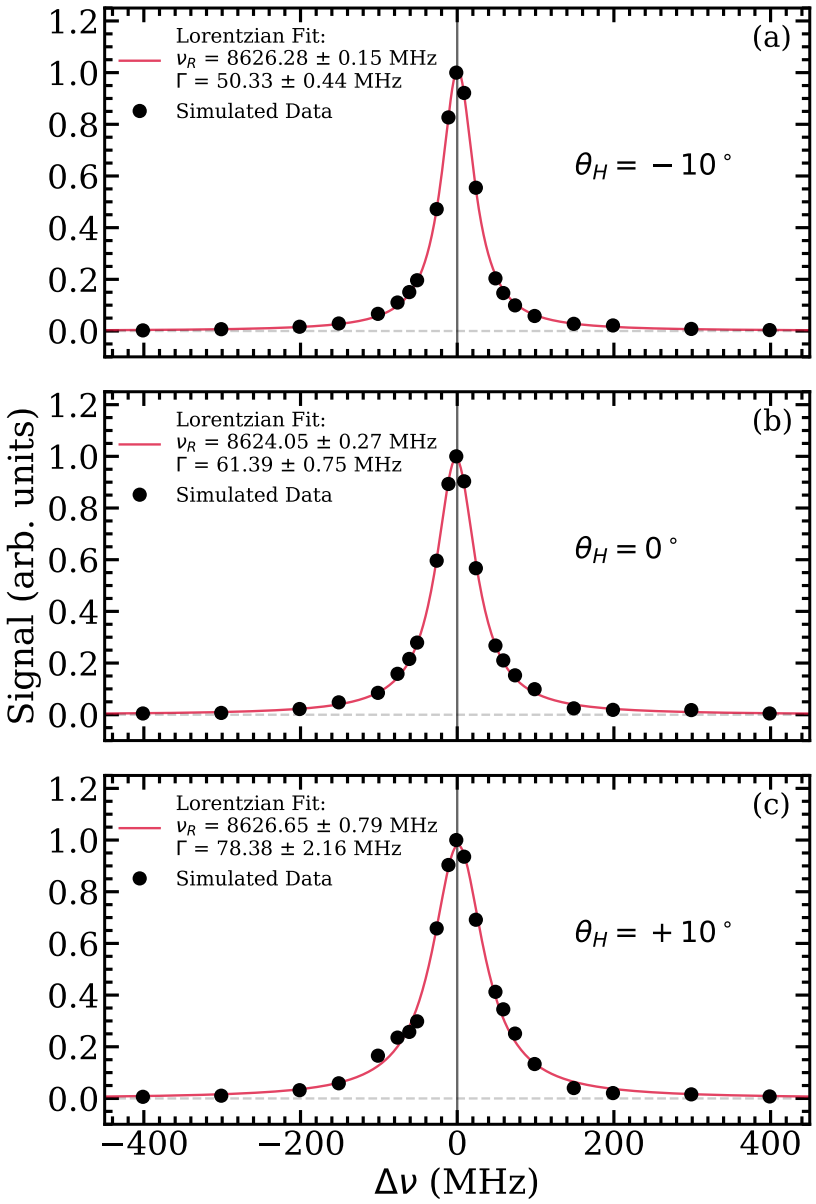

Figure 6.9: Simulated line shapes as described in the text at $L_x = 34$ cm for (a) $\theta_H = -10°$, (b) $\theta_H = 0°$ and (c) $\theta_H = +10°$ fitted with Lorentzian functions. From Reference [243].

vestigate the power broadening of the transition. The simulated data was scaled in the x-axis so that at the χ^2_{reduced} parameter between the experimentally measured widths and the simulated widths was optimised, with the width determined by fitting a Lorentzian function. This was done by making a fit of Equation 2.24 to the simulated line widths and comparing this to the line width at the experimental powers.

Three example line shape simulations are shown in Figure 6.9 for $\theta_H = -10, 0, +10^\circ$ at $L_x = 34$ cm to investigate the effect of microwave field distributions on the line shape. The power scaling was the same for all $L_x = 34$ cm line shapes and was chosen to match the width of the $\theta_H = 0^\circ$ experimental run because P_{input} was kept constant for experimental data runs at $L_x = 34$ cm. Line shapes were simulated for each experimental value of θ_H, but also 9.8° which acts as a sensitivity test to establish if there is any significant line shape variation for small angle changes. There is an estimated $\pm 2^\circ$ error on the simulated θ_H because the absolute orientation of the horn with respect to the chamber is known only to limited accuracy (due to the precision of the measurement technique), and while the simulation is an exact rotation of the apparatus this creates a relative error compared to the experimental data. The line shapes in Figure 6.9 show MHz level shifts with no asymmetry and will be discussed in full in Section 6.3.2.

6.3 Data and Discussion

6.3.1 Saturation Data

Initial measurements were taken to establish the possibility of saturation with a horn antenna. The microwave induced S_γ as a function of P_{input} was recorded for two values of L_x (at $\theta_H = 0^\circ$) and is presented in Figure 6.10. By fitting Equation 2.25 we obtain b parameters of 0.018 ± 0.001 and 0.0035 ± 0.0005 mW^{-1} for $L_x = 21$ and 34 cm, respectively. This equates to saturation powers of $P_{\text{sat.}} > 56 \pm 3$ and 294 ± 42 mW for the two values of L_x, shown as vertical lines on Figure 6.10[1]. As expected, the further the distance of the horn antenna from the atoms the harder it is to saturate the transition due to less power entering the vacuum chamber, resulting in a lower overall intensity[2].

Line shapes were measured at $L_x = 21$ cm and $\theta_H = 0^\circ$ for a series of microwave powers which are shown in Figure 6.11. The centroid and width extracted

[1] $P_{\text{sat.}}$ is the threshold above which saturation occurs as defined by Equation 2.25.

[2] Despite this the data shows that this method can be used as an easy way to quench entire 2S populations in free space as a means to trigger annihilation of a spatially large metastable Ps distribution, as discussed at the end of the previous chapter.

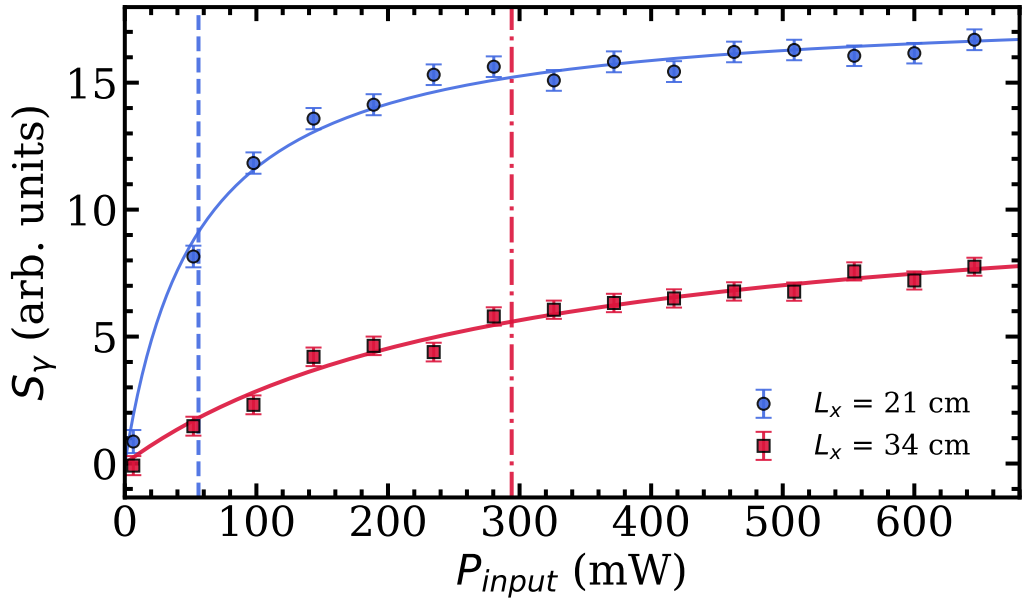

Figure 6.10: Measured saturation curves at $L_x = 21$ cm (blue circles) and at $L_x = 34$ cm (red squares). The associated solid curves are fits to the data by Equation 2.25 with the blue dashed (21 cm) and red dot-dashed (34 cm) vertical lines corresponding to the saturation powers from those fits. Adapted from Reference [243].

from Lorentzian fits to the data are shown in Figure 6.12. Panel (a) confirms increased power does not cause shifts in the fitted centroid of the line shapes due to either ac Stark shifts (which should be less than 10 kHz at the estimated intensity), or selection of additional atoms by the inhomogenous field distribution.

However, this averaged transition frequency of the data, $\nu_R = 8\,623.8 \pm 0.3$ MHz, does display a $> 5\sigma$ shift from the calculated Zeeman shifted value of ν_2^{calc} in a 32 G magnetic field, $\nu_2^{\text{calc}}(32\ G) = 8\,625.58 \pm 0.17$ MHz. The Zeeman shift is calculated for unpolarised microwave radiation driving all $\Delta M_J = 0, \pm 1$ transitions as indicated by the FIT simulation, see Section 2.3 for details on the calculation of the Zeeman shift. The error comes from the error in the B_z measurement and the QED calculations. Even if the microwave radiation had a polarisation of $P_z = 1$ ($\Delta M_J = 0$ transitions only) which provides the maximum possible Zeeman shift the measured transition frequency would still be $> 4\sigma$ from the theory. To produce this Zeeman shift all the atoms (for unpolarised light) would have to be in a field of 51 G, a strength of field that was only present beyond the experimental chamber. Given the QuTip simulations of Figure 4.5 indicate that transitions occur

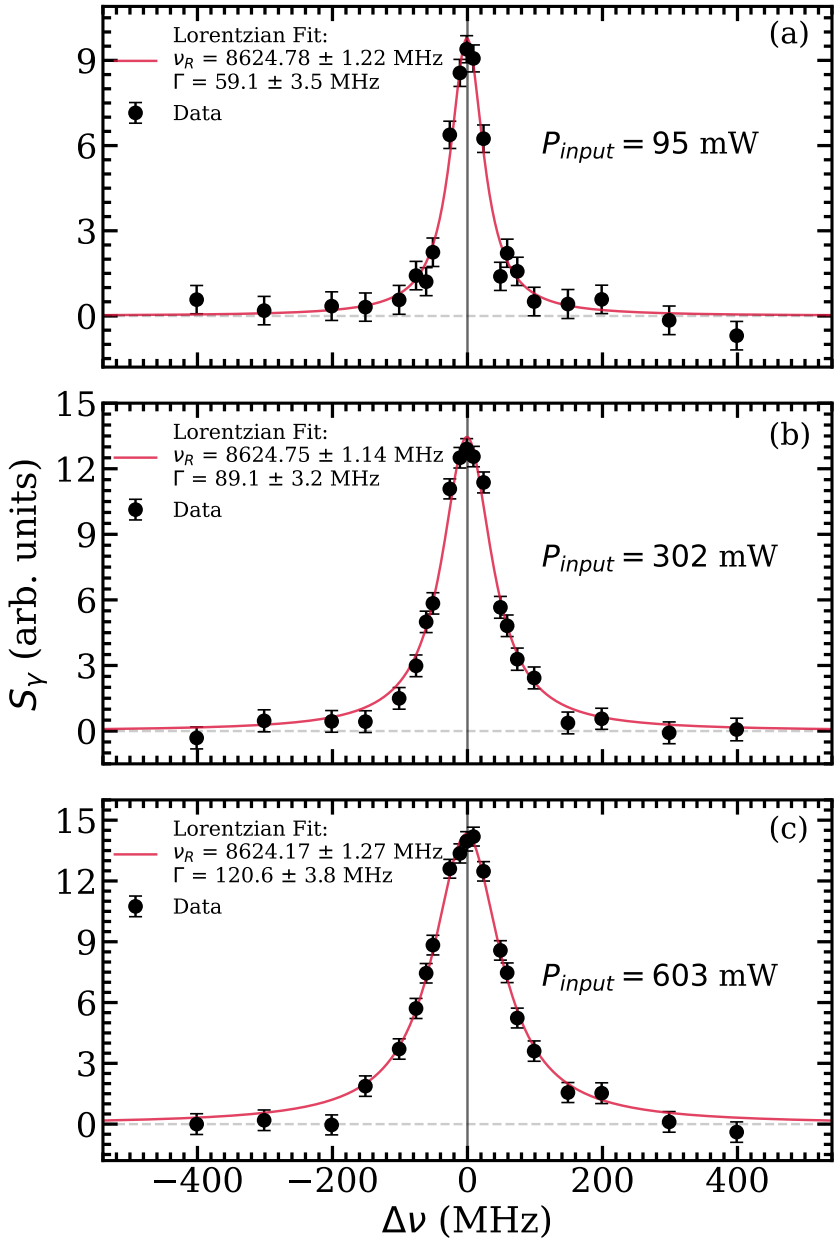

Figure 6.11: Line shapes taken at $L_x = 21$ cm & $\theta_H = 0°$ for three different values of P_{input}; (a) $P_{\text{input}} = 95$ mW, (b) $P_{\text{input}} = 302$ mW and (c) $P_{\text{input}} = 603$ mW. Power broadening is clearly observed in this data. This is an example from one LYSO detector during one data run. Adapted from Reference [243].

fairly soon after t_μ and that any signal this far from E_T would be very weak as seen by the detectors this possibility is discounted.

The data in Figure 6.12(b) have been fitted with a saturation function given by Equation 2.24. The value of Γ_0 should correspond to the natural line width (50 MHz) with additional broadening from Doppler effects (∼0.5 MHz based on

$v_x^{\text{rms}} = 15$ km/s from Equation 2.27) and transit-time broadening (on the order of 1 MHz due to the large interaction region with the microwave field, see Section 2.4). Instead of this, the fit returns a value below the natural line width of $\Gamma_0 = 45.0 \pm 2.2$ MHz, $\sim 3\sigma$ from theory. The fitted b parameter is 0.009 ± 0.001 mW^{-1}, corresponding to a saturation power of $P_{\text{sat.}} = 111 \pm 14$ mW, which disagrees with the fits of Figure 6.10 by 3.9σ.

The disagreement of Γ_0 from theory, and b from measured amplitude data sug-

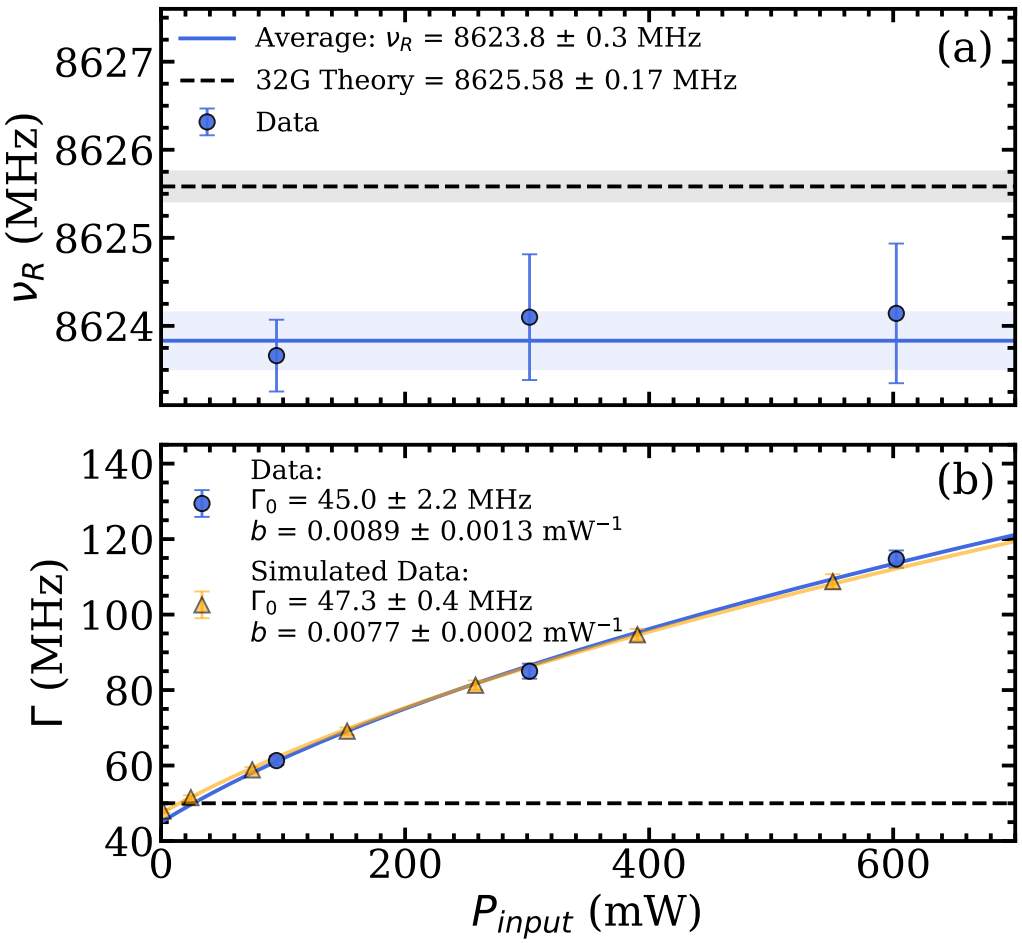

Figure 6.12: Lorentzian fit parameters of (a) the centroid ν_R and (b) the line width Γ as a function of microwave power P_{input} (blue circular points). The average of the centroids (solid blue line with shading representing the error) is 5.9σ from theory (dashed black line). (b) Also shows the simulated line widths (orange triangles) with the power scale adjusted to match the experimental points as closely as possible, both data sets were fitted with the saturation Equation 2.24. These data were recorded with $L_x = 21$ cm and $\theta_H = 0°$. Adapted from Reference [243].

gests that while the transition rate from 2S $\rightarrow$ 2P of the addressed Ps atoms was increasing, there were also new Ps being targeted as the power increased. This would increase S_γ and Γ but not with the same power dependence, resulting in differing b parameters and an incomplete model resulting in the low Γ_0. The measured b parameters are consistent with this whereby when new populations were addressed by the microwaves the amplitude would appear to saturate at a higher power than the widths, which is indeed the case.

Line shapes were simulated to reproduce the experimental power broadening data as described in Section 4.4. The simulated power was scaled by a constant factor to match the broadening trend of the experimental data as closely as possible to determine the correct power to run angle resolved line shape simulations at, hence the close match between the experimental and theoretical line widths in Figure 6.12(b). The simulated Γ and b values are within error of experiment for the appropriately scaled simulated power, with the simulation also returning a line width less than the natural line width. If more atoms are addressed at higher power this may mean Equations 2.24 & 2.25 are not valid, causing the low Γ_0 in both experiment and simulation.

6.3.2 Reflection Effect Data

Line shapes were measured for different horn antenna angles, θ_H, to check the effects of Doppler shifts and microwave reflections. The former effect is possible because rotating the horn will change the direction of propagation of the microwave radiation, resulting in a non-zero net velocity of the Doppler selected 2S atoms as described in Section 4.1.1. The latter effect is possible due to the different standing wave patterns at different values of θ_H resulting in changes in the frequency dependent power.

Figure 6.13 shows example line shapes at three values of θ_H for $L_x = 34$ cm and $P_{\text{input}} = 300$ mW. A visible shift in ν_R can be seen between the $\theta_H = -10^\circ$ and 10° line shapes. The measured ν_R values are shown as a function of θ_H in Figure 6.14 for $L_x = 21$ cm and $L_x = 34$ cm, displaying a total variation of ~ 6 MHz in a $\pm 10^\circ$ range. Linear fits were made to this data to quantify the shift, giving a rate of change

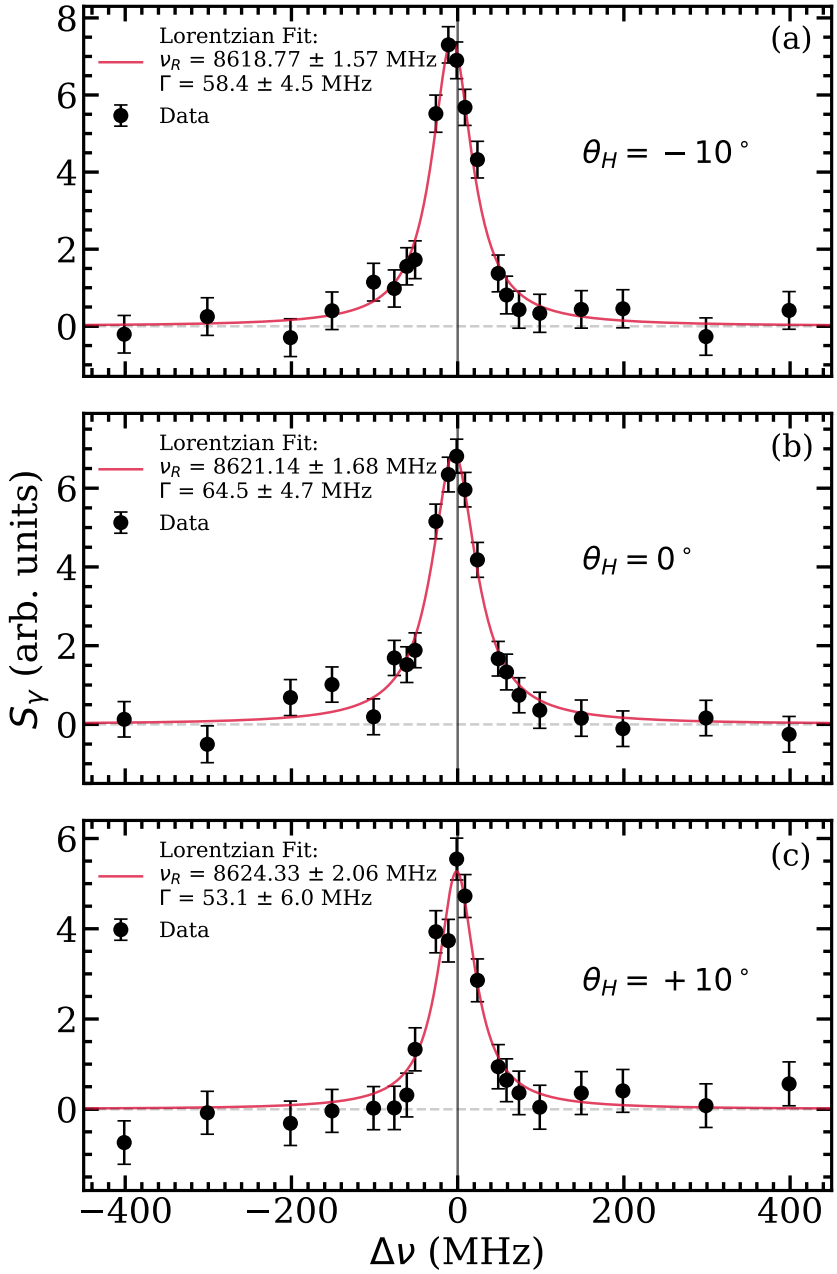

Figure 6.13: Line shapes taken at $L_x = 34$ cm and $P_{\text{input}} = 300$ mW for three different values of θ_H; (a) $\theta_H = -10°$, (b) $\theta_H = 0°$ and (c) $\theta_H = +10°$. The data is fitted with a Lorentzian function (red line) from which a shift is clearly observable in this data. This is an example from one LYSO detector during one data run. Adapted from Reference [243].

of 0.32 ± 0.08 and 0.30 ± 0.06 MHz/degree for $L_x = 21$ and 34 cm, respectively.

Line shapes were simulated for all experimental angles at $L_x = 34$ cm, as described in Section 6.2.3. The values of ν_R from these simulations is presented in Fig-

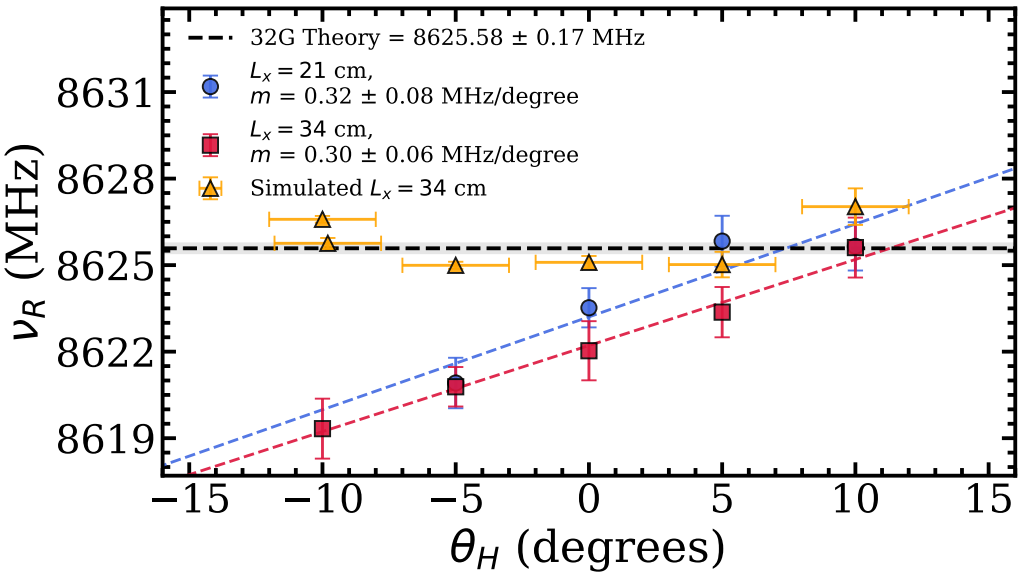

Figure 6.14: Measured ν_R at $L_x = 21$ cm (blue circles) and $L_x = 34$ cm (red squares) as a function of θ_H, with simulations at the latter distance also presented (orange triangles). The dashed gradients show linear fits to the data while the dashed horizontal line is the expected theoretical transition frequency. Adapted from Reference [243].

ure 6.13 and does not present a systematic shift like the experimental data, but does demonstrate the possibility of MHz shifts from radiation pattern changes (without asymmetry).

There are several possible causes for the shift, the first being Doppler effects. For microwave radiation propagating at an angle θ to the Ps ensemble the velocity in the direction of the microwaves will vary by 0.044 MHz/degree as described in Section 4.1.1. This is due to the microwave radiation selecting increasingly large contributions from the mono-directional v_z distribution, inducing a Doppler shift. The calculated shift is an order of magnitude below that observed *and is in the opposite direction*. To explain the experimental data with Doppler shifts would require addressing only the fastest atoms with radiation moving directly towards and directly away from them with no loss of signal which is obviously infeasible. In addition, given the interference patterns of the simulated field maps (Figure 5.2) the microwaves will not have a uniform propagation direction, unlike a waveguide or a highly collimated directional antenna, meaning Doppler effects may be averaged over multiple directions.

Another explanation for the angular shift is that changes in θ_H change the location of the highest field amplitude and thus alters the location and subset of atoms addressed. Figure 6.6 shows that the spatial microwave field pattern is largely consistent for a $\pm 10^\circ$ change in θ_H, with the highest intensity nearest E_T. In addition we have already demonstrated that even the most extreme selection of the fastest atoms cannot explain this data, and the maximum observed shift ($\sim 8\,619.5$ MHz) would require a field of 79 G which is not present in the experiment.

Other systematics reviewed in References [132] & [15] and expanded upon in Section 7.3.1 including ac Stark effect, second order Doppler effect, QI, motional Stark effect and stray electric fields contribute at the sub-MHz level and do not vary with horn antenna angle.

Given the lack of explanatory power for the systematic effects already discussed, we must consider the reflection effects proposed in Reference [15]. These effects create frequency and location dependent power and polarisation, which can induce both apparent shifts and asymmetry, but the data presented in this chapter do not display a significant asymmetry. The average asymmetry for the experimental data across every line shape presented in this chapter was $q_L = -0.54 \pm 0.56$ GHz^{-1}, with the simulations having an average asymmetry of $q_L^{\text{sim}} = -1.7 \pm 0.1$ GHz^{-1}. This is lower than the previous work using waveguides [132] which had an average asymmetry of $q_L = -23.2 \pm 0.5$ GHz^{-1} for the ν_2 transition with clearly asymmetric line shapes.

The q_L of the $L_x = 34$ cm data are shown in Figure 6.15(a) for the experimental and simulated data. They are in agreement, with the average values displaying minimal asymmetry, though the simulated average $q_L = 0.6 \pm 0.2$ GHz^{-1} does indicate a small asymmetry, unlike the experimental average $q_L = 1.7 \pm 1.3$ GHz^{-1} which shows no meaningful asymmetry. QI effects are expected to present asymmetries that cause shifts on the order of < 100 kHz [15]. But due to the > 1 MHz errors on each measured line shape this will not be detectable in this data. This large error means that there may be other asymmetries that the data is not sensitive enough to detect. Because the asymmetry is minimal and the Lorentz and asymmetric Lorentz

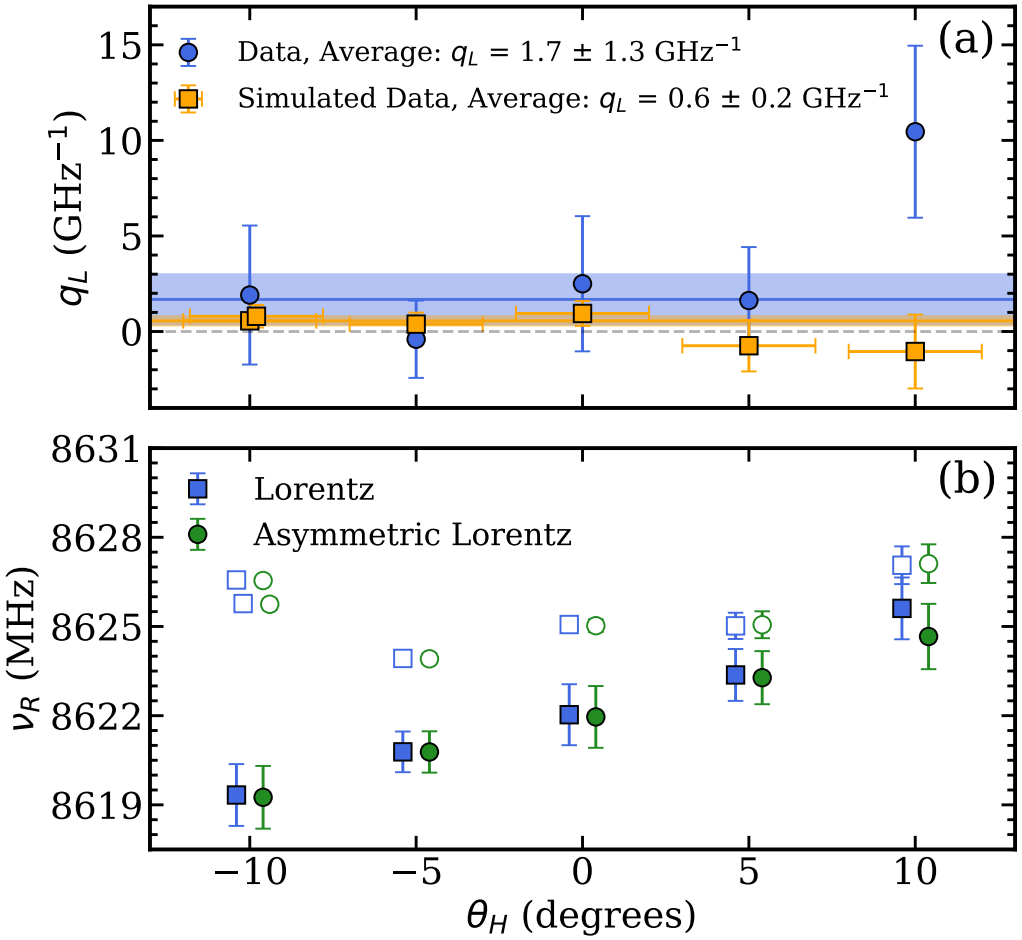

Figure 6.15: The asymmetry of experimental and simulated line shapes for $L_x = 34$ cm and $P_{\text{input}} = 300$ mW is shown in panel (a), and the corresponding ν_R for the Lorentzian and asymmetric Lorentzian are shown in (b). Adapted from Reference [243].

functions are in close agreement, see Figure 6.15(b), the Lorentzian function has been used to compare ν_R values across the data presented here.

It is concluded that the apparent shifts observed in this work are due to distortions of the line shape resulting from a frequency dependent microwave intensity because of reflection effects within the vacuum chamber (if reflections outside the chamber were important the shift at $L_x = 21$ and 34 cm would be different), see Figure 6.5. Simulations of the microwave field strength and polarisation demonstrate the high complexity of the radiation distribution, which is sensitive to small physical changes, and simulated line shapes demonstrate that the field strength distribution alone can cause apparent shifts ~ 1 MHz. The lack of asymmetry in the

data demonstrates the possibility for large shifts with minimal asymmetry. This makes ascertaining if a measurement is subject to reflection effects difficult, such as the recent ν_0 measurement [131]. These reflection effects are highly dominant over all other systematics and present a challenge in using horn antennas for precision measurements.

In order to improve the prospects of precision Ps spectroscopy using horn antennas a few options can be considered. A different chamber could minimise reflections. If the microwaves can pass through and out of the chamber without hitting a reflective surface then the microwave field distribution and antenna gain will be more uniform in space and frequency. In addition, microwave absorbing foam can be used to absorb reflections on either side of the chamber and an in vacuum microwave absorber would be invaluable for the same reason if available. An rf lens system (typically made of plastics) and a horn with a higher nominal gain could improve the collimation of the microwaves resulting is less reflections. This may also improve the overlap with the Ps ensemble allowing selection of specific subsets of atoms. Some of these measures are implemented in the next chapter, but not with a horn antenna due to its fundamental vulnerability to these effects.

6.4 Conclusions

Efficient population transfer of the Ps $2^3S_1 \rightarrow 2^3P_2$ transition using free space $\sim$8.6 GHz microwave radiation from a horn antenna has been shown. Saturation of the transition was achieved at a range of distances demonstrating a method of quenching 2S Ps in free space without the need of an electrode structure to apply an electric quenching field which may impede Ps propagation. This may be achieved using high power, broad band microwave sources with no vacuum compatibility requirements.

However, precision measurements of broad Ps line shapes using free-space microwave radiation are not feasible, as determined from the observation of a significant dependence of the transition frequency on the orientation of the horn antenna with respect to the Ps, despite symmetric line shapes. These shifts cannot

be explained by known systematics and are attributed to small variations in the microwave power at different frequencies due to reflections from the chamber. Numerical simulations of the microwave field and line shapes show complex radiation and polarisation patterns, but corresponding line shape simulations do not exactly reproduce the apparent experimental shifts, despite displaying MHz levels shifts themselves. The data shows MHz shifts without asymmetry, in agreement with previous theoretical studies [15], indicating previously observed shifts and asymmetries can be explained with frequency dependent microwave power variation [132, 133].

These large apparent shifts are a significant problem for precision measurements of transitions with a large natural line width and high spatial spread. The next chapter presents the best effort we can do to reduce reflection effects and represents the most accurate measurement of the Ps $n = 2$ fine structure using these methods.

Chapter 7

Precision Measurement of the Ps $2^3S_1 \rightarrow 2^3P_2$ Interval

This chapter presents work found in:

> Precision measurement of the $2^3S_1 \rightarrow 2^3P_2$ interval in positronium. R. E. Sheldon , T. J. Babij, S. H. Reeder, S. D. Hogan, and D. B. Cassidy, *Phys. Rev. Lett.*, **131**, 043001 (2023) DOI: 10.1103/PhysRevLett.131.043001

The purpose of the work presented in this chapter is to obtain a precision measurement of the $2^3S_1 \rightarrow 2^3P_2$ transition (named the ν_2 transition after the value of J of the final state) without reflection effects by measuring line shapes of the transition in question and extrapolating the Zeeman shifted transition frequencies back to zero-field. The systematic effect of frequency dependent power variations due to microwave reflections has been confirmed to be present in the last set of Ps $n = 2$ fine structure measurements [15,131,132,243] as discussed in Chapter 6. Therefore, in order to perform a higher precision measurement a chamber has been chosen to reduce reflections by allowing the radiation to pass through microwave transparent windows.

Figure 7.1 shows a comparison of the E_z component of microwave radiation within a WR-112 waveguide as a function of frequency for three different cases. The method of simulation and extraction of this data is described in Section 7.2. The three cases examined were: (1) the waveguide mounted in the original chamber

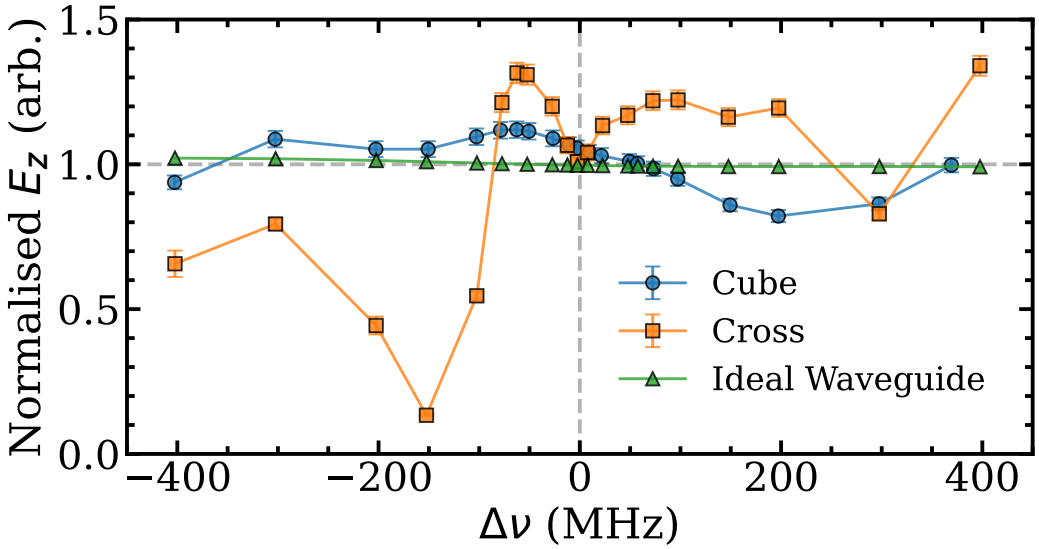

Figure 7.1: A comparison of the variation in the simulated electric field strength of the microwave radiation as a function of frequency within a WR-112 waveguide in a Cube vacuum chamber (blue circles), a Cross vacuum chamber (orange squares), and an ideal waveguide (green triangles). Adapted from Reference [244].

of the 2020 Gurung measurements known as the 'Cross' [133], which is shown in Figure 1.3(a); (2) an ideal waveguide; and (3) the waveguide mounted in a new chamber which allows propagation of the microwaves away from the waveguide, called the 'Cube', shown in Figures 7.2 & 7.3. The previous Cross chamber was simulated as found in Reference [15] with the new Cube chamber simulated in the same way, more information on this can be found in Section 7.2. The ideal waveguide consisted of a void of vacuum with the cross-sectional dimensions of a WR-112 waveguide and a length of 162 mm embedded within a perfect electrical conductor (i.e. $R = 0\ \Omega$). The signal is shown as variation from the mean field to normalise the signals of the three cases.

The simulation shows variations of up to 90% in E_z in a waveguide mounted in the Cross chamber, caused by microwaves coming out of the waveguide and then being reflected back in, causing large apparent shifts in line shape measurements in this setup [15]. By comparison, the cube is more similar to the ideal waveguide, showing variations of $< 20\%$ of the mean. Based on this simulation an experiment was designed and built around this chamber, with other improvements implemented

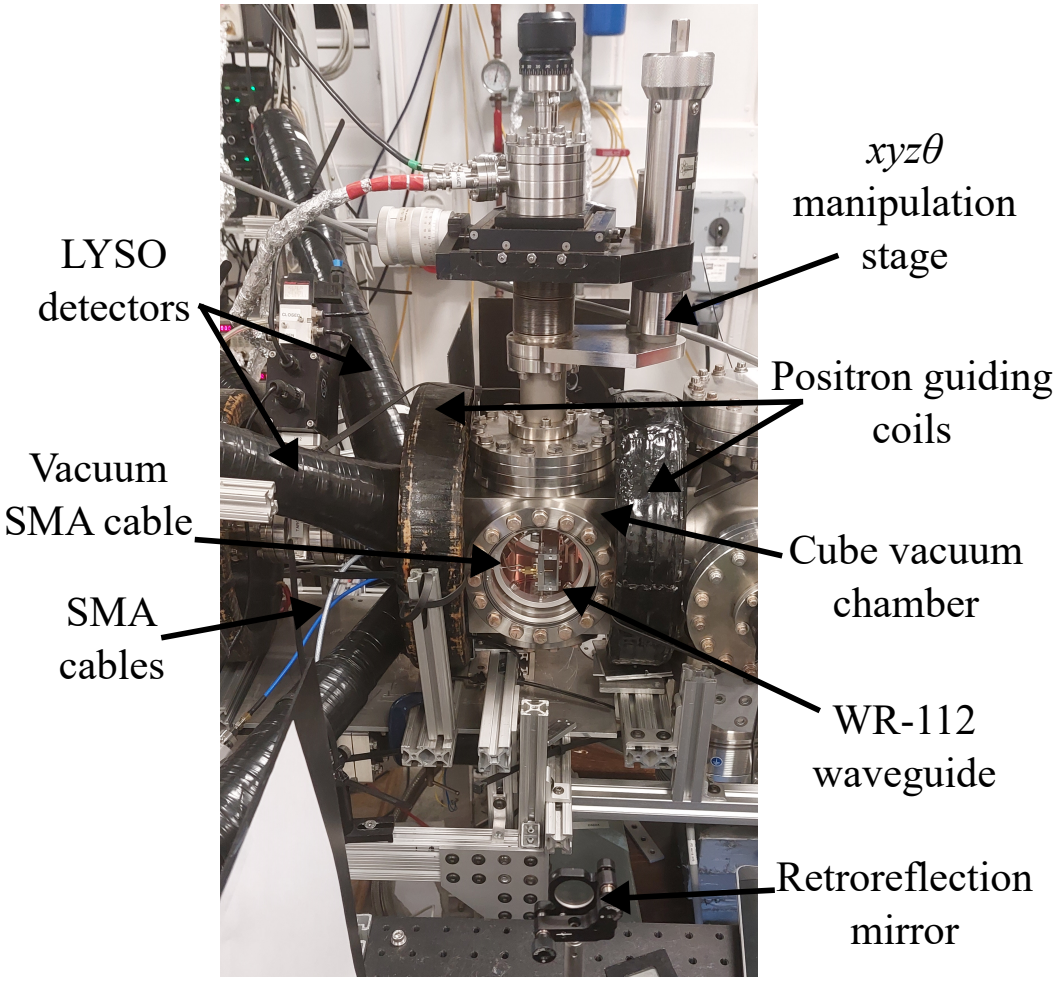

Figure 7.2: An annotated photograph of the waveguide in situ in the Cube chamber without the microwave absorbing foam. The black cylinders on the left are LYSO detectors, the mirror in the foreground is the retro-reflection mirror, and the black coils apply the magnetic field.

to minimise systematic effects, details of which will be described below.

7.1 Experimental Setup & Methodology

The positron beam, as described in Section 3.1, produced 3 mm, ∼3.6 ns FWHM positron pulses which were implanted into a mesoporous silica target E_T at $V_T = -3.5$ kV to create ∼50 meV ground state Ps, see Section 3.4 for details. To control the field within the laser excitation region (LER) a grounded grid electrode E_G was placed $d_{TG} = 8$ mm from the target with the 16 mm diameter hole allowing positron and Ps transmission through a 95 % transmission tungsten mesh, see Figure 3.14.

The Ps underwent laser excitation in the laser excitation region (LER) using a

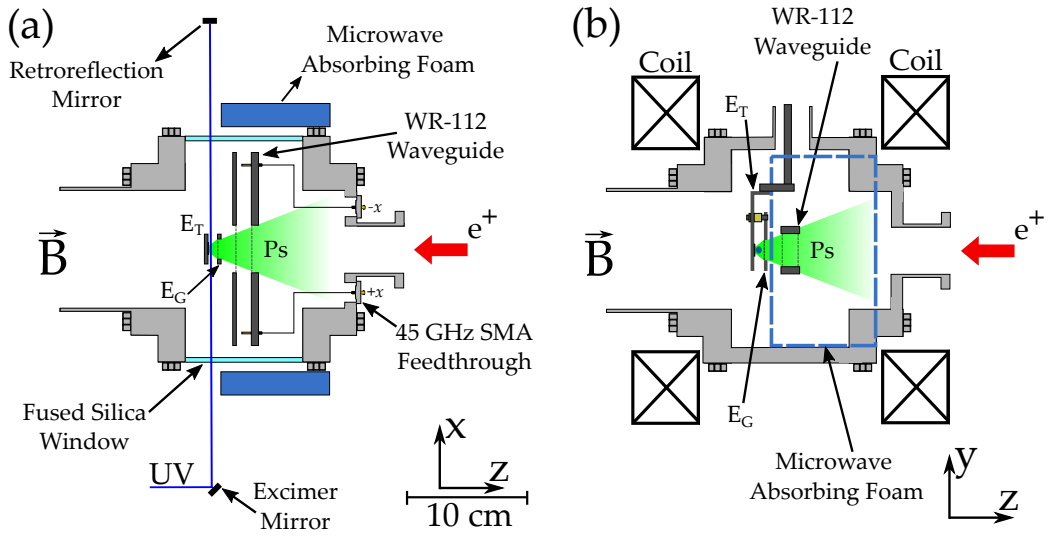

Figure 7.3: Schematic representation of the target chamber and waveguide in (a) the *xz*-plane and (b) the *yz*-plane. Ps atoms (green shading) are produced by positron beam (red arrow) implanted into a SiO_2 target (yellow). The chamber is shown in light grey, dark grey represents Al electrodes and the WG, Au antenna are in yellow. Light blue shows the UV vacuum windows, blue shows the microwave absorbing foam, and dark blue is the UV laser. (b) also shows the position of the magnetic coils which are not shown in (a) for clarity. Adapted from Reference [244].

UV laser of 243 nm at $t_{\text{lsr}} = t_{\text{opt.}}$ (see Section 3.5) in a field of $F_{\text{TG}} = 4.4$ kV/cm. This created the Stark mixed $2^3S_1'$ state which was evolved into pure 2^3S_1 by adiabatically switching the target electrode to 0 V after positron implantation within $t_{rise} = 35$ ns to remove the electric field, the full process of which is described in Section 3.8. The IR laser was present in this experiment for obtaining photoionisation signals, described in Section 3.6.

Retro reflection of the UV laser was implemented to minimise Doppler shifts, as discussed in Section 3.5. The retro-reflected beam ensured that any Doppler selection of the laser was equal and opposite, resulting in a net velocity of 0 km/s along the axis of the laser. If E_T, the laser and the waveguide are not perfectly aligned to one another (i.e. the laser or microwaves are not propagating in the *x*-axis in the atom frame of reference) then a subset of atoms with an asymmetric velocity distribution will be selected. This can cause a Doppler shift, with the full process discussed in Section 4.1.

After excitation the metastable Ps flew through E_G where a WR-112 waveg-

uide was mounted 12 mm from E_G (see Figure 7.3, or Figure 3.14 for a close up). Ps entered the waveguide through 90% tungsten (W) grids which was subject to deformations of $\sim \pm 1$ mm. Electric fields can leak through grids [183,230] and although E_T is turned off > 150 ns before any atoms reach the waveguide the rapid switching of E_T causes ringing in the output voltage of the switch, due to capacitance and impedance mismatches in the system, see Figure 3.27. The fast Ps sees any time varying leaked potential from E_T as a spatially varying electric field. Therefore, to minimise this field E_G was added as the larger the number of grids the larger the attenuation of the field leakage [230], in the previous experiment the waveguide itself was used as the grounding plane for the LER [131].

The $2\,^3S_1 \rightarrow 2\,^3P_2$ transition was driven inside the WR-112 waveguide using a microwave setup specified in Section 3.9. An image of the waveguide is shown in Figure 7.4. The magnetic field induced by the positron guiding coils inside the waveguide was measured as described in Section 3.1.3, varying by ± 0.5 G within the small volume occupied by the Ps. The microwaves were applied by two stub (monopole) antennas, designated as the $+x$ direction (antenna on the UV laser input side) and the $-x$ direction (the antenna on the IR laser input side), in reference to the direction of travel of the TE_{10} mode. Only one antenna at a time was used as a microwave input so the unused antenna was connected to a Keysight U8487A/N1913A power sensor/meter combination to allow monitoring of the microwave radiation during the experiment.

Power leveling was done for each antenna to compensate for losses in the SMA cables and vacuum feedthroughs, this was done for all components up to the last connection before the antenna (see Section 3.9). As a result of this the power going into the antenna P_{input} had variations of < 0.1 dBm which corresponds to a 2.3% uniformity in power. A correction was also applied to account for the waveguide specific power/intensity relation, see Equation 3.6.

The waveguide was open ended, with UV-coated fused quartz vacuum windows < 10 mm from either end, see Figure 7.3. Simulations have shown that reflection effects from these windows are much lower than a full metal chamber, see

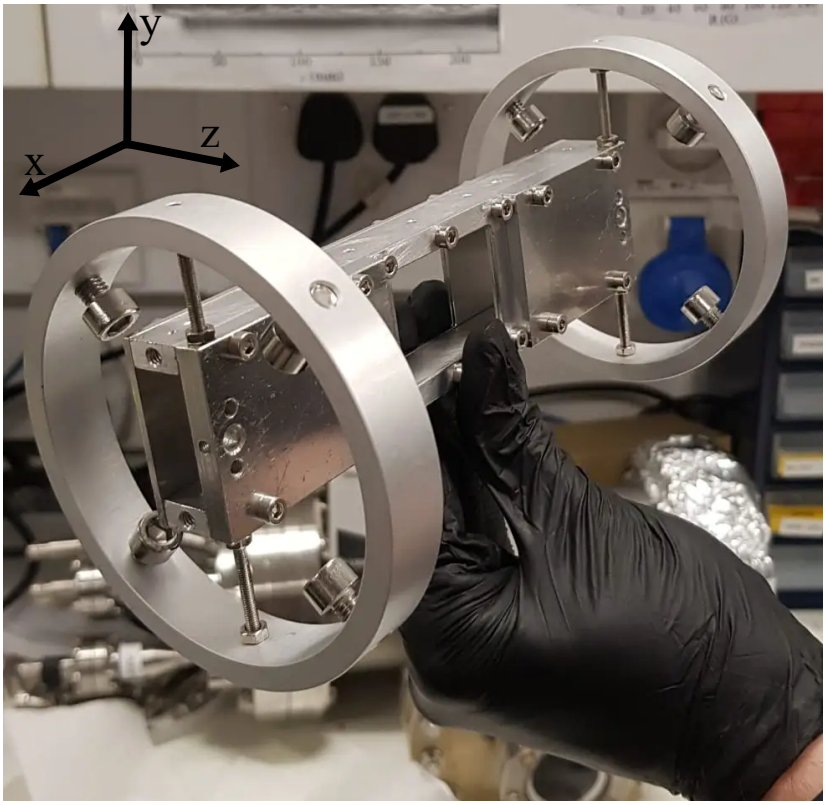

Figure 7.4: A photograph of the waveguide and mounting mechanism before installation into the chamber, and before mounting of the antenna and tungsten grid.

Figure 7.1. For most measurements there was >30 cm of free space outside each window to diffuse the microwaves without reflections. As an alternative method used to confirm the lack of reflections, during some measurements microwave absorbing foam (Eccosorb-AN-75 [172]) was used to prevent reflections outside the vacuum chamber by placing two pads against each window, slightly offset in the z-axis to allow lasers to enter the chamber, see Figure 7.3. This foam had a nominal reflectivity of -25 dB in the range 8 - 9 GHz.

Four LYSO scintillation detectors as described in Section 3.2, were used in this experiment to obtain SSPALS spectra to quantify the transfer of atoms from the long lived 2S state to the shot lived 2P state, see Sections 3.6 & 3.9. The position of these detectors was optimised for maximum SNR of the microwave induced signal (see Figure 7.2).

Figure 7.5 shows saturation curves for the waveguide setup, both at $B_z = 68$ G and $\nu = 8\,626.71$ MHz. The $-x$ data was recorded with microwave absorbing foam

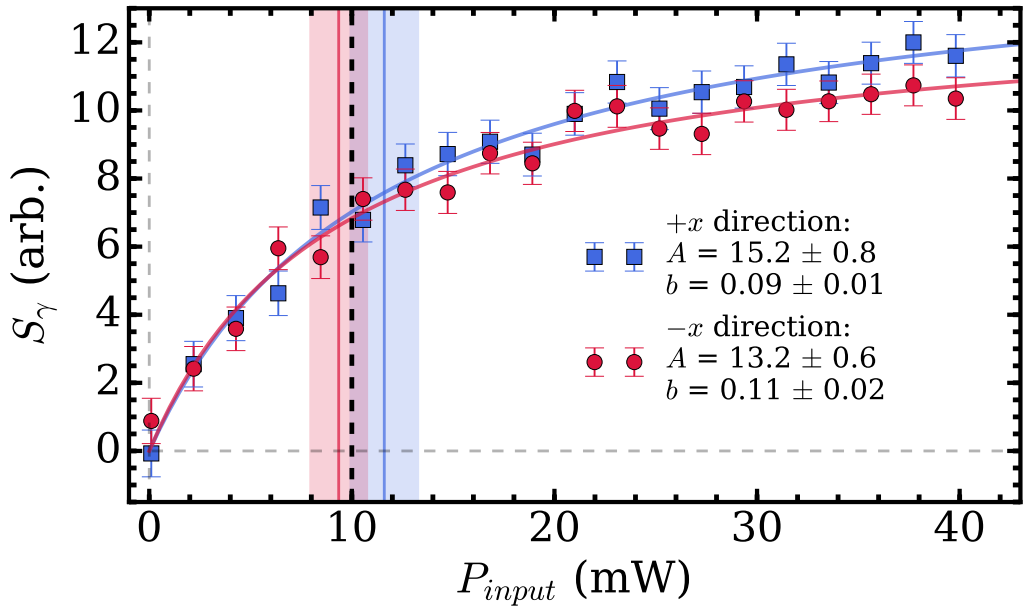

Figure 7.5: The saturation curve of the ν_2 transition within the WR-112 waveguide as a function of P_{input} as measured by one LYSO detector. $-x$ (no foam) shown as red circles and $+x$ (foam) shown as blue squares, both recorded at $B_z =$ 68 G and $\nu = 8626.71$ MHz. The solid curves are fits of Equation 2.25 to the data, the solid vertical lines show the extracted saturation powers, and the shaded bands represent the respective error. The dashed vertical line is the experimental power $P_{\text{input}} = 10$ mW.

present, and the $+x$ data was recorded without the foam due to the randomised order of the measurements. The presence of the foam is not expected to change the saturation parameters as the foam should not significantly change the power in the waveguide[1]. The saturation power of the ν_2 transition for each antenna was determined by fitting Equation 2.25 to these data sets, obtaining saturation powers of $P_{sat} > 11.6 \pm 0.9$ mW from the $-x$ direction antenna and 11.1 ± 0.8 mW from the $+x$ direction antenna. These values are in agreement and indicate that there is no major difference in transmitted power between the antennas. The power applied for line shape measurements was $P_{\text{input}} = 10$ mW which is $\approx P_{sat}$ to ensure reasonable SNR but minimise power broadening.

Line shapes were recorded by measuring the S_γ parameter as a function of ap-

[1]This will be demonstrated by the network analyser measurements below. The saturation measurements were also experimentally verified to be insensitive to the microwave frequency at which the saturation scan was performed, reproducing saturation powers within error, meaning the Zeeman shift at this field will not effect b.

plied microwave frequency to observe the stimulated emission of 2S atoms to the 2P level as described in Section 3.9 and expanded upon in Appendix A. An example line shape is shown in Figure 7.6 with an inset showing the transitions driven whereby $\delta M_J = 0$ within the TE_{10} mode of the WR-112. The line shapes were fitted with a Lorentzian to extract centroids ν_R and line widths Γ values (Equation 2.21).

All line shape measurements were repeated for each antenna. Measuring each line shape from opposite directions removes any systematic Doppler shift. Most line shapes were recorded without microwave absorbing foam present, but a subset of the line shape measurements were repeated with the microwave absorbing foam to ascertain its effect. If a significant change to the transition frequency was observed by adding the foam then it would indicate that reflection effects had not been entirely removed from the system.

Because of the unavoidable magnetic field of the positron beamline the transition frequency, ν_R, was measured in multiple magnetic fields from 40 - 125 G and extrapolated back to zero-field using a quadratic fit. B_z was controlled by changing the current of the positron guiding coils which necessitated small alignment corrections to the positron beam upon changing the current. This will not effect the line shape measurements because the S_γ parameter is self normalising to any population changes which result from small changes in the positron beam alignment and size, or detection efficiency variation from changes within the photo-multiplier tube which can be sensitive to magnetic fields though the light guides minimise this effect also. The measured order of B_z was randomised to minimise any possible systematic effects.

It is important to understand the broadening mechanisms present in experiment because excessive broadening can reduce precision and change the required line shape model (see Section 2.4). The limiting factor is of course the 50 MHz natural line width of the transition. All relevant broadening mechanisms and their estimated magnitudes are included in Table 7.1. The average width of the transition was $\Gamma = 73.0 \pm 0.4$ MHz, averaged across all measured line shapes. As with the previous study [132] no significant variation in Γ was observed as a function of

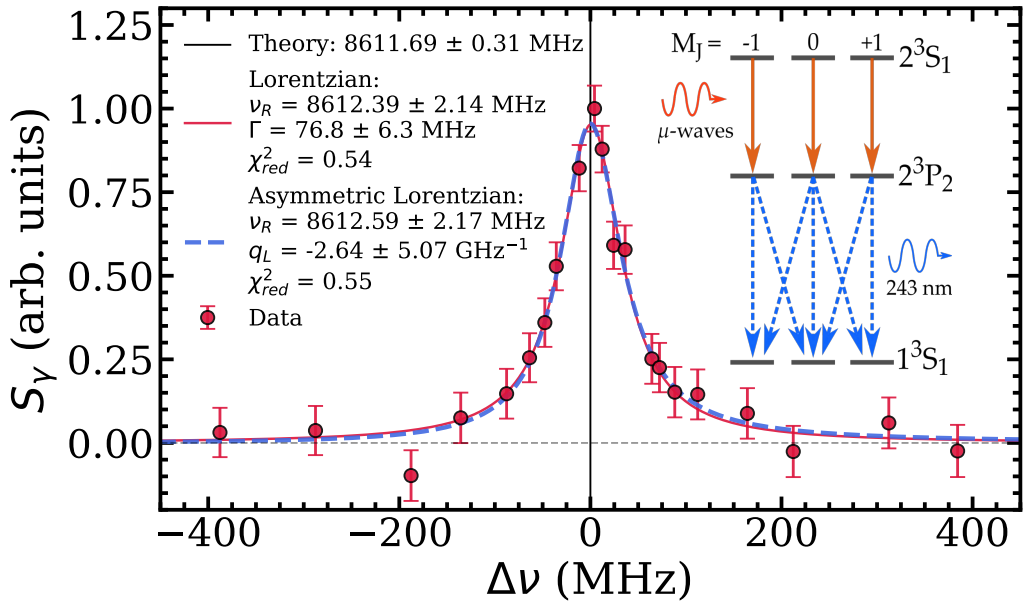

Figure 7.6: An example line shape measured during this experiment for $B_z = 97$ G in the $-x$ direction, without microwave foam (red points). The line shape is fitted with a Lorentzian (solid red), and asymmetric Lorentzian (dashed blue) fit. The inset shows the transitions being driven by the microwaves (solid arrows) and the subsequent fluorescence decay pathways to the ground state from the 2P state (dashed arrows). Adapted from Reference [244].

magnetic field. This indicates that we are not sensitive to the small Zeeman splitting of the $2^3S_1(\pm1) \rightarrow 2^3P_2(\pm1)$ and $2^3S_1(0) \rightarrow 2^3P_2(0)$ transitions (as discussed in Section 2.3), and that the average calculated Zeeman shift is a valid comparison to experiment. The presence of microwave absorbing foam and the direction of microwave propagation also showed no effect on the measured line width.

$\sim$7.5 MHz of this broadening is calculated to be transit-time broadening, as de-

Broadening Mechanism	**Estimated Magnitude (MHz)**
Natural	50
Power	15
Transit Time	7.5
Doppler	0.5
Measured	73.0 ± 0.4

Table 7.1: The sources and estimated magnitudes of line shape broadening in the measured line width of the ν_2 transition as explained in the text.

scribed in Section 2.4. This is based on the average transit velocity $\langle v_z \rangle = 94$ km/s as extracted from ToF data in Figure 4.2 [229], and the width of the WR-112 waveguide, $d = 12.6$ mm. Doppler broadening is minimal, due to the UV laser pre-selecting slower atoms in the x-axis during excitation, and is estimated at only $\sim$0.5 MHz based on Equation 2.27. The remaining broadening of $\sim$15 MHz is therefore attributed to power broadening due to the high degree of saturation required for a statistical error that allows measurements of the line shapes within a reasonable time frame (typically less than a week). This is consistent with previous measurements and the relation calculated in Reference [15] of $\Gamma_{power} = 6.6$ MHz/mW which for $P_{input} = 10$ mW would be 16 MHz.

A vector network analyser (Agilent N5224A) was used to measure the S-parameters [226] of the microwave circuit. This was connected to the microwave circuit at the points shown by the green dots in Figure 3.29(b), measuring the entire circuit, both inside and outside vacuum. The S-parameters measure the reflectivity (e.g. S_{11}) and transmission (e.g. S_{12}) between two rf sources in a system, in this case the two antenna at either end of the WR-112 with 1 being the $-x$ antenna and 2 being the $+x$ antenna. The voltage standing wave ratio (VSWR)[2] is calculated from the S_{11} parameters by the relation [226],

$$\text{VSWR} = \frac{1 + |S_{11}|}{1 - |S_{11}|}, \tag{7.1}$$

and is proportional to the microwave power reflected back to the source (and not emitted from the antenna). Figure 7.7(a) shows the S-parameters for transmission, and (b) shows the VSWR for reflection, with both examining the effect of the microwave absorbing foam. In addition (b) shows the difference between the Cube chamber used in this work and the Cross used previously [131].

The transmission data in Figure 7.7(a) shows a close match between the power transmitted from either antenna, with or without foam, varying by $< 0.2\%$ on average (only one data set is shown with foam for clarity). This demonstrates that the

[2]VSWR is defined as the ratio between the maximum and minimum voltage of the signal in a microwave circuit assuming constant input power and frequency. This will be determined by the standing waves formed from reflections in the system.

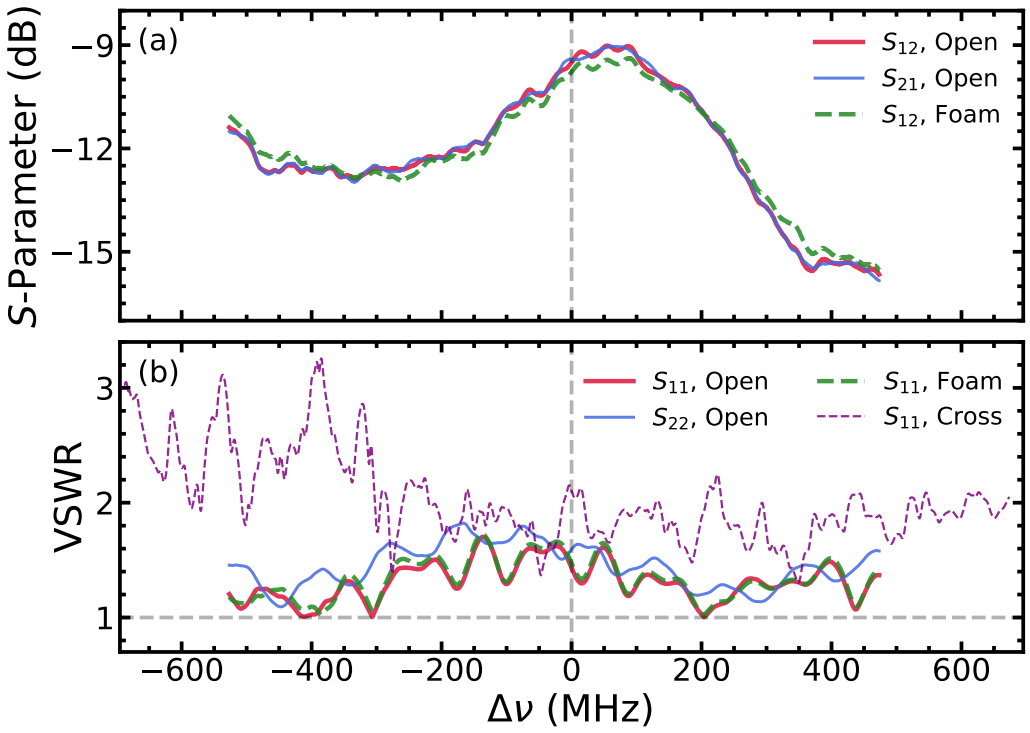

Figure 7.7: (a) The transmission data measured by the network analyser S_{12} (solid read is without foam and dashed green in with foam) and S_{21} (solid blue). (b) The VSWR for the open Cube chamber (solid red), foam sided Cube chamber (dashed green), and the old Cross chamber (thin dashed purple). And the S_{22} for the open Cube case (solid blue). The dashed vertical line at $\Delta\nu = 0$ MHz is the zero field ν_2^{calc} transition frequency.

direction of the microwaves does not significantly change the transmission between antennas. Power loss in the cables was $< 15\%$, as verified using the power meter during loss compensation, but the transmission measured here was $< 10\%$. This loss of power between the antennas is likely due to the unknown pickup properties of the antenna, and therefore this measurement cannot be considered as the real power variation within the waveguide, but it does indicate that there is no significant difference in the power transmitted for each direction of the microwave radiation. This does not rule out differences in the field distribution within the waveguide.

The reflection data in Figure 7.7(b) is shown with open windows (solid) and the microwave absorbing foam (dashed). A VSWR of one would indicate 0% reflection with a larger value corresponding to more reflection. The two antenna do have different reflection properties, with 1.7% and 2.8% reflection on average for the $-x$

and $+x$ antenna. But the reflection varies from $\sim 0\%$ to 8% for both antennas. This is small compared to the $1-27\%$ reflection of the Cross chamber indicating that the previous experiment was highly affected by frequency dependent power. The foam has a negligible effect on reflections, with the average reflection 0.3% higher with the foam present, indicating that variation in the VSWR in the current data is not from reflection effects. There is no way to differentiate between VSWR variation due to impedance mismatching of the microwave circuit, and due to external reflections. This is because the pick up of the antenna will change the measured magnitude of the external reflected component (as seen in Figure 7.7(a)). Unfortunately this means that the VSWR measurements cannot be used to compensate for frequency dependent power, as the power in the waveguide due to reflections may be very different from the pickup response of the antenna.

7.2 Simulations

3-D Simulations of the microwave field were performed to demonstrate the effectiveness of the new chamber in removing reflection effects, as mentioned in the introduction to this chapter, and to explore the effect of construction defects in the waveguide. These simulations were then used to model the $2\,^3S_1 \rightarrow 2\,^3P_2$ transfer rate to confirm the effect of microwave fields outside the waveguide.

7.2.1 Microwave FIT Simulations

Once again CST was used to obtain maps of the electric field component of the microwave radiation in the experimental volume to understand the fields better. The methods for this are described in Section 4.3. This simulation consisted of the Cube chamber, WR-112 waveguide, target, grid, ring mounts, windows and immediately adjacent vacuum flanges, all assigned appropriate properties from the CST materials library. The tungsten grids on the WR-112 and E_G are approximated as a tungsten sheet 100 micron thick due to computational limitations of simulating a true grid of $r = 10$ micron diameter wires, $d = 500$ micron apart. A simulation of a waveguide with an approximated grid of $r = 100$ micron wires $d = 1$ mm apart without the surrounding electrodes and chamber showed negligible microwave leakage through

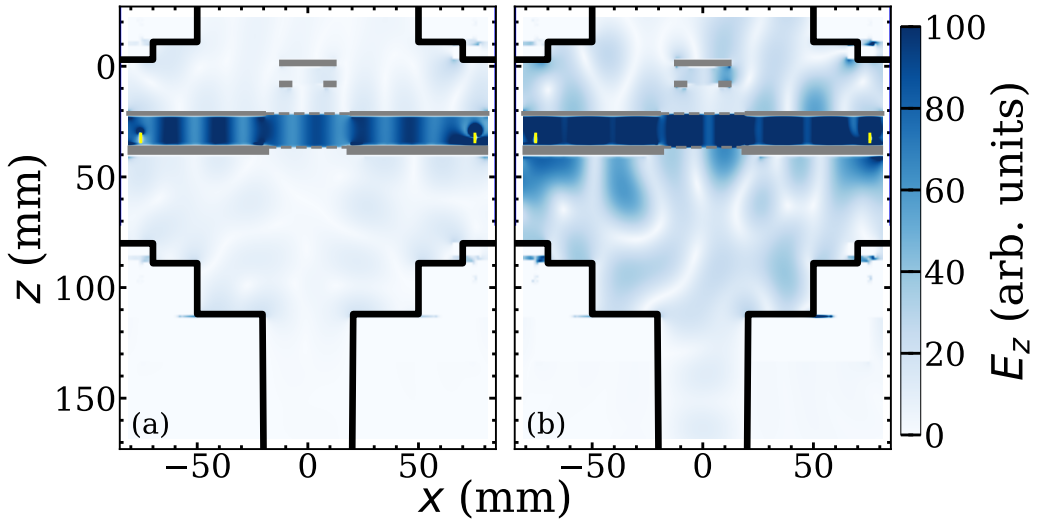

Figure 7.8: A 2D plot of the simulated E_z component of the steady-state microwave field at $\nu = 8\,624$ MHz. (a) The experimental chamber as used to take lines shape measurements. (b) The experimental chamber with the addition of copper plates against the windows of the chamber. The steel chamber is outline in black, the waveguide and electrodes are shown in grey, and the gold antenna are shown in yellow.

the grid.

Figure 7.8(a) shows the steady-state high intensity radiation within the waveguide. Small amounts of leakage out of the sides and through the windows resulted in a field an order of magnitude lower outside the guide compared to inside, and a standing wave inside the waveguide. In addition to the experimental replica two other cases were simulated: (1) the experimental setup with a Cu sheet against the windows on both sides of the chamber to imitate the old Cross chamber, and (2) the experimental setup with the first waveguide grid warped ~ 1 mm inwards at the centre to replicate grid deformation present in experiment. The warped grid does not create any significant change in the microwave field, but the Cu plate increases the magnitude of the reflections in the chamber and inside the waveguide forming a pseudo-cavity, see Figure 7.8(b).

The field strength of the standing wave versus frequency has already been shown in Figure 7.1, demonstrating the much improved power variation of the Cube chamber. Figure 7.9 shows the simulated electric field strength along the waveguide central axis for the cases just described. The intensity of the microwaves inside the

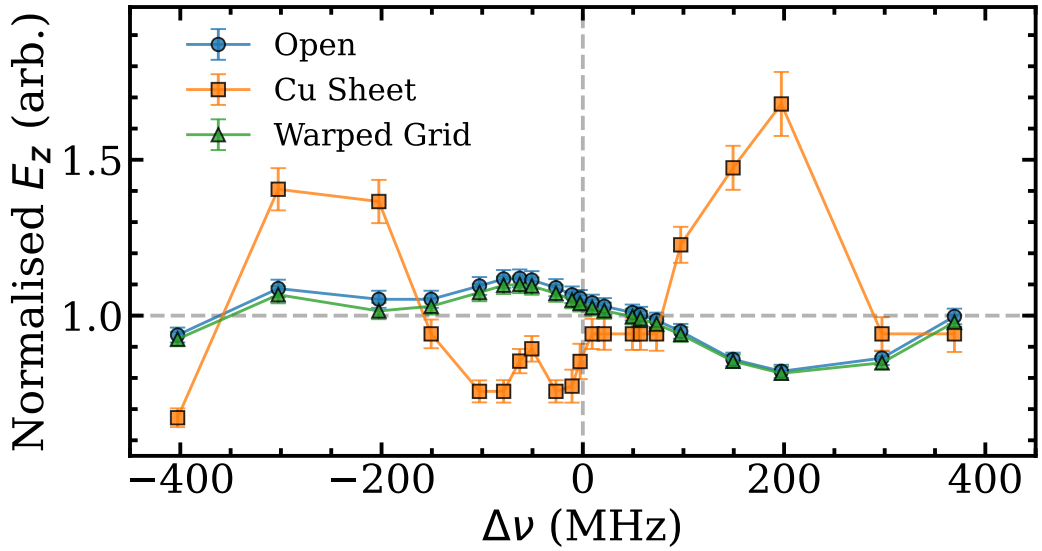

Figure 7.9: A comparison of the simulated microwave electric field strength of the microwaves in the WR-112 for the experimental chamber (blue circles), the experimental chamber with copper plates on the windows (orange squares), and experimental chamber with warped grids on the waveguide (green triangles).

waveguide was characterised by the electric field amplitude of the TE_{10} mode standing wave taken along centre axis of the waveguide which corresponds to $y = 0$ mm, $z = 28$ mm and $x = -30$ to 30 mm. This range is where the Ps atoms will propagate. The field amplitude is obtained by fitting a function to the electric field along this axis [15],

$$E_{SW}(x) = E_0\sqrt{1 + q_{SW}^2 + 2q_{SW}\cos\left[2k_x(L+x)\right]}, \tag{7.2}$$

where L is the offset of the wave origin, q_{SW} is the amplitude coefficient, $k_x = \sqrt{\frac{\omega^2}{c^2} - \frac{\pi^2}{a^2}}$ is the wave vector of the rf field in which ω is the angular frequency of the applied rf radiation, and $a = 28.50$ mm is the height of the waveguide. This is the same method used in Reference [15] to quantify variation in amplitude of the field and to quantify the reflected component of the standing wave.

The Cu sheet makes the Cube setup much more similar to the old Cross chamber with field variation of up to 90%. The small deformation to the grid appears to have minimal impact on E_z, manifesting as a small systematic shift to less than average power. This may be because the cutoff frequency for the effective size of the waveguide at these points is still less than the frequency being used for excitation

with minimal change to the standing wave.

The polarisation of radiation in the WR-112 was calculated as described in Section 4.3 and for all the three cases described above was $> 99.9\%$. As expected the radiation outside the waveguide has effectively randomised polarisation due to it originating from reflections.

7.2.2 State Probability Simulations

State probability simulations as described in Section 4.4 were performed for the simulated electric fields described above to determine where the microwave transitions were taking place. Initial atomic distributions were defined by the positron beam spot size mentioned above, and for v_x by a 100 GHz UV bandwidth, v_y by a $\Delta\lambda = 0.078 \pm 0.001$ nm Doppler width, and v_z by $t_{\text{lsr}} = t_{\text{opt.}}$ ToF data, see Section 4.1 for details. These initial distributions were used to propagate Ps atoms through a model of the experimental setup and the simulated microwave fields described in the section above. From this the microwave field was obtained as a function of time, $E_z(t)$. This data was used as the input for the *qutip.mesolve()* master equation solver which returned the state probability density over time, with decay rates and interactions as described in Equations 4.5 & 4.4. Note the Doppler selection effects considered in Section 4.1.1 were not included and the target, laser and waveguide were considered to be perfectly aligned.

The magnetic field was chosen to match that used in the line shape measurement shown in Figure 7.6 which was $B = 97$ G. This gives a transition frequency of $\nu_{\text{Zeeman}} = 8\,611.69$ MHz and a self-annihilation lifetime of $\tau_{\text{SA}} = 1090$ ns. The simulation was only performed for one antenna direction as the simulation was symmetric in the zy-plane due to practical constraints on replicating the experimental apparatus to that level of accuracy.

The power scaling of the simulated electric field strength was chosen by matching the average line width of all the collected data, 73 MHz, to a simulated line shape of 500 atoms as described in Section 4.4. The resultant power scaling produces the field shown in Figure 7.10(a) for a single atom travelling along the $x = y = 0$ axis at a typical atomic velocity of $v_z = 87$ km/s through the experimental setup. The am-

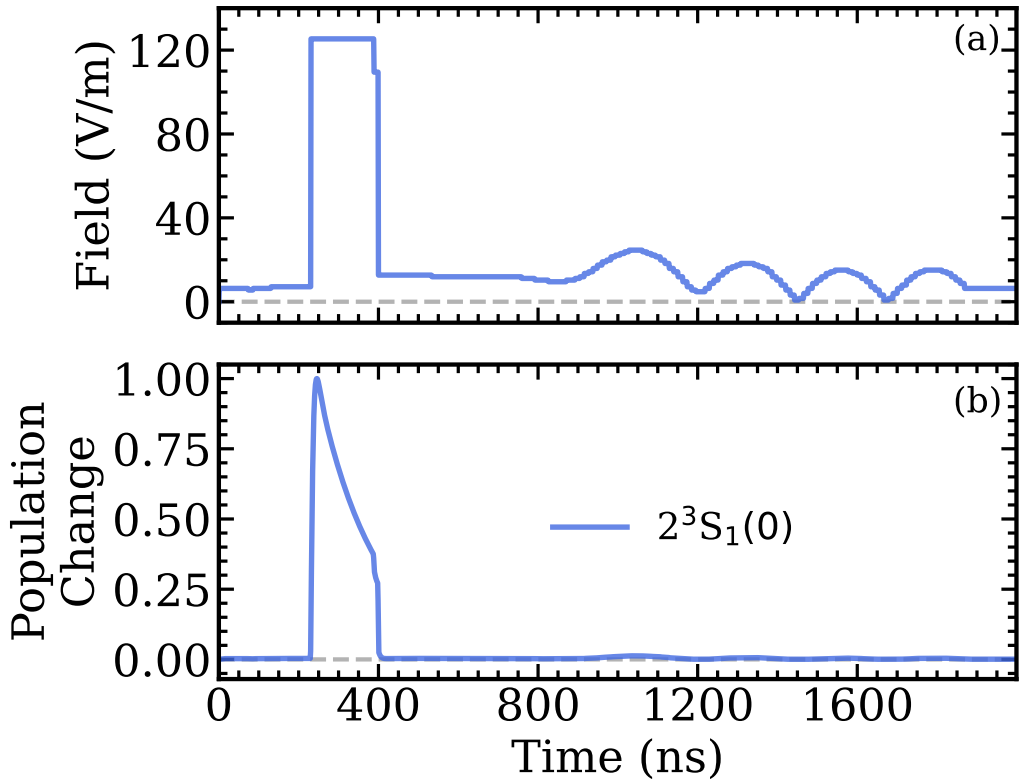

Figure 7.10: (a) The simulated microwave electric field E_z as a function of time as experienced by one atom travelling along the $x = y = 0$ axis at $v_z = 87$ km/s. (b) The simulated normalised rate of change in the 2S population due to stimulated emission based on the microwave field strength given in (a).

plitude of this field is consistent with 10 mW of power confined within a WR-112 waveguide. Panel (b) displays the normalised rate of change in the 2S population due to stimulated emission as a function of time, note the self-annihilation of the 2S state was not included to better illustrate the effect of microwaves outside the waveguide. While the microwave field is on average 11× higher inside the waveguide there is a small contribution to the loss by stimulated emission outside the waveguide. However, the rate of stimulated emission of the 2S state population is 164× higher inside the waveguide compared to outside the waveguide indicating this effect is negligible.

7.3 Data and Discussion

The fitted average Lorentzian centroid ν_R of line shape measurements is shown in Figure 7.11 as a function of B_z for both microwave propagation directions, and

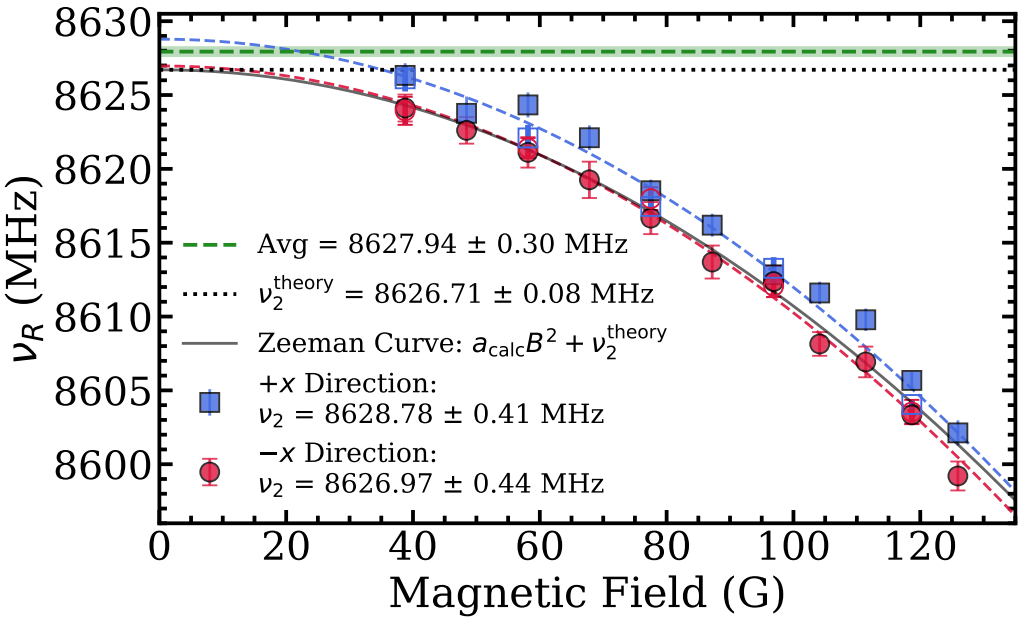

Figure 7.11: The ν_R transition frequency measured for different magnetic fields. The blue squares represent microwave propagation in the $+x$ direction and the red circles in the $-x$ direction. Open points were obtained with microwave absorbing foam on the windows. The solid and dashed gray lines are the calculated Zeeman shift and zero-field frequencies, respectively. The dashed (red and blue) curves are fits to the data ($\chi^2_{red} = 2.18$ and 0.62, respectively). The dashed green line is the average of the ν_2 values. From Reference [244].

with and without microwave absorbing foam present. As well as the statistical error on the ν_R values an error of ± 1 G on each value of B_z is included in the fits (with negligible effect). This error is from magnetic field variation within the Ps interaction volume of the WR-112 waveguide and equipment precision, as measured by the method described in Section 3.1.3. The quadratic fit made to the data was of the form $\nu_R = aB^2 + c$, where the value of c is the zero-field ν_2 frequency, a is a constant, and the magnetic field B was low enough to ignore the linear regime of the Zeeman shift [174].

In Figure 7.11 the solid points represent measurements without microwave foam present, and the hollow points represent measurements with the microwave absorbing foam present and the fits are single fits to the combined foam and no-foam data sets to extract the most precise ν_2 value (one for each direction). However, values obtained from separate quadratic fits to the foam and no foam data (denoted as [F] in the table) are shown in Table 7.2. Also presented in the table are

	$+x$	$-x$
q_L (GHz^{-1})	-4.5 $\pm$ 0.7	-2.2 $\pm$ 0.7
q_L [F] (GHz^{-1})	-6.7 $\pm$ 0.7	-2.7 $\pm$ 0.9
a (kHz/G^2)	-1.65 $\pm$ 0.06	-1.67 $\pm$ 0.06
a [F] (kHz/G^2)	-1.71 $\pm$ 0.07	-1.63 $\pm$ 0.09
ν_2 (MHz)	8628.97 $\pm$ 0.53	8626.77 $\pm$ 0.59
ν_2^{A} (MHz)	8629.15 $\pm$ 0.55	8626.81 $\pm$ 0.61
ν_2 [F] (MHz)	8628.29 $\pm$ 0.66	8627.03 $\pm$ 0.69
ν_2^{A} [F] (MHz)	8628.63 $\pm$ 0.70	8627.26 $\pm$ 0.71

Table 7.2: A summary of the quadratic fit parameters for both microwave propagation directions, with and without foam (entries with [F] are with foam), and for the Asymmetric Lorentz fit denoted by a superscript A. From Reference [244].

the results of quadratic fits to centroid values from asymmetric Lorentzian fits ν_R^{A} with the associated average asymmetry values q_L .

The quadratic fit parameters from the foam data match the no-foam data, with the exception of one asymmetry value for the $+x$ direction. The asymmetry values are the average asymmetry of all asymmetric Lorentzian fits to each detector for all the line shapes in that particular data set[3]. Across all data the asymmetry is -4.2 ± 0.4 GHz^{-1}, much better than the previous results which had $q_L = 23.2 \pm 0.5$ GHz^{-1} [132], though not as good as the horn measurements of the previous chapter. Despite the non-zero asymmetry the quadratic fits agree whether performed on Lorentzian or asymmetric Lorentzian data, indicating the effect of the small asymmetry has a negligible effect on the data at the current level of precision based on these two models.

Fitting the asymmetric Lorentz data for both foam and no-foam data sets combined yields an average zero-field transition frequency of $\nu_2^A = 8628.12 \pm 0.31$ MHz for the two propagation directions, which is just 0.14 MHz from the classical Lorentz fit, well within error. Given the minimal asymmetry and the fact that the zero-field transition frequencies with and without foam are in agreement it appears that we have successfully removed reflection effects as a systematic in this new

[3] As with the measured line widths, q_L displays no dependence on the magnetic field, indicating a lack of sensitivity to the small Zeeman splitting in the driven transitions.

measurement, overcoming a previously large and dominant effect.

Averaging the fitted ν_2 values between the two microwave directions gives $\nu_2 = 8\,627.87 \pm 0.27$ MHz as seen in Figure 7.11, including only statistical error. It should be noted a single quadratic fit to all data averaged at each magnetic field (i.e. foam/no-foam and $+x/-x$) returns the same answer within errors but does not account for additional variation between the two microwave propagation directions so the average of the two directions is used as the final measured value. Indeed there is clear variation between the microwave propagation directions. The ν_2^{+x} and ν_2^{-x} values differ by 1.8 MHz. To understand this better the systematic errors have to be evaluated and will be described here.

7.3.1 Error Budget

At the current experimental precision several systematics must be accounted for. These are summarised in Table 7.3 and important systematics are discussed further below. Some systematics are very small, such as the second-order relativistic Doppler effect which is calculated by $\Delta\nu = \nu_2(v_z^{rms}/2c)^2$, providing a shift of just 0.2 kHz for the average atom of $v_z^{rms} = 94$ km/s. Another small contribution is from rf high harmonics from the generator which can contribute up to 2 kHz in a worst case scenario [15].[4]

Systematic	**Magnitude (kHz)**
Stray Electric Fields	+1.8
ac Stark	+10
Quantum Interference	30
rf High Harmonics	2
Second Order Doppler	0.2

Table 7.3: The sources and magnitudes of the uncertainty in the measured value of ν_2.

[4]Other systematics found in precision measurements are not considered here, such as pressure shifts from atom-atom interactions which is is not relevant due to the low density of the Ps atoms of $< 10^5$ cm^{-1} [59], or the frequency reference which is sub-Hz, far below our other limiting systematics. Likewise gravitational red shift would only be 6 Hz if the waveguide was vertical but the two antenna would cancel this out. Electric quadrupole and magnetic dipole transitions have much lower transition strengths than the electric dipole, and are forbidden by selection rules for the ν_2 transition, and can therefore be ignored.

Residual Fields & Stark Effects: Time dependent electric fields will be present in the waveguide due to ringing in the bias applied to the target electrode when it is switched off during 2^3S_1 production, as discussed in Section 3.8.1. For an average Ps atom of $v_z = 94$ km/s and a ringing with a period of 150 ns this translates into a maximum spatial field of $F_{ring} = 0.03$ V/m, see Figure 7.12(a), as per the data recorded in Figure 3.27. Without the extra grid in E_G this would have been 2.4 V/cm which is much more significant than any other source of electric field that will be discussed here.

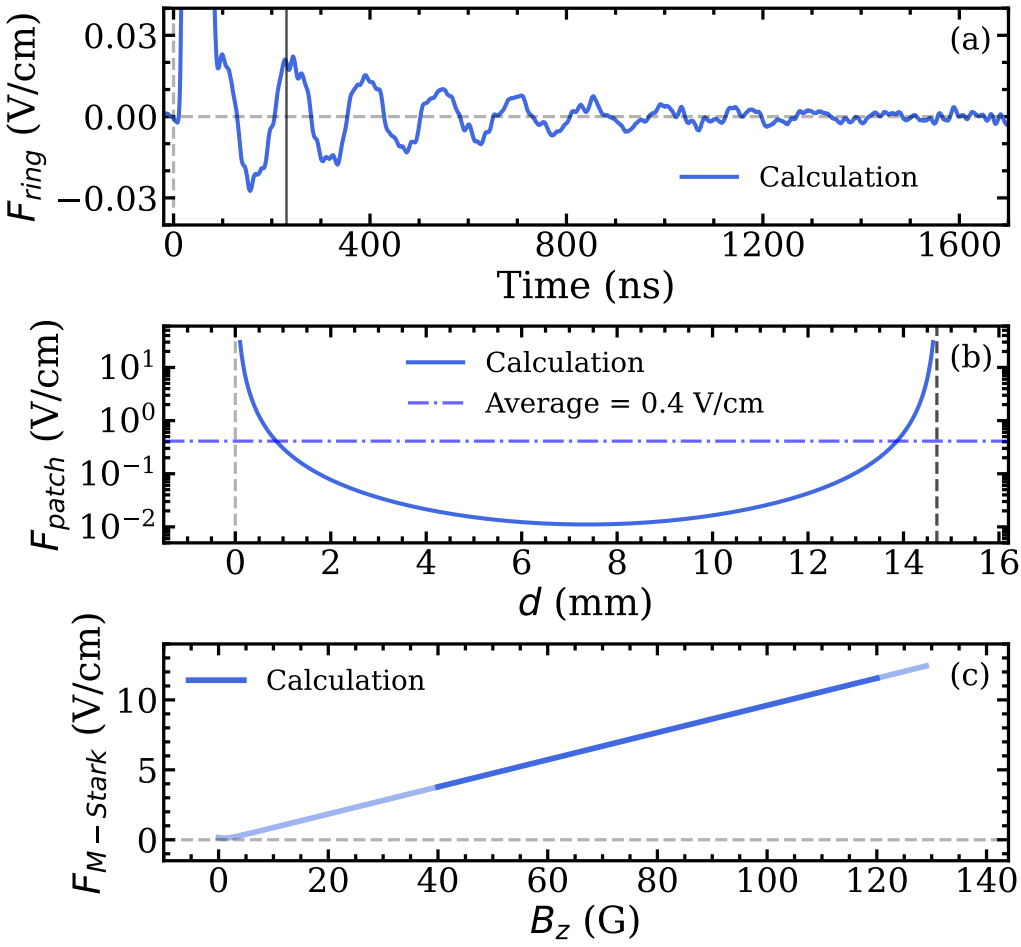

Figure 7.12: (a) The electric field F_{ring} due to the ringing on the target electrode when switching from high voltage. The solid vertical line is the time at which Ps atoms begin entering the waveguide. (b) Patch fields F_{patch} (solid blue line) as a function of distance through the waveguide from grid to grid, which are indicated by the dashed vertical lines. The dot-dashed horizontal line is the average field across the whole guide. (c) Motional Stark fields $F_{M-Stark}$ as a function of B_z. The dark blue part of the line is the experimental range of fields where the trend is linear.

Patch potentials can exist on the Al and W surfaces of the waveguide, despite the waveguide being grounded (e.g. [88, 139]). Based on measurements that used highly field sensitive Rydberg atoms [56, 147] the worst-case stray fields are estimated to be $F_{patch} = 3 \times 10^{-5}/d^2$ V/m based on the maximum size of surface defects, where d is the distance from the waveguide surface, see Figure 7.12(b). Simulations in Figure 7.10 suggest transitions take place within the entire width of the waveguide so the average field across the 12.6 mm wide waveguide (plus 2 mm from the inset W grid) is therefore 0.4 V/cm. Combining the fields produced by leakage and patch potentials gives a field of 0.43 V/cm which returns a Stark shift of 1.8 kHz.

AC Stark Effects: The electric field component of the microwave radiation can cause ac Stark shifts [94]. The power of $P_{input} = 10$ mW within a WR-112 waveguide gives the amplitude of the E-field component of the microwaves to be $E_z = 1.02$ V/cm which would cause ac Stark shifts of approximately 10 kHz[5]. This is an upper estimate as the power coupled into the waveguide will not be the full input power due to losses from the open end of the waveguide and the unknown antenna gain.

Motional Stark Effects: When an electric dipole passes through a magnetic field transverse to its direction of motion an electric field is induced [81]. This electric field is defined by $\vec{F}_{M-Stark} = \vec{v} \times \vec{B}$ where $\vec{v}$ is the velocity vector and $\vec{B}$ is the magnetic field vector. The motional Stark field comes primarily from the transverse v_y motion across B_z as these are the largest $\vec{v}$ and $\vec{B}$ components possible. The maximum perpendicular field is $B_\perp = 1$ G which causes a < 0.2 V/cm field and can be ignored. $F_{M-Stark}$ is calculated from the rms velocities and the worst case magnetic field of $\vec{v} = (15, 96, 94)$ km/s and $\vec{B} = (1, 1, B_z)$ G, see Figure 7.12(c). This has a linear dependency of 0.1 Vcm^{-1}/G with a range of 3.8 - 11.6 V/cm within experiment which would cause a maximum Stark shit of 1.3 MHz. Because the Stark shift in this regime is linear the final shift will be $\Delta\nu \propto B_z^2$ which means the quadratic fit to the data will extrapolate this systematic back to zero as well as

[5]The field is calculated according to $I = P_{input}/A$ where $A = 28.5 \times 12.62 = 360$ mm^{-2} is the area of the waveguide and $E_z = \sqrt{377I}$

the Zeeman shift.

Quantum Interference: For this kind of experiment it has been established that QI shifts depend on the orientation of the gamma-ray detectors and the weighting of each allowed transition [15]. This is because both the direction of annihilation quanta and the QI are dependent on the M_J state of the atom (and thus the ΔM_J of the microwave transitions) [15], see Equations 2.8. Because the gamma-ray detectors do not cover a full 4π solid angle they will preferentially measure certain decay paths more efficiently, changing the overall effect of QI. The QI will also depend on the level of saturation of the transition [15]. This is related to 'flat-top' line shapes that are produced at high microwave power, as discussed in Section 2.4. This effect compounds QI shifts resulting in larger QI shifts at higher power. A calculation with realistic experimental parameters leads to a shift of less than 30 kHz for a worst case scenario [15]. There is also an associated asymmetry but the degree of this asymmetry is far below the statistical error of this experiment to resolve. As indicated by the possible shifts of 30 kHz in a Lorentzian line shape compared to the >1 MHz error on individual measured line shapes in this work. As we cannot account for this with a full line shape model the QI effect is included as a systematic.

Polarisation Effects: Several possible effects can cause $\Delta M_J = \pm 1$ transitions to be driven within the waveguide or unequal weighting of the $\Delta M_J = 0$ set of transitions, despite the dominance of the TE_{10} mode. (1) Microwave polarisation changes induced by waveguide defects and at the grids can cause shifts, however, polarisation changes at the grids have been modeled and lead to just +3 kHz shifts [15]. (2) Misalignment of the waveguide to the magnetic field would result in some $\Delta M_J = \pm 1$ transitions. This effect has been modelled and could lead to +32 kHz shifts for an exaggerated 10° misalignment [15]. (3) ^{22}Na emits spin polarised positrons which have been estimated to be on the order of 30% for similar positron beams [65]. This will result in unequal weightings of the 2S M_J values upon production but only a 2 kHz shift in the line shape [15].

All these effects are small but given the lack of change in the a parameter of the quadratic fits between the microwave propagation directions and the consis-

tency with theory for purely $\Delta M_J = 0$ transitions these effects are either not present or below our current level of sensitivity. In addition, as long as these effects are consistent across the scanned range of B_z, which they should be, any effect will extrapolate back to the zero-field frequency with no effect at zero field where all transitions are degenerate.

Doppler Shifts: Doppler shifts could result from an asymmetric velocity distribution in the direction of propagation of the microwaves. Recoil Doppler effects[6] and laser wavelength drift are eliminated by retro-reflection of the laser. In this experiment Doppler shifts must originate from misalignment of the Ps, laser and waveguide. Simulations of the velocity distribution and the angular selection effects have already been done in Section 4.1 based on an estimated maximum misalignment of $\pm 6^\circ$. From this we estimate the maximum Doppler shift should be ± 260 kHz, but averaging the two microwave propagation directions should remove this systematic entirely. This, however, raises the question of how there can be a 1.8 MHz difference in the measured transition frequency for the two microwave propagation directions, three times as large as expected.

7.3.2 Final Result

The relevant systematic uncertainties described above provide a conservative systematic uncertainty estimate of 100 kHz. However the 1.8 MHz direction difference is still not explained. Stark effects should not depend on the direction of the antenna, and neither should QI or other line shape model effects. Even the maximum Doppler shift of 260 kHz per propagation direction cannot explain the 1.8 MHz difference between the fits.

The data from the network analyser, see Figure 7.7, has demonstrated power variation from the antenna of $0-8\%$, but the lack of effect of the microwave foam on the measured lineshapes demonstrates this is not due to reflection effects. We are therefore forced to conclude we have an additional systematic due to either (1) internal waveguide effects, or (2) variation in the gain between the two antennas that

[6]Recoil Doppler effects occur during laser excitation whereby the photons give the Ps extra velocity in the direction of propagation of the laser. For 243 nm this is 1.5 km/s per atom based on $v_{\text{recoil}} = h/2m_e\lambda_{\text{UV}}$.

was not corrected for. Either of these effects will behave similar to reflection effects, causing changes in power at different microwave frequencies, once again resulting in an incomplete line shape model. The former effect could cause frequency dependent power variation and spatial variations in the TE_{10} mode, independent of P_{input}. This may result in very different power variation at the antennas compared to the Ps interaction region, making it hard to quantify. The latter effect would cause variation in P_{input}, and could not be differentiated from external reflection effects using the network analyser. Either of these effects could explain the 0 - 8% variation in measured reflection shown in Figure 7.7.

Internal waveguide effect can include standing waves formed at the grids [74], or imperfections in the waveguide construction and impedance matching. Simulations, see Figure 7.9, have demonstrated that distorting the grids axially by 1 mm has a minimal effect on the microwave field amplitude inside the waveguide, but other effects such as low reflectivity surfaces or bad joins between the walls of the waveguide may distort the TE_{10} mode. Any improper impedance matching of the two antenna may cause significant frequency dependent power variation. Power variation was corrected for up to the antenna, and during this work the microwave circuit was decoupled and recoupled to each antenna between the foam and no-foam measurements. Given that the foam and no foam data sets agree the current level of precision would appear to not be sensitive to the level of impedance variation caused by the cables. However, if the antenna drastically changed the impedance of the system it could cause significant power variation.

We take a conservative estimate of this new systematic to be the $1.8/2 = 0.9$ MHz. Thus, our final value is $8\,627.94 \pm 0.30_{\text{stat.}} \pm 0.91_{\text{sys.}}$ MHz which is compared to historical measurements and theory in Figure 7.13. This value is 1.23 MHz (1.3σ) away from theory and is therefore in broad agreement.

To minimise any effect which may cause frequency dependent power several measures can be taken:

- The size of the grids can be reduced and their flatness improved using push fit connectors to hold the mesh taut, similar to E_G, see Figure 3.15.

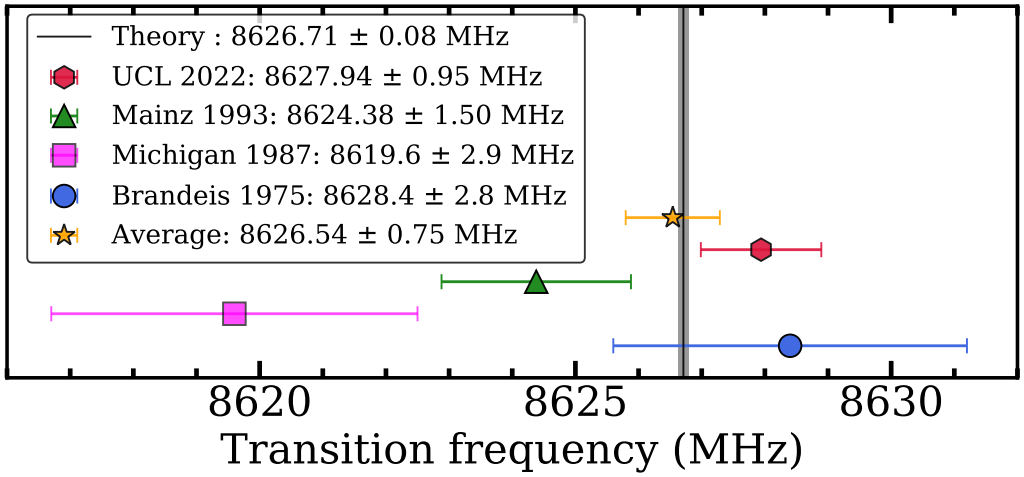

Figure 7.13: All precision measurements of the $2^3S_1 \rightarrow 2^3P_2$ interval over almost 50 years, obtained by by groups from Brandeis [196], Michigan [140], Mainz [134] and the present work (UCL 2022). Where available, systematic and statistical errors have been added in quadrature. The vertical line represents the theory value, taken from [83]. The yellow star represents the weighted average of all current measurements. Adapted from Reference [244].

- The number of joins between the waveguide internal surfaces can be reduced by constructing the waveguide as one part with high precision machining and highly polished surfaces.

- The microwave circuit to each antenna can be impedance matched and fixed in place to minimise the possible frequency dependent power variation between antennas.

- To ensure that external reflection effects are minimised and that there is no impedance mismatch at the end of the waveguide, which once internal effects are resolved may become the dominant systematic error again, in-vacuum waveguide terminators can be designed using CST and in situ measurements with the vector network analyser.

In addition to these measures, the $2^3S_1 \rightarrow 2^1P_1$ (which is possible to excite in a magnetic field) and $2^3S_1 \rightarrow 2^3P_1$ transitions at ~ 11.2 GHz and ~ 13.0 GHz, respectively, both fall within the range of a WR-75 waveguide. By measuring both of these transitions from both microwave propagation directions it would be possible

to confirm if any observed shift is consistent with Doppler shifts at the respective wavelengths, or if it is uncorrelated microwave effects.

To fully understand and quantify fields within the waveguide, fine structure transitions in Rydberg He are being used, which are well mapped and understood, specifically the $37\,^3\mathrm{p} \rightarrow 37\,^3\mathrm{d}$ transition. Supersonic beams of He are more localised than fast Ps beams, travelling at around 2 km/s for a room temperature source, with a diameter of only a few millimeters [135]. This allows the rf field to be measured across the width of the waveguide by pulsing the microwave radiation when the He is at different locations within its 7 μs transit of the waveguide. This can be used to make a full 3-D map of the electric and magnetic fields within the waveguide as well as verify directional asymmetries in the microwave field as determined by shifts and broadening of the measured line shapes.

7.4 Conclusions

Using microwave radiation propagated in a WR-112 waveguide we have mitigated the significant effects of microwave reflections and eliminated Doppler effects to perform the most precise measurement of the Ps $2\,^3\mathrm{S}_1 \rightarrow 2\,^3\mathrm{P}_2$ interval to date of $8\,627.94 \pm 0.95$ MHz, that is a precision of 110 ppm. This is 1.3σ from the theory value of $8\,626.71 \pm 0.08$ MHz. If all historical measurements are combined then the experimental measurement of this transition stands at $8\,626.54 \pm 0.75$ MHz, in agreement with theory.

However, a large systematic uncertainty has been identified, stemming from waveguide and microwave circuit imperfections, causing apparent shifts in the transition frequency that depended on the microwave propagation direction but which cannot be explained by Doppler shifts. Even if a much more precise design of the microwave apparatus and circuit are made involving simulation in CST and practical testing using a vector network analyser, this methodology of fine structure measurements would appear to have significant limiting factors. As a result of this, new measurements using interferometry techniques have been proposed [37] with the apparatus having been built [211] and initial measurements underway.

Chapter 8

General Conclusions

Three measurements have been performed on $n = 2$ Ps as a means to test bound state QED in a lepton-only system. The first measurement in Chapter 5 was that of the annihilation lifetime of the metastable 2^3S_1 state, measured by determining the loss in population of 2S atoms over time, correcting for additional losses with long lived Rydberg states. This yielded a result of $\Gamma_{2S} = 843 \pm 72$ kHz which is in agreement with the Zeeman adjusted theoretical value of 890.0 ± 1.4 kHz, but with an 8.5% error it cannot be considered a precision measurement. This is the first measurement of an excited-state Ps annihilation decay rate and several methods of improving this technique have already been given, including using colder Ps and a better detector setup with large solid angle coverage. A better setup would also enable the measurement of the 2^1S_0 annihilation decay rate by measuring the 2^3S_1 decay rate as a function of magnetic field and extrapolating back to zero-field, much like the previous p-Ps decay rate measurements [16].

The second measurement, in Chapter 6, evaluated the effect of microwave reflection on line shapes of the Ps $2^3S_1 \rightarrow 2^3P_2$ interval using free space microwave radiation from a horn antenna. The technique is sufficient to saturate the transition, but rotation of the horn antenna caused large apparent shifts in the symmetric measured transition frequency of ± 4 MHz. These were attributed to reflection effects causing frequency dependent power, with no other source of shifts large enough to explain the effect. This makes precision line shape measurements with horn antenna subject to large and unpredictable apparent shifts when performed in environments

with significant reflective properties like vacuum chambers. This will also effect any measurement with an open microwave system, and confirms the previous fine structure measurements at UCL [131, 132] had a reflection dependent systematic of several MHz whether they displayed asymmetry or not.

This type of reflection effect may be relevant for proposed measurements of the Rydberg constant using THz radiation to drive the $n = 21 \rightarrow 24$ transition at 874 GHz. This frequency uses a WR-1.0 waveguide which has dimensions of 0.254×0.127 mm. Because it is not feasible to propagate Ps through a structure this small, free space radiation will have to be used despite the problems identified here. This will require the minimisation of reflection effects, likely through a highly collimated and efficiently terminated THz beam with a narrow intersection with the Ps ensemble to minimise possible selection effects and position dependent power and polarisation.

The final measurement, in Chapter 7, was the most precise experimental determination of the $2^3S_1 \rightarrow 2^3P_2$ energy interval to date. Designed to test bound state QED this measurement obtained a value of $8\,627.94 \pm 0.95$ MHz, in broad agreement with the theoretical value of $8\,626.71 \pm 0.08$ MHz with a difference of 1.3σ. If all historical measurements are combined then the best experimental measurement of this transition is $8\,626.54 \pm 0.75$ MHz, in agreement with theory. Unfortunately this is not precise enough to conclusively test the $\mathscr{O}(\alpha^6)$ order correction which has a 1.46 MHz shift from $\mathscr{O}(\alpha^5)$ and is therefore well within 2σ of the measurement.

Despite a two-fold improvement in precision over previous studies this measurement was limited by persistent microwave field related systematic effects as identified in this measurement by a 1.8 MHz difference between the measured transition frequency for opposite microwave propagation directions. To overcome the limitations of reflection, structural and impedance matching related effects in these naturally wide line shapes an alternative method is required. An experiment has recently been proposed [37] (and is under construction [211]) to utilise the separated oscillatory fields (SOF) [228] and frequency-offset separated oscillatory fields (FOSOF) [265] techniques which use Ramsey type interferometry to get around

some of the problems outlined in this thesis.

The SOF technique exposes the 2S Ps to two regions of microwave radiation of the same frequency with a π or 0 rad phase offset. Subtracting line shapes produced by the two different phase offsets produces an interference signal from which the transition frequency can be extracted. The first region excites the 2S atoms to a superposition with the short lived 2P state, 2S', and the second re-excites them back to the long lived 2S state for detection. By increasing the spatial separation between the two microwave regions longer lived 2S' states can be selected, reducing the natural line width (known as uncertainty principle narrowing), albeit with a sacrifice of signal. Further reduction of the line width comes from interference narrowing due to the effect of the two field regions and their phase offset [106]. A narrower line width will increase the precision of the fitting and reduce the effect of any frequency dependent reflections present in the geometry of the experiment. Though once any measurement reaches a precision of $\sim$ 100 kHz QI effects will need to be included in the line shape model [15].

The SOF technique requires fast Ps to allow a statistically significant fraction of the 2S' Ps produced by the first field region to survive to make it into the second field region[1]. A fast metastable 2S Ps beam with a tunable energy range of 10 - 120 eV and an angular divergence of just 4.2° has been constructed using positron collisions with Xe gas to make the metastable 2S state directly with 10% efficiency [211]. If the two regions of field are defined by two waveguides placed 63 mm apart a 40 eV beam would take 27 ns to transit the field free region between the two. The 2S' state would suffer a 99.98% loss in this time, demonstrating the need for a fast beam. The waveguides can be placed closer together but this lowers the amplitude of the interference signal and increases the line width. Because this gas cell beam works in transmission geometry it is also possible to properly terminate the magnetic fields used for positron guiding, enabling the measurement to be done is low magnetic fields and not requiring the Zeeman extrapolation used in this

[1] Unless a much colder source of Ps can be produced to perform time separated SOF, rather than spatially separated SOF. This could also be achieved with trapped Ps, which may soon be possible using Rydberg atoms in electric fields [148] or laser cooling [245].

work.[2]

SOF measurements can still suffer from reflection and waveguide induced frequency dependent power. A FOSOF measurement, unlike SOF, totally removes any dependence on line shape model, not only rendering reflection effects irrelevant but also QI and internal waveguide systematics [37]. Like SOF, this technique uses two regions of separated field but the radiation in each region has a small frequency offset. This frequency offset induces a phase difference in the interference signal which is linearly dependent on the frequency offset and the resonance frequency. Other systematics such as Stark, Zeeman and Doppler shifts are still relevant but these are easier to control and compensate for. This technique may also be used to expand the microwave spectroscopy of Ps into the $n = 3$ state [12] fine structure, the $n = 2$ hyperfine splitting [50] and further measurements of CP violation [74].

Although more progress is still required until Ps bound-state QED tests can rival theoretical calculations (an improvement of two orders of magnitude in precision is needed) and the measurement precision of other test-species (an improvement of six orders of magnitude in precision is needed to be comparable to studies of H), the purely leptonic nature of Ps makes it a valuable tool in understanding possible matter/antimatter asymmetries and answering why the universe is so dominated by matter. In conclusion, this work presents the latest update to precision tests of bound-state QED within Ps atom, and represents a step forward in the techniques used to do so.

[2]Using this fast, energy tunable beam another method to measure the $n = 2$ fine structure intervals would be to use a fixed periodic structure, similar to that used by Nagata et al. who measured the ground state hyperfine interval of Ps using an energy tunable beam derived from accelerating Ps^- ions [209]. A structure with a periodicity of $a = 400$ μm would allow excitation of the ν_2 transition within the energy range of the 2S beam (20 - 120 eV [211]). This method removes the effect of microwave frequency dependent power variation. However, a high precision measurement is unlikely due to difficulties in manufacturing the structure, and the broad 1 eV energy spread of the 2S beam.

Appendix A

Appendix: Line Shape Analysis

Line shapes of the ν_2 transition are obtained as described in Section 3.9. An S_γ value is obtained where the signal is 2S atoms with microwave radiation present and a background of 2S atoms with no microwave radiation present. S_γ is measured for a range of frequencies with a higher measurement density within the expected

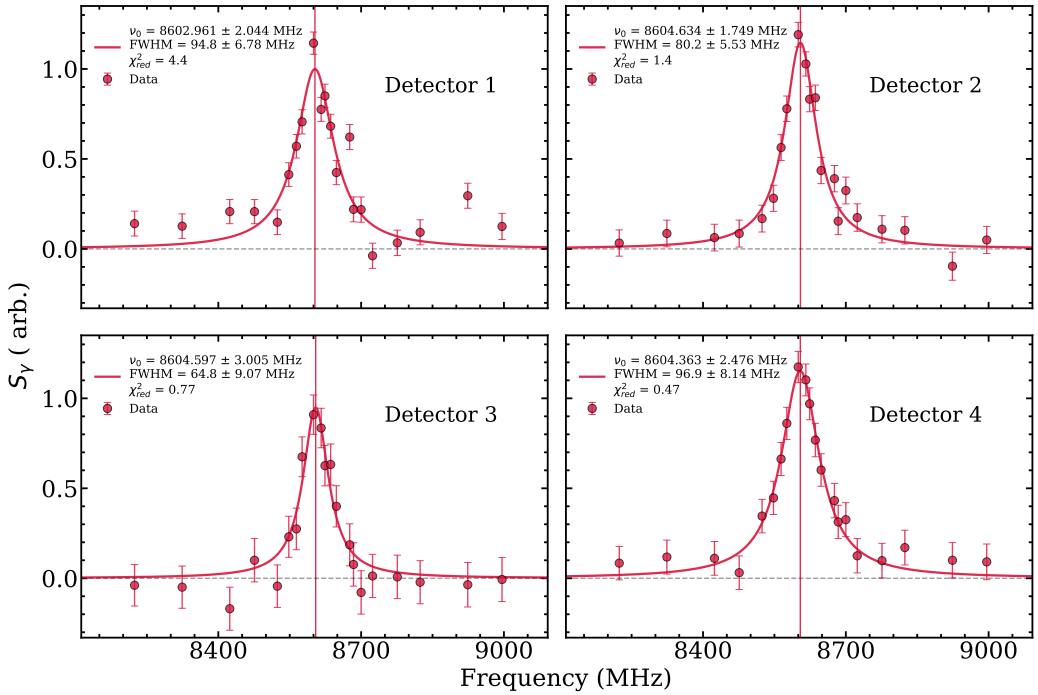

Figure A.1: Line shapes recorded for one data run at 119 G and 10 mW propagating in the $-x$ direction with no microwave absorbing foam present using the methods in Chapter 7. The amplitudes have been normalised to that of Detector 1 and the vertical line is the fitted ν_R value of each line shape. The red circles are the measured data and the solid red line is a Lorentzian fit.

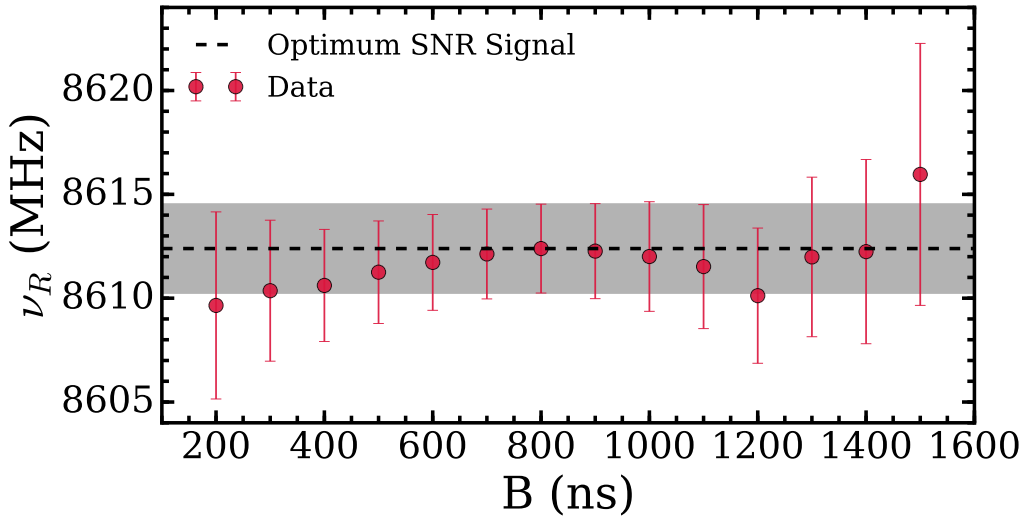

Figure A.2: The fitted Lorentzian centroid as a function of the integration parameter B for one data run at 97 G made using the setup described in Chapter 7 (10 mW, $+x$ direction). In this case A = -30 ns and C = 1600 ns.

range of the centroid to enable better constraint of the fitted Lorentzian function to ν_R. The window of denser points is $\pm$50 MHz to ether side of the calculated QED transition frequency, 1.75$\times$ larger than the expected Zeeman shift. The data acquisition time for a single line shape data run varied from $\sim$ 12 to 72 hours, depending on the signal-to-noise ratio (SNR) of the data.

Each line shape is measured on multiple LYSO detectors and the data processing on each detector is separate up to and including the Lorentzian fitting. The line shape data presented in Chapters 6 & 7 is obtained with the methods described here, where the final ν_R, Γ and q_L values presented in this work are averaged across multiple detectors and data runs. Figure A.1 shows the line shapes measured on four detectors for the data presented in Chapter 7 at 119 G and 10 mW propagating in the $-x$ direction with no microwave absorbing foam present. For data taken using a waveguide the power correction of Equation 3.6 is applied to each line shape before function fitting.

For each line shape the integration parameters A, B and C are fixed at values that give the maximum SNR for the point of maximum amplitude. However, detuning the microwaves from ν_R changes the Rabi frequency of the transition, and therefore the rate of transfer from the 2S $\rightarrow$ 2P state which can cause the time at

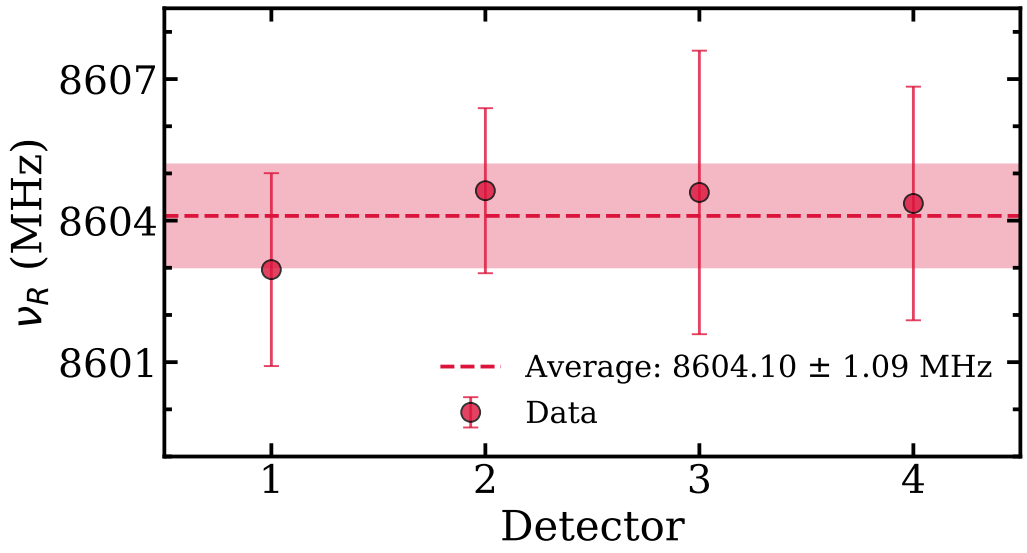

Figure A.3: The value of ν_R as extracted from the data in Figure A.1 for each detector. The dashed line and shaded band represents the weighted average of the data and the associated error.

which Ps annihilates to be later at more off resonant microwave frequencies. Because S_γ is dependent on fixed time windows the S_γ parameter may not be a true representation of the change in population if this change in annihilation time at highly detuned frequencies has a significant effect. This is because changes in the time at which annihilation occurs due to a detuned microwave frequency may cause events to move from the AB window to the BC window of the SSPALS spectra. This could cause the measured signal to be lower or higher than a true representation of the amount of 2S atoms that annihilate due to the applied microwave radiation.

To test if the integration window effects the measured transition frequency an example line shape was fitted with a Lorentzian for different values of B, because B has the most influence on the measured S_γ. This data is shown in Figure A.2 and demonstrates that ν_R has no dependence on B, therefore the choosing of the B parameter for optimum SNR is valid. Note this data is for a different set of parameters than the other data presented in this appendix.

Figure A.3 shows the centroid extracted for each detector displayed in Figure A.1. The weighted average of all fit parameters is made using the Python *numpy.average()* function [137]. The weights w are calculated from the error σ

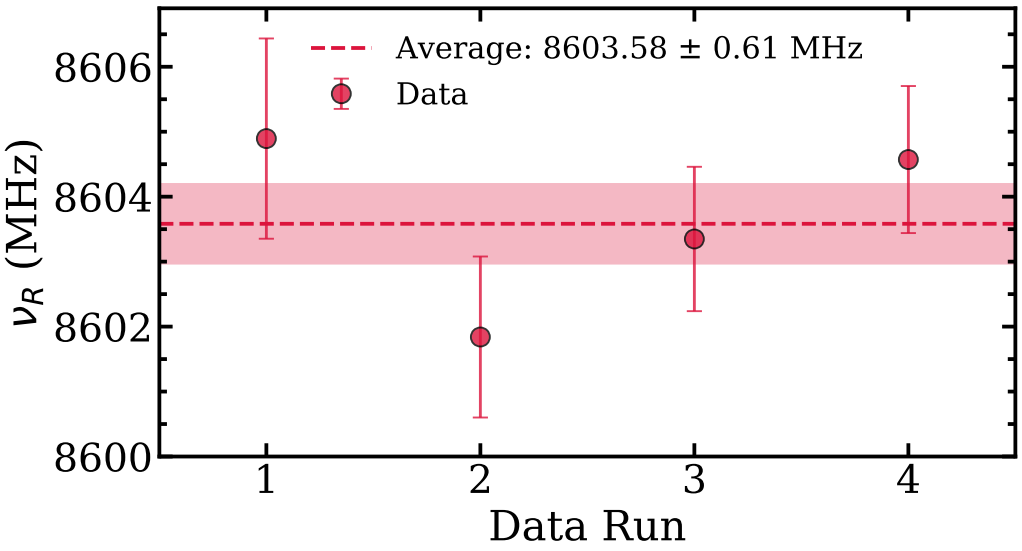

Figure A.4: The detector averaged ν_R for four different data runs for the same experimental parameters: 119 G and 10 mW with the microwave radiation propagating in the $-x$ direction without microwave absorbing foam present. The dashed line and shaded band represents the weighted average of the data and the associated error.

of each data point by $w = 1/\sigma^2$. The error of the weighted average is $\sigma_{average} = 1/\sqrt{\sum_i w_i}$ where i is the number of values being averaged. The final result of this calculation is shown in Figure A.3 for the centroid values.[1]

For each unique set of parameters (i.e. magnetic field, microwave power, propagation direction etc.) it is typical that multiple data runs will be made to obtain a level of statistical error that is comparable on all measured sets of parameters. For example, this is typically between $1 - 2-$ MHz for values of ν_R. This would allow the immediate observation of large effects, but cannot be improved much further due to the often long data acquisition time already required to reach this level of precision. Certain experimental configurations inherently have higher statistical error due to detector placement, microwave power etc. And the data acquisition is broken up into multiple runs to facilitate maintenance to the positron beam (i.e. growing a new moderator), the lasers (i.e. a dye change or Doppler scan to verify UV wavelength) or other such circumstances which can reduce statistical error. Figure A.4 shows the value of ν_R already averaged across detector for four data runs

[1] Note this weighting is also used for the lifetime measurements in Chapter 5.

for the same experimental configuration as in Figures A.1 & A.3. These are then averaged using the same weighting method as discussed above to produce the final result for this unique set of experimental parameters.

Bibliography

[1] CST studio suite, dassault systemes. URL: https://www.3ds.com/products-services/simulia/products/cst-studio-suite/.

[2] Simion software. https://simion.com/.

[3] G S Adkins. Higher order corrections to positronium energy levels. *Journal of Physics: Conference Series*, 1138:012005, Nov 2018. doi:10.1088/1742-6596/1138/1/012005.

[4] Gregory S. Adkins, Richard N. Fell, and J. Sapirstein. Order α^2 corrections to the decay rate of orthopositronium. *Phys. Rev. Lett.*, 84:5086–5089, May 2000. doi:10.1103/PhysRevLett.84.5086.

[5] Gregory S. Adkins, Richard N. Fell, and J. Sapirstein. Two-loop correction to the orthopositronium decay rate. *Annals of Physics*, 295(2):136 – 193, 2002. doi:http://dx.doi.org/10.1006/aphy.2001.6219.

[6] Gregory S. Adkins, Minji Kim, Christian Parsons, and Richard N. Fell. Three-photon-annihilation contributions to positronium energies at order $m\alpha^7$. *Phys. Rev. Lett.*, 115:233401, Dec 2015. doi:doi.org/10.1103/PhysRevLett.115.233401.

[7] Gregory S. Adkins, Christian Parsons, M. D. Salinger, and Ruihan Wang. Positronium energy levels at order $m\alpha^7$: Vacuum polarization corrections in the two-photon-annihilation channel. *Phys. Lett. B*, 747, Jul 2015. doi:doi.org/10.1016/j.physletb.2015.06.050.

[8] Gregory S. Adkins, Christian Parsons, M. D. Salinger, Ruihan Wang, and Richard N. Fell. Positronium energy levels at order $m\alpha^7$: Light-by-light scattering in the two-photon-annihilation channel. *Phys. Rev. A*, 90:042502, Oct 2014. doi:10.1103/PhysRevA.90.042502.

[9] Gregory S. Adkins, Lam M. Tran, and Ruihan Wang. Positronium energy levels at order $m\alpha^7$: Product contributions in the two-photon-annihilation channel. *Phys. Rev. A*, 93:052511, May 2016. doi:10.1103/PhysRevA.93.052511.

[10] G.S. Adkins, D.B. Cassidy, and J. Pérez-Ríos. Precision spectroscopy of positronium: Testing bound-state qed theory and the search for physics beyond the standard model. *Physics Reports*, 975:1–61, 2022. doi:https://doi.org/10.1016/j.physrep.2022.05.002.

[11] P. Adrich, P. Blumer, G. Caratsch, et al. Production of antihydrogen atoms by 6 kev antiprotons through a positronium cloud. *Eur. Phys. J. C*, 83:1004, 2023. doi:10.1140/epjc/s10052-023-12137-y.

[12] S. Aghion et al. Laser excitation of the $n = 3$ level of positronium for antihydrogen production. *Phys. Rev. A*, 94:012507, Jul 2016. doi:10.1103/PhysRevA.94.012507.

[13] S. Aghion et al. Producing long-lived $2\,^3$S positronium via $3\,^3$P laser excitation in magnetic and electric fields. *Phys. Rev. A*, 98:013402, Jul 2018. doi:10.1103/PhysRevA.98.013402.

[14] M. Ahmadi et al. Characterization of the 1S–2S transition in antihydrogen. *Nature*, 557:71–75, 2018. doi:10.1038/s41586-018-0017-2.

[15] L. A. Akopyan, T. J. Babij, K. Lakhmanskiy, D. B. Cassidy, and A. Matveev. Line-shape modeling in microwave spectroscopy of the positronium $n = 2$ fine-structure intervals. *Phys. Rev. A*, 104:062810, Dec 2021. doi:10.1103/PhysRevA.104.062810.

[16] A. H. Al-Ramadhan and D. W. Gidley. New precision measurement of the decay rate of singlet positronium. *Phys. Rev. Lett.*, 72:1632–1635, Mar 1994. doi:10.1103/PhysRevLett.72.1632.

[17] A. I. Alekseev. Two-Photon Annihilation of Positronium in the P-State. *Soviet Phys. JETP.*, 7:826, 1958.

[18] A. I. Alekseev. Three-Photon Annihilation of Positronium in the P-State. *Soviet Phys. JETP.*, 9:1312, 1959.

[19] Alexandrou, Constantia. Novel applications of Lattice QCD: Parton Distributions, proton charge radius and neutron electric dipole moment. *EPJ Web Conf.*, 137:01004, 2017. doi:10.1051/epjconf/201713701004.

[20] A. M. Alonso. *Spectroscopy and manipulation of positronium in excited states*. PhD thesis, UCL, Nov 2018.

[21] A. M. Alonso, B. S. Cooper, A. Deller, and D. B. Cassidy. Single-shot positron annihilation lifetime spectroscopy with LYSO scintillators. *Nuclear Instruments and Methods in Physics Research Section A: Accelerators, Spectrometers, Detectors and Associated Equipment*, 828:163 – 169, 2016. doi:http://dx.doi.org/10.1016/j.nima.2016.05.049.

[22] A. M. Alonso, B. S. Cooper, A. Deller, L. Gurung, S. D. Hogan, and D. B. Cassidy. Velocity selection of rydberg positronium using a curved electrostatic guide. *Phys. Rev. A*, 95:053409, May 2017. doi:10.1103/PhysRevA.95.053409.

[23] A. M. Alonso, B. S. Cooper, A. Deller, S. D. Hogan, and D. B. Cassidy. Controlling Positronium Annihilation with Electric Fields. *Phys. Rev. Lett.*, 115:183401, Oct 2015. doi:10.1103/PhysRevLett.115.183401.

[24] A. M. Alonso, B. S. Cooper, A. Deller, S. D. Hogan, and D. B. Cassidy. Positronium decay from n=2 states in electric and magnetic fields. *Phys. Rev. A*, 93:012506, Jan 2016. doi:10.1103/PhysRevA.93.012506.

[25] A. M. Alonso, L. Gurung, B. A. D. Sukra, S. D. Hogan, and D. B. Cassidy. State-selective electric-field ionization of Rydberg positronium. *Phys. Rev. A*, 98:053417, Nov 2018. doi:10.1103/PhysRevA.98.053417.

[26] A. M. Alonso, S. D. Hogan, and D. B. Cassidy. Production of 2^3S_1 positronium atoms by single-photon excitation in an electric field. *Phys. Rev. A*, 95:033408, Mar 2017. doi:10.1103/PhysRevA.95.033408.

[27] S. L. Andersen, D. B. Cassidy, J. Chevallier, B. S Cooper, A. Deller, T. E Wall, and U. I. Uggerhøj. Positronium emission and cooling in reflection and transmission from thin meso-structured silica films. *Journal of Physics B: Atomic, Molecular and Optical Physics*, 48(20):204003, 2015. doi:10.1088/0953-4075/48/20/204003.

[28] Søren L. Andersen, Rasmus R. Johansen, Jakob B. Overgaard, Johan K. Mortensen, Kristoffer K. Andersen, Heine D. Thomsen, Mikkel D. Lund, Jacques Chevallier, Helge Knudsen, and Ulrik I. Uggerhøj. Positronium formation from porous silica in backscattering and transmission geometries. *The European Physical Journal D*, 68(5):124, 2014. doi:10.1140/epjd/e2014-40762-x.

[29] Carl D. Anderson. The apparant existance of easily deflectable positives. *Science*, 76(1967):238–239, 1932. doi:10.1126/science.76.1967.238.

[30] E. K. Anderson, C. J. Baker, W. Bertsche, et al. Observation of the effect of gravity on the motion of antimatter. *Nature*, 621:716–722, 2023. doi:10.1038/s41586-023-06527-1.

[31] Aldo Antognini, Daniel M. Kaplan, Klaus Kirch, Andreas Knecht, Derrick C. Mancini, James D. Phillips, Thomas J. Phillips, Robert D. Reasenberg, Thomas J. Roberts, and Anna Soter. Studying antimatter gravity with muonium. *Atoms*, 6(2), 2018. doi:10.3390/atoms6020017.

[32] M. Antonello et al. Efficient $2\,^3S$ positronium production by stimulated decay from the $3\,^3P$ level. *Phys. Rev. A*, 100:063414, Dec 2019. doi:10.1103/PhysRevA.100.063414.

[33] A. Ariga, S. Cialdi, G. Costantini, A. Ereditato, R. Ferragut, M. Giammarchi, M. Leone, G. Maero, L. Miramonti, C. Pistillo, M. Romé, S. Sala, P. Scampoli, and V. Toso. The QUPLAS experimental apparatus for antimatter interferometry. *Nuclear Instruments and Methods in Physics Research Section A: Accelerators, Spectrometers, Detectors and Associated Equipment*, 951:163019, 2020. doi:https://doi.org/10.1016/j.nima.2019.163019.

[34] S. Asai, O. Jinnouchi, and T. Kobayashi. Solution of the orthopositronium lifetime puzzle. *International Journal of Modern Physics A*, 19(23):3927–3938, 2004. doi:10.1142/S0217751X0402018X.

[35] S. Asai, S. Orito, and N. Shinohara. New measurement of the orthopositronium decay rate. *Physics Letters B*, 357(3):475 – 480, 1995. doi:http://dx.doi.org/10.1016/0370-2693(95)00916-9.

[36] C. Azevedo, V. P. Gonçalves, and B. D. Moreira. True muonium production in ultraperipheral Pb-Pb collisions. *Phys. Rev. C*, 101:024914, Feb 2020. doi:10.1103/PhysRevC.101.024914.

[37] T. J. Babij and D. B. Cassidy. Positronium microwave spectroscopy using Ramsey interferometry. *The European Physical Journal D*, 76(7):121, Jul 2022. URL: https://doi.org/10.1140/epjd/s10053-022-00448-w.

[38] M. Baker, P. Marquard, A. A. Penin, J. Piclum, and M. Steinhauser. Hyperfine Splitting in Positronium to $\mathcal{O}(\alpha^7 m_e)$: One Photon Annihilation Contribution. *Phys. Rev. Lett.*, 112:120407, Mar 2014. doi:10.1103/PhysRevLett.112.120407.

[39] Andrzej Banburski and Philip Schuster. Production and discovery of true muonium in fixed-target experiments. *Phys. Rev. D*, 86:093007, Nov 2012. doi:10.1103/PhysRevD.86.093007.

[40] V. B. Berestetski. On the spectrum of system consisting of a positron and electron. *J. Exptl. Theoret. Phys. (U.S.S.R.)*, 19:1130, 1949.

[41] W. Bernreuther, U. Löw, J. P. Ma, and O. Nachtmann. How to test CP, T, and CPT invariance in the three photon decay of polarized $^3S_1$ positronium. *Zeitschrift für Physik C Particles and Fields*, 41(1):143–158, 1988. doi:10.1007/BF01412589.

[42] W. Bernreuther and O. Nachtmann. Weak interaction effects in positronium. *Zeitschrift für Physik C Particles and Fields*, 11(3):235–245, 1981. doi:10.1007/BF01545680.

[43] H. A. Bethe and E. E. Salpeter. *Quantum Mechanics of One- and Two-Electron Atoms*. Springer, Berlin, 1957.

[44] N. Bezginov, T. Valdez, M. Horbatsch, A. Marsman, A. C. Vutha, and E. A. Hessels. A measurement of the atomic hydrogen lamb shift and the proton charge radius. *Science*, 365(6457):1007–1012, 2019. doi:10.1126/science.aau7807.

[45] G. W. Biedermann, X. Wu, L. Deslauriers, S. Roy, C. Mahadeswaraswamy, and M. A. Kasevich. Testing gravity with cold-atom interferometers. *Phys. Rev. A*, 91:033629, Mar 2015. doi:10.1103/PhysRevA.91.033629.

[46] P. T. Boggs and J. E. Rogers. Orthogonal Distance Regression. *Contemporary Mathematics*, 112:186, 1990.

[47] M. Born and V Fock. Beweis des adiabatensatzes. *Z. Physik*, 51:165–180, 1928. doi:10.1007/BF01343193.

[48] G. C. Branco, R. González Felipe, and F. R. Joaquim. Leptonic *CP* violation. *Rev. Mod. Phys.*, 84:515–565, Apr 2012. doi:10.1103/RevModPhys.84.515.

[49] R. A. Brienza, Y. Lu, C. Wang, S. K. Kanungo, T. C. Killian, F. B. Dunning, J. Burgdörfer, and S. Yoshida. Microwave spectroscopy of low-l singlet strontium Rydberg states at intermediate n, 50 n 70. *Phys. Rev. A*, 108:022815, Aug 2023. doi:10.1103/PhysRevA.108.022815.

[50] R. G. Bullis, C. Rasor, W. L. Tavis, S. A. Johnson, M. R. Weiss, and D. C. Yost. Ramsey spectroscopy of the $2s_{1/2}$ hyperfine interval in atomic hydrogen. *Phys. Rev. Lett.*, 130:203001, May 2023. doi:10.1103/PhysRevLett.130.203001.

[51] K. F. Canter, P. G. Coleman, T. C. Griffith, and G. R. Heyland. Measurement of total cross sections for low energy positron-helium collisions. (Positron backscattering from metal surface). *J. Phys. B*, 5(8):L167, 1972. URL: http://stacks.iop.org/0022-3700/5/i=8/a=007.

[52] K. F. Canter, A. P. Mills, Jr., and S. Berko. Observations of Positronium Lyman-α Radiation. *Phys. Rev. Lett.*, 34:177–180, Jan 1975. doi:10.1103/PhysRevLett.34.177.

[53] E. R. Carlson, V. W. Hughes, M. L. Lewis, and I. Lindgren. Higher-precision determination of the fine-structure interval in the ground state of positronium, and the fine-structure density shift in nitrogen. *Phys. Rev. Lett.*, 29:1059–1061, Oct 1972. doi:10.1103/PhysRevLett.29.1059.

[54] E. R. Carlson, V. W. Hughes, and I. Lindgren. Precision determination of the fine-structure interval in the ground state of positronium. iii. *Phys. Rev. A*, 15:241–250, Jan 1977. doi:10.1103/PhysRevA.15.241.

[55] Alan Carrington, Christine A. Leach, Andrew J. Marr, Andrew M. Shaw, Mark R. Viant, Jeremy M. Hutson, and Mark M. Law. Microwave spec-

troscopy and interaction potential of the long-range He...Ar^+ ion. *The Journal of Chemical Physics*, 102(6):2379–2403, 02 1995. doi:10.1063/1.468670.

[56] J. D. Carter and J. D. D. Martin. Energy shifts of rydberg atoms due to patch fields near metal surfaces. *Phys. Rev. A*, 83:032902, Mar 2011. doi:10.1103/PhysRevA.83.032902.

[57] D. Cassidy, T. Hisakado, H. Tom, and A. P. Mills, Jr. Positronium formation via excitonlike states on Si and Ge surfaces. *Phys. Rev. B*, 84:195312, Nov 2011. doi:10.1103/PhysRevB.84.195312.

[58] D. B. Cassidy, P. Crivelli, T. H. Hisakado, L. Liszkay, V. E. Meligne, P. Perez, H. W. K. Tom, and A. P. Mills, Jr. Positronium cooling in porous silica measured via Doppler spectroscopy. *Phys. Rev. A*, 81:012715, Jan 2010. doi:10.1103/PhysRevA.81.012715.

[59] D. B. Cassidy, S. H. M. Deng, R. G. Greaves, T. Maruo, N. Nishiyama, J. B. Snyder, H. K. M. Tanaka, and A. P. Mills, Jr. Experiments with a High-Density Positronium Gas. *Phys. Rev. Lett.*, 95:195006, Nov 2005. doi:10.1103/PhysRevLett.95.195006.

[60] D. B. Cassidy, S. H. M. Deng, R. G. Greaves, and A. P. Mills, Jr. Accumulator for the production of intense positron pulses. *Rev. Sci. Instrum.*, 77(7):073106, 2006. doi:10.1063/1.2221509.

[61] D. B. Cassidy, S. H. M. Deng, and A. P. Mills. Evidence for positronium molecule formation at a metal surface. *Phys. Rev. A*, 76:062511, Dec 2007. doi:10.1103/PhysRevA.76.062511.

[62] D. B. Cassidy, S. H. M. Deng, H. K. M. Tanaka, and A. P. Mills, Jr. Single shot positron annihilation lifetime spectroscopy. *Appl. Phys. Lett.*, 88(19):194105, 2006. doi:10.1063/1.2203336.

[63] D. B. Cassidy, T. H. Hisakado, H. W. K. Tom, and A. P. Mills, Jr. Optical Spectroscopy of Molecular Positronium. *Phys. Rev. Lett.*, 108:133402, Mar 2012. doi:10.1103/PhysRevLett.108.133402.

[64] D. B. Cassidy, T. H. Hisakado, H. W. K. Tom, and A. P. Mills, Jr. Positronium hyperfine interval measured via saturated absorption spectroscopy. *Phys. Rev. Lett.*, 109:073401, Aug 2012. doi:10.1103/PhysRevLett.109.073401.

[65] D. B. Cassidy, V. E. Meligne, and A. P. Mills, Jr. Production of a fully spin-polarized ensemble of positronium atoms. *Phys. Rev. Lett.*, 104:173401, Apr 2010. doi:10.1103/PhysRevLett.104.173401.

[66] D. B. Cassidy and A. P. Mills, Jr. The production of molecular positronium. *Nature*, 449(7159):195–197, Sep 2007. doi:10.1038/nature06094.

[67] David B. Cassidy. Experimental progress in positronium laser physics. *The European Physical Journal D*, 72(3):53, Mar 2018. doi:10.1140/epjd/e2018-80721-y.

[68] William E. Caswell, G. Peter Lepage, and Jonathan Sapirstein. $\mathcal{O}(\alpha)$ corrections to the decay rate of orthopositronium. *Phys. Rev. Lett.*, 38:488–491, Feb 1977. doi:10.1103/PhysRevLett.38.488.

[69] Hubert Ceeh, Christoph Hugenschmidt, Klaus Schreckenbach, Stefan A. Gärtner, Peter G. Thirolf, Frank Fleischer, and Dirk Schwalm. Precision measurement of the decay rate of the negative positronium ion Ps^-. *Phys. Rev. A*, 84:062508, Dec 2011. doi:10.1103/PhysRevA.84.062508.

[70] D. Z. Chan and J. D. D. Martin. Comment on "matter-wave interferometry with helium atoms in low-l rydberg states". *Phys. Rev. A*, 109:017301, Jan 2024. doi:10.1103/PhysRevA.109.017301.

[71] J. H. Christenson, J. W. Cronin, V. L. Fitch, and R. Turlay. Evidence for the 2π decay of the k_2^0 meson. *Phys. Rev. Lett.*, 13:138–140, Jul 1964. doi:10.1103/PhysRevLett.13.138.

[72] S. Chu and A. P. Mills, Jr. Excitation of the positronium $1^3S_1 \rightarrow 2^3S_1$ two-photon transition. *Phys. Rev. Lett.*, 48:1333–1337, May 1982. doi:10.1103/PhysRevLett.48.1333.

[73] Steven Chu, Allen P. Mills, Jr., and John L. Hall. Measurement of the positronium $1^3S_1 - 2^3S_1$ interval by doppler-free two-photon spectroscopy. *Phys. Rev. Lett.*, 52:1689–1692, May 1984. doi:10.1103/PhysRevLett.52.1689.

[74] R. S. Conti, S. Hatamian, L. Lapidus, A. Rich, and M. Skalsey. Search for C-violating, P-conserving interactions and observation of $2\,^3\mathrm{S}_1$ to $2\,^1\mathrm{P}_1$ transitions in positronium. *Physics Letters A*, 177(1):43–48, 1993. doi:https://doi.org/10.1016/0375-9601(93)90371-6.

[75] R. S. Conti, S. Hatamian, and A. Rich. Tests of the discrete symmetries C , P , and T in one-photon transitions of positronium. *Phys. Rev. A*, 33:3495–3498, May 1986. doi:10.1103/PhysRevA.33.3495.

[76] D. W. Cooke, K. J. McClellan, B. L. Bennett, J. M. Roper, M. T. Whittaker, R. E. Muenchausen, and R. C. Sze. Crystal growth and optical characterization of cerium-doped $\mathrm{Lu}_{1.8}\mathrm{Y}_{0.2}\mathrm{SiO}_5$. *Journal of Applied Physics*, 88(12):7360–7362, 12 2000. doi:10.1063/1.1328775.

[77] B. Cooper. *Laser excitation of positronium produced by various materials at a range of temperatures*. PhD thesis, UCL, Oct 2017. URL: https://uclpositronium.files.wordpress.com/2018/03/bencooperthesis.pdf.

[78] B. S. Cooper, A. M. Alonso, A. Deller, L. Liszkay, and D. B. Cassidy. Positronium production in cryogenic environments. *Phys. Rev. B*, 93:125305, Mar 2016. doi:10.1103/PhysRevB.93.125305.

[79] B. S. Cooper, A. M. Alonso, A. Deller, T. E. Wall, and D. B. Cassidy. A trap-based pulsed positron beam optimised for positronium laser spectroscopy. *Review of Scientific Instruments*, 86(10), 2015. doi:http://dx.doi.org/10.1063/1.4931690.

[80] P. Crivelli, C. L. Cesar, and U. Gendotti. Advances towards a new measurement of the 1S–2S transition of positronium. *Canadian Journal of Physics*, 89(1):29–35, 2011. URL: https://doi.org/10.1139/P10-101.

[81] S. M. Curry. Combined Zeeman and motional Stark effects in the first excited state of positronium. *Phys.Rev. A*, 7:447–450, February 1973. doi:10.1103/PhysRevA.7.447.

[82] Andrzej Czarnecki, Kirill Melnikov, and Alexander Yelkhovsky. Positronium hyperfine splitting: Analytical value at $o(m\alpha^6)$. *Phys. Rev. Lett.*, 82:311–314, Jan 1999. doi:10.1103/PhysRevLett.82.311.

[83] Andrzej Czarnecki, Kirill Melnikov, and Alexander Yelkhovsky. Positronium s -state spectrum: Analytic results at $\mathcal{O}(m\alpha^6)$. *Phys. Rev. A*, 59:4316–4330, Jun 1999. doi:10.1103/PhysRevA.59.4316.

[84] Stefan Czesla, Sebastian Schröter, Christian P. Schneider, Klaus F. Huber, Fabian Pfeifer, Daniel T. Andreasen, and Mathias Zechmeister. PyA: Python astronomy-related packages, Jun 2019. arXiv:1906.010.

[85] R. J. Daly, R. E. Sheldon, and D. B. Cassidy. Measurement of the fluorescence decay rate of $2\,^3\mathrm{P}_J$ positronium. *In Preparation*.

[86] R. J. Damburg and V. V. Kolosov. A hydrogen atom in a uniform electric field. III. *Journal of Physics B: Atomic and Molecular Physics*, 12(16):2637, 1979. URL: http://stacks.iop.org/0022-3700/12/i=16/a=011.

[87] R. J. Damburg and V. V. Kolosov. Theoretical studies of hydrogen Rydberg atoms in electric fields. In R. F. Stebbings and F. B. Dunning, editors, *Ry-*

dberg States of Atoms and Molecules, pages 31–72. Cambridge University Press, Cambridge, 1983.

[88] T. W. Darling, F. Rossi, G. I. Opat, and G. F. Moorhead. The fall of charged particles under gravity: A study of experimental problems. *Rev. Mod. Phys.*, 64:237–257, Jan 1992. doi:10.1103/RevModPhys.64.237.

[89] J. C. De Vries. *A Precision Millimeter-Wave Measurement of the Rydberg Frequency*. PhD thesis, Massachusetts Institute of Technology, 2001.

[90] A. Deller, A. M. Alonso, B. S. Cooper, S. D. Hogan, and D. B. Cassidy. Electrostatically guided Rydberg positronium. *Phys. Rev. Lett.*, 117:073202, Aug 2016. doi:10.1103/PhysRevLett.117.073202.

[91] A. Deller, A. M. Alonso, B. S. Cooper, S. D. Hogan, and D. B. Cassidy. Measurement of Rydberg positronium fluorescence lifetimes. *Phys. Rev. A*, 93:062513, Jun 2016. doi:10.1103/PhysRevA.93.062513.

[92] A. Deller, B. S. Cooper, T. E. Wall, and D. B. Cassidy. Positronium emission from mesoporous silica studied by laser-enhanced time-of-flight spectroscopy. *New Journal of Physics*, 17(4):043059, 2015. URL: http://stacks.iop.org/1367-2630/17/i=4/a=043059.

[93] A. Deller, T. Mortensen, C. A. Isaac, D. P. van der Werf, and M. Charlton. Radially selective inward transport of positrons in a Penning–Malmberg trap. *New Journal of Physics*, 16(7):073028, Jul 2014. doi:10.1088/1367-2630/16/7/073028.

[94] W. Demtröder. *Laser Spectroscopy*. Springer, New York, fourth edition, 2008.

[95] C. D. Dermer and J. C. Weisheit. Perturbative analysis of simultaneous Stark and Zeeman effects on $n = 1 \rightarrow n = 2$ radiative transitions in positronium. *Phys. Rev. A*, 40:5526–5532, November 1989. doi:10.1103/PhysRevA.40.5526.

[96] M. Deutsch. Evidence for the formation of positronium in gases. *Phys. Rev.*, 82:455–456, May 1951. doi:10.1103/PhysRev.82.455.

[97] M. Deutsch. Three-quantum decay of positronium. *Phys. Rev.*, 83:866–867, Aug 1951. doi:10.1103/PhysRev.83.866.

[98] M. Deutsch and S. C. Brown. Zeeman effect and hyperfine splitting of positronium. *Phys. Rev.*, 85:1047–1048, Mar 1952. doi:10.1103/PhysRev.85.1047.

[99] Martin Deutsch and Everett Dulit. Short range interaction of electrons and fine structure of positronium. *Phys. Rev.*, 84:601–602, Nov 1951. doi:10.1103/PhysRev.84.601.

[100] P. A. M. Dirac. The quantum theory of the electron. *Proceedings of the Royal Society of London A: Mathematical, Physical and Engineering Sciences*, 117(778):610–624, 1928. doi:10.1098/rspa.1928.0023.

[101] P. A. M. Dirac. On the annihilation of electrons and protons. *Mathematical Proceedings of the Cambridge Philosophical Society*, 26:361–375, 7 1930. doi:10.1017/S0305004100016091.

[102] M. Doser et al. Aegis at elena: outlook for physics with a pulsed cold antihydrogen beam. *Philosophical Transactions of the Royal Society A: Mathematical, Physical and Engineering Sciences*, 376(2116):20170274, 2018. doi:10.1098/rsta.2017.0274.

[103] R. M. Drisko. Spin and polarization effects in the annihilation of triplet positronium. *Phys. Rev.*, 102:1542–1544, Jun 1956. doi:10.1103/PhysRev.102.1542.

[104] P. O. Egan, V. W. Hughes, and M. H. Yam. Precision determination of the fine-structure interval in the ground state of positronium. iv. measurement of positronium fine-structure density shifts in noble gases. *Phys. Rev. A*, 15:251–260, Jan 1977. doi:10.1103/PhysRevA.15.251.

[105] Michael I. Eides and Valery A. Shelyuto. Three-loop corrections to the lamb shift in muonium and positronium. *Phys. Rev. A*, 105:012803, Jan 2022. doi:10.1103/PhysRevA.105.012803.

[106] C. W. Fabjan and F. M. Pipkin. Resonance-narrowed-lamb-shift measurement in hydrogen, $n = 3$. *Phys. Rev. A*, 6:556–570, Aug 1972. doi:10.1103/PhysRevA.6.556.

[107] U. Fano. Effects of configuration interaction on intensities and phase shifts. *Phys. Rev.*, 124:1866–1878, Dec 1961. doi:10.1103/PhysRev.124.1866.

[108] M. S. Fee, A. P. Mills, Jr., S. Chu, E. D. Shaw, K. Danzmann, R. J. Chichester, and D. M. Zuckerman. Measurement of the positronium 1^3S_1-2^3S_1 interval by continuous-wave two-photon excitation. *Phys. Rev. Lett.*, 70:1397–1400, Mar 1993. doi:10.1103/PhysRevLett.70.1397.

[109] R. A. Ferrell. *The Fine Structure of Positronium*. PhD thesis, Princeton University, 1951.

[110] R. A. Ferrell. The Positronium Fine Structure. *Phys. Rev.*, 84:858–859, Nov 1951. doi:10.1103/PhysRev.84.858.

[111] G. Fields, R. Brienza, F. B. Dunning, S. Yoshida, and J. Burgdörfer. High-n limit of quantum defects for high-ℓ strontium rydberg states. *Phys. Rev. A*, 104:032817, Sep 2021. doi:10.1103/PhysRevA.104.032817.

[112] Frank Fleischer, Kai Degreif, Gerald Gwinner, Michael Lestinsky, Vitaly Liechtenstein, Florian Plenge, and Dirk Schwalm. Measurement of the decay rate of the negative ion of positronium (Ps^-). *Phys. Rev. Lett.*, 96:063401, Feb 2006. doi:10.1103/PhysRevLett.96.063401.

[113] C.J. Foot. *Atomic physics*. Oxford master series in physics. Oxford University Press, 2005.

[114] Thomas Fulton and Paul C. Martin. Radiative corrections in positronium. *Phys. Rev.*, 93:903–904, Feb 1954. doi:10.1103/PhysRev.93.903.

[115] Thomas Fulton and Paul C. Martin. Two-body system in quantum electrodynamics: Energy levels of positronium. *Phys. Rev.*, 95:811–822, Aug 1954. doi:10.1103/PhysRev.95.811.

[116] T. F. Gallagher. *Rydberg Atoms*. Cambridge University Press, Cambridge, UK, 1994.

[117] Beatriz Gato-Rivera. *Matter–Antimatter Asymmetry*, pages 193–229. Springer International Publishing, Cham, 2021. doi:10.1007/978-3-030-67791-6_7.

[118] D. A. Gedcke and W. J. McDonald. A constant fraction of pulse height trigger for optimum time resolution. *Nuclear Instruments and Methods*, 55:377–380, 1967. doi:https://doi.org/10.1016/0029-554X(67)90145-0.

[119] D. W. Gidley, A. Rich, P. W. Zitzewitz, and D. A. L. Paul. New experimental value for the orthopositronium decay rate. *Phys. Rev. Lett.*, 40:737–740, Mar 1978. doi:10.1103/PhysRevLett.40.737.

[120] H. J. Goldman. *Apparatus for Ultrahigh Precision Measurement of the 1S-2S Interval in Positronium*. PhD thesis, UC Riverside, 2018.

[121] Vittorio Gorini, Andrzej Kossakowski, and E. C. G. Sudarshan. Completely positive dynamical semigroups of N-level systems. *Journal of Mathematical Physics*, 17(5):821–825, 1976. doi:10.1063/1.522979.

[122] Jan Govaerts and Marc Van Caillie. Neutrino decay of positronium in the standard model and beyond. *Physics Letters B*, 381(4):451–457, 1996. doi:https://doi.org/10.1016/0370-2693(96)00623-5.

[123] R. G. Greaves and J. M. Moxom. Compression of trapped positrons in a single particle regime by a rotating electric field. *Phys. Plasmas*, 15:072304, 2008. doi:10.1063/1.2956335.

[124] R. G. Greaves and C. M. Surko. Positron trapping and the creation of high-quality trap-based positron beams. *Nuclear Instruments and Methods in Physics Research Section B: Beam Interactions with Materials and Atoms*, 192(1):90–96, 2002. doi:https://doi.org/10.1016/S0168-583X(02)00717-6.

[125] T C Griffith, G R Heyland, K S Lines, and T R Twomey. The decay rate of ortho-positronium in vacuum. *Journal of Physics B: Atomic and Molecular Physics*, 11(23):L743, 1978. URL: http://stacks.iop.org/0022-3700/11/i=23/a=007.

[126] Alexey Grinin, Arthur Matveev, Dylan C. Yost, Lothar Maisenbacher, Vitaly Wirthl, Randolf Pohl, Theodor W. Hänsch, and Thomas Udem. Two-photon frequency comb spectroscopy of atomic hydrogen. *Science*, 370(6520):1061–1066, 2020. doi:10.1126/science.abc7776.

[127] T. Grund, Karin Maier, and Alfred Seeger. Rare-gas solids as positron moderators in "critical environments". In *Positron Annihilation - ICPA-9*, volume 105 of *Materials Science Forum*, pages 1879–1882. Trans Tech Publications Ltd, 1 1992. doi:10.4028/www.scientific.net/MSF.105-110.1879.

[128] E. M. Gullikson and A. P. Mills, Jr. Positron dynamics in rare-gas solids. *Phys. Rev. Lett.*, 57:376–379, Jul 1986. doi:10.1103/PhysRevLett.57.376.

[129] L. Gurung. *Precision Microwave Spectroscopy of the Positronium $n = 2$ Fine Structure*. PhD thesis, University College London, 2021. URL: https://uclpositronium.files.wordpress.com/2021/10/gurung_10125029_thesis.pdf.

[130] L Gurung, A M Alonso, T J Babij, B S Cooper, A L Shluger, and D B Cassidy. Positronium emission from MgO smoke nanocrystals. *Journal of Physics B: Atomic, Molecular and Optical Physics*, 52(10):105004, apr 2019. doi:10.1088/1361-6455/ab0f06.

[131] L. Gurung, T. J. Babij, S. D. Hogan, and D. B. Cassidy. Precision microwave spectroscopy of the positronium $n = 2$ fine structure. *Phys. Rev. Lett.*, 125:073002, Aug 2020. doi:10.1103/PhysRevLett.125.073002.

[132] L. Gurung, T. J. Babij, J. Pérez-Ríos, S. D. Hogan, and D. B. Cassidy. Observation of asymmetric line shapes in precision microwave spectroscopy of the positronium $2^3S_1 \rightarrow 2^3P_J$ ($J = 1, 2$) fine-structure intervals. *Phys. Rev. A*, 103:042805, Apr 2021. doi:10.1103/PhysRevA.103.042805.

[133] L. Gurung, B. S. Cooper, S. D. Hogan, and D. B. Cassidy. Resonant shifts of positronium energy levels in MgO powder. *Phys. Rev. A*, 101:012701, Jan 2020. doi:10.1103/PhysRevA.101.012701.

[134] D. Hagena, R. Ley, D. Weil, G. Werth, W. Arnold, and H. Schneider. Precise measurement of n = 2 positronium fine-structure intervals. *Phys. Rev. Lett.*, 71:2887–2890, Nov 1993. doi:10.1103/PhysRevLett.71.2887.

[135] T. Halfmann, J. Koensgen, and K. Bergmann. A source for a high-intensity pulsed beam of metastable helium atoms. *Measurement Science and Technology*, 11(10):1510, 2000. URL: http://stacks.iop.org/0957-0233/11/i=10/a=312.

[136] Otto Halpern. Magnetic quenching of the positronium decay. *Phys. Rev.*, 94:904–907, May 1954. doi:10.1103/PhysRev.94.904.

[137] Charles R. Harris, K. Jarrod Millman, Stéfan J. van der Walt, Ralf Gommers, Pauli Virtanen, David Cournapeau, Eric Wieser, Julian Taylor, Sebastian Berg, Nathaniel J. Smith, Robert Kern, Matti Picus, Stephan Hoyer, Marten H. van Kerkwijk, Matthew Brett, Allan Haldane, Jaime Fernández

del Río, Mark Wiebe, Pearu Peterson, Pierre Gérard-Marchant, Kevin Sheppard, Tyler Reddy, Warren Weckesser, Hameer Abbasi, Christoph Gohlke, and Travis E. Oliphant. Array programming with NumPy. *Nature*, 585(7825):357–362, sep 2020. doi:10.1038/s41586-020-2649-2.

[138] F.J. Harris. On the use of windows for harmonic analysis with the discrete fourier transform. *Proceedings of the IEEE*, 66(1):51–83, 1978. doi:10.1109/PROC.1978.10837.

[139] A. Härter, A. Krükow, A. Brunner, and J. H. Denschlag. Long-term drifts of stray electric fields in a Paul trap. *Appl. Phys. B*, 114:275–281, November 2014. doi:https://doi.org/10.1007/s00340-013-5688-7.

[140] S. Hatamian, R. S. Conti, and A. Rich. Measurements of the 2^3S_1-2^3P_J ($J = 0,1,2$) fine-structure splittings in positronium. *Phys. Rev. Lett.*, 58:1833–1836, May 1987. doi:10.1103/PhysRevLett.58.1833.

[141] Michael W. Heiss, Gunther Wichmann, André Rubbia, and Paolo Crivelli. The positronium hyperfine structure: Progress towards a direct measurement of the $2^3\mathrm{S}_1 \rightarrow 2^1\mathrm{S}_0$ transition in vacuum. *Journal of Physics: Conference Series*, 1138(1):012007, nov 2018. doi:10.1088/1742-6596/1138/1/012007.

[142] Michael Wolfgang Heiss. *Precision Spectroscopy of Positronium Using a Pulsed Slow Positron Beam*. PhD thesis, ETH Zurich, 2021.

[143] Helmut Hellwig, Robert F. C. Vessot, Martin W. Levine, Paul W. Zitzewitz, David W. Allan, and David J. Glaze. Measurement of the unperturbed hydrogen hyperfine transition frequency. *IEEE Transactions on Instrumentation and Measurement*, 19(4):200–209, 1970. doi:10.1109/TIM.1970.4313902.

[144] Richard J. Hill and G. Peter Lepage. $\mathcal{O}(\alpha^2\Gamma, \alpha^3\Gamma)$ binding effects in orthopositronium decay. *Phys. Rev. D*, 62:111301, Oct 2000. doi:10.1103/PhysRevD.62.111301.

[145] S. D. Hogan. Calculated photoexcitation spectra of positronium Rydberg states. *Phys. Rev. A*, 87:063423, Jun 2013. doi:10.1103/PhysRevA.87.063423.

[146] S. D. Hogan. Rydberg-stark deceleration of atoms and molecules. *EPJ Techniques and Instrumentation*, 3:1, 2016. doi:10.1140/epjti/s40485-015-0028-4.

[147] S. D. Hogan, P. Allmendinger, H. Saßmannshausen, H. Schmutz, and F. Merkt. Surface-electrode Rydberg-Stark decelerator. *Phys. Rev. Lett.*, 108:063008, Feb 2012. doi:10.1103/PhysRevLett.108.063008.

[148] S. D. Hogan and F. Merkt. Demonstration of three-dimensional electrostatic trapping of state-selected Rydberg atoms. *Phys. Rev. Lett.*, 100:043001, Jan 2008. doi:10.1103/PhysRevLett.100.043001.

[149] S. D. Hogan, Ch. Seiler, and F. Merkt. Motional, isotope and quadratic Stark effects in Rydberg-Stark deceleration and off-axis electric trapping of H and D. *J. Phys. B.: At. Mol. Opt. Phys.*, 46:045303, 2013. doi:10.1088/0953-4075/46/4/045303.

[150] M. Horbatsch and E. A. Hessels. Shifts from a distant neighboring resonance. *Phys. Rev. A*, 82:052519, Nov 2010. doi:10.1103/PhysRevA.82.052519.

[151] V. W. Hughes, S. Marder, and C. S. Wu. Hyperfine structure of positronium in its ground state. *Phys. Rev.*, 106:934–947, Jun 1957. doi:10.1103/PhysRev.106.934.

[152] Akinori Igarashi, Isao Shimamura, and Nobuyuki Toshima. Photodetachment cross sections of the positronium negative ion. *New Journal of Physics*, 2(1):17, 2000. URL: http://stacks.iop.org/1367-2630/2/i=1/a=317.

[153] A. Ishida, T. Namba, S. Asai, T. Kobayashi, H. Saito, M. Yoshida, K. Tanaka, and A. Yamamoto. New precision measurement of hyperfine splitting of positronium. *Physics Letters B*, 734:338 – 344, 2014. doi:10.1016/j.physletb.2014.05.083.

[154] Takahisa Itahashi, Hideyuki Sakamoto, Akira Sato, and Keiji Takahisa. Low energy muon apparatus for true muonium production. *JPS Conf. Proc.*, 8:025004, 2015. doi:10.7566/JPSCP.8.025004.

[155] D. Ivanenko and A. Sokolov. *Dokl. Akad. Nauk SSSR*, 61, 1948.

[156] J. R. Johansson, P. D. Nation, and F. Nori. Qutip: An open-source python framework for the dynamics of open quantum systems. *Comp. Phys. Comm.*, 183:1760–1772, 2012. doi:10.1016/j.cpc.2012.02.021.

[157] J. R. Johansson, P. D. Nation, and F. Nori. Qutip 2: A python framework for the dynamics of open quantum systems. *Comp. Phys. Comm.*, 184:1234–1240, 2013. doi:10.1016/j.cpc.2012.11.019.

[158] A. C. L. Jones, J. Moxom, H. J. Rutbeck-Goldman, K. A. Osorno, G. G. Cecchini, M. Fuentes-Garcia, R. G. Greaves, D. J. Adams, H. W. K. Tom, A. P. Mills, and M. Leventhal. Focusing of a rydberg positronium beam with an ellipsoidal electrostatic mirror. *Phys. Rev. Lett.*, 119:053201, Aug 2017. doi:10.1103/PhysRevLett.119.053201.

[159] S. Kanda, Y. Fukao, Y. Ikedo, K. Ishida, M. Iwasaki, D. Kawall, N. Kawamura, K.M. Kojima, N. Kurosawa, Y. Matsuda, T. Mibe, Y. Miyake, S. Nishimura, N. Saito, Y. Sato, S. Seo, K. Shimomura, P. Strasser, K.S. Tanaka, T. Tanaka, H.A. Torii, A. Toyoda, and Y. Ueno. New precise spectroscopy of the hyperfine structure in muonium with a high-intensity pulsed muon beam. *Physics Letters B*, 815:136154, 2021. doi:https://doi.org/10.1016/j.physletb.2021.136154.

[160] J. P. Karr and D. Marchand. Progress on the proton-radius puzzle. *Nature*, 575(7781):61–62, 2019. URL: https://www.nature.com/articles/d41586-019-03364-z.

[161] S. G Karshenboim. Precision study of positronium: testing bound state QED theory. *International Journal of Modern Physics A*, 19(23):3879–3896, 2004. doi:10.1142/S0217751X04020142.

[162] S. G. Karshenboim. Precision physics of simple atoms: QED tests, nuclear structure and fundamental constants. *Physics Reports*, 422:1 – 63, 2005. doi:http://dx.doi.org/10.1016/j.physrep.2005.08.008.

[163] Y. Kataoka, S. Asai, and T. Kobayashi. First test of $O(\alpha^2)$ correction of the orthopositronium decay rate. *Physics Letters B*, 671(2):219 – 223, 2009. doi:http://dx.doi.org/10.1016/j.physletb.2008.12.008.

[164] K. Kato, T. D. G. Skinner, and E. A. Hessels. Ultrahigh-precision measurement of the $n = 2$ triplet p fine structure of atomic helium using frequency-offset separated oscillatory fields. *Phys. Rev. Lett.*, 121:143002, Oct 2018. doi:10.1103/PhysRevLett.121.143002.

[165] A. Kellerbauer et al. Proposed antimatter gravity measurement with an antihydrogen beam. *Nuclear Instruments and Methods in Physics Research Section B: Beam Interactions with Materials and Atoms*, 266(3):351 – 356, 2008. Low Energy Positron and Positronium Physics Proceedings of the XIV International Workshop on Low Energy Positron and Positronium Physics. doi:http://dx.doi.org/10.1016/j.nimb.2007.12.010.

[166] R. Khatri, M. Charlton, P. Sferlazzo, K. G. Lynn, A. P. Mills, Jr., and L. O. Roellig. Improvement of rare-gas solid moderators by using conical geometry. *Appl. Phys. Lett.*, 57(22):2374–2376, 1990. doi:10.1063/1.103856.

[167] Bernd A. Kniehl, Anatoly V. Kotikov, and Oleg L. Veretin. Orthopositronium lifetime: Analytic results in $\mathcal{O}(\alpha)$ and $\mathcal{O}(\alpha^3 \ln \alpha)$. *Phys. Rev. Lett.*, 101:193401, Nov 2008. doi:10.1103/PhysRevLett.101.193401.

[168] Bernd A. Kniehl and Alexander A. Penin. Order $\alpha^7 \ln(1/\alpha)$ contribution to positronium hyperfine splitting. *Phys. Rev. Lett.*, 85:5094–5097, Dec 2000. doi:10.1103/PhysRevLett.85.5094.

[169] Mark Kowitt. Gravitational repulsion and dirac antimatter. *Int. J. Theor. Phys.*, 35:605631, Mar 1996. doi:10.1007/BF02082828.

[170] J. J. Krauth, K. Schuhmann, and M. A. Ahmed. Measuring the α-particle charge radius with muonic helium-4 ions. *Nature*, 589:527–531, Jan 2021. doi:10.1038/s41586-021-03183-1.

[171] Bernd Krietenstein, Peter Thoma, Thomas Weiland, and Rolf Schuhmann. The perfect boundary approximation technique facing the big challenge of high precision field computation. 1998. URL: https://api.semanticscholar.org/CorpusID:53448092.

[172] Laird Technologies, Inc. *Microwave Absorbing Foams: Eccosorb AN*. URL: https://www.laird.com/products/absorbers/microwave-absorbing-foams/multi-layer-foams/eccosorb-an.

[173] Willis E. Lamb. Theory of an optical maser. *Phys. Rev.*, 134:A1429–A1450, Jun 1964. doi:10.1103/PhysRev.134.A1429.

[174] M. L. Lewis and V. W. Hughes. Higher-Order Relativistic Contributions to the Combined Zeeman and Motional Stark Effects in Positronium. *Phys. Rev. A*, 8:625–639, Aug 1973. doi:10.1103/PhysRevA.8.625.

[175] Richard Ley, D. Hagena, D. Weil, G. Werth, W. Arnold, and H. Schneider. Spectroscopy of excited state positronium. *Hyperfine Interac-*

tions, 89(1):327–341, 1994. URL: http://dx.doi.org/10.1007/BF02064517, doi:10.1007/BF02064517.

[176] David R. Lide (ed.). *CRC Handbook of Chemistry and Physics, Internet Version*. CRC Press, Boca Raton, FL, 2005.

[177] E. M. Lifshitz. *Dokl. Akad. Nauk SSSR*, 60, 1948.

[178] G. Lindblad. On the generators of quantum dynamical semigroups. *Commun. Math. Phys.*, 48:199–130, 1976. doi:10.1007/BF01608499.

[179] L. Liszkay, M. F. Barthe, C. Corbel, P. Crivelli, P. Desgardin, M. Etienne, T. Ohdaira, P. Perez, R. Suzuki, V. Valtchev, and A. Walcarius. Orthopositronium annihilation and emission in mesostructured thin silica and silicalite-1 films. *Appl. Surf. Sci.*, 255(1):187–190, 2008. doi:10.1016/j.apsusc.2008.05.210.

[180] L. Liszkay, C. Corbel, P. Perez, P. Desgardin, M. F. Barthe, T. Ohdaira, R. Suzuki, P. Crivelli, U. Gendotti, A. Rubbia, M. Etienne, and A. Walcarius. Positronium reemission yield from mesostructured silica films. *Appl. Phys. Lett.*, 92(6):063114, 2008. doi:10.1063/1.2844888.

[181] S. R. Lundeen and F. M. Pipkin. Separated oscillatory field measurement of the lamb shift in H, $n = 2$. *Metrologia*, 22(1):9, jan 1986. doi:10.1088/0026-1394/22/1/003.

[182] B. Mansoulié. Status of the GBAR experiment at CERN. *Hyperfine Interact.*, 240, 2019. doi:10.1007/s10751-018-1550-y.

[183] Valter Mariani Primiani, Franco Moglie, and Anna Pia Pastore. Field penetration through a wire mesh screen excited by a reverberation chamber field: FDTD analysis and experiments. *IEEE Transactions on Electromagnetic Compatibility*, 51(4):883–891, 2009. doi:10.1109/TEMC.2009.2032650.

[184] S. Mariazzi, B. Rienäcker, R. Magrin Maffei, L. Povolo, S. Sharma, R. Caravita, L. Penasa, P. Bettotti, M. Doser, and R. S. Brusa. Forward emission of positronium from nanochanneled silicon membranes. *Phys. Rev. B*, 105:115422, Mar 2022. doi:10.1103/PhysRevB.105.115422.

[185] A. Marsman, M. Horbatsch, and E. A. Hessels. Shifts due to neighboring resonances for microwave measurements of the 2 ^3p fine structure of helium. *Phys. Rev. A*, 86:012510, Jul 2012. doi:10.1103/PhysRevA.86.012510.

[186] Arthur Matveev, Christian G. Parthey, Katharina Predehl, Janis Alnis, Axel Beyer, Ronald Holzwarth, Thomas Udem, Tobias Wilken, Nikolai Kolachevsky, Michel Abgrall, Daniele Rovera, Christophe Salomon, Philippe Laurent, Gesine Grosche, Osama Terra, Thomas Legero, Harald Schnatz, Stefan Weyers, Brett Altschul, and Theodor W. Hänsch. Precision measurement of the hydrogen $1s-2s$ frequency via a 920-km fiber link. *Phys. Rev. Lett.*, 110:230801, Jun 2013. doi:10.1103/PhysRevLett.110.230801.

[187] R. A. McFarlane, W. R. Bennett Jr., and W. E. Lamb Jr. Single mode tuning dip in the power output of an he-ne optical maser. *Applied Physics Letters*, 2(10):189–190, 1963. URL: http://dx.doi.org/10.1063/1.1753727.

[188] F. Merkt and R. N. Zare. On the lifetimes of Rydberg states probed by delayed pulsed field ionization. *The Journal of Chemical Physics*, 101(5):3495–3505, 1994. URL: http://dx.doi.org/10.1063/1.467534.

[189] L. Michel. Selection rules imposed by charge conjugation. *Il Nuovo Cimento (1943-1954)*, 10(3):319–339, 1953. doi:10.1007/BF02786202.

[190] Koji Michishio, Tsuneto Kanai, Susumu Kuma, Toshiyuki Azuma, Ken Wada, Izumi Mochizuki, Toshio Hyodo, Akira Yagishita, and Yasuyuki Nagashima. Observation of a shape resonance of the positronium negative

ion. *Nature Communications*, 7:11060–, March 2016. doi:10.1038/ncomms11060.

[191] Koji Michishio, Susumu Kuma, Yugo Nagata, Luca Chiari, Taro Iizuka, Riki Mikami, Toshiyuki Azuma, and Yasuyuki Nagashima. Threshold photodetachment spectroscopy of the positronium negative ion. *Phys. Rev. Lett.*, 125:063001, Aug 2020. doi:10.1103/PhysRevLett.125.063001.

[192] A. P. Mills, Jr. Time bunching of slow positrons for annihilation lifetime and pulsed laser photon absorption experiments. *Appl. Phys.*, 22(3):273–276, 1980. doi:10.1007/BF00899876.

[193] A. P. Mills, Jr. Line-shape effects in the measurement of the positronium hyperfine interval. *Phys. Rev. A*, 27:262–267, Jan 1983. doi:10.1103/PhysRevA.27.262.

[194] A. P. Mills, Jr. Measurement of the decay rate of the positronium negative ion. *Phys. Rev. Lett.*, 50:671–674, Feb 1983. doi:10.1103/PhysRevLett.50.671.

[195] A. P. Mills, Jr. and G. H. Bearman. New measurement of the positronium hyperfine interval. *Phys. Rev. Lett.*, 34:246–250, Feb 1975. doi:10.1103/PhysRevLett.34.246.

[196] A. P. Mills, Jr., S. Berko, and K. F. Canter. Fine-Structure Measurement in the First Excited State of Positronium. *Phys. Rev. Lett.*, 34:1541–1544, Jun 1975. doi:10.1103/PhysRevLett.34.1541.

[197] A. P. Mills, Jr. and E. M. Gullikson. Solid neon moderator for producing slow positrons. *Appl. Phys. Lett.*, 49:1121, 1986. doi:http://dx.doi.org/10.1063/1.97441.

[198] A. P. Mills, Jr., E. D. Shaw, M. Leventhal, R. J. Chichester, and D. M. Zuckerman. Thermal desorption of cold positronium from oxygen-treated

Al(111) surfaces. *Phys. Rev. B*, 44:5791–5799, Sep 1991. doi:10.1103/PhysRevB.44.5791.

[199] A. P. Mills, Jr., S. S. Voris, and Tamara S. Andrew. Solid Kr moderator for producing slow positrons. *Journal of Applied Physics*, 76(4):2556–2558, 1994. doi:http://dx.doi.org/10.1063/1.357550.

[200] Akira Miyazaki. *Direct Measurement of the Hyperfine Structure Interval of Positronium Using High-Power Millimeter Wave Technology*. Springer Tokyo, 2015. doi:10.1007/978-4-431-55606-0.

[201] O. E. Mogensen. Spur reaction model of positronium formation. *The Journal of Chemical Physics*, 60(3):998–1004, 1974. doi:http://dx.doi.org/10.1063/1.1681180.

[202] St. Mohorovičić. Möglichkeit neuer elemente und ihre bedeutung für die astrophysik. *Astronomische Nachrichten*, 253(4):93–108, 1934. doi:10.1002/asna.19342530402.

[203] P. Moskal, A. Gajos, et al. Testing CPT symmetry in ortho-positronium decays with positronium annihilation tomography. *Nature Communications*, 12:5658, 2021. URL: https://www.nature.com/articles/s41467-021-25905-9.

[204] X. Mougeot. Reliability of usual assumptions in the calculation of β and ν spectra. *Phys. Rev. C*, 91:055504, May 2015. doi:10.1103/PhysRevC.91.055504.

[205] T. J. Murphy and C. M. Surko. Positron trapping in an electrostatic well by inelastic collisions with nitrogen molecules. *Phys. Rev. A*, 46:5696–5705, Nov 1992. doi:10.1103/PhysRevA.46.5696.

[206] John E. Nafe and Edward B. Nelson. The hyperfine structure of hydrogen and deuterium. *Phys. Rev.*, 73:718–728, Apr 1948. doi:10.1103/PhysRev.73.718.

[207] Y. Nagashima, M. Kakimoto, T. Hyodo, K. Fujiwara, A. Ichimura, T. Chang, J. Deng, T. Akahane, T. Chiba, K. Suzuki, B. T. A. McKee, and A. T. Stewart. Thermalization of free positronium atoms by collisions with silica-powder grains, aerogel grains, and gas molecules. *Phys. Rev. A*, 52:258–265, Jul 1995. doi:10.1103/PhysRevA.52.258.

[208] Y. Nagashima, Y. Morinaka, T. Kurihara, Y. Nagai, T. Hyodo, T. Shidara, and K. Nakahara. Origins of positronium emitted from SiO_2. *Phys. Rev. B*, 58:12676–12679, Nov 1998. doi:10.1103/PhysRevB.58.12676.

[209] Y. Nagata, K. Michishio, T. Iizuka, H. Kikutani, L. Chiari, F. Tanaka, and Y. Nagashima. Motion-induced transition of positronium through a static periodic magnetic field in the sub-THz region. *Phys. Rev. Lett.*, 124:173202, Apr 2020. doi:10.1103/PhysRevLett.124.173202.

[210] M. R. Natisin, J. R. Danielson, and C. M. Surko. Formation of buffer-gas-trap based positron beams. *Physics of Plasmas*, 22(3), 2015. doi:http://dx.doi.org/10.1063/1.4913354.

[211] D. M. Newson, T. J. Babij, and D. B. Cassidy. An energy tunable continuous 2^3S_1 positronium beam. *Review of Scientific Instruments*, 94(8):083201, 08 2023. doi:10.1063/5.0167125.

[212] M. M. Nieto, R. J. Hughes, and T. Goldman. Gravity and antimatter. *Scientific American*, 258(3):48–56, 1988. doi:doi:10.1038/scientificamerican0388-48.

[213] M. K. Oberthaler. Anti-matter wave interferometry with positronium. *Nuclear Instruments and Methods in Physics Research Section B: Beam Interactions with Materials and Atoms*, 192(1):129–134, 2002. doi:https://doi.org/10.1016/S0168-583X(02)00793-0.

[214] B. Ohayon, G. Janka, I. Cortinovis, Z. Burkley, L. de Sousa Borges, E. Depero, A. Golovizin, X. Ni, Z. Salman, A. Suter, C. Vigo, T. Prokscha, and

P. Crivelli. Precision measurement of the lamb shift in muonium. *Phys. Rev. Lett.*, 128:011802, Jan 2022. doi:10.1103/PhysRevLett.128.011802.

[215] A. Ore and J. L. Powell. Three-Photon Annihilation of an Electron-Positron Pair. *Phys. Rev.*, 75:1696–1699, Jun 1949. doi:10.1103/PhysRev.75.1696.

[216] K. Pachucki and S. G. Karshenboim. Higher-order recoil corrections to energy levels of two-body systems. *Phys. Rev. A*, 60:2792–2798, Oct 1999. doi:10.1103/PhysRevA.60.2792.

[217] J. Palmer and S. D. Hogan. Electric Rydberg-Atom Interferometry. *Phys. Rev. Lett.*, 117:250404, 2019. doi:10.1103/PhysRevLett.122.250404.

[218] J. Palmer and S. D. Hogan. Matter-wave interferometry with atoms in high Rydberg states. *Molecular Physics*, 95:3108–3119, 2019. doi:doi.org/10.1080/00268976.2019.1607916.

[219] P. Pérez et al. The GBAR antimatter gravity experiment. *Hyperfine Interactions*, 233(1):21–27, 2015. doi:10.1007/s10751-015-1154-8.

[220] M. P. Petkov, K. G. Lynn, L. O. Roellig, and T. D. Troev. An investigation of positrons interacting with solid argon, krypton and xenon. *Applied Surface Science*, 116:13 – 18, 1997. URL: http://www.sciencedirect.com/science/article/pii/S016943329600966X.

[221] A. Pineda and J. Soto. Potential NRQED: The positronium case. *Phys. Rev. D*, 59:016005, Dec 1998. doi:10.1103/PhysRevD.59.016005.

[222] J. Pirenne. *Le champ propre et l'interaction des particules de Dirac suivant l'electrodynamique quantique; Propositions donnees par la Faculte*. PhD thesis, University of Paris, 1944.

[223] Randolf Pohl et al. The size of the proton. *Nature*, 466(7303):213–216, July 2010. URL: http://dx.doi.org/10.1038/nature09250.

[224] Andrzej Pokraka and Andrzej Czarnecki. Positronium decay into a photon and neutrinos. *Phys. Rev. D*, 94:113012, Dec 2016. doi:10.1103/PhysRevD.94.113012.

[225] M. R. Poulsen, M. Charlton, J. Chevallier, B. I. Deutch, L. V. Jorgensen, and G. Laricchia. Thermal activation of positronium from thin Ag(100) films in backscattering and transmission geometries. *Journal of Physics: Condensed Matter*, 3(17):2849, 1991. URL: http://stacks.iop.org/0953-8984/3/i=17/a=002.

[226] David M. Pozar. *Microwave Engineering*. Wiley, forth edition, 2012.

[227] Mariusz Puchalski, Andrzej Czarnecki, and Savely G. Karshenboim. Positronium-ion decay. *Phys. Rev. Lett.*, 99:203401, Nov 2007. doi:10.1103/PhysRevLett.99.203401.

[228] Norman F. Ramsey. A new molecular beam resonance method. *Phys. Rev.*, 76:996–996, Oct 1949. doi:10.1103/PhysRev.76.996.

[229] M. H. Rayment, L. Gurung, R. E. Sheldon, S. D. Hogan, and D. B. Cassidy. Multiring electrostatic guide for rydberg positronium. *Phys. Rev. A*, 100:013410, Jul 2019. doi:10.1103/PhysRevA.100.013410.

[230] F. H. Read, N. J. Bowring, P. D. Bullivant, and R. R. A. Ward. Penetration of electrostatic fields and potentials through meshes, grids, or gauzes. *Review of Scientific Instruments*, 69(5):2000–2006, 1998. doi:10.1063/1.1148888.

[231] B. Rienäcker, T. Gigl, G. Nebbia, F. Pino, and C. Hugenschmidt. Absolute fraction of emitted Ps determined by geant4-supported analysis of gamma spectra. *Phys. Rev. A*, 102:062212, Dec 2020. doi:10.1103/PhysRevA.102.062212.

[232] M. W. Ritter, P. O. Egan, V. W. Hughes, and K. A. Woodle. Precision determination of the hyperfine-structure interval in the ground state of positronium. v. *Phys. Rev. A*, 30:1331–1338, Sep 1984. doi:10.1103/PhysRevA.30.1331.

[233] Arthur E. Ruark. Positronium. *Phys. Rev.*, 68:278–278, Dec 1945. doi:10.1103/PhysRev.68.278.

[234] Andrei D Sakharov. Violation of CP invariance, C asymmetry, and baryon asymmetry of the universe. *Soviet Physics Uspekhi*, 34(5):392, may 1991. doi:10.1070/PU1991v034n05ABEH002497.

[235] Simone Sala, Fabrizio Castelli, Marco Giammarchi, Stefano Siccardi, and Stefano Olivares. Matter-wave interferometry: towards antimatter interferometers. *Journal of Physics B: Atomic, Molecular and Optical Physics*, 48(19):195002, 2015. URL: http://stacks.iop.org/0953-4075/48/i=19/a=195002.

[236] Y. Sasaki, A. Miyazaki, A. Ishida, T. Namba, S. Asai, T. Kobayashi, H. Saito, K. Tanaka, and A. Yamamoto. Measurement of positronium hyperfine splitting with quantum oscillation. *Physics Letters B*, 697(2):121 – 126, 2011. doi:http://dx.doi.org/10.1016/j.physletb.2011.01.052.

[237] Paola Scampoli and James Storey. The AEgIS experiment at CERN for the measurement of antihydrogen gravity acceleration. *Modern Physics Letters A*, 29(17):1430017, 2014. doi:10.1142/S0217732314300171.

[238] J. Scherk. Antigravity: A crazy idea? *Physics Letters B*, 88(3):265 – 267, 1979. doi:http://dx.doi.org/10.1016/0370-2693(79)90463-5.

[239] P. J. Schultz and K. G. Lynn. Interaction of positron beams with surfaces, thin films, and interfaces. *Rev. Mod. Phys.*, 60:701–779, July 1988. doi:10.1103/RevModPhys.60.701.

[240] C. Schwob, L. Jozefowski, B. de Beauvoir, L. Hilico, F. Nez, L. Julien, F. Biraben, O. Acef, J.-J. Zondy, and A. Clairon. Optical frequency measurement of the $2S-12D$ transitions in hydrogen and deuterium: Rydberg constant and lamb shift determinations. *Phys. Rev. Lett.*, 82:4960–4963, Jun 1999. doi:10.1103/PhysRevLett.82.4960.

[241] J. Shapiro and G. Breit. Metastability of 2*S* states of hydrogenic atoms. *Phys. Rev.*, 113:179–181, Jan 1959. doi:10.1103/PhysRev.113.179.

[242] R. E. Sheldon, T. J. Babij, B. A. Devlin-Hill, L. Gurung, and D. B. Cassidy. Measurement of the annihilation decay rate of $2\,^3S^1$ positronium. *Europhysics Letters*, 132(1):13001, Nov 2020. doi:10.1209/0295-5075/132/13001.

[243] R. E. Sheldon, T. J. Babij, S. H. Reeder, S. D. Hogan, and D. B. Cassidy. Microwave spectroscopy of positronium atoms in free space. *Phys. Rev. A*, 107:042810, Apr 2023. doi:10.1103/PhysRevA.107.042810.

[244] R. E. Sheldon, T. J. Babij, S. H. Reeder, S. D. Hogan, and D. B. Cassidy. Precision microwave spectroscopy of the positronium $2\,^3S_1 \rightarrow 2\,^3P_2$ interval. *Phys. Rev. Lett.*, 131:043001, Jul 2023. doi:10.1103/PhysRevLett.131.043001.

[245] K Shu, X Fan, T Yamazaki, T Namba, S Asai, K Yoshioka, and M Kuwata-Gonokami. Study on cooling of positronium for bose einstein condensation. *Journal of Physics B: Atomic, Molecular and Optical Physics*, 49(10):104001, 2016. doi:10.1088/0953-4075/49/10/104001.

[246] M. Skalsey and J. Van House. First test of *CP* invariance in the decay of positronium. *Phys. Rev. Lett.*, 67:1993–1996, Oct 1991. doi:10.1103/PhysRevLett.67.1993.

[247] Aaron L. Stancik and Eric B. Brauns. A simple asymmetric lineshape for fitting infrared absorption spectra. *Vibrational Spectroscopy*, 47(1):66–69,

2008. doi:https://doi.org/10.1016/j.vibspec.2008.02.009.

[248] G. Strang. *Linear Algebra and Its Applications*. Academic Press, Inc., Orlando, FL, second edition, 1980.

[249] Michael A. Stroscio and John M. Holt. Radiative corrections to the decay rate of orthopositronium. *Phys. Rev. A*, 10:749–755, Sep 1974. doi:10.1103/PhysRevA.10.749.

[250] C. M. Surko, M. Leventhal, and A. Passner. Positron plasma in the laboratory. *Phys. Rev. Lett.*, 62:901–904, Feb 1989. doi:10.1103/PhysRevLett.62.901.

[251] S. J. Tao. The formation of positronium in molecular substances. *Applied physics*, 10(1):67–79, 1976. doi:10.1007/BF00929530.

[252] E. D. Theriot, R. H. Beers, and V. W. Hughes. Precision redetermination of the hyperfine structure interval of positronium. *Phys. Rev. Lett.*, 18:767–769, May 1967. doi:10.1103/PhysRevLett.18.767.

[253] E. D. Theriot, R. H. Beers, V. W. Hughes, and K. O. H. Ziock. Precision redetermination of the fine-structure interval of the ground state of positronium and a direct measurement of the decay rate of parapositronium. *Phys. Rev. A*, 2:707–721, Sep 1970. doi:10.1103/PhysRevA.2.707.

[254] J. D. R. Tommey and S. D. Hogan. Matter-wave interferometry with helium atoms in low-l rydberg states. *Phys. Rev. A*, 104:033305, Sep 2021. doi:10.1103/PhysRevA.104.033305.

[255] R. S. Vallery, P. W. Zitzewitz, and D. W. Gidley. Resolution of the Orthopositronium-Lifetime Puzzle. *Phys. Rev. Lett.*, 90:203402, May 2003. doi:10.1103/PhysRevLett.90.203402.

[256] J. Van House and P. W. Zitzewitz. Probing the positron moderation process using high-intensity, highly polarized slow-positron beams. *Phys. Rev. A*, 29:96–105, Jan 1984. doi:10.1103/PhysRevA.29.96.

[257] Guido Van Rossum and Fred L. Drake. *Python 3 Reference Manual*. CreateSpace, Scotts Valley, CA, 2009.

[258] Guido Van Rossum and Fred L Drake Jr. *Python reference manual*. Centrum voor Wiskunde en Informatica Amsterdam, 1995.

[259] A. Vehanen, K. G. Lynn, P. J. Schultz, and M. Eldrup. Improved slow-positron yield using a single crystal tungsten moderator. *Appl. Phys. A*, 32:163–167, Nov 1983. doi:10.1007/BF00616613.

[260] C. Vigo, L. Gerchow, L. Liszkay, A. Rubbia, and P. Crivelli. First search for invisible decays of orthopositronium confined in a vacuum cavity. *Phys. Rev. D*, 97:092008, May 2018. doi:10.1103/PhysRevD.97.092008.

[261] C. Vigo, L. Gerchow, B. Radics, M. Raaijmakers, A. Rubbia, and P. Crivelli. New bounds from positronium decays on massless mirror dark photons. *Phys. Rev. Lett.*, 124:101803, Mar 2020. doi:10.1103/PhysRevLett.124.101803.

[262] Pauli Virtanen, SciPy 1.0 Contributors, and Others. SciPy 1.0: Fundamental Algorithms for Scientific Computing in Python. *Nature Methods*, 17:261–272, 2020. doi:10.1038/s41592-019-0686-2.

[263] E. Vliegen, S. D. Hogan, H. Schmutz, and F. Merkt. Stark deceleration and trapping of hydrogen Rydberg atoms. *Phys. Rev. A*, 76:023405, Aug 2007. doi:10.1103/PhysRevA.76.023405.

[264] John Volakis. *Antenna Engineering Handbook, Fourth Edition*. McGraw-Hill Professional, 2007. doi:10.1036/0071475745.

[265] A. C. Vutha and E. A. Hessels. Frequency-offset separated oscillatory fields. *Phys. Rev. A*, 92:052504, Nov 2015. doi:10.1103/PhysRevA.92.052504.

[266] T. E. Wall, A. M. Alonso, B. S. Cooper, A. Deller, S. D. Hogan, and D. B. Cassidy. Selective Production of Rydberg-Stark States of Positronium. *Phys. Rev. Lett.*, 114:173001, Apr 2015. doi:10.1103/PhysRevLett.114.173001.

[267] P. Wallyn, W. A. Mahoney, P. Durouchoux, and C. Chapuis. The Positronium Radiative Combination Spectrum: Calculation in the Limit of Thermal Positrons and Low Densities. *apj*, 465:473, July 1996. doi:10.1086/177434.

[268] M. H. Weber, S. Tang, S. Berko, B. L. Brown, K. F. Canter, K. G. Lynn, A. P. Mills, L. O. Roellig, and A. J. Viescas. Observation of positronium specular reflection from LiF. *Phys. Rev. Lett.*, 61:2542–2545, Nov 1988. doi:10.1103/PhysRevLett.61.2542.

[269] T. Weiland. A discretization method for the solution of maxwell's equations for six-component fields. *Electronics and Communications*, 31:116–120, 1977.

[270] T. Weiland. Time domain electromagnetic field computation with finite difference methods. *International Journal of Numerical Modelling: Electronic Networks, Devices and Fields*, 9(4):295–319, 1996. URL: https://onlinelibrary.wiley.com/doi/abs/10.1002/%28SICI%291099-1204%28199607%299%3A4%3C295%3A%3AAID-JNM240%3E3.0.CO%3B2-8,

[271] M. Weinstein, R. Deutsch and S. C. Brown. Fine structure of positronium. *Phys. Rev.*, 94:758, Mar 1954.

[272] M. Weinstein, R. Deutsch and S. C. Brown. Fine structure of positronium. *Phys. Rev.*, 98:223, 1955.

[273] C. I. Westbrook, D. W. Gidley, R. S. Conti, and A. Rich. New precision measurement of the orthopositronium decay rate: A discrepancy with theory. *Phys. Rev. Lett.*, 58:2153–2153, May 1987. doi:10.1103/PhysRevLett.58.2153.6.

[274] J. A. Wheeler. Polyelectrons. *Annals of the New York Academy of Sciences*, 48(3):219–238, 1946. doi:10.1111/j.1749-6632.1946.tb31764.x.

[275] A. I. Williams, D. J. Murtagh, S. E. Fayer, S. L. Andersen, J. Chevallier, Á. Kövér, P. Van Reeth, J. W. Humberston, and G. Laricchia. Moderation and diffusion of positrons in tungsten meshes and foils. *Journal of Applied Physics*, 118(10):105302, 2015. doi:10.1063/1.4930033.

[276] William H. Wing. Electrostatic Trapping of Neutral Atomic Particles. *Phys. Rev. Lett.*, 45:631–634, Aug 1980. doi:10.1103/PhysRevLett.45.631.

[277] L. Wolfenstein and D. G. Ravenhall. Some Consequences of Invariance under Charge Conjugation. *Phys. Rev.*, 88:279–282, Oct 1952. doi:10.1103/PhysRev.88.279.

[278] W. Xiong, A. Gasparian, H. Gao, et al. A small proton charge radius from an electron–proton scattering experiment. *Nature*, 575:147–150, 2019. doi:https://doi.org/10.1038/s41586-019-1721-2.

[279] T. Yamazaki, A. Miyazaki, T. Suehara, T. Namba, S. Asai, T. Kobayashi, H. Saito, I. Ogawa, T. Idehara, and S. Sabchevski. Direct Observation of the Hyperfine Transition of Ground-State Positronium. *Phys. Rev. Lett.*, 108:253401, Jun 2012. doi:10.1103/PhysRevLett.108.253401.

[280] T. Yamazaki, T. Namba, S. Asai, and T. Kobayashi. Search for *CP* Violation in Positronium Decay. *Phys. Rev. Lett.*, 104:083401, Feb 2010. doi:10.1103/PhysRevLett.104.083401.

[281] C. N. Yang. Selection rules for the dematerialization of a particle into two photons. *Phys. Rev.*, 77:242–245, Jan 1950. doi:10.1103/PhysRev.77.242.

[282] Jacek Zatorski. $\mathscr{O}(m\alpha^6)$ corrections to energy levels of positronium with nonvanishing orbital angular momentum. *Phys. Rev. A*, 78:032103, Sep 2008. doi:10.1103/PhysRevA.78.032103.

[283] K. P. Ziock, R. H. Howell, F. Magnotta, R. A. Failor, and K. M. Jones. First observation of resonant excitation of high- n states in positronium. *Phys. Rev. Lett.*, 64:2366–2369, May 1990. doi:10.1103/PhysRevLett.64.2366.